UNIVERSITY*of*
TASMANIA

Australo-Antarctica in the supercontinent cycle

Alessandro Maritati

MSc, The University of Western Australia

Institute for Marine and Antarctic Studies (IMAS)

Submitted in fulfilment of the requirements for the degree of

Doctor of Philosophy

University of Tasmania

November 2020

Declaration of originality

This thesis contains no material which has been accepted for a degree or diploma by the University or any other institution, except by way of background information and duly acknowledged in the thesis, and to the best of my knowledge and belief no material previously published or written by another person except where due acknowledgement is made in the text of the thesis, nor does the thesis contain any material that infringes copyright.

Authority of access

This thesis may be made available for loan and limited copying and communication in accordance with the Copyright Act 1968.

Statement regarding published work contained in this thesis

The publishers of the papers comprising Chapters 2 and 3 hold the copyright for that content and access to the material should be sought from the respective journals. The remaining non published content of the thesis may be made available for loan and limited copying and communication in accordance with the Copyright Act 1968.

Signed: **Dated:** 15/08/2020

Statement of Co-Authorship

The following people and institutions contributed to the publication of work undertaken as part of this thesis:

Candidate: Alessandro Maritati, Institute for Marine and Antarctic Studies (IMAS), University of Tasmania
Author 1: Jacqueline Halpin, Supervisor, Institute for Marine and Antarctic Studies (IMAS), University of Tasmania
Author 2: Joanne Whittaker, Supervisor, Institute for Marine and Antarctic Studies (IMAS), University of Tasmania
Author 3: Nathan Daczko, ARC Centre of Excellence for Core to Crust Fluid Systems and GEMOC, Department of Earth and Planetary Sciences, Macquarie University
Author 4: Martin Danišík, John de Laeter Centre/The Institute for Geoscience Research, Curtin University
Author 5: Alan Aitken, School of Earth Sciences, University of Western Australia
Author 6: Carmine Wainman, Australian School of Petroleum, University of Adelaide

Contribution of work by co-authors for each paper:

Paper 1: Located in Chapter 2
Maritati, A., Halpin, J. A, Whittaker, J. M., Daczko, N. R. (2019). Fingerprinting Proterozoic Bedrock in Interior Wilkes Land, East Antarctica. Scientific Reports, 9(1), 1–12.

Candidate designed the study and led the planning and writing of the paper. Candidate is responsible for U–Pb zircon and monazite geochronology of sandstone erratic samples, Hf analyses and interpretation of aeromagnetic data. Author 1 performed U– Pb geochronology of Chick Island samples. Authors 1, 2 and 3 contributed to writing and revision of the paper.

Paper 2: Located in Chapter 3
Maritati, A., Danišík, M., Halpin, J. A., Whittaker, J. M., Aitken, A. R. A. (2020). Pangea Rifting Shaped the East Antarctic Landscape. Tectonics, 39, e2020TC006180.

Candidate designed the study and led the planning and writing of the paper. Author 4 performed (U–Th)/He thermochronology. Candidate and Author 4 performed the thermal modelling work. Author 2 and Author 5 conceived the research project and acquired analytical funding. Authors 1, 2, 4 and 5 contributed to writing and revision of the paper.

Paper 3: Located in Chapter 4
Maritati, A., Halpin, J. A, Whittaker, J. M., Daczko, N. R., Wainman, C. C. Provenance of Late Jurassic–Early Cretaceous strata in the Mentelle Basin, southwestern Australia, reveals a trans-Gondwanan fluvial pathway (paper submitted to Gondwana Research).

Candidate designed the study and led the planning and writing of the paper. Candidate conceived the research project, acquired analytical funding and conducted U–Pb

geochronology and Hf analyses. Authors 1, 2, 3 and 6 contributed to writing and revision of the paper.

We, the undersigned, endorse the above stated contribution of work undertaken for each of the published (or submitted) peer-reviewed manuscripts contributing to this thesis:

Signed:

Alessandro Maritati
Candidate
Institute for Marine and Antarctic Studies
University of Tasmania
Date: 23/07/2020

Joanne M Whittaker
Primary Supervisor
Institute for Marine and Antarctic Studies
University of Tasmania
Date: 23/07/2020

Neil J Holbrook
Head of Centre, Oceans and Cryosphere
Institute for Marine and Antarctic Studies
University of Tasmania
Date: 13/08/2020

Preface

This PhD thesis consists of two articles that have been published in international, peer-reviewed journals (Chapters 2 and 3), and one article prepared for submission to an international, peer-reviewed journal (Chapter 4). The publications in Chapters 2 and 3 have been readapted to match the formatting and referencing style of this thesis. The thesis also contains an introductory chapter that provides an overview of the concepts and topics discussed in the subsequent chapters, and a discussion chapter that ties together the themes of each article. The Appendix include the supporting material for the three research chapters and the online version of Chapters 2 and 3.

Acknowledgements

These last years have been some of the most exciting and rewarding of my life and I wish to thank everyone who has supported and encouraged me throughout this endeavour.

Firstly, to my supervisors Jo and Jacqui. Thank you for all your enthusiasm, support and for constantly pushing me to think more critically about my own ideas. You both made a great supervisory team and I hope to continue collaborating with you in the future. Jo, thank you for offering me the chance to work on this project and giving me many opportunities to grow as a researcher, whether it be through advice, opening up collaborations or pushing me to attend conferences. Jacqui, your guidance throughout this PhD has been invaluable. Thank you for showing me the ropes of isotope geochemistry and always making time to chat with me; your breadth of knowledge always gave me new ideas and paths to lead my PhD down.

Thanks to Alan Aitken, Nathan Daczko Martin Danišík and all the people I have collaborated with throughout these years. Alan, it's always a pleasure getting lost in conversation about Antarctic geology with you, I look forward to the next chat. Nathan, thank you for all the time you spent chatting with me looking down the microscope during my visits at Macquarie Uni. Martin, thank you for always being available to answer all my questions and providing your expertise in thermochronology.

This project would not have happened without the continued support, skills and expertise from the team, both past and present, at CSL and CODES. Special thanks to Sandrin Feig, Karsten Goemann, Sebastien Meffre, Jay Thomson and James Tolley who patiently assisted me and answered all my questions.

To my family, Rosa and Sofia. Thank you for being by my side every step of the way; none of this would have been possible without you.

Abstract

The large-scale continental domains that make up East Antarctica are important to global plate reconstructions. A key piece in this continental jigsaw puzzle is the Australo-Antarctic domain that formed part of the Gondwana–Pangea (0.5–0.3 Ga), Rodinia (1.0 Ga), and Nuna (1.7 Ga) supercontinents. Its vast underexplored bedrock can inform tectonic and paleogeographic reconstructions through deep time. The central aim of this thesis is to constrain the poorly-known continental evolution of Australo-Antarctica in the context of supercontinent cycles. This aim is addressed by examining the geological record of frontier regions of Australo-Antarctica and the conjugate southern Australian region using a combination of regional geophysical data and rock- and sediment-based geological analysis in a plate reconstruction framework.

The first research chapter explores the poorly known age, composition and tectonic affinity of Precambrian basement and sedimentary cover of interior Wilkes Land. Zircon U–Pb–Hf isotopic data from isolated coastal outcrops are combined with regional aeromagnetic data to map Mesoproterozoic (c. 1600–1300 Ma) basement provinces across southern Australia and East Antarctica. This new analysis provides a revised basement architecture shaped through orogenic cycles associated with the Nuna and Rodinia supercontinents. Into the interior, the enigmatic subglacial Sabrina Basin mapped previously from geophysics, is here sampled for the first time via sandstone erratics deposited at the coast. Coupled *in situ* authigenic monazite and detrital zircon isotopic data reveal that these sandstones were deposited during the Neoproterozoic (before c. 633 Ma). Similarities in age and provenance between these Sabrina Basin samples and other Neoproterozoic strata in the Transantarctic Mountains (Beardmore Group) and southern Australia (Officer Basin) suggest that Neoproterozoic sedimentary rocks likely covered a large sector of the Australo-Antarctic domain, forming an extensive platform basin on the proto-Pacific rifting margin of Rodinia.

The second research chapter of this thesis examines the Phanerozoic tectonic history of Australo-Antarctica, with a focus on the age and tectonic origin of onshore sedimentary

basins. (U–Th)/He thermochronology data from basement rocks in the Bunger Hills region is used to investigate the timing of extensional tectonism of the inaccessible Knox Rift. Inverse modelling of thermochronology data support ~2–4 km of exhumation of local basement in the Late Paleozoic–Triassic during extension in the Knox Rift. These new results are combined with existing low-temperature (<300°C) thermochronology constraints from East Antarctic basement rocks to propose widespread basement exhumation in the Late Paleozoic–Triassic driven by intraplate extension during the earliest stages of Pangea rifting. This phase of tectonic activity is responsible for the formation of large basins across Pangea including the Knox Rift as well as the Aurora, Vincennes and Wilkes subglacial basins further east across Australo-Antarctica.

Paleozoic–Mesozoic km-scale exhumation of East Antarctic basement generated a significant volume of clastic material that filled basins across East Gondwana. The third research chapter focuses on refining sediment dispersal patterns using International Ocean Discovery Program (IODP) cores from Mesozoic strata in the frontier Mentelle Basin of southwestern Australia. Provenance of these sedimentary rocks is explored using detrital zircon and monazite isotopic data and is compared with the provenance record of other Antarctic and Australian Paleozoic–Mesozoic strata. The results provide the first record of a transcontinental sediment pathway connecting basement regions within the Gondwana-forming Kuunga Orogen (0.7–0.5 Ga) with the Tethys Ocean via a series of intra-Gondwanan rift basins. Together with other proposed large-scale sediment pathways, this was one of the principal modes of siliciclastic sediment delivery to Paleozoic–Mesozoic sedimentary basins in East Antarctica and Australia.

The results presented in this thesis reveal plate-scale processes in Australo-Antarctica in unprecedented detail, and in doing so more clearly frame its continental evolution into current plate tectonic models. This body of work will inform both future regional studies and global tectonic reconstructions.

Table of Contents

Chapter 1

Introduction

1.1 Preamble

East Antarctica preserves a rich geological record spanning more than three billion years that has enabled significant contributions to our understanding of plate tectonics and the evolution of the continents in deep time. East Antarctica's bedrock was involved in the amalgamation and breakup cycles of the Gondwana–Pangea (c. 0.5–0.3 Ga), Rodinia (c. 1.0 Ga), and Nuna (c. 1.7 Ga) supercontinents and holds insights into their tectonic evolution and paleogeography (Harley et al., 2013). However, limited rock exposure and geophysical coverage allows only glimpses into the processes that have shaped the East Antarctic bedrock over billions of years.

Plate reconstructions provide important constraints to refine the continental evolution of East Antarctica based on correlations with its better-known Gondwanan neighbours. East Antarctica is broadly divisible in three continent-scale domains with geological affinities to southern Africa, eastern India and southern Australia that were incorporated into Gondwana by "Pan-African" (c. 600–500 Ma) orogenic belts (Boger, 2011). This thesis focuses on the continental evolution of the Australo-Antarctic portion of East Antarctica, defined here as the sector west of the Transantarctic Mountains conjugate to southern Australia. The key aim of the work presented in this thesis is to fill significant gaps in the geological and tectonic evolution of Australo-Antarctica and understand its history in the context of supercontinent cycles.

1.2 Tectonic history of Australo-Antarctica

Australo-Antarctica (Fig. 1.1) encompasses the geographical regions of Queen Mary Land, Wilkes Land, Terre Adélie and George V Land, which together comprise some of the most inaccessible regions of the Antarctic continent. In the traditional interpretation, the vast majority of Australo-Antarctica consists of crystalline basement of Neoarchean–Late Mesoproterozoic age (Fitzsimons, 2003). In this paradigm, it shares a common tectonic history with southern Australia having formed during orogenic cycles associated with the Nuna and Rodinia supercontinents and remaining co-joined within Gondwana prior to

continental breakup in the Late Cretaceous (Boger, 2011; Fitzsimons, 2003) (Fig. 1.1). In the east, Neoarchean–Paleoproterozoic basement rocks of Terre Adélie and George V Land are equivalent to the Gawler Craton that together formed the cratonic nucleus of the Mawson Continent/Craton (Fanning et al., 1996; Fitzsimons, 2003). In the west, the Windmill Islands and Bunger Hills regions are dominated by Late Mesoproterozoic magmatic and metamorphic basement rocks that correlate with the Albany-Fraser Orogen of southwestern Australia (Morrissey et al., 2017; Post et al., 1997; Tucker et al., 2020; Zhang et al., 2012). These regions comprise the broader Albany-Fraser-Wilkes Orogen which, together with the Musgrave Orogen, have traditionally been interpreted to represent a collisional suture between the Mawson Craton and West/North Australian cratons during the amalgamation of Rodinia (e.g. Myers et al., 1996). The western margin of Australo-Antarctica subsequently amalgamated with Indo-Antarctica along the Kuunga Orogen forming part of Gondwana (Daczko et al., 2018 and references therein).

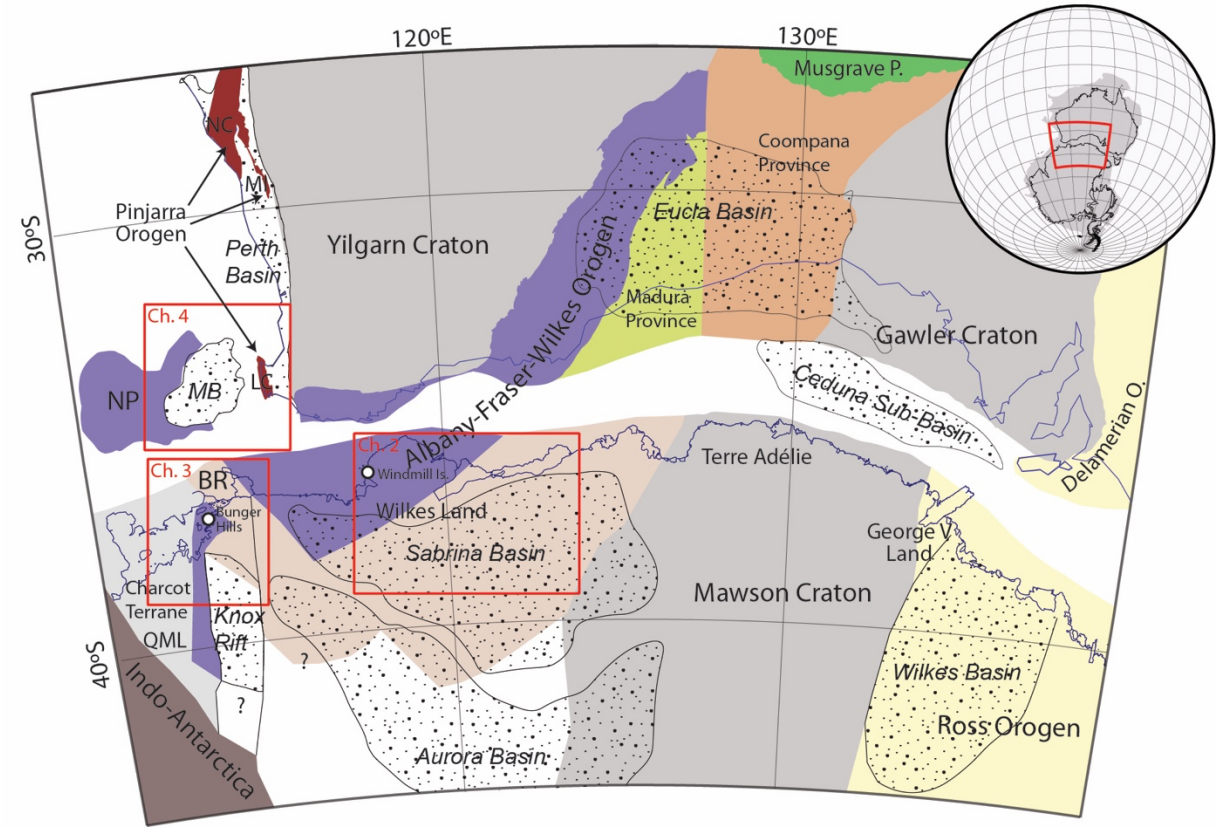

Figure 1.1. Palinspastic reconstruction of tectonic elements of southwestern Australia and Australo-Antarctica within Gondwana using plate geometries and rotation poles of Matthews et al. (2016). In this reconstruction, Australia is fixed in its present-day position. Australian tectonic elements are simplified from Raymond et al. (2018); for illustrative purposes, Australian sedimentary basins post-dating the breakup of Australia-Antarctica (i.e. Eucla Basin and Ceduna sub-basin) are also shown. Australo-

Antarctic tectonic elements are based on Aitken et al. (2014); Daczko et al. (2018); Halpin et al. (2020); Maritati et al. (2016). The location of regions investigated in the chapters of the thesis are also indicated. Abbreviations are in Australia: BR – Bruce Rise; LC – Leeuwin Complex; MB – Mentelle Basin; MI – Mullingarra Inlier; NC – Northampton Complex; NP – Naturaliste Plateau; QML– Queen Mary Land.

Within the past few years, insights provided by deep drilling and geophysical campaigns across the Proterozoic basement of the Coompana and Madura provinces of Australia (Fig. 1.1, comprising basement between the Gawler Craton and the Albany-Fraser Orogen) have identified juvenile crustal components suggestive of active-margin activity between 1.6 and 1.3 Ga (Kirkland et al., 2017; Spaggiari & Smithies, 2015; Spaggiari et al., 2018; Wise et al., 2018). From these and other regional datasets, a generation of more nuanced tectonic models are emerging that invoke convergence of the Mawson Craton with the West and North Australian cratons via a series of extensional-accretionary processes (e.g. Aitken et al., 2016a; Smits et al., 2014). These magmatic and accretionary events remain largely unknown across the rifted margin into Antarctica; however, recent models of basement architecture based on geophysical interpretations in a plate reconstruction context indicate that equivalent rocks may underlie the ice sheet in Australo-Antarctica (Aitken et al., 2016a).

Ice-penetrating radar data has revealed that vast regions in the interior are characterised by large subglacial depressions grounded below sea level and contrast with the high topography in the other large-scale Precambrian domains of East Antarctica. Gravity and depth to magnetic basement data reveal that these depressions likely contain extensive sedimentary basins overlying Precambrian basement (Aitken et al., 2014). The largest of these basins are the Knox Basin in the Bunger Hills region, the Aurora and Vincennes basins in interior Wilkes Land and the Wilkes Basin in George V Land. Contrary to the prevailing models which suggest Australo-Antarctica was largely unaffected by Phanerozoic tectonic events (e.g. Boger, 2011), these sedimentary basins support onshore extensional tectonism that is not represented in the exposed geological record and postdates the Late Mesoproterozoic assembly of the Australo-Antarctica. While fundamental characteristics such as extent, sediment thickness and overall geometry have been defined through geophysical modelling (e.g. Aitken et al., 2016b; Frederick et al., 2016; Maritati et al., 2016; Paxman et al., 2018), very little is known about the tectonic

origin of these Australo-Antarctic sedimentary basins. Current hypotheses suggest that these basins represent the onshore expression of extensional tectonic activity associated with the Mesozoic breakup of East Gondwana (Aitken et al., 2014; Eagles, 2019; Maritati et al., 2016) or younger intraplate Cenozoic tectonism (Cianfarra & Maggi, 2017) based on comparisons with basins on the western and southern Australian margin (i.e. Mentelle, Perth, Bight/Ceduna and Eucla basins). 2D gravity modelling and depth to magnetic basement estimates suggest that Australo-Antarctic sedimentary basins contain kilometre thick sedimentary sequences. Sedimentary thicknesses vary between the 1–2 km-thick Sabrina Basin (Aitken et al., 2016b) to the 4–7 km-thick Knox, Aurora, Vincennes and Wilkes basins (Aitken et al., 2016b; Ferraccioli et al., 2009; Frederick et al., 2016; Maritati et al., 2016) and raise key questions regarding the provenance of the sediments and pathways for sediment dispersal during East Gondwana breakup. Investigation of the age, tectonic origin and provenance of these onshore sedimentary basins offers vast opportunities to refine the continental evolution of Australo-Antarctica after its Late Mesoproterozoic assembly.

1.3 Research aims and chapters outline

The central aim of this thesis is to examine the geological record and tectonic history of underexplored regions of Australo-Antarctica and place this evolution within recent models of supercontinent assembly and breakup. The specific objectives of this thesis are to:

(1) *Test and refine the relationship between the Precambrian basement provinces of Australo-Antarctica and southern Australia;*
(2) *Constrain the age and tectonic origin of Australo-Antarctic sedimentary basins;*
(3) *Examine the offshore sedimentary record to characterise source-to-sink pathways during East Gondwana rifting;*
(4) *Explore the impact of onshore extension on the topographic evolution of Australo-Antarctica;*

These specific objectives are achieved by interrogating the geological record of three key frontier regions of Australo-Antarctica and its conjugate Australian margin, 1) Wilkes

Land, 2) the Bunger Hills region, and 3) the Mentelle Basin of southwestern Australia. Following this introductory chapter, the results of this thesis are presented in three research chapters. A summary of the research chapters and relevance to the specific objectives of this study is presented below:

Chapter 2: Maritati, A., Halpin, J. A., Whittaker, J. M., Daczko, N. R. (2019). Fingerprinting Proterozoic Bedrock in Interior Wilkes Land, East Antarctica, *Scientific Reports*. 9(*1*), 1–12.

This paper explores the age and composition of largely subglacial Precambrian basement and sedimentary cover of the Sabrina Basin, Wilkes Land, between the well-studied outcrops of the Windmill Islands and Terre Adélie. This work fills a notable gap in the age and composition of subglacial bedrock in this sector of Australo-Antarctica and further contextualises its Proterozoic evolution in the supercontinent cycle. In situ zircon U–Pb–Hf isotopic data from rare exposed basement are combined with regional aeromagnetic data interpretations to provide the first evidence for Precambrian basement provinces in Wilkes Land equivalent to the Madura and Coompana Provinces of southern Australia. A clear geometrical framework is proposed for the correlation of Precambrian basement provinces across southern Australia and East Antarctica. Coupled in situ authigenic monazite and detrital zircon isotopic data from glacial sedimentary erratics sourced from the enigmatic Sabrina Basin provide the first evidence for the presence of Neoproterozoic sedimentary strata. This paper highlights the similarities in age and provenance between the Sabrina Basin erratic samples and other Neoproterozoic sedimentary sequences in the Transantarctic Mountains (Beardmore Group) and southern Australia (Officer Basin) formed during the breakup of Rodina. These connections suggest that Neoproterozoic sedimentary rocks likely covered a large sector of the Australo-Antarctic domain, forming an extensive platform basin on the proto-Pacific rifting margin of Rodinia.

Chapter 3: Maritati, A., Danisik, M., Halpin, J. A., Whittaker, J. M., Aitken, A. R. A. (2020). Pangea Rifting Shaped the East Antarctic Landscape. *Tectonics*, 39, e2020TC006180.

Sedimentary basins in the interior of Australo-Antarctica are inaccessible and available constraints on the timing of onshore extensional events are solely based on geophysical datasets. However, extensional tectonism typically leaves a thermal footprint which is preserved in the low-temperature (<200°C) cooling history of exposed basement rocks in the vicinity of tectonic structures. This paper utilises this thermal footprinting to investigate the timing of onshore tectonism in the Knox Rift, the site of a postulated Phanerozoic sedimentary basin in western Wilkes Land. Zircon and apatite (U–Th)/He thermochronology data of exposed Precambrian bedrock in the Bunger Hills region is used for inverse modelling, which reveals cooling of basement rocks from temperatures of 90–60 °C implying 2–4 km of exhumation of local basement during the Late Paleozoic–Triassic (c. 300–200 Ma), related to extension in the Knox Rift. This was followed by a second period of minor cooling from 40°C implying <1 km of exhumation in some regions during the Late Jurassic-Cretaceous (c. 160–120 Ma). These new results are compared with widespread evidence for a Late Paleozoic –Triassic basement exhumation event in other regions of Australo-Antarctica and Indo-Antarctica to define a major period of exhumation driven by Pangea-wide extensional tectonism. The paper proposes that sedimentary basins of Australo-Antarctica which include the Knox, Aurora and Wilkes basins were established during Late Paleozoic–Triassic intracontinental extension and links their formation to the broader geodynamic framework of Pangea-wide extension. The paper concludes with the overarching implications on the topographic evolution of Australo-Antarctica, and East Antarctica more broadly, establishing that widespread onshore extension has provided a key topographic framework influencing subsequent long-term erosion on the continent.

Chapter 4: Maritati, A., Halpin, J. A., Whittaker, J. M., Daczko, N. R., Wainman, C. C. Provenance of Late Jurassic–Early Cretaceous strata in the Mentelle Basin, southwestern Australia, reveals a trans-Gondwanan fluvial pathway (prepared submission for *Gondwana Research*).

This paper examines the provenance of Late Jurassic–Early Cretaceous rift sequences in the Mentelle Basin, southwestern Australia, that were deposited during the separation of India from Australia-Antarctica. Based on plate reconstructions, these rift strata have been correlated with the Knox Rift and may also offer insights into the provenance of equivalent

sedimentary rocks in Australo-Antarctica. New monazite and zircon isotopic data from sedimentary intervals cored during International Ocean Discovery Program (IODP) expedition 369 are presented. Late Jurassic syn-rift sediments are interpreted to be derived from the Gamburtsev Subglacial Mountains (GSM) in interior East Antarctica. The transition to proximal basement sources recorded in Early Cretaceous post-breakup strata is interpreted to indicate a shift to a predominantly local provenance after the breakup of India. These new data are compared with the provenance of other Antarctic and Australian Paleozoic–Mesozoic strata to define an Early Permian–Early Cretaceous sediment pathway connecting basement regions within the interior Antarctic Gondwana-forming Kuunga Orogen to the Tethys Ocean via a series of intra-Gondwanan rift basins. Together with other proposed trans-Gondwanan sediment pathways, this was one of the principal modes of siliciclastic sediment delivery to Paleozoic–Mesozoic sedimentary basins in East Antarctica and Australia.

The final discussion in **Chapter 5** summarises the progress made towards achieving the specific objectives of this study and presents an improved framework for the tectonic evolution of Australo-Antarctica that incorporates the new findings of this thesis and outlines key avenues for future work.

1.4 References

Aitken, A. R. A., Betts, P. G., Young, D. A., Blankenship, D. D., Roberts, J. L., & Siegert, M. J. (2016a). The Australo-Antarctic Columbia to Gondwana transition. *Gondwana Research, 29*(1), 136-152. doi:10.1016/j.gr.2014.10.019

Aitken, A. R. A., Roberts, J. L., van Ommen, T. D., Young, D. A., Golledge, N. R., Greenbaum, J. S., Blankenship, D. D., & Siegert, M. J. (2016b). Repeated large-scale retreat and advance of Totten Glacier indicated by inland bed erosion. *Nature, 533*(7603), 385-389. doi:10.1038/nature17447

Aitken, A. R. A., Young, D. A., Ferraccioli, F., Betts, P. G., Greenbaum, J. S., Richter, T. G., Roberts, J. L., Blankenship, D. D., & Siegert, M. J. (2014). The subglacial geology of Wilkes Land, East Antarctica. *Geophysical Research Letters, 41*(7), 2014GL059405. doi:10.1002/2014gl059405

Boger, S. D. (2011). Antarctica - Before and after Gondwana. *Gondwana Research, 19*(2), 335-371.

Cianfarra, P., & Maggi, M. (2017). Cenozoic extension along the reactivated Aurora Fault System in the East Antarctic Craton. *Tectonophysics, 703-704*, 135-143. doi:https://doi.org/10.1016/j.tecto.2017.02.019

Daczko, N. R., Halpin, J. A., Fitzsimons, I. C. W., & Whittaker, J. M. (2018). A cryptic Gondwana-forming orogen located in Antarctica. *Scientific Reports, 8*(1), 8371. doi:10.1038/s41598-018-26530-1

Eagles, G. (2019). A little spin in the Indian Ocean plate circuit. *Tectonophysics, 754*, 80-100.

Fanning, C., Moore, D., Bennett, V., & Daly, S. (1996). *The 'Mawson Continent': Archaean to Proterozoic crust in the East Antarctic Shield and Gawler Craton, Australia. A cornerstone in Rodinia and Gondwanaland.* Paper presented at the Geol. Soc. Aust. Abstr.

Ferraccioli, F., Armadillo, E., Jordan, T., Bozzo, E., & Corr, H. (2009). Aeromagnetic exploration over the East Antarctic Ice Sheet: A new view of the Wilkes Subglacial Basin. *Tectonophysics, 478*(1-2), 62-77. doi:10.1016/j.tecto.2009.03.013

Fitzsimons, I. C. W. (2003). Proterozoic basement provinces of southern and southwestern Australia, and their correlation with Antarctica. *Geological Society, London, Special Publications, 206*(1), 93-130. doi:10.1144/gsl.sp.2003.206.01.07

Frederick, B. C., Young, D. A., Blankenship, D. D., Richter, T. G., Kempf, S. D., Ferraccioli, F., & Siegert, M. J. (2016). Distribution of subglacial sediments across the Wilkes Subglacial Basin, East Antarctica. *Journal of Geophysical Research: Earth Surface*. doi:10.1002/2015jf003760

Halpin, J. A., Daczko, N. R., Direen, N. G., Mulder, J. A., Murphy, R. C., & Ishihara, T. (2020). Provenance of rifted continental crust at the nexus of East Gondwana breakup. *Lithos, 354-355*. doi:10.1016/j.lithos.2019.105363

Harley, S. L., Fitzsimons, I. C. W., & Zhao, Y. (2013). Antarctica and supercontinent evolution: historical perspectives, recent advances and unresolved issues. *Geological Society, London, Special Publications, 383*. doi:10.1144/sp383.9

Kirkland, C. L., Smithies, R. H., Spaggiari, C. V., Wingate, M. T. D., Quentin de Gromard, R., Clark, C., Gardiner, N. J., & Belousova, E. A. (2017). Proterozoic crustal evolution of

the Eucla basement, Australia: Implications for destruction of oceanic crust during emergence of Nuna. *Lithos, 278-281*, 427-444. doi:10.1016/j.lithos.2017.01.029

Maritati, A., Aitken, A. R. A., Young, D. A., Roberts, J. L., Blankenship, D. D., & Siegert, M. J. (2016). The tectonic development and erosion of the Knox Subglacial Sedimentary Basin, East Antarctica. *Geophysical Research Letters, 43*(20), 10728-10737. doi:10.1002/2016gl071063

Matthews, K. J., Maloney, K. T., Zahirovic, S., Williams, S. E., Seton, M., & Müller, R. D. (2016). Global plate boundary evolution and kinematics since the late Paleozoic. *Global and Planetary Change, 146*, 226-250. doi:10.1016/j.gloplacha.2016.10.002

Morrissey, L. J., Payne, J. L., Hand, M., Clark, C., Taylor, R., Kirkland, C. L., & Kylander-Clark, A. (2017). Linking the Windmill Islands, east Antarctica and the Albany–Fraser Orogen: Insights from U–Pb zircon geochronology and Hf isotopes. *Precambrian Research, 293*, 131-149. doi:10.1016/j.precamres.2017.03.005

Myers, J. S., Shaw, R. D., & Tyler, I. M. (1996). Tectonic evolution of proterozoic Australia. *Tectonics, 15*(6), 1431-1446.

Paxman, G. J. G., Jamieson, S. S. R., Ferraccioli, F., Bentley, M. J., Ross, N., Armadillo, E., Gasson, E. G. W., Leitchenkov, G., & DeConto, R. M. (2018). Bedrock Erosion Surfaces Record Former East Antarctic Ice Sheet Extent. *Geophysical Research Letters, 45*(9), 4114-4123. doi:10.1029/2018gl077268

Post, N. J., Hensen, B. J., & Kinny, P. D. (1997). Two metamorphic episodes during a 1340 - 1180 Ma convergent tectonic event in the Windmill Islands, east Antarctica. In C. A. Ricci (Ed.), *The Antarctic Region: Geological Evolution and Processes* (pp. 157-161). Siena: Terra Antarctica.

Raymond, O. L., Totterdell, J. M., Stewart, A. J., & Woods, M. A. (2018). Australian Geological Provinces, 2018.01 edition [Digital Dataset]. Geoscience Australia, Commonwealth of Australia, Canberra. http://www.ga.gov.au.

Smits, R. G., Collins, W. J., Hand, M., Dutch, R., & Payne, J. (2014). A Proterozoic Wilson cycle identified by Hf isotopes in central Australia: Implications for the assembly of Proterozoic Australia and Rodinia. *Geology, 42*(3), 231-234. doi:10.1130/G35112.1

Spaggiari, C. V., & Smithies, R. H. (2015). Eucla basement stratigraphic drilling results release workshop extended abstracts *Geological Survey of Western Australia, Record 2015/10*, 70p.

Spaggiari, C. V., Smithies, R. H., Kirkland, C. L., Wingate, M. T. D., England, R. N., & Lu, Y.-J. (2018). Buried but preserved: The Proterozoic Arubiddy Ophiolite, Madura Province, Western Australia. *Precambrian Research, 317*, 137-158. doi:10.1016/j.precamres.2018.08.025

Tucker, N. M., Hand, M., & Clark, C. (2020). The Bunger Hills: 60 years of geological and geophysical research. *Antarctic Science, 32*(2), 85-106.

Wise, T., Dutch, R., Pawley, M., Foss, C., & Thiel, S. (2018). Building the Coompana Province. *MESA Journal, 88*, 25-37.

Zhang, S. H., Zhao, Y., Liu, X. C., Liu, Y. S., Hou, K. J., Li, C. F., & Ye, H. (2012). U-Pb geochronology and geochemistry of the bedrocks and moraine sediments from the Windmill Islands: Implications for Proterozoic evolution of East Antarctica. *Precambrian Research, 206-207*, 52-71.

Chapter 2

Fingerprinting Proterozoic Bedrock in Interior Wilkes Land, East Antarctica

Alessandro Maritati[1], Jacqueline A. Halpin[1], Joanne M. Whittaker[1], and Nathan R. Daczko[2]

[1]Institute for Marine and Antarctic Studies, University of Tasmania, Australia

[2]ARC Centre of Excellence for Core to Crust Fluid Systems and GEMOC, Department of Earth and Planetary Sciences, Macquarie University, Australia

Abstract

Wilkes Land in East Antarctica remains one of the last geological exploration frontiers on Earth. Hidden beneath kilometres of ice, its bedrock preserves a poorly-understood tectonic history that mirrors that of southern Australia and holds critical insights into past supercontinent cycles. Here, we use new and recently published Australian and Antarctic geological and geophysical data to present a novel interpretation of the age and character of crystalline basement and sedimentary cover of interior Wilkes Land. We combine new zircon U–Pb and Hf isotopic data from remote Antarctic outcrops with aeromagnetic data observations from the conjugate Australian-Antarctic margins to identify two new Antarctic Mesoproterozoic basement provinces corresponding to the continuation of the Coompana and Madura provinces of southern Australia into Wilkes Land. Using both detrital zircon U–Pb–Hf and authigenic monazite U–Th–Pb isotopic data from glacial erratic sandstone samples, we identify the presence of Neoproterozoic sedimentary rocks covering Mesoproterozoic basement. Together, these new geological insights into the ice-covered bedrock of Wilkes Land substantially improve correlations of Antarctic and Australian geological elements and provide key constraints on the tectonic architecture of this sector of the East Antarctic Shield and its role in supercontinent reconstructions.

1. Exploring subglacial geology in interior Wilkes Land

The interior of Wilkes Land remains one of the most remote and unexplored sectors of the Precambrian East Antarctic Shield (Aitken et al., 2014). Revealing ice-covered geology in this region is critical to understanding the assembly and breakup of the Nuna/Columbia, Rodinia and Gondwana supercontinents of which Wilkes Land was a

centrepiece (Boger, 2011; Fitzsimons, 2003). The bedrock also exerts important controls on the evolution of the Antarctic ice sheet (Aitken et al., 2016b), underlying some of East Antarctica's largest and most vulnerable glacial drainage basins (i.e. Vanderford, Totten, Moscow University Ice Shelf–MUIS) which together have the potential to contribute up to 3 m of global sea level rise in a warming climate (Gulick et al., 2017). However, due to thick ice cover and very limited rock exposure / sampling, our understanding of the age and composition of the Wilkes Land interior is inferred from the largely unconstrained projection of Australian geological counterparts into Antarctica (Boger, 2011) and ages of detrital grains from glacio-marine sediments offshore of East Antarctica (Pierce et al., 2014; Roy et al., 2007).

Recent tectonic reconstructions of Gondwana that reconcile geological and geophysical signatures from the conjugate Australian and Antarctic plates revealed the presence of three large-scale Proterozoic basement provinces in Wilkes Land that accreted during supercontinent assembly (Aitken et al., 2016a). The Wilkes province (Fig. 1a) occupies the region west of the Totten Glacier, including the well-studied outcrops of the Windmill Islands to the west of Law Dome (Morrissey et al., 2017; Zhang et al., 2012). This province has relatively robust links with two main peaks of magmatism and metamorphism (c. 1330–1260 Ma and c. 1220–1140 Ma) also documented in the Nornalup Zone of the Albany Fraser Orogen of southwestern Australia (Spaggiari et al., 2011). The Mawson Craton (East Mawson Craton of Aitken et al. (2014)) comprises the Archean to Paleoproterozoic rocks in Terre Adélie and George V Lands and has geological affinities with the Gawler Craton of South Australia (Fitzsimons, 2003) (Fig. 1a).

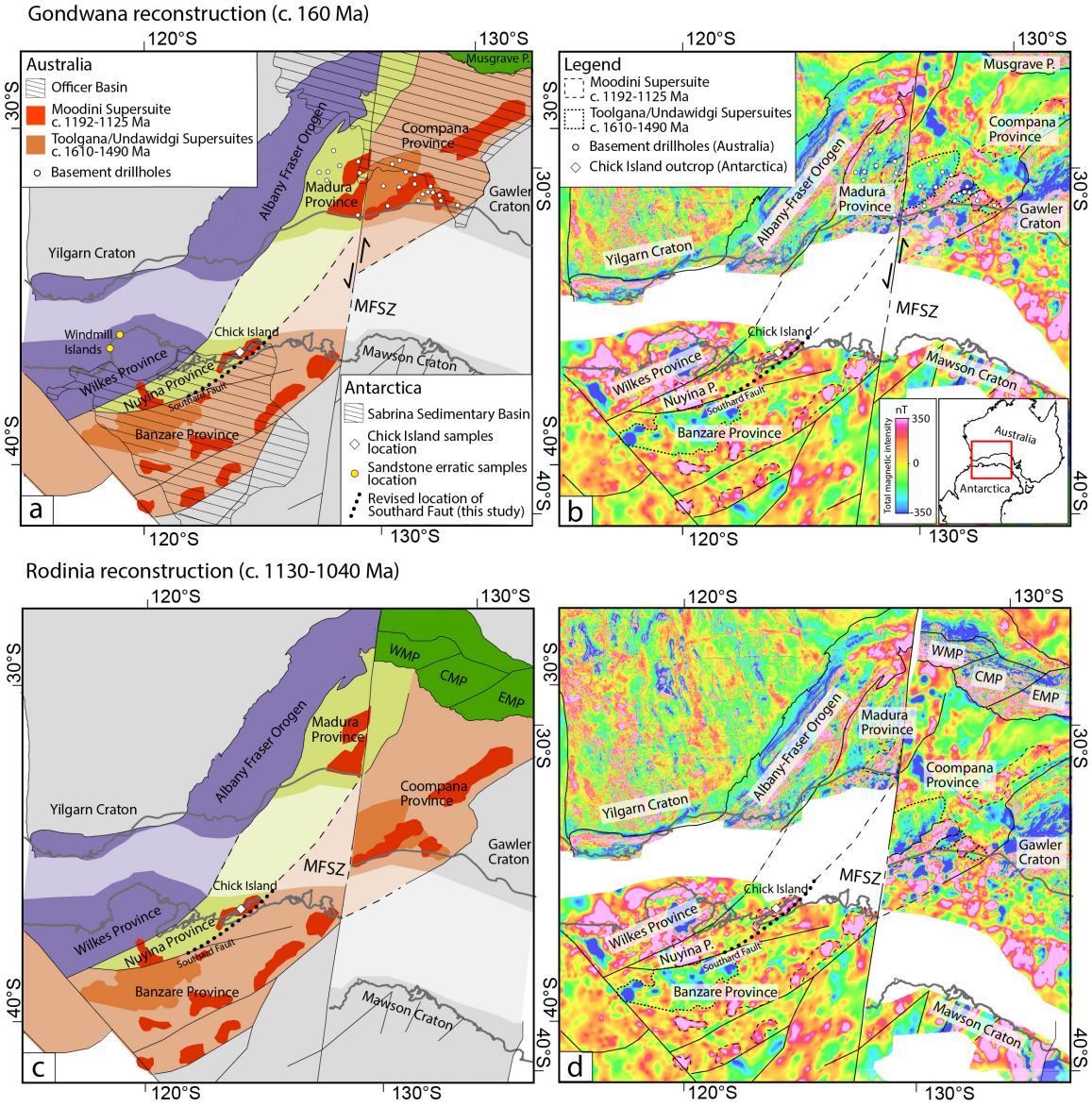

Figure 1. (Top) Reconstruction of (**a**) conjugate Proterozoic tectonic provinces and (**b**) total magnetic intensity (TMI) anomaly data of southwestern Australia and Wilkes Land in the Gondwana full-fit model of Aitken et al. (2014) with Australia fixed in its present-day reference frame. (Bottom) Reconstruction of (**c**) conjugate Proterozoic tectonic provinces and (**d**) total magnetic intensity (TMI) anomaly data of southwestern Australia and Wilkes Land in the late Mesoproterozoic reconstruction of the Rodinia configuration (c. 1130 - 1040 Ma) of Aitken et al. (2016a) following retro-deformation of approximately 330 km of sinistral offset on the Mundrabilla-Frost Shear Zone. Australian tectonic elements are simplified from Raymond et al. (2018); interpretation of tectonic elements, geophysical lineaments and intrusive suites in Wilkes Land is from Aitken et al. (2014); simplified outline of the Sabrina Sedimentary Basin is adapted from Aitken et al. (2016b); half arrows next to the Mundrabilla-Frost Shear Zone indicate sinistral displacement. Abbreviations are: CMP–central Musgrave Province; EMP–eastern Musgrave Province; MFSZ–Mundrabilla-Frost Shear Zone; WMP–West Musgrave Province.

The intervening region (West Mawson Craton of Aitken et al. (2014)), underlying most of the combined Vanderford-Totten-MUIS continental ice sheet, is only characterised by sparse legacy geological data (McLeod & Gregory, 1967; Ravich et al., 1968) and remains vastly underexplored. This region is interpreted to be the Antarctic extension of the unexposed Coompana and/or Madura provinces of southern Australia(Aitken et al., 2016a) (Fig. 1a). Recent isotopic and geochemical data from drillhole samples in these Australian provinces fingerprint a distinctively juvenile isotopic character, similar to the central Australian Musgrave Province, that has been interpreted to represent c. 1950 Ma oceanic crust reworked by a series of accretionary tectonic events throughout the Mesoproterozoic, involving significant mantle input (Hartnady et al., 2018; Kirkland et al., 2017; Kirkland et al., 2013). The Coompana Province is characterised by two dominant magmatic supersuites – the c. 1610 Ma Toolgana Supersuite with chemical and isotopic characteristics of primitive arc, and the rift-related c. 1490 Ma Undawidgi Supersuite (Jagodzinski & Bodorkos, 2018; Kirkland et al., 2017; Wingate et al., 2015a), while the Madura Province comprises a series of oceanic crustal assemblages that define oceanic subduction-related events between 1475 and 1389 Ma (Spaggiari et al., 2018; Wingate et al., 2015b). Both the Coompana and Madura provinces are extensively intruded by granitic rocks of the c. 1192–1125 Ma Moodini Supersuite (Jagodzinski & Bodorkos, 2018; Wingate et al., 2015a, 2015b). The Coompana and Madura provinces are separated by the transcontinental Mundrabilla-Frost Shear Zone which experienced approximately 330 km sinistral offset during the last phases of Rodinia assembly (1130–1040 Ma) (Aitken et al., 2016a; Spaggiari et al., 2018) and extends into East Antarctica (Fig. 1a; Fig, 1c). While strike-slip movement resulted in the truncation of structural trends and the displacement of the original boundary between the two provinces in Australia, this shear zone cuts east of the conjugate crust of East Antarctica into the Mawson Craton (Fig. 1).

2D gravity modelling and depth to magnetic basement estimates also reveal that large areas of the interior Wilkes Land are blanketed by the ≥ 1 km-thick Sabrina Sedimentary Basin, covering an area of approximately 500,000 km^2 (Aitken et al., 2016b) (Fig. 1a). In Australia, parts of the Coompana and Madura provinces are covered by extensive sedimentary basins, including the Neoproterozoic to Devonian Officer Basin (part of Centralian Superbasin) (Lindsay & Leven, 1996) and the Mesozoic Bight and Cenozoic Eucla basins (Espurt et al., 2012; Lowry, 1970). Aitken et al. (2014) correlated the

Sabrina Sedimentary Basin and the Bight/Eucla basins based on the pre-Gondwanan breakup proximity. The Sabrina Sedimentary Basin is not exposed, although, the presence of rare glaciogenic sedimentary material along the Wilkes Land coast (Goldthwait, 1959; Goodwin, 1995; Mackintosh et al., 2014) provides a unique opportunity to study this basin.

In this paper, we analyse geological samples from crystalline basement and sedimentary cover in order to characterise part of the subglacial bedrock of interior Wilkes Land between the Wilkes Province and Mawson Craton. We combine new U–Pb–Hf isotopic data of coastal basement outcrops in Antarctica with the aeromagnetic signature of conjugate Australian-Antarctic basement domains to identify two new Mesoproterozoic basement provinces of Coompana and Madura affinity in Wilkes Land and resolve their geometry in their Rodinian and Gondwanan configurations. We then use detrital zircon U–Pb–Hf and authigenic monazite U–Th–Pb isotopic data from rare sandstone erratic samples to suggest the presence of Neoproterozoic sedimentary rocks in the Sabrina Sedimentary Basin and correlate this basin with the eastern Neoproterozoic Officer Basin. Our new interpretations of subglacial bedrock strengthen correlations between Antarctic and Australian geological counterparts and provide key constraints for global supercontinent reconstructions.

2. Methods

2.1 Zircon sample preparation and U–Pb–Hf analyses

Location of samples used in this study is given in Supplementary Table S1. Igneous zircon grains were separated from crushed rocks using a standard plastic pan and warm water and subsequent magnetic separation. Detrital zircon were separated from crushed rocks using heavy liquid separation. Grains were mounted in 25-mm diameter epoxy discs. Mounts were polished to half grain thickness to expose grain centres, carbon coated and imaged using a cathodoluminescence (CL) detector on a FEI Quanta 600 Environmental Scanning Electron Microscope (ESEM) at Central Science Laboratory, University of Tasmania, to identify compositional domains for analysis.

U–Pb zircon ages were collected at the University of Tasmania, Australia using laser ablation-inductively coupled plasma-mass spectrometry (LA-ICP-MS). U–Pb zircon analyses were performed in two different sessions on an Agilent 7900cs quadrupole ICPMS

with a 193 nm Coherent Ar–F gas laser and a Resonetics S-155 ablation cell at the School of Earth Sciences, University of Tasmania. Each analysis was pre-ablated with 5 laser pulses to remove any surface contamination then the blank gas was analysed for 30 s followed by 30 s of zircon ablation at 5 Hz and 2 J/cm^2 on a spot size of 29 μm. Elements measured include ^{49}Ti, ^{56}Fe, ^{90}Zr, ^{178}Hf, ^{202}Hg, ^{204}Pb, ^{206}Pb, ^{207}Pb, ^{208}Pb, ^{232}Th and ^{238}U with each element being measured sequentially every 0.16 s with longer counting time on the Pb isotopes compared to the other elements. The international glass standard NIST610 was ablated at the beginning and end of the analytical session to correct for mass bias on the ^{207}Pb /^{206}Pb ratio. Each run consisted of 30–50 analyses of our unknowns, bracketed by 4–6 analyses of the primary reference zircon standard 91500 (Wiedenbeck et al., 1995) used to correct for mass bias, machine drift and down-hole fractionation on the Pb/U and Pb/Th ratios, and 4 analyses (two each) of secondary standards TEMORA 1 (Black et al., 2003) and GJ-1 (Jackson et al., 2004) / Plesovice (Sláma et al., 2008) to provide an independent control to assess accuracy and precision. Full tabulation of U–Pb isotopic data of unknowns and standards is reported in Supplementary Table S2. Data reduction calculations and error propagations were done with Microsoft Excel® via macros designed at the University of Tasmania using the techniques outlined by Sack et al. (2011). The degree of metamictisation was also determined in igneous zircon by using U and Th concentrations and ^{207}Pb/^{206}Pb ages to calculate the dose of α-events for each zircon grain. Zircon grains were classified as 'highly crystalline' when alpha dose was <3 α/mg × 10^{15}, 'moderately damaged' when >3 and <8 α/mg × 10^{15} and 'highly metamict' when >8 α/mg × 10^{15} (Markwitz & Kirkland, 2018). U–Pb Tera-Wasserburg plots of igneous zircons were constructed using isoplotR (Vermeesch, 2018). Error ellipses on Tera-Wasserburg plots are calculated at the two-sigma level. ^{207}Pb/^{206}Pb data are used for all age determinations. The quoted analytical uncertainties on individual analyses are given at the 2r level. Weighted mean ages are calculated to their 95% confidence level using analyses that are ≤±10% discordant (within 2r uncertainty of concordia). Probability density plots (PDP) of detrital zircon were calculated with DensityPlotter (Vermeesch, 2012) using ^{207}Pb/^{206}Pb ages and their 1σ uncertainties for data ≤±5% discordant. Histogram bin size in all PDPs is 20 Myr. Two-sample Kolmogorov–Smirnov (K-S) tests were performed on the detrital zircon age data using the online statistics calculator of Kirkman (1996) to determine if the samples

were derived from different sources by comparing the distance between the cumulative age distribution curves.

Lu–Hf isotope analyses were performed on a subset of zircon grains already analysed for U–Pb using a New Wave/Merchantek LUV213 laser-ablation microprobe, attached to a Nu Plasma multi-collector inductively coupled plasma mass spectrometer (LA-MC-ICPMS) at GEMOC, Macquarie University (Sydney, Australia). Griffin et al. (2004) describe the methodology in detail. A blank gas was analysed for 60 s followed by 120 s of ablation at 5 Hz and 2 J/cm^2 and a beam diameter of 40–50 μm (depending on the size of the zircon grain). Zircon CL images were used to ensure that Hf isotope analyses were contained within the same domain analysed for U–Pb. Our samples were measured in two analytical sessions. Zircons from the Mud Tank carbonatite locality were analysed together with the samples in each session to monitor accuracy of the results. Most data and the mean $^{176}Hf/^{177}Hf$ value are within 2 standard deviations (SD) of the recommended value [0.282522 ± 42 (2σ)] (Griffin et al., 2006). Temora zircon was also run as an independent check on the accuracy of the Yb correction. Temora zircon has an average $^{176}Yb/^{177}Hf$ ratio of 0.04, which is similar to the mean $^{176}Yb/^{177}Hf$ ratio of zircon in this study. The average $^{176}Hf/^{177}Hf$ ratio for Temora is consistent with the published value for the Temora standard [0.282687 ± 24 (2σ) (Hawkesworth & Kemp, 2006)]. The initial $^{176}Hf/^{177}Hf$ (Hf_i) value in zircon is calculated using the measured $^{176}Hf/^{177}Hf$ and apparent $^{207}Pb/^{206}Pb$ age. Calculation of εHf_i values employed the decay constant of Scherer et al. (2001) of 1.865×10^{-11}. Full tabulation of zircon Hf isotopic data of unknown and standards is presented in Supplementary Table S3. Initial $^{176}Hf/^{177}Hf$ and εHf_i plots were constructed in Microsoft Excel®; zircon U–Pb and Hf isotopes from our samples are compared to a compilation of Australian and Antarctic isotopic data (provided in Supplementary Table S4).

2.2 Monazite sample preparation and in situ U–Th–Pb analyses

Rock chips for in situ U–Th–Pb monazite dating were mounted with epoxy resin in ~12 mm thick x 25 mm diameter steel cylinder and polished using a 0.25μm diamond polishing lap. Monazite grains were identified in rock chip laser mounts using Sparse Phase Liberation-Lite analysis (SPL-LT). Representative images of monazite grains selected for geochronology were taken using a FEI Quanta 600 SEM. Grains were also imaged using

high contrast BSE imaging to detect zoning within the grains on a Hitachi SU-70 Field Emission Scanning Electron Microscope (FE-SEM).

Monazite grains from each of the three sandstone erratic samples were investigated for in situ U–Th–Pb analyses following the analytical procedures reported in Halpin et al. (2014) on the same LA-ICP-MS system used to collect U–Pb detrital zircon ages. Pre-ablation and ablation times follow the monazite methodology highlighted in Halpin et al. (2014) with operating conditions of 5 Hz and ~2 J/cm^2 on a spot size of 9 μm. Elements measured include ^{27}Al, ^{31}P, ^{43}Ca, ^{140}Ce, ^{172}Yb, ^{202}Hg, ^{204}Pb, ^{206}Pb, ^{207}Pb, ^{208}Pb, ^{232}Th and ^{238}U. The international glass standard NIST610 was used as a primary standard for trace element quantification assuming stoichiometric Ce in monazite and as a primary standard for the ^{207}Pb/^{206}Pb ratio correction factor for monazite. The down hole fractionation, instrument drift and mass bias correction factors for Pb/U and Pb/Th ratios on monazite grains were calculated using two analyses on the primary standard (14971-Mon–in-house standard) and one analysis on each of the secondary standard monazites RGL4B(Rubatto et al., 2001), Bananeira(Gonçalves et al., 2016), and 94-222(Maidment, 2005) analysed at the beginning of the session and every 16–20 unknowns using the same spot size and conditions as used on the samples. Following the recommendations of Grand'Homme et al. (2016); Seydoux-Guillaume et al. (2012), ^{208}Pb/^{232}Th ages are preferred to the ^{206}Pb/^{238}U ages in all age determinations due to common Pb contamination and the relatively high Th/U ratio of monazite. Results are presented graphically in a ^{206}Pb/^{238}U vs ^{208}Pb/^{232}Th modified concordia plot. Uncertainties on individual spot ages are 1σ. Full tabulation of U–Th–Pb isotopic data of monazite unknowns and standards and modified concordia plot are reported in Supplementary Table S5. Data reduction calculations and error propagations were done with Microsoft Excel® via macros designed at the University of Tasmania using the techniques outlined by Sack et al. (2011) and Halpin et al. (2014). Age calculations. ^{206}Pb/^{238}U vs ^{208}Pb/^{232}Th modified Concordia diagrams were made in Microsoft Excel®.

2.3 Aeromagnetic data interpretation and tectonic reconstructions

We use the most recent magnetic anomaly map of the Antarctic (ADMAP-2)(Golynsky et al., 2018) and the comparable Australian dataset available from Geoscience Australia in conjunction with geological data to match the aeromagnetic signature of the Coompana / Madura provinces and interior Wilkes Land in the Gondwana full-fit (c. 160

Ma) plate reconstruction framework of Aitken et al. (2016a) and identify broad basement domains and lineaments. Our interpretation of Antarctic aeromagnetic data builds on the most recent tectonic model of Wilkes Land of Aitken et al. (2014) and preliminary interpretation of the 2015 Coompana aeromagnetic survey(Wise et al., 2015) based on the most recent drillhole data available from the Coompana Province. We reproduce the Late Mesoproterozoic reconstruction of the Rodinia configuration (c. 1130–1040 Ma) of Aitken et al. (2016a) with reversal of approximately 330 km of sinistral offset on the Mundrabilla-Frost Shear Zone to reconstruct the geometry of the Madura / Coompana and Antarctic conjugate provinces across Australia-Antarctica.

3. U–Pb–Hf geochronology of Chick Island

We analysed zircon from three igneous bedrock samples from the remote Chick Island outcrop east of the Totten Glacier and along the Banzare Coast (Fig. 2a), including one sample of the main pluton and two petrologically-similar xenolith samples (Fig. 2b), to provide constraints on the age and composition of Precambrian basement in this poorly exposed region.

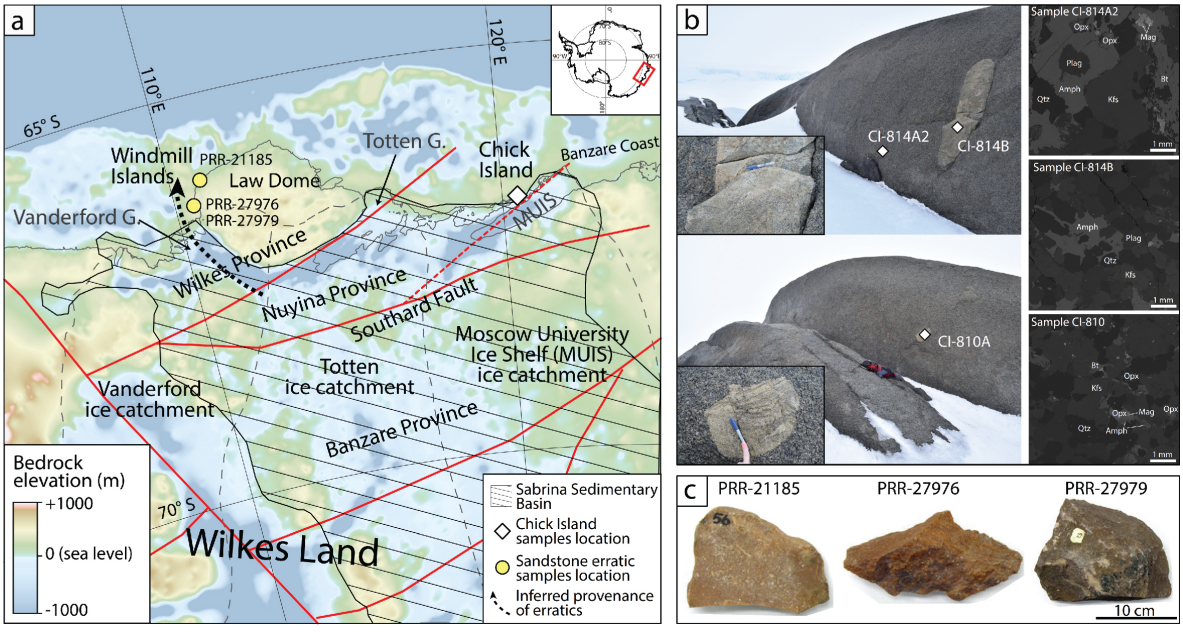

Figure 2. (**a**) Subglacial bedrock elevation map showing location of samples of this study, ice catchment basins (Mouginot et al., 2017) (dashed black lines) and major structural lines (Aitken et al., 2016a) (solid red lines); revised path of the Southard Fault is also shown as dotted red segment; (**b**) (left) Location of sampling sites at Chick Island and (right) annotated detail of backscatter electron (BSE) image of each

sample; (**c**) glacial sandstone erratic samples used in this study. Abbreviations are: Amph–Amphibole; Bt–Biotite; Kfs–K-feldspar; Mag–Magnetite; Opx–Orthopyroxene; Plag–Plagioclase; Qtz–Quartz.

Sample CI-814A2, the main rock type exposed at Chick Island, is a coarse-grained orthopyroxene-bearing granodiorite (based on Quartz-Alkali Feldspar-Plagioclase (QAP) modal classification of Streckeisen (1976)) and contains quartz (~33%), K-feldspar (~19%), plagioclase (~43%) as well as biotite, orthopyroxene, amphibole, ilmenite and magnetite (~5%), with accessory apatite and zircon (Fig. 2b). Zircon grains extracted from this sample are 100–250 μm long and equant to elongate, with aspect ratios from 1:1–4:1 (Fig. 3a). Under cathodoluminescence (CL), zircon grains are medium to brightly luminescent, commonly displaying oscillatory (e.g. spot 008, 017) and/or sector (e.g. spot 021) zoning (Fig. 3a). Thirty-six U–Pb analyses were collected from 31 grains across the spectrum of internal domains observed under CL. However, regardless of zonation, concordant analyses yield a $^{207}Pb/^{206}Pb$ weighted average age of 1148 ± 11 Ma (n = 34, mean square of weighted deviates [MSWD] = 1.34), interpreted to represent the crystallisation age of this sample (Fig. 3a). These zircon grains possess a steep HREE pattern, positive Ce and negative Eu anomalies and a Th/U ratio (0.86-2.03) consistent with magmatic zircon (see Supplementary Fig. S1). Twenty-four Hf isotope analyses of concordant primary igneous zircon grains yield initial $^{176}Hf/^{177}Hf$ (Hf_i) ratios in the range 0.28206–0.28216 (Fig. 4) and initial epsilon Hf (εHf_i) values between -0.53 and +4.87. A single outlier (spot 019) yielding Hf_i ratio of 0.28101 and εHf_i of -36.74 was excluded from the interpretation.

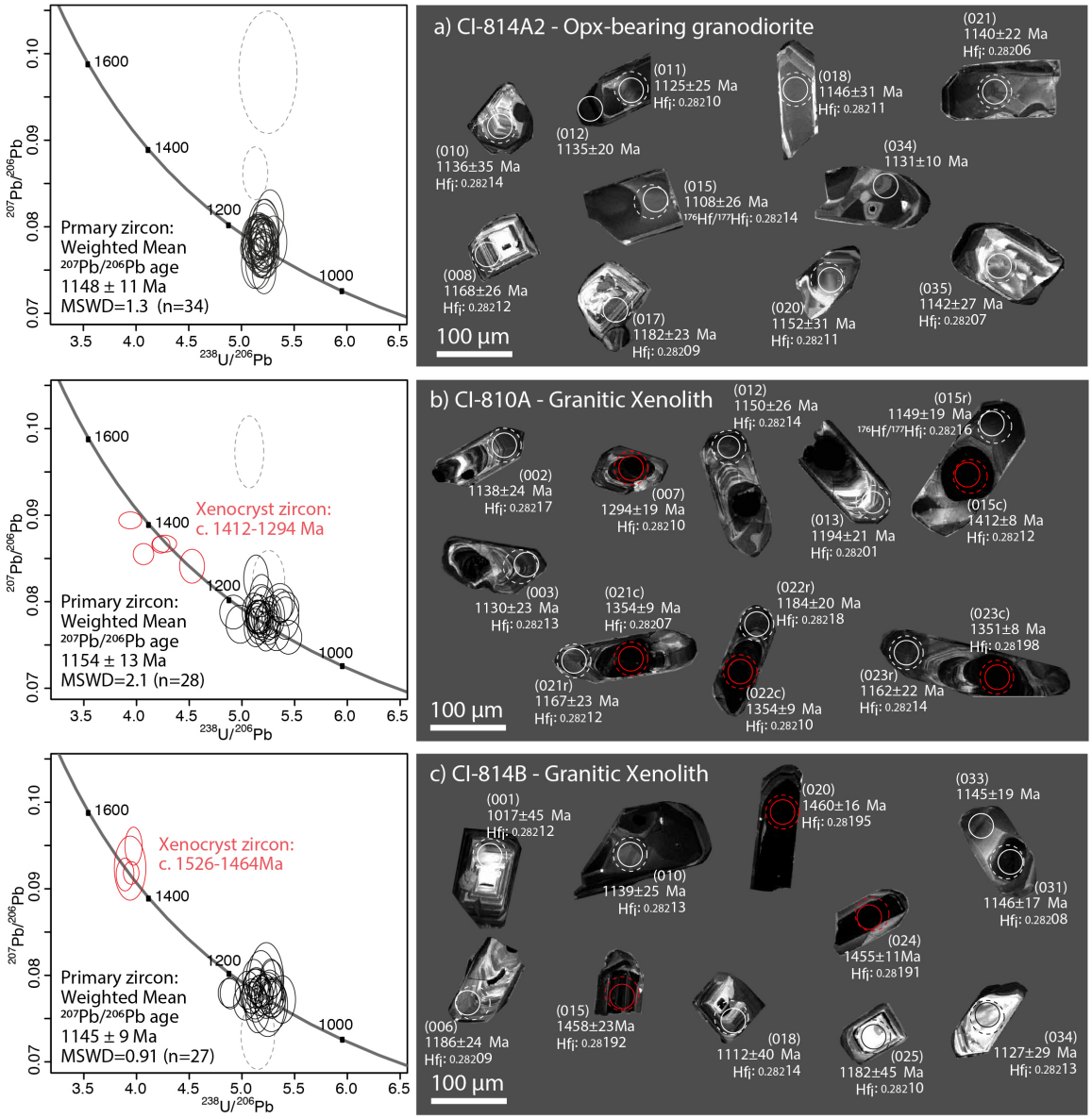

Figure 3. (left) U–Pb Tera-Wasserburg plots and (right) representative zircon CL images from each Chick Island sample. On Tera–Wasserburg plots, dashed grey ellipses denote analyses that have been excluded from age calculations on the basis of discordance (>10%). On CL images, U–Pb and Lu–Hf analysis locations are displayed as solid and dashed circles, respectively. Corresponding spot number (in brackets), apparent $^{207}Pb/^{206}Pb$ ages and initial $^{177}Hf/^{176}Hf$ ratio (Hf_i) and are also given for each analysis. Solid red ellipses on Tera–Wasserburg plots and red circles on CL images correspond to xenocryst zircon analyses.

Two xenoliths hosted in the granodiorite bedrock (samples CI-810A and CI-814B) have a granitic composition and contain igneous microstructures characterised by a lack of recrystallisation and the presence of interstitial igneous green amphibole. Samples contain quartz (~38%), K-feldspar (~24%), plagioclase (~33%) as well as amphibole and

orthopyroxene (~5%) and accessory apatite and zircon (Fig. 2b). The apparent foliation observed at the outcrop scale is due to magmatic compositional banding into K-feldspar-rich versus plagioclase-rich domains that may reflect accumulation or magmatic flow processes.

Zircon grains in sample CI-810A are 100–200 μm long and have aspect ratios that vary from 1:2–1:4. Under CL (Fig. 3b), the majority of zircon grains contain dark resorbed cores with low-CL response (e.g. spots 023c, 021c) that are overgrown by moderate CL oscillatory zoned rims (e.g. spots 002, 021r) or more diffusely zoned rims (e.g. 015r).

Thirty-five U–Pb analyses were collected from twenty-one zircon grains, including seven grains where both cores and rims were analysed. Rim domains represent the main concordant zircon population, which yields a $^{207}Pb/^{206}Pb$ weighted average age of 1154 ± 13 Ma (n = 28, MSWD = 2.1; Fig. 3b), within error of the interpreted age of crystallisation of the host granodiorite (sample CI-814A2). This c. 1154 Ma population possesses high (0.38-1.45) Th/U ratios, steep HREE patterns, positive Ce and negative Eu anomalies (Supplementary Fig. S1), consistent with those of primary igneous zircon in sample CI-814A2. Accordingly, we interpret this c. 1154 Ma population in the xenoliths to date cognate inclusions. Hf isotopic analyses of eighteen concordant zircon grains from the c. 1154 Ma zircon population yield Hf_i ratios in the range 0.28200–0.28222 (Fig. 4) and εHf_i values from -1.47 to +5.45. Five older analyses corresponding to dark CL cores reveal high concentrations of U (419–3565 ppm) with individual apparent $^{207}Pb/^{206}Pb$ ages spread along Concordia between c. 1412 Ma to c. 1294 Ma (Fig. 3b). Trace element ratios (Th/U) and REE patterns for these zircon cores are distinct from the primary igneous zircon population (Supplementary Fig. S1). Five core domains yield Hf_i ratios in the range 0.28198–0.28212 (Fig. 4) and εHf_i values from +2.05 to +8.30. We interpret this population to represent xenocrystic components, and the spread in apparent ages as the result of variable resetting of metamict zircon (alpha dose > 8 α/mg $\times 10^{15}$) during post-crystallisation modification

(Supplementary Tab. S2).

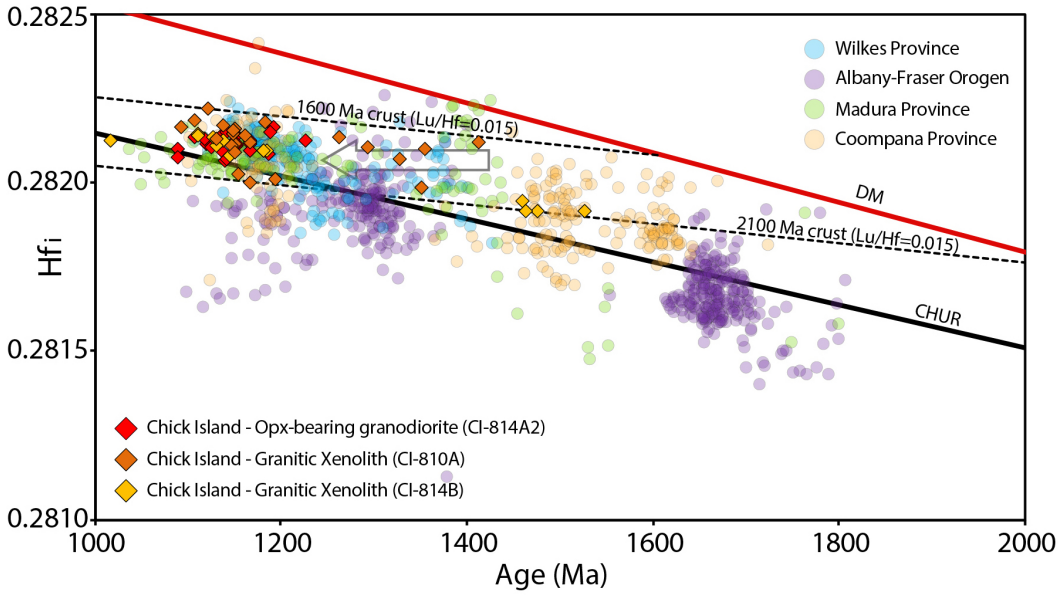

Figure 4. Initial $^{177}Hf/^{176}Hf$ ratios (Hf_i) for concordant zircon from Chick Island samples. The ratios are plotted against the apparent $^{207}Pb/^{206}Pb$ age for each analysis. Hf_i of Chick Island zircon is compared to U–Pb–Hf data of igneous zircon from: Albany-Fraser Orogen (Kirkland et al., 2011a; Kirkland et al., 2011b); GSWA geochronology records as compiled by Smits et al. (2014)), Windmill Islands (Morrissey et al., 2017; Zhang et al., 2012), Coompana and Madura provinces(Kirkland et al., 2017). Grey arrow indicates possible Pb-loss trajectory in xenocryst zircon from sample CI-814A. Zircons plotting below the CHUR (chondritic uniform reservoir) reference line reflect an increasingly crustal melt source, whereas those plotting at progressively more positive Hf_i values above CHUR reflect an increasing contribution from the depleted mantle (DM) to magmas from which the zircon formed. Crustal growth curves using a bulk crust value of $^{176}Lu/^{177}Hf = 0.015$(Griffin et al., 2002) are drawn through the most evolved (c. 2100 Ma) and least evolved (c. 1600 Ma) Chick Island zircon.

Zircon grains in sample CI-814B are 70–200 µm long and have aspect ratios that vary from 1:1–1:4. Many of the larger zircon grains show medium to high CL response (Fig. 3c) with oscillatory (e.g. spots 001, 006) or diffuse banded (e.g. spot 33) zoning. A subset of the grains contains low-CL domains that are typically unzoned (e.g. spot 020). Thirty-two analyses were collected from thirty-one grains representing the range of observed morphologies and zonation. The main concordant zircon population yields a $^{207}Pb/^{206}Pb$ weighted average age of 1145 ± 9 Ma (n = 27, MSWD = 0.91; Fig. 3c), with the majority of these grains exhibiting high (0.54-1.90) Th/U ratios and REE trace element signatures typical of igneous zircon (Supplementary Fig. S1). Hf isotopic analyses from the c. 1145 Ma

zircon population yield Hf_i ratios in the range 0.28208–0.28214 (Fig. 4) and εHf_i values between -0.47 to +2.37. As for sample CI-814B, we interpret this population as indicating a cognate inclusion relationship for both xenoliths. Four older analyses on homogenous dark zircon domains yield apparent $^{207}Pb/^{206}Pb$ ages ranging from c. 1526 Ma to c. 1464 Ma, have slightly more REE-enriched compositions compared to the main population (Fig. 3c) and yield Hf_i ratios in the range 0.28191–0.28195 (Fig. 4) and εHf_i values between +2.17 to +3.64. We interpret this population to represent xenocrysts and suggest their clustered U–Pb–Hf signature fingerprints the character of early Mesoproterozoic (c. 1500 Ma) basement at depth.

4. Basement correlations between Wilkes Land and Australia

Aeromagnetic signatures from the conjugate Australian-Antarctic margins suggest the presence of similar basement domains in the Coompana / Madura Provinces and Wilkes Land. In southern Australia, the Coompana Province has variable magnetic intensity(Wise et al., 2015) and is characterised by large areas of low to moderate magnetic intensity (<-300 nT) associated with the c. 1610–1490 Ma plutons of the Toolgana and Undawidgi Supersuites (Fig. 1b). In contrast, the Madura Province exhibits overall higher-frequency anomalies with moderate to strong magnetic intensity (0-100 nT). The c. 1192–1125 Ma Moodini Supersuite in both the Coompana and Madura provinces exhibits a distinct NE directional trend and is the source of the highest magnetic intensities (up to 400 nT) in both provinces (Fig. 1b).

In Antarctica, we suggest that two large and magnetically distinct intrusive suites identified by Aitken et al. (2014) match, in type and character, the magnetic anomalies associated with the Undawidgi–Toolgana and Moodini supersuites (Fig. 1b). The older suite is characterised by strong relative magnetic lows, providing a good match with magnetic anomalies corresponding to the Toolgana and Undawidgi supersuites. The younger suite, is interpreted to occur throughout the entire region based on identical high magnetic character and north-easterly directional trend as c. 1150 Ma granitoids across southwestern Australia(Aitken et al., 2014) which crosscut the major regional structural grain. We suggest this suite is likely equivalent to the Moodini Supersuite granites.

The spatial distribution of these suites in Wilkes Land defines two distinct geophysical domains with different magnetic character: these are separated by a previously

un-named ENE-WSW geophysical lineament(Aitken et al., 2014) that marks a sharp change in overall intensity and frequency of magnetic anomalies (Fig. 1b). We suggest that the presence of high-amplitude magnetic anomalies associated with Undawidgi–Toolgana and Moodini supersuites exclusively south of this lineament fingerprints a Coompana-type basement complex. In contrast, the overall relatively higher magnetic intensity and frequency of magnetic anomalies combined with the absence of a geophysical signal like that of the Undawidgi–Toolgana plutons indicates the presence of a Madura-type basement complex in the portion of Wilkes Land wedged between the ENE-WSW lineament and the Wilkes Province (Fig. 1b). We identify this ENE-WSW lineament as the boundary between Coompana- and Madura-type crust in Antarctica and name the Antarctic conjugates of the Coompana and Madura provinces the Banzare Province and Nuyina Province, respectively.

The Chick Island outcrop corresponds with an interpreted Moodini Supersuite pluton located approximately 100 km north of the inferred boundary between the Banzare and Nuyina provinces (Fig. 1a; Fig 1b); our new U–Pb–Hf zircon data provide insight into its crustal affinity and a test of the tectonic correlation based on aeromagnetic data. The Chick Island granodiorite pluton (sample CI-814A2) has a crystallisation age of c. 1148 Ma and Hf_i isotopic values consistent with the emplacement age and Hf signature of the Moodini Supersuite in the Coompana and Madura provinces (Kirkland et al., 2017), as well as isotopically-similar igneous rocks found in the Wilkes Province (e.g. Ardery Charnockite in the Windmill Islands (Morrissey et al., 2017)) (Fig. 4). Two cognate inclusions yield c. 1150 Ma primary zircon populations and xenocrystic zircon grains that fingerprint crustal contamination. The distinct Hf_i isotopic character of xenocrystic zircon suggests at least two isotopically different components in the source: the less radiogenic xenocrysts (c. 1526–1464 Ma; sample CI-814B) overlap in age and Hf signature with zircon from the Coompana Province, and the more radiogenic xenocryst group (c. 1412–1294 Ma; sample CI-810A), though displaying variable Pb loss possibly from c. 1420 Ma, overlap the isotopic signature of the more juvenile Madura Province (Fig. 4). We suggest that these U–Pb–Hf patterns are indicative of crustal contamination from both Coompana- (c. 1610–1490 Ma) and Madura-type (c. 1475–1389 Ma) crust at depth, and thus fingerprint the presence of a tectonic boundary between the Banzare and Nuyina provinces in Antarctica, with Chick Island being the most likely coastal location of this boundary.

Based on our new geological data, we revise the path of the tectonic boundary between the Banzare and Nuyina provinces identified in aeromagnetic data (ENE-WSW lineament of Aitken et al. (2014)) to intersect the coast in the proximity of the Chick Island outcrop (dotted segment in Fig. 1 and Fig. 2). We name this composite tectonic boundary the Southard Fault (after Cape Southard).

Correlations of the Coompana/Madura and Banzare/Nuyina provinces across Australia-Antarctica are offset by approximately 330 km sinistral strike-slip motion along the Mundrabilla-Frost Shear Zone (Fig. 1). To reconstruct the configuration of these provinces prior to this motion, we link the Southard Fault with a major NE-trending structure identified in aeromagnetic data by Aitken et al. (2014), which we suggest may represent the conjugate boundary between the Coompana and Madura provinces in Australia (Fig. 1c; Fig. 1d). Despite the lack of geological data from this region, this structure appears to represent the southerly expression of the boundary between the West Musgrave and central Musgrave provinces which preserve evidence of tectono-magmatic affinity with the Madura and Coompana provinces, respectively (Aitken et al., 2016a; Howard et al., 2015) (Fig. 1c; Fig. 1d). This connection allows the Madura Province to continue across the Mundrabilla-Frost Shear Zone in Australia and resolves the geometry of Coompana and Madura provinces and the conjugate Banzare and Nuyina provinces before and after strike-slip motion in their Rodinia (c. 1130–1040 Ma) and Gondwana (c. 160 Ma) configurations.

5. Provenance and age of sandstone erratics

To probe the provenance and age of sedimentary rocks overlying crystalline basement in interior Wilkes Land, we analysed three glacially-transported sedimentary samples (Fig. 2c) collected at two localities in the Windmill Islands (Goldthwait, 1959) (Fig. 2a) by combining detrital zircon and authigenic monazite dating. The glacial erratics are faceted and angular, suggesting these samples were derived from a proximal sedimentary source (Fig. 2a). Samples are well sorted quartz-arenites (Fig. 5) dominated by monocrystalline quartz (>95%, derived from point counting) and small proportions of K-feldspar (up to 3%). This composition suggests a dominantly granitic sediment source and a "craton interior" tectonic provenance for the three samples. The presence of fine-grained (~10 μm) interstitial muscovite and sericitised feldspar grains (Fig. 5) indicates post-

depositional interaction with hydrothermal fluids.

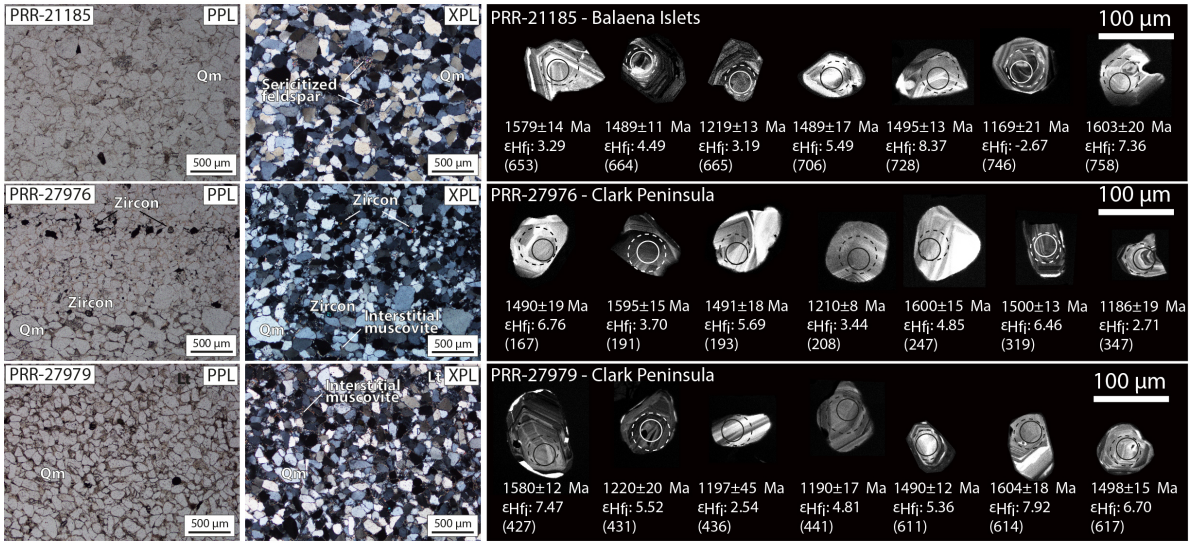

Figure 5. (left to right) Plane-polarised (PPL) and cross-polarised (XPL) microphotographs with descriptive labels, and CL images of representative detrital zircons used for U–Pb–Hf dating from each sandstone erratic sample. On CL images, U–Pb and Lu–Hf analysis locations are displayed as solid and dashed circles, respectively. Corresponding apparent $^{207}Pb/^{206}Pb$ ages (Ma), initial epsilon Hf (εHf_i) and spot number (in brackets) are also shown for each analysis. Abbreviations are: Lt–Lithic fragment; Qm–Quartz monocrystalline.

Zircon are sub-rounded to sub-euhedral, with the majority of grains having aspect ratios from 1:2–1:3 and indicating an overall local sourcing of sediments. U–Pb zircon ages from the three samples reveal similar age peaks and have a statistically similar detrital distribution according to the performed K-S test (maximum difference between age distribution curves [D] = 0.0891–0.1471 and p-values > 0.05) (see Supplementary Fig. S2). The composite detrital zircon age spectrum, derived from a total of 468 concordant (<± 5% discordant) U–Pb zircon analyses from the three samples, indicates sedimentary source regions dominated by c. 1600–1470 Ma (48% of total) and c. 1180 Ma zircons (34%), with a lower proportion of zircons in the age range from c. 2400 Ma to 1700 Ma (18%) (Fig. 6). Most zircon grains in the two main groups display oscillatory zoning (Fig. 5) and average Th/U of ~0.64, typical of igneous zircon. An estimate of the maximum deposition age for the sandstones is 1091 ± 7 Ma (n = 40, MSWD = 1.4), based on the youngest detrital zircon population. The zircon εHf_i data from the sandstone erratic samples are dominated by positive values in each of the main detrital populations reflecting a significant mantle

contribution in the source magmas. The c. 1600–1470 Ma zircons have overall positive εHf_i values between +11.52 and -1.08, while the c. 1180 zircons have a range of εHf_i values between +9.34 to -2.67 (Fig. 6).

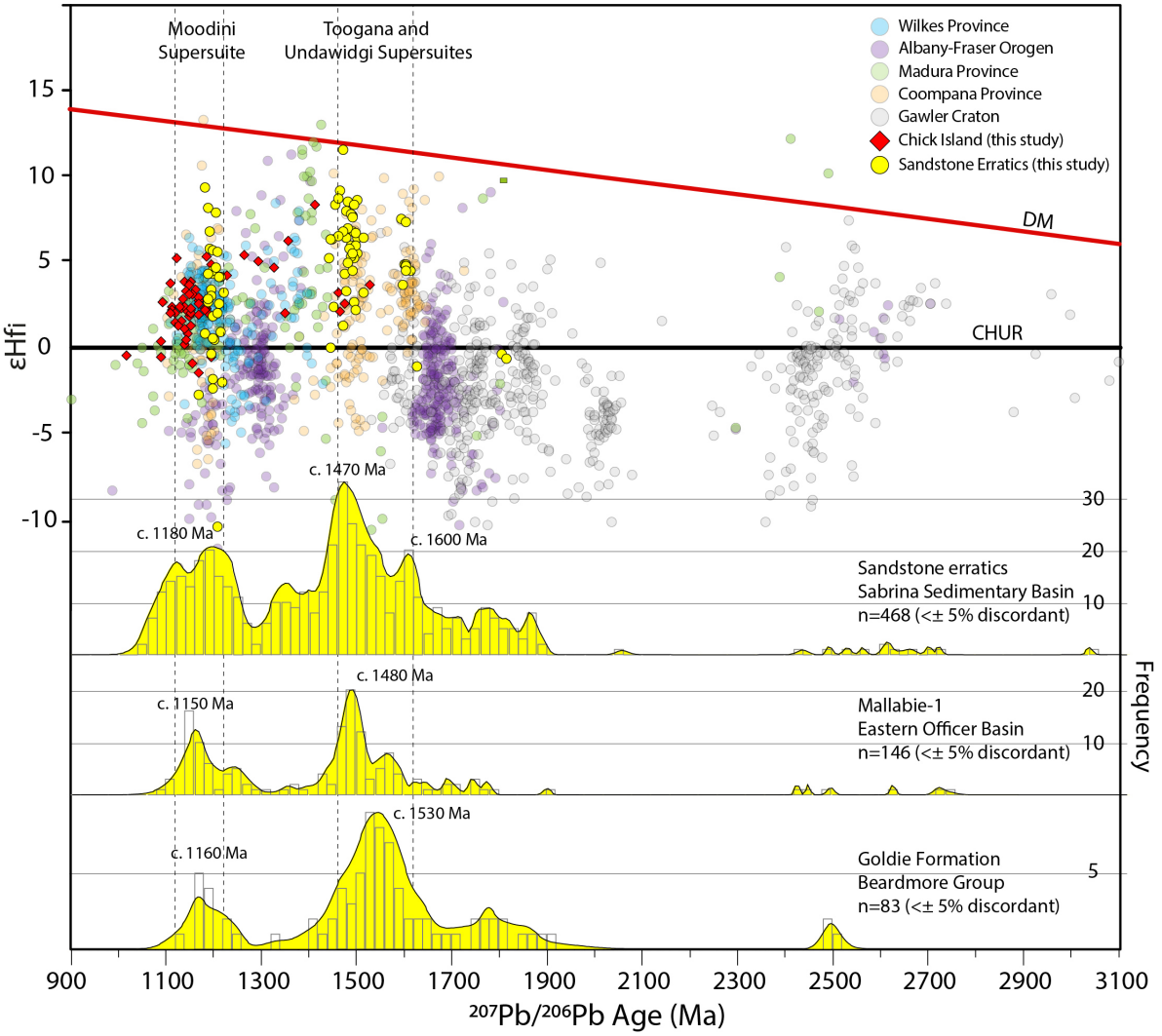

Figure 6. Initial epsilon Hf (εHf_i) values (yellow dots) versus probability density plot (yellow fill) and histograms for detrital zircon from the sandstone erratic samples. εHf_i ratio is compared to the same U–Pb–Hf data compilation used in Figure 3 with the addition of >1500 Ma zircon from Gawler Craton (Belousova et al., 2009). Composite probability density plots and histograms for the Mallabie-1 sedimentary samples (Officer Basin) (Fraser & Neumann, 2016) and the Goldie Formation (Beardmore Group) (Goodge et al., 2004) are also shown for comparison.

Rare monazite typically occurs as irregular grains (~15–50 μm) amongst the fine-grained interstitial muscovite (Fig. 7 inset). This texture, together with the relatively high Th (mostly ~10,000 ppm) and low U (mostly <100 ppm), suggests the analysed monazite grains are authigenic and likely formed due to an interaction with hydrothermal fluids

during or after deposition (Seydoux-Guillaume et al., 2012). A total of 32 grains were analysed from the three sandstone erratic samples. Seven analysis were discarded due to low analytical signal intensity for the U, Th and Pb isotopes. U/Pb systems in analysed monazite grains are overall disturbed due to common Pb contamination and depletion of U relative to Th, resulting in overestimated $^{206}Pb/^{238}U$ ages and large analytical uncertainties (Fig. 7). The well-resolved $^{208}Pb/^{232}Th$ ages obtained confirm instead minor disturbance of the Pb/Th systems and provide more reasonable age estimates.

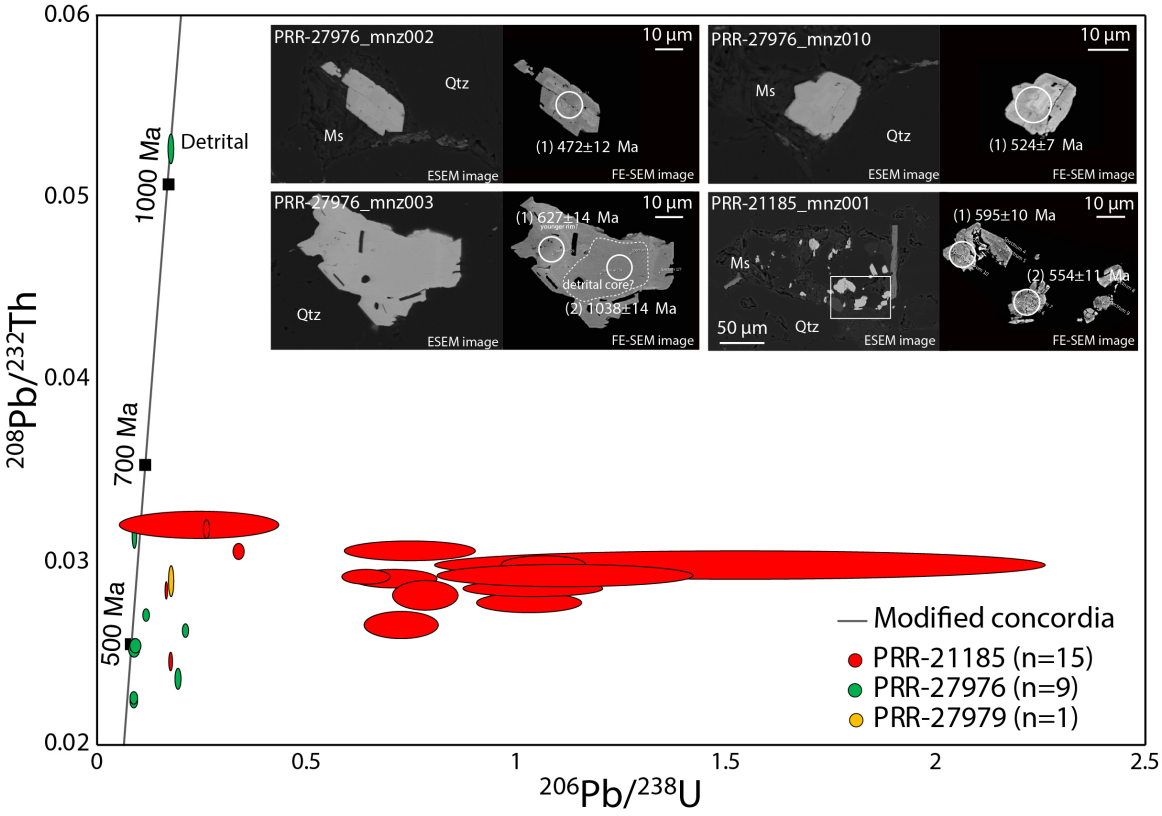

Figure 7. $^{206}Pb/^{238}U$ vs $^{208}Pb/^{232}Th$ modified concordia diagram with twenty-five analyses obtained by in situ U–Th–Pb dating for twenty-one monazite grains. Data-point error ellipses are 1σ; (inset) annotated ESEM image (left) and FE-SEM image (right) of four representative monazite grains used for in situ U–Th–Pb dating. Sample and grain number are indicated for each image. U–Th–Pb spots are 9 µm; spot numbers are shown in brackets; apparent ages are reported as $^{208}Pb/^{232}Th$ ages; Abbreviations are: Ms–Muscovite; Qtz–Quartz.

Fifteen authigenic monazite grains analysed in sample PRR-21185 yield apparent $^{232}Th/^{208}Pb$ ages ranging between c. 639–490 Ma (Fig. 7). Eight authigenic monazite analyses from sample PRR-27976 yield ages ranging between c. 627–449 Ma (Fig. 7). A $^{232}Th/^{208}Pb$ apparent age of c. 1038 Ma obtained for one older monazite grain core

exhibiting relatively lower Th (4282 ppm) and higher U (1664 ppm) is interpreted as a detrital relict. A single analysis obtained from sample PRR-27979 yielded an apparent $^{232}Th/^{208}Pb$ age of 577 ± 17 Ma (Fig. 7).

The observed spread in $^{232}Th/^{208}Pb$ ages could indicate different stages of authigenic monazite formation during the Late Neoproterozoic-Cambrian; we suggest that the oldest analyses in samples PRR-21185 and PRR-27976 may be closer to the depositional age of the sandstone while the apparently younger analyses record subsequent generation(s) of post-depositional authigenic monazite formation/hydrothermal alteration. An age of c. 633 Ma (average of two oldest $^{232}Th/^{208}Pb$ ages in samples PRR-21185 and PRR-27976) is therefore considered a minimum deposition age for the sandstone samples. The age of the single detrital monazite core also further constrains the maximum deposition age of the sandstones to 1038 ± 16 Ma.

6. A Neoproterozoic Sedimentary Basin in Interior Wilkes Land

New zircon U–Pb–Hf isotopic data from sandstone erratic samples allowed us to investigate, for the first time, the age and provenance of the enigmatic Sabrina Sedimentary Basin, interpreted to cover vast tracts of interior Wilkes Land (Fig. 1a; Fig 2a). Present-day ice divides and ice-flow directions (Mouginot et al., 2017; Rignot et al., 2011) indicate that the sandstone erratics were likely eroded from inland areas of the Vanderford ice catchment and transported to their present locations during a former expansion of the Vanderford Glacier (Goodwin, 1995; Mackintosh et al., 2014) (Fig. 2a). To our knowledge, these sandstone erratics represent the first samples of the Sabrina Sedimentary Basin ever to be examined in detail.

The Sabrina Sedimentary Basin has been interpreted as the Antarctic equivalent of Australian Mesozoic-Cenozoic break-up sedimentary basins (Aitken et al., 2014). However, U–Pb dating of detrital zircon and in-situ authigenic monazite constrain a much older Neoproterozoic (c. 1038–633 Ma) depositional age range for at least part of the basin. This is further supported by the lack of Pan-African aged (c. 600–500 Ma) detrital zircon which instead are consistently present in younger Australian Palaeozoic to Cenozoic sedimentary deposits (Reid et al., 2013; Yao et al., 2018). This age range broadly corresponds to the deposition of the Neoproterozoic sedimentary sequences in the eastern Officer Basin (Wade et al., 2005) of southern Australia (Fig. 1a), as well as Neoproterozoic sedimentary

rocks of the Beardmore Group in the Transantarctic Mountains (Goodge et al., 2004). We therefore suggest that sedimentary cover similar in age and composition to the Neoproterozoic eastern Officer Basin and Beardmore Group occupies an area of approximately 100,000 km^2 in the Vanderford ice catchment, and could extend over large parts of the Sabrina Sedimentary Basin further east.

The detrital signature of the sandstone erratics is defined by a broadly bimodal distribution: 1) the c. 1600–1470 Ma detrital zircon age and εHf_i signatures match the character of igneous zircons from the Toolgana and Undawidgi supersuites in the Coompana Province (Fig. 6), and 2) the c. 1180 Ma detrital zircon population is broadly similar in age and εHf_i to igneous zircons of the Moodini Supersuite of the Coompana and Madura provinces (Kirkland et al., 2017), and Chick Island (this study), as well as isotopically-similar granitic rocks found in the Wilkes Province (e.g. Ardery Charnockite (Morrissey et al., 2017) (Fig. 6). We suggest granitic source rocks of these ages and isotopic compositions contribute to the main detrital zircon signature in Neoproterozoic sedimentary rocks in the Sabrina Sedimentary Basin and indicate a predominantly local derivation of sediments from the Banzare and Nuyina provinces and / or Australian equivalent basement provinces. Older age components between c. 1700 Ma and 2400 Ma, correlate with the age of known magmatic events in the Gawler/Mawson cratons (Belousova et al., 2009) (Fig. 6) and could be interpreted to indicate minor sedimentary input from the east.

In Australia, the southerly extension of the eastern Officer Basin in the Coompana and Madura provinces is poorly known and concealed by the Mesozoic and Cenozoic cover of the Bight and Eucla basins. Two sandstone samples from the Mallabie-1 drill hole in the Coompana Province are tentatively linked to the eastern Officer Basin and yield similar age spectra to our sandstone erratic samples (Fraser & Neumann, 2016) (Fig. 6). While we note some differences in the dominant peak ages in the zircon age spectra between these Officer Basin sedimentary rocks and our samples, the overall detrital zircon age spectra signatures in the former also suggests a strong influence of proximal sediment contributions (i.e. Coompana Province and Musgrave Province) (Barham et al., 2018). A similar provenance is also shared by parts of the Neoproterozoic Beardmore Group (i.e. Goldie Formation) which is also interpreted to reflect a dominantly Mesoproterozoic sediment source form interior Wilkes Land (Goodge et al., 2004).

7. Implications of Subglacial Geology

Our new zircon U–Pb–Hf and monazite U–Th–Pb geochronology, combined with regional age data and aero-geophysical observations have allowed us to interpret the age and composition of bedrock in interior Wilkes Land and test tectonic models.

We provide the first geological evidence for the Antarctic counterparts of the Mesoproterozoic Coompana and Madura provinces, previously only documented in southern Australia and resolve the geometry of these conjugate Mesoproterozoic basement provinces in both a Rodinia and Gondwana configuration. The addition of these two new Antarctic provinces confirm the presence of a progressively westerly-younging sequence of juvenile magmatic arc-related rocks retreating away from the Mawson Craton and provides additional evidence for a subduction-driven Mesoproterozoic evolution of Australo-Antarctica as supported by recent tectonic models (Aitken et al., 2016a). The improved geometrical correlation between basement provinces of Wilkes Land and southern Australia will be fundamental in further understanding the Mesoproterozoic evolution of Australo-Antarctica and as such, inform plate tectonic models for the amalgamation of Nuna and Rodinia and the configuration of Gondwana.

New zircon and monazite data from sandstone erratics demonstrate the presence of Neoproterozoic sedimentary rocks in the Sabrina Sedimentary Basin that are equivalent in age and provenance to the eastern Officer Basin of Australia and Beardmore Group in the Transantarctic Mountains. The occurrence of sedimentary rocks of this age was previously unknown for this sector of East Antarctica and has broader implications for understanding the Rodinia-to-Gondwana transition during the Neoproterozoic. Similarities in age and provenance between our sandstone erratics and the Beardmore Group in the Transantarctic Mountains suggest that Neoproterozoic sedimentary rocks may have once covered a large sector of East Antarctica, forming an extensive platform basin on the proto-pacific rifting Rodina margin (Goodge et al., 2004). However, due to the limited geological samples available, we are unable to define the extent of the newly identified Neoproterozoic Sabrina Basin outside the confines of the Vanderford ice catchment region. It therefore remains unclear whether the Neoproterozoic Sabina Basin formed an Antarctic extension of the larger Centralian Superbasin or constitutes a different Neoproterozoic Antarctic basin sharing provenance similarities with the Officer Basin. Furthermore, we do not exclude the presence of a younger Mesozoic or Cenozoic basin phase in the Sabrina

Sedimentary Basin as previously hypothesised by Aitken et al. (2014), which could overlie older sedimentary sequences as seen in southern Australia with the overlap of the Bight and Eucla basins over the Officer Basin.

Our improved geological correlation between southern Australia and Wilkes Land, and interpretation of age and composition of subglacial bedrock, can also help inform estimations of the spatial distribution of crustal radiogenic heat production(Carson et al., 2014) and geothermal heat flow (Pollett et al., 2018) across the Australian-Antarctic margin, with potential implications for ice sheet models that simulate past and future Antarctic ice sheet behaviour.

Acknowledgements

We thank S. Phipps and T. Staal for fieldwork at Chick Island. S. Meffre, J. Mulder, A. Stepanov and J. Thompson (ARC [Australian Research Council] Centre of Excellence in Ore Deposit, CODES, University of Tasmania), K. Goemann and S. Feig (Central Science Laboratory, University of Tasmania) and Y. Greau (ARC Centre of Excellence for Core to Crust Fluid Systems, CCFS, Macquarie University, Australia) are thanked for analytical assistance. This research used samples provided by the Polar Rock Repository (PRR). The PRR is sponsored by the National Science Foundation Office of Polar Programs. AM is supported by an Australian Government Research Training Program (RTP) Scholarship. This research is supported by the Australian Research Council's Special Research Initiative for Antarctic Gateway Partnership (Project ID SR140300001). We thank two anonymous reviewers for their constructive reviews on the manuscript.

References

Aitken, A. R. A., Betts, P. G., Young, D. A., Blankenship, D. D., Roberts, J. L., & Siegert, M. J. (2016a). The Australo-Antarctic Columbia to Gondwana transition. *Gondwana Research, 29*(1), 136-152. doi:10.1016/j.gr.2014.10.019

Aitken, A. R. A., Roberts, J. L., van Ommen, T. D., Young, D. A., Golledge, N. R., Greenbaum, J. S., Blankenship, D. D., & Siegert, M. J. (2016b). Repeated large-scale retreat and advance of Totten Glacier indicated by inland bed erosion. *Nature, 533*(7603), 385-389. doi:10.1038/nature17447

Aitken, A. R. A., Young, D. A., Ferraccioli, F., Betts, P. G., Greenbaum, J. S., Richter, T. G., Roberts, J. L., Blankenship, D. D., & Siegert, M. J. (2014). The subglacial geology of Wilkes Land, East Antarctica. *Geophysical Research Letters, 41*(7), 2014GL059405. doi:10.1002/2014gl059405

Barham, M., Reynolds, S., Kirkland, C. L., O'Leary, M. J., Evans, N. J., Allen, H. J., Haines, P. W., Hocking, R. M., & McDonald, B. J. (2018). Sediment routing and basin evolution in Proterozoic to Mesozoic east Gondwana: A case study from southern Australia. *Gondwana Research, 58*, 122-140. doi:10.1016/j.gr.2018.03.006

Belousova, E. A., Reid, A. J., Griffin, W. L., & O'Reilly, S. Y. (2009). Rejuvenation vs. recycling of Archean crust in the Gawler Craton, South Australia: Evidence from U–Pb and Hf isotopes in detrital zircon. *Lithos, 113*(3-4), 570-582. doi:10.1016/j.lithos.2009.06.028

Black, L. P., Kamo, S. L., Allen, C. M., Aleinikoff, J. N., Davis, D. W., Korsch, R. J., & Foudoulis, C. (2003). TEMORA 1: a new zircon standard for Phanerozoic U–Pb geochronology. *Chemical Geology, 200*(1), 155-170.

Boger, S. D. (2011). Antarctica - Before and after Gondwana. *Gondwana Research, 19*(2), 335-371.

Carson, C. J., McLaren, S., Roberts, J. L., Boger, S. D., & Blankenship, D. D. (2014). Hot rocks in a cold place: high sub-glacial heat flow in East Antarctica. *Journal of the Geological Society, 171*(1), 9-12. doi:10.1144/jgs2013-030

Espurt, N., Callot, J. P., Roure, F., Totterdell, J. M., Struckmeyer, H. I., & Vially, R. (2012). Transition from symmetry to asymmetry during continental rifting: an example from the Bight Basin–Terre Adélie (Australian and Antarctic conjugate margins). *Terra Nova, 24*(3), 167-180.

Fitzsimons, I. C. W. (2003). Proterozoic basement provinces of southern and southwestern Australia, and their correlation with Antarctica. *Geological Society, London, Special Publications, 206*(1), 93-130. doi:10.1144/gsl.sp.2003.206.01.07

Fraser, G. L., & Neumann, N. L. (2016). Under the Nullarbor: New SHRIMP UPb zircon ages from the Coompana, Madura and Albany-Fraser Provinces, and Officer Basin, western South Australia and eastern Western Australia: July 2014–June 2015. Record 2016/16. Geoscience Australia, Canberra.

Goldthwait, R. P. (1959). USNC-IGY Antarctic glaciological data field work 1957 and 1958. *The Ohio State University Research Foundation, Report. 825-2-Part VI*(IGY Project. No. 4.10), 17-18.

Golynsky, A. V., Ferraccioli, F., Hong, J. K., Golynsky, D. A., von Frese, R. R. B., Young, D. A., Blankenship, D. D., Holt, J. W., Ivanov, S. V., Kiselev, A. V., Masolov, V. N., Eagles, G., Gohl, K., Jokat, W., Damaske, D., Finn, C., Aitken, A., Bell, R. E., Armadillo, E., Jordan, T. A., Greenbaum, J. S., Bozzo, E., Caneva, G., Forsberg, R., Ghidella, M., Galindo-Zaldivar, J., Bohoyo, F., Martos, Y. M., Nogi, Y., Quartini, E., Kim, H. R., & Roberts, J. L. (2018). New Magnetic Anomaly Map of the Antarctic. *Geophysical Research Letters, 45*(13), 6437-6449. doi:doi:10.1029/2018GL078153

Gonçalves, G. O., Lana, C., Scholz, R., Buick, I. S., Gerdes, A., Kamo, S. L., Corfu, F., Marinho, M. M., Chaves, A. O., Valeriano, C., & Nalini, H. A. (2016). An assessment of monazite from the Itambé pegmatite district for use as U–Pb isotope reference material for microanalysis and implications for the origin of the "Moacyr" monazite. *Chemical Geology, 424*, 30-50. doi:10.1016/j.chemgeo.2015.12.019

Goodge, J. W., Williams, I. S., & Myrow, P. (2004). Provenance of Neoproterozoic and lower Paleozoic siliciclastic rocks of the central Ross orogen, Antarctica: Detrital record of rift-, passive-, and active-margin sedimentation. *Bulletin of the Geological Society of America, 116*(9-10), 1253-1279.

Goodwin, I. D. (1995). On the Antarctic contribution to Holocene sea-level [Doctoral dissertation]: University of Tasmania, 111 p.

Grand'Homme, A., Janots, E., Bosse, V., Seydoux-Guillaume, A. M., & De Ascenção Guedes, R. (2016). Interpretation of U-Th-Pb in-situ ages of hydrothermal monazite-(Ce) and xenotime-(Y): evidence from a large-scale regional study in clefts from the western alps. *Mineralogy and Petrology, 110*(6), 787-807. doi:10.1007/s00710-016-0451-5

Griffin, W. L., Belousova, E. A., Shee, S. R., Pearson, N. J., & O'Reilly, S. Y. (2004). Archean crustal evolution in the northern Yilgarn Craton: U–Pb and Hf-isotope evidence from detrital zircons. *Precambrian Research, 131*(3-4), 231-282. doi:10.1016/j.precamres.2003.12.011

Griffin, W. L., Pearson, N. J., Belousova, E. A., & Saeed, A. (2006). Comment: Hf-isotope heterogeneity in zircon 91500. *Chemical Geology, 233*(3-4), 358-363. doi:10.1016/j.chemgeo.2006.03.007

Griffin, W. L., Wang, X., Jackson, S. E., Pearson, N. J., O'Reilly, S. Y., Xu, X., & Zhou, X. (2002). Zircon chemistry and magma mixing, SE China: In-situ analysis of Hf isotopes, Tonglu and Pingtan igneous complexes. *Lithos, 61*(3), 237-269. doi:https://doi.org/10.1016/S0024-4937(02)00082-8

Gulick, S. P. S., Shevenell, A. E., Montelli, A., Fernandez, R., Smith, C., Warny, S., Bohaty, S. M., Sjunneskog, C., Leventer, A., Frederick, B., & Blankenship, D. D. (2017). Initiation and long-term instability of the East Antarctic Ice Sheet. *Nature, 552*(7684), 225-229. doi:10.1038/nature25026

Halpin, J. A., Jensen, T., McGoldrick, P., Meffre, S., Berry, R. F., Everard, J. L., Calver, C. R., Thompson, J., Goemann, K., & Whittaker, J. M. (2014). Authigenic monazite and detrital zircon dating from the Proterozoic Rocky Cape Group, Tasmania: Links to the Belt-Purcell Supergroup, North America. *Precambrian Research, 250*(0), 50-67. doi:http://dx.doi.org/10.1016/j.precamres.2014.05.025

Hartnady, M. I. H., Kirkland, C. L., Dutch, R. I., Bodorkos, S., & Jagodzinski, E. A. (2018). Zircon Hf isotopic signatures of the Coompana Province in South Australia. *In R Dutch, T Wise, M Pawley and A Petts eds, Coompana Drilling and Geochemistry Workshop 2018 extended abstracts, Report Book 2018/00019. Department for Energy and Mining, South Australia, Adelaide.*

Hawkesworth, C. J., & Kemp, A. I. (2006). Evolution of the continental crust. *Nature, 443*(7113), 811-817. doi:10.1038/nature05191

Howard, H. M., Smithies, R. H., Kirkland, C. L., Kelsey, D. E., Aitken, A., Wingate, M. T. D., Quentin de Gromard, R., Spaggiari, C. V., & Maier, W. D. (2015). The burning heart — The Proterozoic geology and geological evolution of the west Musgrave Region, central Australia. *Gondwana Research, 27*(1), 64-94. doi:10.1016/j.gr.2014.09.001

Jackson, S. E., Pearson, N. J., Griffin, W. L., & Belousova, E. A. (2004). The application of laser ablation-inductively coupled plasma-mass spectrometry to in situ U–Pb zircon geochronology. *Chemical Geology, 211*(1), 47-69.

Jagodzinski, E. A., & Bodorkos, S. (2018). U-Pb geochronology of the eastern Coompana Province, South Australia. *In R Dutch, T Wise, M Pawley and A Petts eds, Coompana Drilling and Geochemistry Workshop 2018 extended abstracts, Report Book 2018/00019. Department for Energy and Mining, South Australia, Adelaide.*

Kirkland, C., Poujol, M., Kirkland, C. L., Spaggiari, C. V., Pawley, M. J., Wingate, M. T. D., Smithies, R. H., Howard, H. M., Tyler, I. M., Belousova, E. A., & Poujol, M. (2011a). On the edge: U-Pb, Lu-Hf, and Sm-Nd data suggests reworking of the Yilgarn craton margin during formation of the Albany-Fraser Orogen. *Precambrian Research, 187*(3-4), 223-247.

Kirkland, C., Wingate, M., Johnson, S., Spaggiari, C., Belousova, E., & Murphy, R. (2011b). Lu–Hf isotopes: implications for understanding crustal evolution. In *GSWA 2011 extended abstracts: promoting the prospectivity of Western Australia* (pp. 7-9): Geological Survey of Western Australia.

Kirkland, C. L., Smithies, R. H., Spaggiari, C. V., Wingate, M. T. D., Quentin de Gromard, R., Clark, C., Gardiner, N. J., & Belousova, E. A. (2017). Proterozoic crustal evolution of the Eucla basement, Australia: Implications for destruction of oceanic crust during emergence of Nuna. *Lithos, 278-281*, 427-444. doi:10.1016/j.lithos.2017.01.029

Kirkland, C. L., Smithies, R. H., Woodhouse, A. J., Howard, H. M., Wingate, M. T., Belousova, E. A., Cliff, J. B., Murphy, R. C., & Spaggiari, C. V. (2013). Constraints and deception in the isotopic record; the crustal evolution of the west Musgrave Province, central Australia. *Gondwana Research, 23*(2), 759-781.

Kirkman, T. W. (1996). Statistics to use. *http://www.physics.csbsju.edu/stats/*, (3 Mar 2019).

Lindsay, J. F., & Leven, J. H. (1996). Evolution of a Neoproterozoic to Palaeozoic intracratonic setting, Officer Basin, South Australia. *Basin Research, 8*(4), 403-424. doi:doi:10.1046/j.1365-2117.1996.00223.x

Lowry, D. C. (1970). *Geology of the Western Australian part of the Eucla Basin*: Geological Survey of Western Australia.

Mackintosh, A. N., Verleyen, E., O'Brien, P. E., White, D. A., Jones, R. S., McKay, R., Dunbar, R., Gore, D. B., Fink, D., Post, A. L., Miura, H., Leventer, A., Goodwin, I., Hodgson, D. A., Lilly, K., Crosta, X., Golledge, N. R., Wagner, B., Berg, S., van Ommen, T., Zwartz, D., Roberts, S. J., Vyverman, W., & Masse, G. (2014). Retreat history of the East Antarctic Ice Sheet since the Last Glacial Maximum. *Quaternary Science Reviews, 100*, 10-30. doi:10.1016/j.quascirev.2013.07.024

Maidment, D. W. (2005). Palaeozoic high-grade metamorphism within the Centralian Superbasin, Harts Range region, central Australia.

Markwitz, V., & Kirkland, C. L. (2018). Source to sink zircon grain shape: Constraints on selective preservation and significance for Western Australian Proterozoic basin provenance. *Geoscience Frontiers, 9*(2), 415-430. doi:10.1016/j.gsf.2017.04.004

McLeod, I. R., & Gregory, C. M. (1967). *Geological investigations along the Antarctic coast between longitudes 108°E and 166°E*. Canberra: Bureau of Mineral Resources, Geology and Geophysics.

Morrissey, L. J., Payne, J. L., Hand, M., Clark, C., Taylor, R., Kirkland, C. L., & Kylander-Clark, A. (2017). Linking the Windmill Islands, east Antarctica and the Albany–Fraser Orogen: Insights from U–Pb zircon geochronology and Hf isotopes. *Precambrian Research, 293*, 131-149. doi:10.1016/j.precamres.2017.03.005

Mouginot, J., Scheuchl, B., & Rignot, E. (2017). MEaSUREs Antarctic Boundaries for IPY 2007-2009 from Satellite Radar, Version 2. [Indicate subset used]. Boulder, Colorado USA. NASA National Snow and Ice Data Center Distributed Active Archive Center. doi: https://doi.org/10.5067/AXE4121732AD. [24-04-2018].

Pierce, E. L., Hemming, S. R., Williams, T., van de Flierdt, T., Thomson, S. N., Reiners, P. W., Gehrels, G. E., Brachfeld, S. A., & Goldstein, S. L. (2014). A comparison of detrital U–Pb zircon, 40Ar/39Ar hornblende, 40Ar/39Ar biotite ages in marine sediments off East Antarctica: Implications for the geology of subglacial terrains and provenance studies. *Earth-Science Reviews, 138*, 156-178. doi:http://dx.doi.org/10.1016/j.earscirev.2014.08.010

Pollett, A., Hand, M., Bendall, B., Raimondo, T., Halpin, J., & McLaren, S. (2018). Constraining basal heat flux in eastern Antarctica using new heat flow data from formerly contiguous geological terranes of southern Australia. *Geophysical Research Abstracts, Vol. 20, EGU2018-5774, 2018. EGU General Assembly 2018.*

Ravich, M. G., Solov'ev, D. S., & Klimov, L. V. (1968). *The Pre-Cambrian of East Antarctica*. Jerusalem: Israel Program for Scientific Translations [available from the U.S. Dept. of Commerce, Clearinghouse for Federal Scientific and Technical Information, Springfield, Va.].

Raymond, O. L., Totterdell, J. M., Stewart, A. J., & Woods, M. A. (2018). Australian Geological Provinces, 2018.01 edition [Digital Dataset]. Geoscience Australia, Commonwealth of Australia, Canberra. http://www.ga.gov.au.

Reid, A., Keeling, J., Boyd, D., Belousova, E., & Hou, B. (2013). Source of zircon in world-class heavy mineral placer deposits of the Cenozoic Eucla Basin, southern Australia from LA-ICPMS U–Pb geochronology. *Sedimentary Geology, 286–287*(0), 1-19. doi:http://dx.doi.org/10.1016/j.sedgeo.2012.10.008

Rignot, E., Mouginot, J., & Scheuchl, B. (2011). Ice flow of the antarctic ice sheet. *Science, 333*(6048), 1427-1430. doi:10.1126/science.1208336

Roy, M., van de Flierdt, T., Hemming, S. R., & Goldstein, S. L. (2007). 40Ar/39Ar ages of hornblende grains and bulk Sm/Nd isotopes of circum-Antarctic glacio-marine sediments: Implications for sediment provenance in the southern ocean. *Chemical Geology, 244*(3–4), 507-519. doi:http://dx.doi.org/10.1016/j.chemgeo.2007.07.017

Rubatto, D., Williams, I. S., & Buick, I. S. (2001). Zircon and monazite response to prograde metamorphism in the Reynolds Range, central Australia. *Contributions to Mineralogy and Petrology, 140*(4), 458-468.

Sack, P. J., Berry, R. F., Meffre, S., Falloon, T. J., Gemmell, J. B., & Friedman, R. M. (2011). In situ location and U-Pb dating of small zircon grains in igneous rocks using laser ablation–inductively coupled plasma–quadrupole mass spectrometry. *Geochemistry, Geophysics, Geosystems, 12*(5).

Scherer, E., Münker, C., & Mezger, K. (2001). Calibration of the Lutetium-Hafnium Clock. *Science, 293*(5530), 683.

Seydoux-Guillaume, A. M., Montel, J. M., Bingen, B., Bosse, V., de Parseval, P., Paquette, J. L., Janots, E., & Wirth, R. (2012). Low-temperature alteration of monazite: Fluid mediated coupled dissolution-precipitation, irradiation damage, and disturbance of the U-Pb and Th-Pb chronometers. *Chemical Geology, 330*, 140-158.

Sláma, J., Košler, J., Condon, D. J., Crowley, J. L., Gerdes, A., Hanchar, J. M., Horstwood, M. S. A., Morris, G. A., Nasdala, L., Norberg, N., Schaltegger, U., Schoene, B., Tubrett, M. N., & Whitehouse, M. J. (2008). Plešovice zircon - A new natural reference material for U-Pb and Hf isotopic microanalysis. *Chemical Geology, 249*(1-2), 1-35. doi:http://dx.doi.org/10.1016/j.chemgeo.2007.11.005

Smits, R. G., Collins, W. J., Hand, M., Dutch, R., & Payne, J. (2014). A Proterozoic Wilson cycle identified by Hf isotopes in central Australia: Implications for the assembly of Proterozoic Australia and Rodinia. *Geology, 42*(3), 231-234. doi:10.1130/G35112.1

Spaggiari, C. V., Kirkland, C. L., Pawley, M. J., Smithies, R. H., Wingate, M. T. D., Doyle, M. G., Blenkinsop, T. G., Clark, C., Oorschot, C. W., Fox, L. J., & Savage, J. (2011). *The Geology of the East Albany-Fraser Orogen: A Field Guide*: Geological Survey of Western Australia.

Spaggiari, C. V., Smithies, R. H., Kirkland, C. L., Wingate, M. T. D., England, R. N., & Lu, Y.-J. (2018). Buried but preserved: The Proterozoic Arubiddy Ophiolite, Madura Province, Western Australia. *Precambrian Research, 317*, 137-158. doi:10.1016/j.precamres.2018.08.025

Streckeisen, A. (1976). To each plutonic rock its proper name. *Earth-Science Reviews, 12*(1), 1-33. doi:https://doi.org/10.1016/0012-8252(76)90052-0

Vermeesch, P. (2012). On the visualisation of detrital age distributions. *Chemical Geology, 312-313*, 190-194. doi:10.1016/j.chemgeo.2012.04.021

Vermeesch, P. (2018). IsoplotR: A free and open toolbox for geochronology. *Geoscience Frontiers, 9*(5), 1479-1493. doi:10.1016/j.gsf.2018.04.001

Wade, B. P., Hand, M., & Barovich, K. M. (2005). Nd isotopic and geochemical constraints on provenance of sedimentary rocks in the eastern Officer Basin, Australia; implications for the duration of the intracratonic Petermann Orogeny. *Journal of the Geological Society of London, 162, Part 3*, 513-530. doi:10.1144/0016-764904-001

Wiedenbeck, M., Alle, P., Corfu, F., Griffin, W., Meier, M., Oberli, F. v., Quadt, A. v., Roddick, J., & Spiegel, W. (1995). Three natural zircon standards for U-Th-Pb, Lu-Hf, trace element and REE analyses. *Geostandards and Geoanalytical Research, 19*(1), 1-23.

Wingate, M. T. D., Kirkland, C. L., Spaggiari, C. V., & Smithies, R. H. (2015a). U–Pb geochronology of the Forrest Zone of the Coompana Province. *Eucla basement stratigraphic drilling results release workshop: extended abstracts compiled by CV Spaggiari and RH Smithies: Geological Survey of Western Australia, Record 2015/10*, p. 37-40.

Wingate, M. T. D., Kirkland, C. L., Spaggiari, C. V., & Smithies, R. H. (2015b). U–Pb geochronology of the Madura Province. *Eucla basement stratigraphic drilling results release workshop: extended abstracts compiled by CV Spaggiari and RH Smithies: Geological Survey of Western Australia, Record 2015/10*, p. 14-16.

Wise, T. W., Pawley, M. J., & Dutch, R. A. (2015). Preliminary interpretations from the 2015 Coompana aeromagnetic survey. *MESA Journal, 79*(4), 22-30.

Yao, W., Li, Z.-X., Spencer, C. J., & Martin, E. L. (2018). Indian-derived sediments deposited in Australia during Gondwana assembly. *Precambrian Research, 312*, 23-37. doi:10.1016/j.precamres.2018.05.006

Zhang, S. H., Zhao, Y., Liu, X. C., Liu, Y. S., Hou, K. J., Li, C. F., & Ye, H. (2012). U-Pb geochronology and geochemistry of the bedrocks and moraine sediments from the Windmill Islands: Implications for Proterozoic evolution of East Antarctica. *Precambrian Research, 206-207*, 52-71.

Chapter 3

Pangea Rifting Shaped the East Antarctic Landscape

Alessandro Maritati[1], Martin Danišík[2], Jacqueline A. Halpin[1], Joanne M. Whittaker[1], Alan R. A. Aitken[3]

[1]Institute for Marine and Antarctic Studies, University of Tasmania, Australia

[2]John de Laeter Centre/The Institute for Geoscience Research, Curtin University, Australia

[3]School of Earth Sciences, University of Western Australia, Australia

Abstract

East Antarctica remains one of the few continental regions on Earth where an understanding of the origin and causal processes responsible for topographic relief is largely missing. Low-temperature thermochronology studies of exposed Precambrian basement revealed discrete episodes of cooling and denudation during the Paleozoic–Mesozoic; however, the significance of these thermal events and their relationship to topography across the continental interior remains unclear. Here we use zircon and apatite (U–Th)/He thermochronology to resolve the low-temperature thermal evolution of a poorly-exposed section of East Antarctic basement in the Bunger Hills region and gain insights into the chronology and style of landscape evolution across East Antarctica. Thermal history modelling results indicate that Precambrian basement in the Bunger Hills region experienced a distinct cooling episode during the Late Paleozoic–Triassic, which we relate to ~2–4 km of regional exhumation associated with intracontinental rifting, followed by a second episode of localized cooling and ≤1 km exhumation during the Late Jurassic–Cretaceous separation of India from East Gondwana. These findings, combined with existing thermochronological and tectonic evidence, support a continent-scale denudation event associated with uplift and exhumation of large sections of Precambrian basement during Late Paleozoic–Triassic Pangea-wide intracontinental extension. By contrast, continental extension associated with the Jurassic–Cretaceous breakup of East Gondwana resulted in significant denudation only locally in regions west of the Bunger Hills. We propose that the combined effects of these Paleozoic–Mesozoic tectonic events had a profound impact on the topography across the East Antarctic interior and influenced the long-term landscape evolution of East Antarctica.

1. Introduction

The origin of topographic relief in old and tectonically stable continental interiors is a long-standing problem in continental dynamics (e.g. Ferraccioli et al., 2011; Hu et al., 2018). East Antarctica comprises one of the largest composite Precambrian shields on Earth and is a chief example of a vast continental region with topographic variability akin to tectonically active regions (Creyts et al., 2014). The most significant morphological variations across East Antarctica broadly correlate with the Precambrian domains of Australo-Antarctica and Indo-Antarctica, which amalgamated during the ~600–550 Ma assembly of Gondwana (e.g., Mulder et al., 2019). Despite preserving Precambrian crust with broadly similar thicknesses (Pappa et al., 2019), these two domains exhibit remarkably distinct hypsometry (O'Donnell & Nyblade, 2014; Fig. 1a). Indo-Antarctica possesses elevated, high-relief topography above the global average with narrow and deep rift basins (Ferraccioli et al., 2011). By contrast, the Australo-Antarctic domain comprises smoother topography at longer wavelengths and features large subglacial sedimentary basins where the vast majority of topography is below sea level (Aitken et al., 2014; Frederick et al., 2016; Maritati et al., 2016). Proposed models for the origin and long-term evolution of topography of ancient cratonic regions include high-standing passive margin formation during continental breakup [e.g., southern Africa; Wildman et al. (2016)], large-scale denudation of Phanerozoic cover [e.g., Yilgarn Craton; Weber et al. (2005)], and far-field deformation transmitted from collisional plate interactions [e.g., Canadian Shield; Pinet (2016)]. However, an understanding of the causal processes responsible for the large-scale hypsometric variability across East Antarctica remains largely missing due to its poorly understood Phanerozoic landscape evolution.

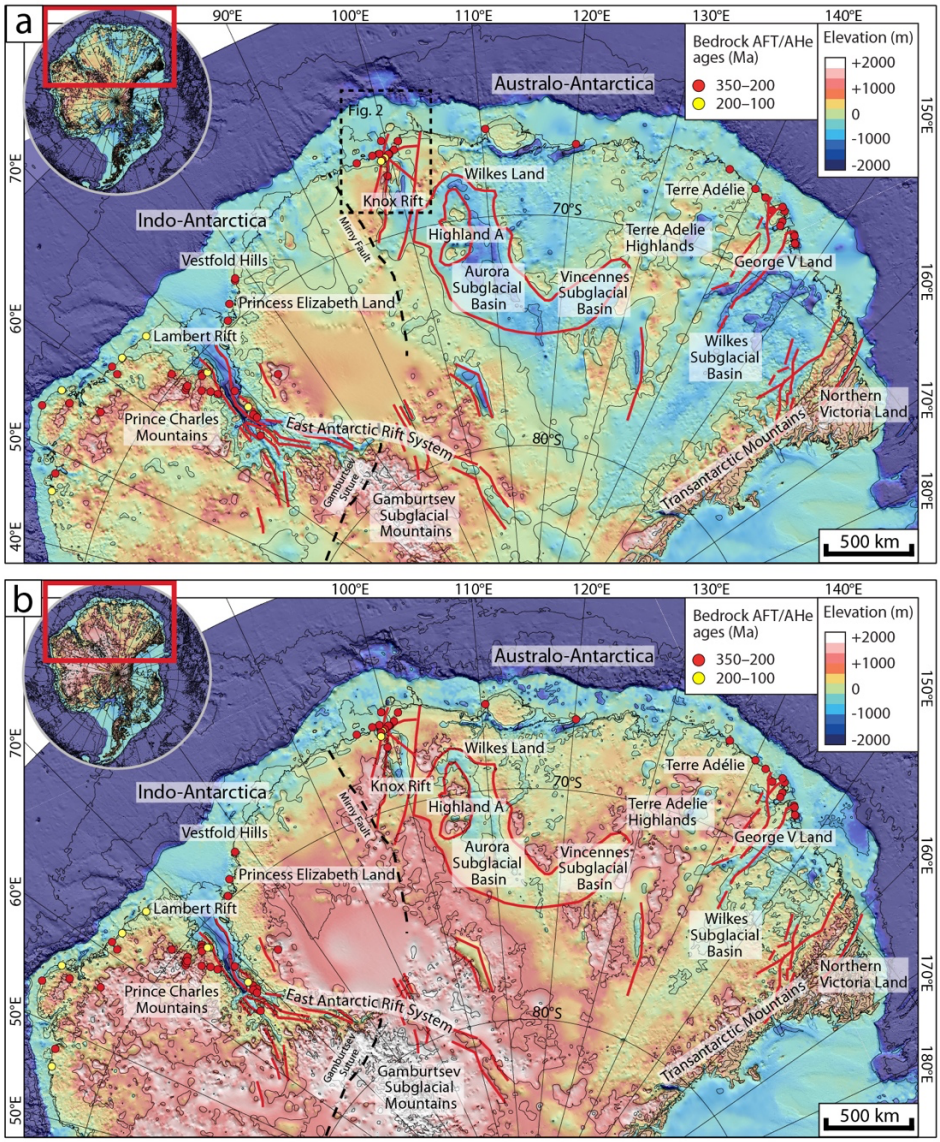

Figure 1. (**a**) Present-day bedrock topography of the Indo-Antarctic and Australo-Antarctic sectors of East Antarctica from BedMachine (Morlighem et al., 2020); **(b)** Bedrock topography after isostatic rebound due to the removal of the present-day ice load (Paxman et al., 2019b). Bedrock elevations on both grids are contoured at 1 km intervals. Colored circles show published bedrock AFT and AHe data from the Lambert Rift area (Arne, 1994; Lisker et al., 2003; Lisker et al., 2007a), Vestfold Hills (Lisker et al., 2007b) and Terre Adélie /George V Land (Lisker & Olesch, 2003; Rolland et al., 2019) as well as reconnaissance AFT data of Arne et al. (1993). Sedimentary basin-bounding faults in the EARS (Ferraccioli et al., 2011), Knox Rift (Maritati et al., 2016), Aurora and Vincennes Subglacial basins, (Aitken et al., 2016b), Wilkes Subglacial Basin (Paxman et al., 2019a and references therein) are highlighted in red; dashed black lines correspond to the inferred path the Mirny Fault (Daczko et al., 2018) and Gamburtsev Suture (Ferraccioli et al., 2011), which together represent the paleo-plate boundary between Indo-Antarctica and Australo-Antarctica (Mulder et al., 2019); dashed box in panel (**a**) indicates a detail of the Bunger Hills region shown in Figure 2.

Low-temperature (<300°C) thermochronology (LTT) has been widely used to quantify spatial and temporal patterns of cooling in continental settings, which in turn can provide constraints on the rates and mechanisms of landscape evolution (Kohn & Gleadow, 2019). Existing LTT data from Precambrian basement outcrops in the Indo-Antarctic and Australo-Antarctic domains suggest major cooling of East Antarctic basement during the Paleozoic–Mesozoic (Fig. 1); however, the significance of these observed Paleozoic–Mesozoic tectono-thermal events across interior East Antarctica, and any link in establishing the different topographic response of each domain, remains elusive. In the Indo-Antarctic domain, apatite fission-track (AFT) data from basement rocks in the northern Prince Charles Mountains (PCM) and Vestfold Hills record cooling associated with up to 5 km of basement exhumation during two discrete phases of continental rifting in the Lambert Rift (Arne, 1994; Lisker et al., 2003; Lisker et al., 2007a; Lisker et al., 2007b) and broader East Antarctic Rift System [EARS; Ferraccioli et al. (2011)] in the Late Paleozoic–Triassic (~310–200 Ma) and Cretaceous (~120–100 Ma). In the Australo-Antarctic domain west of the Transantarctic Mountains (TAM), AFT and apatite (U–Th)/He (AHe) data record a single Late Paleozoic–Triassic cooling event between ~350–200 Ma. This cooling has been interpreted to result from 3–4 km denudation triggered by either tectonic uplift synchronous with extension in the Wilkes Subglacial Basin (Lisker & Olesch, 2003), or denudation during large-scale glacial erosion of the Late Paleozoic Ice Age (Rolland et al., 2019). Investigations based on geophysical data and plate reconstructions have also suggested significant Cretaceous–Cenozoic onshore extensional tectonic activity in the interior of the Australo-Antarctic domain associated with plate divergence during the breakup of East Gondwana (Aitken et al., 2014; Eagles, 2019; Maritati et al., 2016) or intraplate strike-slip tectonics (e.g. Cianfarra & Maggi, 2017).

In this paper, we seek to establish a link between LTT data and Phanerozoic continent-scale geodynamic processes and the generation of variable hypsometry across East Antarctica. We use new (U–Th)/He data on zircon and apatite to reconstruct the low-temperature thermal evolution of Precambrian basement in the Bunger Hills region, located near the transition between high-relief regions of Indo-Antarctica and the low-lying subglacial basins of Australo-Antarctica. Our new results, combined with existing thermochronological, stratigraphic and tectonic constraints, provide evidence for a major denudational event across the East Antarctic interior associated with Late Paleozoic–

Triassic Pangea-wide intracontinental extension. We interpret these new results in the context of their Pangea-wide tectonic setting and discuss the influence of topographic development at this stage on the landscape evolution of East Antarctica more broadly.

2. The Bunger Hills region

Located in the western Wilkes Land sector of East Antarctica, the Bunger Hills region features a series of Precambrian–Early Cambrian coastal basement outcrops and remote inland nunataks, which together comprise the largest ice-free oasis in the western Australo-Antarctic domain (Tucker et al., 2020; Fig. 2)). These outcrops lie east of the inferred crustal boundary between Indo-Antarctica and Australo-Antarctica and record a complex tectonic history culminated in the suturing of Australo-Antarctica and Indo-Antarctica along the Ediacaran–Cambrian Kuunga Orogen (Mulder et al., 2019). Exposed basement in the region forms the western flank of the Knox Rift, a Phanerozoic rift basin that is characterized solely from geophysical data (Maritati et al., 2016; Fig. 2). The Knox Rift overprints basement and exerts a key influence on the regional topographic relief: while its flanks exhibit elevated (~1200 m) and rugged topography, its central depression has focused erosion from the Denman and Scott Glaciers, two of the largest ice streams in the region and hosts the deepest continental trench on Earth (Morlighem et al., 2020). The timing of extension in the Knox Rift, as well as the age of the sedimentary infill, is poorly known; plate reconstructions overall support a tectonic correlation with the Paleozoic–Mesozoic Perth Basin of western Australia within Gondwana. However, different phases of extension have been proposed in the Late Paleozoic–Triassic coeval with the Lambert Rift and EARS (Veevers, 2018), and during the Late Jurassic–Cretaceous separation of India from East Gondwana (Maritati et al., 2016).

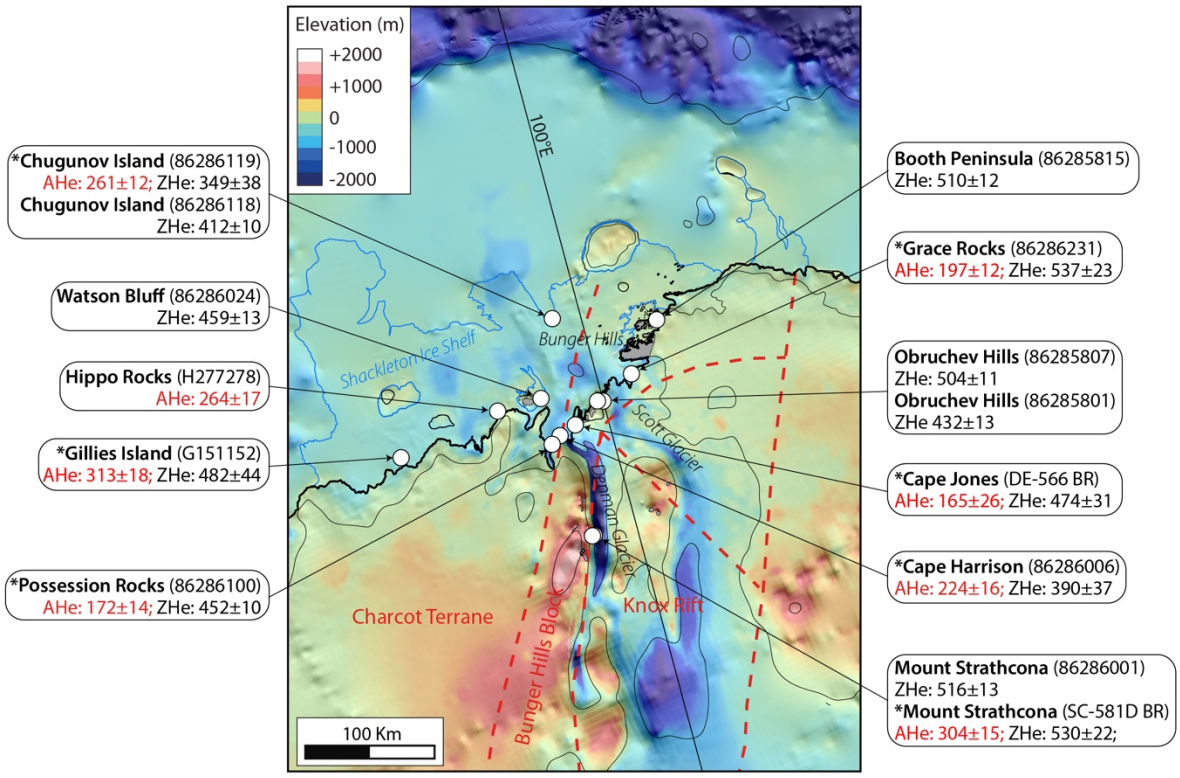

Figure 2. Bedrock topography map of Bunger Hills region showing exposed bedrock (grey areas), coastline (solid black line), and topographic contours at 1 km intervals (thin black lines). Simplified regional tectonic lineaments from Maritati et al. (2016) are shown as dashed red lines. The basement domains of the Bunger Hills Block and Charcot Terrane form the western flank of the Knox Rift. White circles represent location of Precambrian basement samples. For each sample, the weighted mean AHe (red) and ZHe ages (black) and respective 1σ uncertainties in Ma are indicated. Asterisks indicate samples for which modelled time-temperature (t-T) diagrams are presented in Figure 3.

3. Methods

3.1 (U–Th)/He analysis

(U–Th)/He analysis was performed at the John de Laeter Centre (Curtin University, Perth). A summary of the samples used is given in Supplementary Table S1. Apatite and zircon crystals of suitable size, shape, and quality were hand-picked from mineral concentrates or plucked from epoxy mounts, previously used for U-Pb geochronology. Selected grains were then photographed and measured for dimensions to calculate alpha-ejection correction factor, and individually loaded in Pt (apatite) and Nb microtubes (zircon). Radiogenic ^{4}He was extracted at ~1250°C (zircon) or ~960°C (apatite) under ultra-high vacuum using a diode laser and its amount was determined by isotope dilution

using ^{3}He spike on a Pfeiffer Prisma QMS 200 mass spectrometer. Following the ^{4}He measurements, microtubes containing the crystals were retrieved from the laser cell, spiked with ^{235}U and ^{230}Th, dissolved in acids following the procedure of Evans et al. (2005) and the solutions were analyzed by isotope dilution for U and Th, and by external calibration for Sm on an Agilent 7500 ICP-MS. Total analytical uncertainty of uncorrected (U–Th)/He ages was calculated by propagating uncertainties of U, Th, Sm and He measurements. The uncorrected zircon (U–Th)/He (ZHe) and AHe ages were corrected for α-ejection (Ft correction) after Farley et al. (1996), whereby a homogenous distribution of U, Th, and Sm was assumed for the crystals. The accuracy of (U–Th)/He dating procedure was monitored by replicate analyses of Fish Canyon Tuff zircon (n =11) and Durango apatite (n =12) measured over the period of this study as internal standards, yielded mean (U–Th)/He ages of 29.2 ± 1.0 Ma and 31.8 ± 1.1 Ma, respectively. These ages are in good agreement with the reference ages of 28.3 ± 1.3 Ma [Fish Canyon Tuff; Reiners et al. (2002)] and 31.13±1.01 Ma [Durango; McDowell et al. (2005)]. (U–Th)/He analytical results are presented in Supplementary Table S2.

3.2 Time-temperature modelling of LTT data

Inverse thermal history modelling was carried out using HeFTy v1.9 software (Ketcham, 2005) to find time-temperature (t–T) paths that can reproduce measured thermochronological data and test plausible geological evolution scenarios. Only samples for which both zircon and apatite (U–Th)/He data are available were modelled. The models were parameterized as follows: diffusion kinetic parameters for zircon and apatite (U–Th)/He systems were adopted from Reiners et al. (2004) and Farley (2000), respectively; radii of the spherical diffusion domains were based on the measured size of the analyzed crystals and calculated equivalent sphere size; measured single grain ages that were closest to the population mean age were modelled as representative for the samples. A Monte-Carlo search method with 10,000 search tries was applied to find thermal trajectories that could reconcile the pre-defined parameters and constraints. 'Acceptable' and 'good' thermal paths were defined as having a goodness-of-fit (GOF) of >0.05 and >0.5, respectively.

4. Results and interpretation

4.1 Zircon and apatite (U–Th)/He thermochronology results

We report 72 zircon and 57 apatite single-grain (U–Th)/He ages from 14 basement outcrop samples from the western flank of the Knox Rift (Fig. 2; Supplementary Table S2). Reproducibility of replicates within samples is good with the majority of single grain ages overlapping within uncertainty. Our analysis shows that ZHe ages are in the range of ~537–365 Ma. In contrast, AHe ages are systematically younger than ZHe ages in each sample and range between ~313–165 Ma. AHe ages are consistent with an AFT age of 243±13 Ma previously reported for a single sample from the Bunger Hills (Arne et al., 1993) and overall confirm the Late Paleozoic–Mesozoic age trend of AHe and AFT basement ages in the Indo-Antarctic and Australo-Antarctic domains. Sampling resolution is limited to mainly coastal and low-elevation basement outcrops hindering identification of spatial age trends across the Bunger Hills region. However, we note that AHe ages around the Denman and Scott glaciers (i.e., Possession Rocks, Cape Harrison, Cape Jones and Grace Rocks) appear to form a cluster of relatively younger Triassic–Jurassic (224–165 Ma) ages while progressively older Late Carboniferous–Permian AHe ages occur to the west (Gillies Island and Hippo Rocks), south (Mount Strathcona), and north (Chugunov Island).

4.2 Phanerozoic thermal history of the Bunger Hills region

We explore the implications of the (U–Th)/He data for the Phanerozoic thermal history of Precambrian basement in the Bunger Hills region using t–T modelling of 7 samples for which we have both ZHe and AHe data. To extract realistic thermal histories, we have incorporated in our models a framework of t–T constraints based on available geological constraints: In all model runs, the end of the t–T path was set to -10°C according to the present-day annual mean surface temperature recorded at the Antarctic station of Casey; the starting point was set to a temperature of 500°C at 550 Ma reflecting minimum peak temperatures during the Kuunga orogenic event. Although not exposed in outcrop, we presume that the contact between Precambrian basement and sedimentary rocks at the base of the Knox Rift likely forms an erosional unconformity. A similar erosional surface separating Precambrian basement rocks from the overlying glaciogenic Latest Carboniferous–Permian sedimentary sequences exists in the conjugate south Perth Basin in Australia (Norvick, 2004). We therefore incorporate this constraint in our models and force a cooling to near-surface temperatures (T= -10–20°C) between 350–300 Ma. Using

these three fixed constraints, we model three different scenarios to test presence and magnitude of reheating during proposed extensional phases of the Knox Rift in the Late Paleozoic–Triassic (Veevers, 2018), Late Jurassic–Cretaceous (Maritati et al., 2016), and in both of these periods. Accordingly, for these periods we introduce additional constraints permitting temperatures of 30–220°C reflecting near-surface temperature conditions and maximum temperature limit of He retention in zircon, respectively. More specifically, the Late Paleozoic–Triassic extension was implemented by forcing reheating to temperatures between 30–220°C during the Late Paleozoic–Triassic (300–200 Ma) from Carboniferous near-surface temperatures. Late Jurassic–Cretaceous extension was implemented by forcing the samples to a surface temperature of ~20°C in the Early Jurassic (200–160 Ma) from Carboniferous near-surface temperatures, followed by reheating between 30–220°C in the Late Jurassic–Cretaceous (160–120 Ma). Finally, a two-stage extension scenario where Late Paleozoic–Triassic extension is followed by rapid cooling in the Late Triassic–Early Jurassic and renewed reheating in the Late Jurassic–Cretaceous was also implemented by combining the constraints of the two previous scenarios. In all models, timing of extension is calibrated to the conjugate Perth Basin which possesses well-documented stratigraphic and kinematic evidences for both a Late Paleozoic–Triassic and a Late Jurassic–Cretaceous extensional phase (Norvick, 2004). A summary of t-T modelling results is given in Figure 3 and in Supplementary Table S3.

Thermal history models reveal that cooling of Precambrian basement in the Bunger Hills region to near-surface temperatures (<30°C) after the Kuunga Orogeny 350–300 Ma must have been followed by at least one reheating-cooling episode between the Late Paleozoic and/or Cretaceous. Given that all our samples are located on the western rift flank in regions that are free of sedimentary cover and likely did not experience substantial (km-scale) burial of sedimentary rocks (Maritati et al., 2016), we infer the reheating-cooling episodes were achieved by an increase in the regional geothermal gradient due to rift-related processes. Thermochronology data for Gillies Island, Mount Strathcona, Grace Rocks and Chugunov Island are best reproduced with a single reheating-cooling episode in the Late Paleozoic–Triassic reaching peak temperatures of ~90–60°C (Fig. 3a). Paleogeothermal gradient estimates during extension in the Lambert Rift suggest an increase to ~30°C km^{-1} in the vicinity of the rift from a stable geothermal gradient of 19–20°C km^{-1} (Lisker et al., 2003). Similar estimates may be also reasonable during extension in

the Knox Rift, where a geothermal gradient increase of similar magnitude (~10°C km^{-1}) would explain the resetting of AHe systems from near-surface temperatures in basement samples on the western rift flank (Fig. 4a). Cooling of basement samples at Gillies Island, Mount Strathcona, Grace Rocks and Chugunov Island was most likely produced by thermal relaxation of the rift-related anomaly; for any assumed geothermal gradient estimates between 20–30°C km^{-1}, cooling must have been associated with a maximum exhumation and erosion of ~2–4 km of basement overburden at these localities (Fig. 4a). Thermal models for these samples also indicate that a phase of reheating between ~160–120 Ma is unlikely as samples could not exceed temperatures of 40°C in both the Late Jurassic–Cretaceous extension and two-stage extension scenarios (Fig. 3b and 3c).

Figure 3 (next page). Modelled thermal histories of seven basement samples from the Bunger Hills region displayed as time-temperature (t-T) diagrams. t-T diagrams are shown for each of the three model scenarios (**a**–**c**). In each t-T diagram, green and pink lines indicate "acceptable" (GOF >0.05) and "good" (GOF >0.5) thermal trajectories, respectively; thick blue lines represent the best-fit trajectories; dashed boxes represent predefined t-T constraints; red star indicate the preferred model scenario for each sample. Approximate temperature ranges of AHe partial retention zone [AHe PRZ, 40–80°C; Farley (2000)] and ZHe partial retention zone [ZHe PRZ, 160–200°C; Reiners et al. (2004)] are also shown. Measured and modelled ZHe and AHe ages with their respective GOF values for each set of models are indicated in Supplementary Table S3.

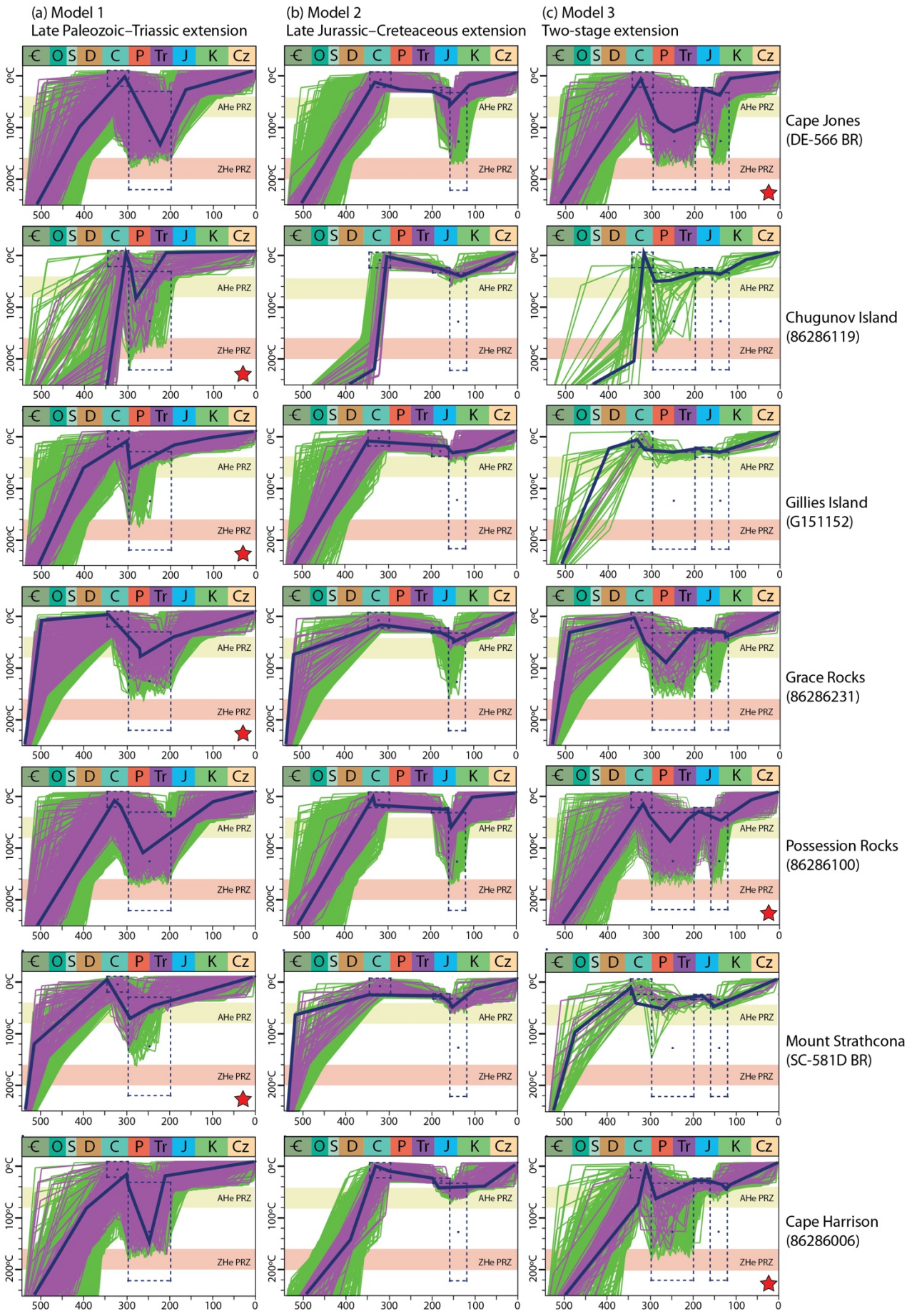
(a) Model 1
Late Paleozoic–Triassic extension
(b) Model 2
Late Jurassic–Creteaceous extension
(c) Model 3
Two-stage extension
Є O S D C P Tr J K Cz
0°C
100°C
200°C
AHe PRZ
ZHe PRZ
500 400 300 200 100 0
Cape Jones
(DE-566 BR)
Chugunov Island
(86286119)
Gillies Island
(G151152)
Grace Rocks
(86286231)
Possession Rocks
(86286100)
Mount Strathcona
(SC-581D BR)
Cape Harrison
(86286006)

Thermal histories for Cape Jones, Cape Harrison and Possession Rocks permit reheating to temperatures greater than 40°C in the Late Paleozoic–Triassic, Late Jurassic–Cretaceous, or in both these intervals (Fig. 3a–c). Maximum paleotemperatures in models simulating a single reheating phase in the Late Paleozoic–Triassic range between 160°C and 120°C and require the development of a substantially elevated paleogeothermal gradient in excess of 60°C km^{-1} (Fig. 3a). The two-stage extension scenario, in contrast, suggests lower Late Paleozoic–Triassic maximum paleotemperatures of ~90–60°C, which are consistent with those extracted from the Gillies Island, Mount Strathcona, Grace Rocks and Chugunov Island samples and indicate ~2 km of post-Permian basement exhumation (Fig. 3c; Fig. 4b). Furthermore, it allows for a second phase of modest rift-related reheating of basement to temperatures of ~40–50°C from Late Jurassic surface temperatures of 20°C in the Late Jurassic–Cretaceous, which indicates ≤1 km of post-Cretaceous basement exhumation (assuming a paleogeothermal gradient of ~20–30°C km^{-1}) in addition to ~2 km of Permian–Jurassic basement exhumation (Fig. 4b).

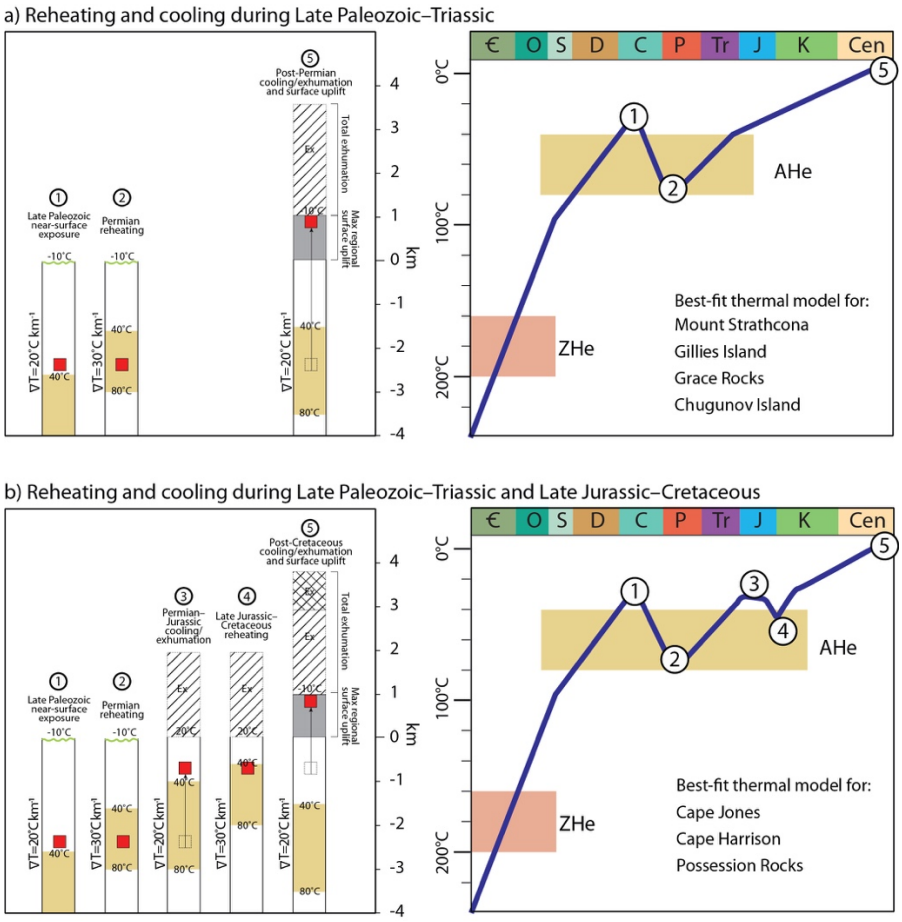

Figure 4. Schematic representation of the relationship between reheating-cooling episodes of basement samples (red squares) and rock uplift with respect to best-fit time-temperature (t-T) trajectories

modelled for the (**a**) Late Paleozoic–Triassic extension scenario and (**b**) two-stage extension scenario. Rock uplift equals to the amount of exhumation (Ex) plus the amount of surface uplift (grey shading) with respect to a reference surface (England & Molnar, 1990). Exhumation at each time period equals basement paleotemperature divided by the assumed geothermal gradient (∇T). Surface temperature used in t-T models and approximate temperature ranges of AHe partial retention zone [AHe PRZ, 40–80°C, brown fill; Farley (2000)] and ZHe partial retention zone [ZHe PRZ, 160–200°C, red fill; Reiners et al. (2004)] are also shown.

In summary, thermal history models support regional cooling to Late Paleozoic near-surface temperatures after the Kuunga tectono-thermal event, followed by reheating and cooling through ~90–60°C during Late Paleozoic–Triassic triggered by the rift-related thermal anomaly and exhumation of Precambrian basement on the western rift flank. The magnitude of cooling suggests ~2–4 km exhumation for reasonable amounts of assumed paleogeothermal gradients. A second thermal event in the Late Jurassic–Cretaceous and minor exhumation of ≤1 km is identified locally in three samples near the coast and may be associated with localized reactivation of rift structures during the onset of early rifting between Antarctica, Australia and India. These results are consistent with the establishment of topographic relief during continental extension and associated rift-flank basement uplift predominantly in the Late Paleozoic–Triassic, with additional localized uplift during the Late-Jurassic–Cretaceous in the Denman Glacier area.

5. Discussion

5.1 Phanerozoic thermal history of the Indo-Antarctic and Australo-Antarctic basement

Inversion of thermochronological data allows us to interrogate the low-temperature thermal history of Precambrian basement in the Bunger Hills region, providing key constraints to understand the pattern and magnitude of cooling, and to reconstruct the morpho-tectonic evolution of this sector of East Antarctica during the Phanerozoic. Circa 313–200 Ma AHe ages from the Bunger Hills region are consistent with the predominantly Late Paleozoic–Triassic age trend recorded by previously published AFT and AHe thermochronometers in the Indo-Antarctic and Australo-Antarctic domains, supporting a single large-scale cooling event of East Antarctic basement from temperatures of at least 120°C [upper limit of AFT partial annealing zone (PAZ); Wagner et al. (1989)]. Our

thermal models suggest that the cooling pattern of Precambrian basement in the Bunger Hills region requires ~2–4 km exhumation during Late Paleozoic–Triassic (~300–200 Ma) intracontinental extension in the Knox Rift. This interpretation is consistent with the timing and style of Late Palaeozoic–Triassic cooling and exhumation associated with extension in the Lambert Rift (Lisker et al., 2003), and the Wilkes Subglacial Basin (Lisker & Olesch, 2003), and indicates that the East Antarctic basement between the Lambert Rift and George V Land may have been part of a single denudational system. We therefore suggest that the uplift and erosion of large sections of Precambrian basement during Late Paleozoic–Triassic intracontinental extension provide an explanation for the cooling pattern of AFT and AHe systems in Precambrian basement rocks across both Indo-Antarctica and Australo-Antarctica which can be reconciled with the tectonic and topographic response of extension in the Lambert Rift–EARS, Knox Rift and Wilkes Subglacial Basin (Fig. 5a). Furthermore, the formation of high-relief topography in the vicinity of these tectonic structures requires coeval basement exhumation and subsidence in the basins and is incompatible with the concept of large-scale homogenous denudation of East Antarctic basement during the Late Paleozoic Ice Age (~340–300 Ma) proposed by Rolland et al. (2019).

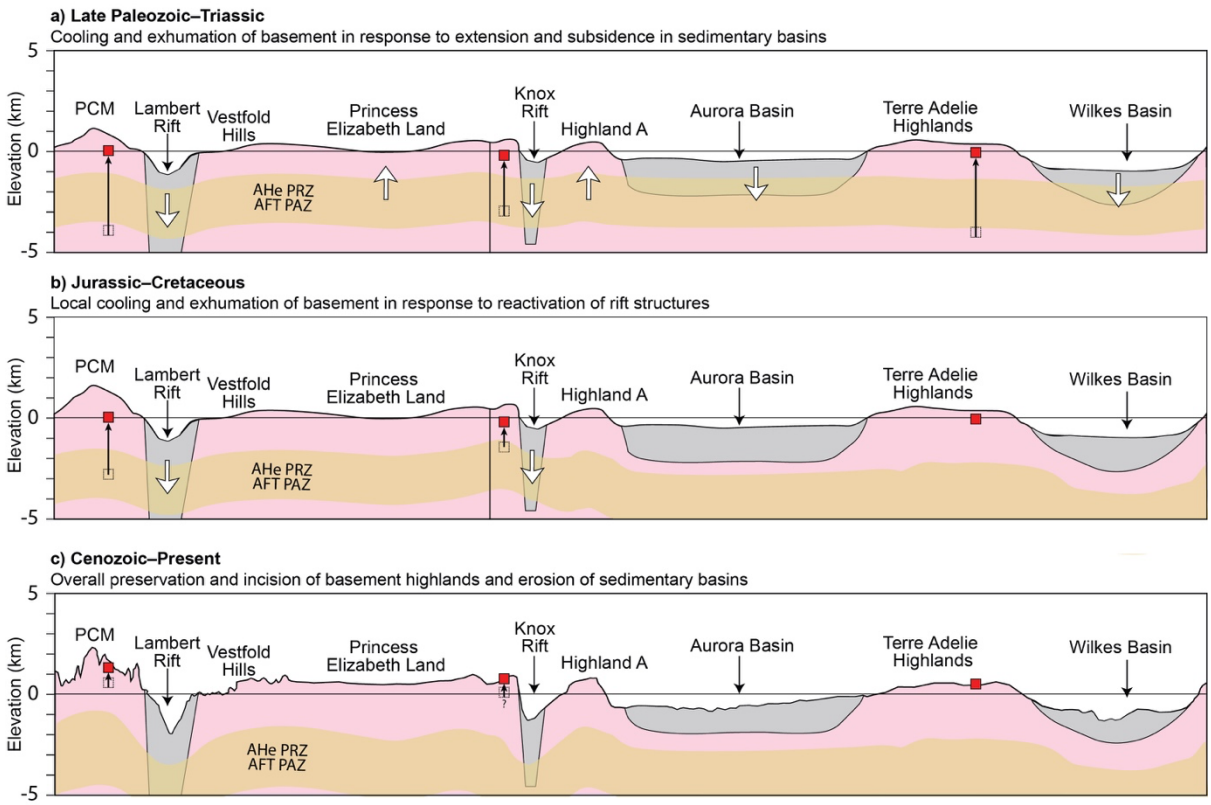

Figure 5. Conceptual cartoon illustrating the interpreted morpho-tectonic evolution of the Indo-

Antarctic and Australo-Antarctic domains. (**a**) Exhumation of Precambrian basement in response to widespread extension and subsidence in sedimentary basins during Pangea-wide rifting. (**b**) Exhumation of Precambrian basement in response to reactivation of structures during the Jurassic–Cretaceous breakup of East Gondwana (i.e., Lambert and Knox rifts). (**c**) Slow cooling of uplifted basement to present-day surface temperatures and overall preservation of high-standing topographic features throughout the Cenozoic. In each panel, red squares represent the position of representative samples as inferred from LTT data. Approximate temperature ranges of the combined AHe PRZ and AFT PAZ (40–120°C) are shown in each panel. For accuracy, we show the possible effects of increased geothermal gradient during rifting phases and the influence of finite-amplitude topography on the morphology of the combined AHe PRZ and AFT PAZ in each schematic profile. Elevations in the Late Paleozoic-Triassic and Jurassic-Cretaceous panels are approximate.

Our thermal modelling results allow modest localized Late Jurassic–Cretaceous cooling of basement in the Bunger Hills region during East Gondwana breakup from palaeotemperatures of ~40°C, which refers to an additional ≤1 km of exhumation in the Denman Glacier area. These estimates do not support significant regional exhumation of magnitude comparable to the up to 4 km Cretaceous exhumation across the Lambert Rift (Arne, 1994; Lisker et al., 2003) and are instead overall consistent with the slow and meagre denudation of the low-standing margin segments of the Australo-Antarctic domain as suggested by AFT results reported by Arne et al. (1993) and Lisker and Olesch (2003) (Fig. 5b). We therefore suggest that if any significant Cretaceous or younger thermal events between the Bunger Hills region and the TAM occurred, these must be limited in terms of cooling and denudation and therefore not recorded by currently available LTT at the coast.

5.2 Linking Late Paleozoic–Triassic cooling to geodynamic processes and topographic relief

The widespread Late Paleozoic–Triassic heating-cooling pattern of East Antarctic basement overlaps with a major phase of thermal instability throughout Pangea marked by geodynamic activity at the periphery of the supercontinent (Frizon de Lamotte et al., 2015). During this time, the propagation of far-field stresses from active plate boundaries resulted in large-scale intracontinental extension and the deposition of ~300–200 Ma Pangea Megasequences in sedimentary basins across all former Gondwana continents (Wopfner & Jin, 2009; Fig. 6). We suggest that this phase of extensive intracontinental extension across

the hinterland of Gondwana triggered the exhumation of large sections of Precambrian basement in the continental interior of East Antarctica (Fig. 5a). Plate convergence along the Panthalassan convergent margin (Veevers & Powell, 1994) led to the deposition of the foreland and back-arc deposits of the Beacon Supergroup in the Wilkes Subglacial Basin (Ferraccioli et al., 2009) and TAM (Elliot, 2013) in Antarctica, and the Cooper-Bowen, Sydney (Korsch et al., 2009), and Tasmanian (Fielding et al., 2010) basins of eastern Australia. Divergence on the northern Gondwana margin resulted in the opening of the Paleo-Tethys Ocean and in the development of a complex Late Carboniferous–Triassic intra-Gondwana rift system (Harrowfield et al., 2005) which includes the Lambert Rift–EARS and Knox Rift together with their Indian [i.e., Mahanadi Basin; Veevers and Tewari (1995)] and Australian [i.e., Perth Basin; Norvick (2004)] conjugate basins. Finally, thermal sag and transtension controlled large Permian–Triassic interior basins like those of central Australia [e.g., Canning and Cooper basins; Wopfner (1980)], sub-equatorial western Africa [e.g., Congo, Karoo basins; Catuneanu et al. (2005)] and South America [e.g., Parana Basin; Zalán et al. (1990)]. A similar geodynamic origin may be plausible for the broad Aurora Subglacial Basin in the interior of the Australo-Antarctic domain where Late Paleozoic–Mesozoic intracontinental transtension along large-scale faults has been proposed (Aitken et al., 2016a). Together, these geodynamic processes provide a driver for extensional tectonic activity onshore East Antarctica, which can be reconciled with thermochronological, structural and stratigraphic evidence supporting widespread Late Paleozoic–Triassic extension. Furthermore, the pattern of ~350–200 Ma AFT and AHe cooling ages on basement highs near Late Paleozoic–Triassic depocenters supports the formation of topographic relief predominantly via differential basement uplift during Late Paleozoic–Triassic intracontinental extension. Low-magnitude denudation of sections of uplifted basement may have also provided sediment sources for intracontinental basins in East Antarctica and on adjacent continents [e.g., Australia; Morón et al. (2019)].

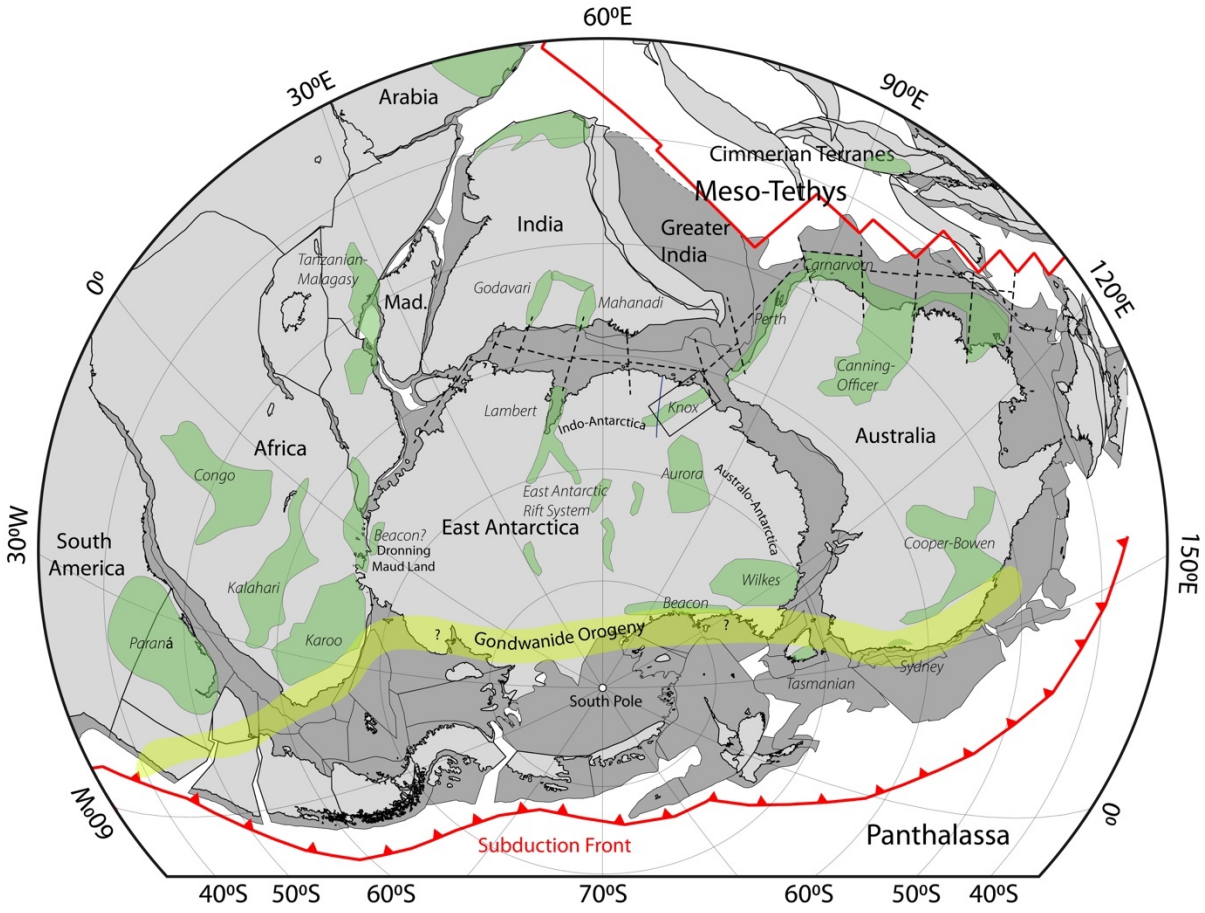

Figure 6. Permian Gondwana tectonic reconstruction (~270 Ma) using GPlates and plate geometries and rotation poles of Matthews et al. (2016). Widespread extensional deformation across the supercontinent was driven by plate convergence along the Panthalassan margin and rifting on the northern margin of Gondwana which resulted in the separation of the Cimmerian Continent and opening of the Meso-Tethys behind it (Metcalfe, 2013). The intracontinental East Gondwanan Late Carboniferous–Triassic rift system [dashed black line; modified from Harrowfield et al. (2005)], the distribution of sedimentary basins containing the Pangea Megasequence [green polygons; after Wopfner and Jin (2009)] and the approximate location of the Gondwanide orogenic front (yellow shading) are also shown. The location of the Bunger Hills region and Knox Rift is indicated by the black box.

While the imprint of Late Paleozoic–Triassic Pangea-wide tectonics is widespread in both the Indo-Antarctic and Australo-Antarctic domains, significant Jurassic–Cretaceous thermal events associated with the breakup of East Gondwana are not equally observed across the two domains (Fig. 5b). In the Indo-Antarctic domain, Cretaceous cooling and exhumation of Precambrian basement occurs locally in the Lambert Rift and may be coincident with reactivation of older Late Paleozoic–Triassic structures during large igneous province activity and/or continental rifting between East Antarctica and India

(Lisker et al., 2003; Lisker et al., 2007a). Geophysical models also predict significant Cretaceous uplift in the interior of the Indo-Antarctic domain along the EARS (Ferraccioli et al., 2011); however, Cretaceous cooling ages are not documented in the offshore detrital LTT record of Prydz Bay (Tochilin et al., 2012) and any significant Cretaceous extensional tectonism in the interior remains therefore poorly constrained. In the Australo-Antarctic domain, onshore Cretaceous–Cenozoic tectonic activity had been suggested on basis of geophysical data and plate reconstructions (Aitken et al., 2014; Cianfarra & Maggi, 2017; Eagles, 2019; Maritati et al., 2016). However, limited post-Triassic cooling reported across the Australo-Antarctic domain indicates that rifting between Australia and Antarctica did not significantly impact the long-term landscape evolution of the domain and may have only produced local and relatively minor denudational responses (c.f. Bunger Hills region).

The record of large-scale topographic evolution driven by Paleozoic–Mesozoic extensional events helps to fill a critical gap in our understanding of the mechanisms responsible for relief variability in the East Antarctic interior. We propose that large-scale variations in amplitude and wavelength of topographic relief across Indo-Antarctica and Australo-Antarctica can largely be accounted for by the effects of intracontinental rifting of Precambrian crust during the Late Paleozoic–Triassic and the subsequent local reactivation of rift structures during Jurassic–Cretaceous breakup of East Gondwana. Phases of continental extension in the Lambert Rift, EARS, and Knox Rift produced narrow rift zones which are responsible for the majority of the high-relief topography that is characteristic of Indo-Antarctic domain and the Bunger Hills region across the transition with the Australo-Antarctic domain. The extensional regime marked by Late Paleozoic–Triassic thermal sag and back-arc extension in most of the Australo-Antarctic domain may instead have led to a more diffuse deformation and the overall low-amplitude long-wavelength topography that characterizes the Australo-Antarctic domain.

5.3 Influence of tectonic relief on the long-term landscape evolution of East Antarctica

The interpreted morpho-tectonic evolution of the Indo-Antarctic and Australo-Antarctic domains highlights the key role of Paleozoic–Mesozoic tectonic relief in influencing the long-term landscape evolution of East Antarctica. Paleozoic–Mesozoic LTT bedrock ages indicate low long-term erosion rates (10–20 m Ma^{-1}) for uplifted basement

highs and suggest the overall preservation of high-standing topographic features at broad wavelengths throughout the Cenozoic (Fig. 5c). Subglacial basement highs in the continental interior may also represent tectonically uplifted basement and be characterized by similarly low erosion rates as suggested by detrital LTT studies (e.g. Cox et al., 2010). Examples of such regions are Highland A in the Aurora Subglacial Basin and Terre Adélie Highlands in Australo-Antarctica, as well as plateau regions such as Princess Elizabeth Land in Indo-Antarctica, all of which can be seen at isostatically rebounded elevations of 1500–2000 m (Fig. 1b). Flexural models for high-standing bedrock in the Gamburtsev Subglacial Mountains demonstrate that fluvial incision and alpine-style glacial erosion may have also contributed to the long-term landscape evolution of basement highs and be responsible for ~500–700 m of flexural uplift in response to unloading (Paxman et al., 2016). However, the magnitude of cooling and denudation associated with these events is below the detection limit of the AHe and AFT methods, which requires at least 2–3 km of denudation.

Long-term erosion was instead preferentially steered within sedimentary basins, reflecting the strong contrast in erodibility potential between cover sediments and crystalline rocks. However, we suggest that the different morphologies inherited from Late Paleozoic–Triassic extension had a profound influence on the style of erosion. Narrow rifts such as the Lambert and Knox rifts focused fluvial and glacial erosion, which caused amplification of topographic relief through selective erosion (Jamieson et al., 2005; Maritati et al., 2016; Thomson et al., 2013) and associated flexural uplift of these structures (Paxman et al., 2016). In contrast, the broad and low-elevation morphology of basins in the central Australo-Antarctic domain allowed for the development of larger fluvial braided systems and river deltas (Paxman et al., 2019a; Sauermilch et al., 2019), which provided a substantial amount of detrital material to the Gondwana-breakup passive margin basins (Sauermilch et al., 2019). The expansion of the East Antarctic Ice Sheet since the Eocene exacerbated these conditions with high erosion rates (~100 m Ma^{-1}) in the Lambert Rift (Thomson et al., 2013) and dynamic erosion from a marine-based ice sheet in the Aurora (Young et al., 2011) and Wilkes Subglacial Basin (Paxman et al., 2018; Paxman et al., 2019a). Together, these observations suggest that tectonic-controlled relief has exerted a key influence on long-term denudation rates and the evolution of the subglacial landscape of East Antarctica, providing a unique example of a continental interior where long-term

erosion and associated dynamic responses (i.e., flexure) over millions of years acted to reinforce pre-existing topographic relief.

6. Conclusions

We present a model for the origin of topography in the sector of interior East Antarctica between the Lambert Rift and George V Land which establishes a link between Paleozoic–Mesozoic AFT and AHe cooling ages and continent-scale geodynamic processes. We used new ZHe and AHe data from Precambrian basement outcrops to determine the timing, magnitude and style of Phanerozoic cooling of the Bunger Hills region, a poorly exposed section of East Antarctic basement near the boundary between the two large-scale basement domains of Indo-Antarctica and Australo-Antarctica. Our results indicate that Precambrian basement experienced cooling and ~2–4 km regional exhumation during the Late Paleozoic–Triassic associated with the formation of the Knox Rift, followed by a second episode of localized cooling and <1 km exhumation associated with the reactivation of rift structures during the Late Jurassic–Cretaceous separation of India from East Gondwana. Late Paleozoic–Triassic cooling and exhumation in the Bunger Hills region is consistent with the timing and magnitude of rift-related cooling and exhumation reported in the Lambert Rift and George V Land, suggesting a single denudational system driven by Pangea-wide extension. We propose that this event had a profound impact on the formation of topographic relief of East Antarctica via the exhumation of large sections of basement and the formation of vast intracontinental sedimentary deposits across the East Antarctic interior. By contrast, extension associated with the Jurassic–Cretaceous breakup of East Gondwana did not provide an equally widespread denudational response across the East Antarctic interior. The topographic framework formed during the Paleozoic–Mesozoic had a significant impact on the long-term landscape evolution of East Antarctica and provided a template for Cenozoic erosion on the continent.

Acknowledgements

This research is supported through funding from the Australian Government's Australian Antarctic Program (Project ID 4460) and the Australian Research Council's Special Research Initiative for Antarctic Gateway Partnership (Project ID SR140300001). A.M. is supported by an Australian Government Research Training Program (RTP) Scholarship.

M.D. was supported by ARC Discovery funding scheme (DP160102427), the AuScope NCRIS2 program and Curtin Research Fellowship. M.D. acknowledges the help of C. May, C. Scadding and A. Frew with solution ICP-MS analyses, and I. Dunkl for sharing PepiFLEX software for ICP-MS data reduction. We thank Fausto Ferraccioli and an anonymous reviewer for their constructive criticism and helpful comments which greatly helped improve the manuscript.

References

Aitken, A. R. A., Betts, P. G., Young, D. A., Blankenship, D. D., Roberts, J. L., & Siegert, M. J. (2016a). The Australo-Antarctic Columbia to Gondwana transition. *Gondwana Research, 29*(1), 136-152. doi:10.1016/j.gr.2014.10.019

Aitken, A. R. A., Roberts, J. L., van Ommen, T. D., Young, D. A., Golledge, N. R., Greenbaum, J. S., Blankenship, D. D., & Siegert, M. J. (2016b). Repeated large-scale retreat and advance of Totten Glacier indicated by inland bed erosion. *Nature, 533*(7603), 385-389. doi:10.1038/nature17447

Aitken, A. R. A., Young, D. A., Ferraccioli, F., Betts, P. G., Greenbaum, J. S., Richter, T. G., Roberts, J. L., Blankenship, D. D., & Siegert, M. J. (2014). The subglacial geology of Wilkes Land, East Antarctica. *Geophysical Research Letters, 41*(7), 2014GL059405. doi:10.1002/2014gl059405

Arne, D., Kelly, P., Brown, R., & GLEADOW, A. (1993). *Reconnaissance apatite fission-track data from the East Antarctic Shield.* Paper presented at the Gondwana symposium.

Arne, D. C. (1994). Phanerozoic exhumation history of northern Prince Charles Mountains (East Antarctica). *Antarctic Science, 6*(1), 69-84.

Catuneanu, O., Wopfner, H., Eriksson, P., Cairncross, B., Rubidge, B., Smith, R., & Hancox, P. (2005). The Karoo basins of south-central Africa. *Journal of African Earth Sciences, 43*(1-3), 211-253.

Cianfarra, P., & Maggi, M. (2017). Cenozoic extension along the reactivated Aurora Fault System in the East Antarctic Craton. *Tectonophysics, 703-704*, 135-143. doi:https://doi.org/10.1016/j.tecto.2017.02.019

Cox, S. E., Thomson, S. N., Reiners, P. W., Hemming, S. R., & van de Flierdt, T. (2010). Extremely low long-term erosion rates around the Gamburtsev Mountains in interior

East Antarctica. *Geophysical Research Letters, 37*(22), n/a-n/a. doi:10.1029/2010gl045106

Creyts, T. T., Ferraccioli, F., Bell, R. E., Wolovick, M., Corr, H., Rose, K. C., Frearson, N., Damaske, D., Jordan, T., & Braaten, D. (2014). Freezing of ridges and water networks preserves the Gamburtsev Subglacial Mountains for millions of years. *Geophysical Research Letters, 41*(22), 8114-8122.

Daczko, N. R., Halpin, J. A., Fitzsimons, I. C. W., & Whittaker, J. M. (2018). A cryptic Gondwana-forming orogen located in Antarctica. *Scientific Reports, 8*(1), 8371. doi:10.1038/s41598-018-26530-1

Eagles, G. (2019). A little spin in the Indian Ocean plate circuit. *Tectonophysics, 754*, 80-100.

Elliot, D. H. (2013). The geological and tectonic evolution of the Transantarctic Mountains: a review. *Geological Society, London, Special Publications, 381*(1), 7-35. doi:10.1144/sp381.14

England, P., & Molnar, P. (1990). Surface uplift, uplift of rocks, and exhumation of rocks. *Geology, 18*(12), 1173-1177. doi:10.1130/0091-7613(1990)018<1173:Suuora>2.3.Co;2

Evans, N., Wilson, N., Cline, J., McInnes, B., & Byrne, J. (2005). Fluorite (U–Th)/He thermochronology: constraints on the low temperature history of Yucca Mountain, Nevada. *Applied Geochemistry, 20*(6), 1099-1105.

Farley, K. (2000). Helium diffusion from apatite: General behavior as illustrated by Durango fluorapatite. *Journal of Geophysical Research: Solid Earth, 105*(B2), 2903-2914.

Farley, K., Wolf, R., & Silver, L. (1996). The effects of long alpha-stopping distances on (U–Th)/He ages. *Geochimica Et Cosmochimica Acta, 60*(21), 4223-4229.

Ferraccioli, F., Armadillo, E., Jordan, T., Bozzo, E., & Corr, H. (2009). Aeromagnetic exploration over the East Antarctic Ice Sheet: A new view of the Wilkes Subglacial Basin. *Tectonophysics, 478*(1-2), 62-77. doi:10.1016/j.tecto.2009.03.013

Ferraccioli, F., Finn, C. A., Jordan, T. A., Bell, R. E., Anderson, L. M., & Damaske, D. (2011). East Antarctic rifting triggers uplift of the Gamburtsev Mountains. *Nature, 479*(7373), 388-392. doi:10.1038/nature10566

Fielding, C. R., Frank, T. D., Isbell, J. L., Henry, L. C., & Domack, E. W. (2010). Stratigraphic signature of the late Palaeozoic Ice Age in the Parmeener Supergroup of Tasmania, SE Australia, and inter-regional comparisons. *Palaeogeography, Palaeoclimatology, Palaeoecology, 298*(1-2), 70-90. doi:10.1016/j.palaeo.2010.05.023

Frederick, B. C., Young, D. A., Blankenship, D. D., Richter, T. G., Kempf, S. D., Ferraccioli, F., & Siegert, M. J. (2016). Distribution of subglacial sediments across the Wilkes Subglacial Basin, East Antarctica. *Journal of Geophysical Research: Earth Surface*. doi:10.1002/2015jf003760

Frizon de Lamotte, D., Fourdan, B., Leleu, S., Leparmentier, F., & de Clarens, P. (2015). Style of rifting and the stages of Pangea breakup. *Tectonics, 34*(5), 1009-1029. doi:10.1002/2014tc003760

Harrowfield, M., Holdgate, G. R., Wilson, C. J. L., & McLoughlin, S. (2005). Tectonic significance of the Lambert graben, East Antarctica: Reconstructing the Gondwanan rift. *Geology, 33*(3), 197. doi:10.1130/g21081.1

Hu, J., Liu, L., Faccenda, M., Zhou, Q., Fischer, K. M., Marshak, S., & Lundstrom, C. (2018). Modification of the Western Gondwana craton by plume–lithosphere interaction. *Nature Geoscience, 11*(3), 203-210. doi:10.1038/s41561-018-0064-1

Jamieson, S. S. R., Hulton, N. R. J., Sugden, D. E., Payne, A. J., & Taylor, J. (2005). Cenozoic landscape evolution of the Lambert basin, East Antarctica: the relative role of rivers and ice sheets. *Global and Planetary Change, 45*(1-3), 35-49. doi:10.1016/j.gloplacha.2004.09.015

Ketcham, R. A. (2005). Forward and inverse modeling of low-temperature thermochronometry data. *Reviews in Mineralogy and Geochemistry, 58*(1), 275-314.

Kohn, B., & Gleadow, A. (2019). Application of Low-Temperature Thermochronology to Craton Evolution. In M. G. Malusà & P. G. Fitzgerald (Eds.), *Fission-Track Thermochronology and its Application to Geology* (pp. 373-393). Cham: Springer International Publishing.

Korsch, R. J., Totterdell, J. M., Cathro, D. L., & Nicoll, M. G. (2009). Early Permian East Australian Rift System. *Australian Journal of Earth Sciences, 56*(3), 381-400. doi:10.1080/08120090802698703

Lisker, F., Brown, R., & Fabel, D. (2003). Denudational and thermal history along a transect across the Lambert Graben, northern Prince Charles Mountains, Antarctica, derived from apatite fission track thermochronology. *Tectonics, 22*(5), 10-11 - 10-14.

Lisker, F., Gibson, H., Wilson, C., & Läufer, A. (2007a). Denudation and uplift of the Mawson Escarpment (eastern Lambert Graben, Antarctica) as indicated by apatite fission track data and geomorphological observation. *Antarctica. In: Cooper, AK & Raymond, CR*

(eds) A Keystone in a Changing World–Online Proceedings of the 10th ISAES. USGS Open-File Report, 6.

Lisker, F., & Olesch, M. (2003). Long-term landscape evolution of George V Land as indicated by fission track data. *Terra Antartica, 10*(3), 249-256.

Lisker, F., Wilson, C. J. L., & Gibson, H. J. (2007b). Thermal history of the Vestfold Hills (East Antarctica) between Lambert rifting and Gondwana break-up, evidence from apatite fission track data. *Antarctic Science, 19*(1), 97-106. doi:10.1017/s0954102007000144

Maritati, A., Aitken, A. R. A., Young, D. A., Roberts, J. L., Blankenship, D. D., & Siegert, M. J. (2016). The tectonic development and erosion of the Knox Subglacial Sedimentary Basin, East Antarctica. *Geophysical Research Letters, 43*(20), 10728-10737. doi:10.1002/2016gl071063

Matthews, K. J., Maloney, K. T., Zahirovic, S., Williams, S. E., Seton, M., & Müller, R. D. (2016). Global plate boundary evolution and kinematics since the late Paleozoic. *Global and Planetary Change, 146*, 226-250. doi:10.1016/j.gloplacha.2016.10.002

McDowell, F. W., McIntosh, W. C., & Farley, K. A. (2005). A precise 40Ar–39Ar reference age for the Durango apatite (U–Th)/He and fission-track dating standard. *Chemical Geology, 214*(3-4), 249-263.

Metcalfe, I. (2013). Gondwana dispersion and Asian accretion: Tectonic and palaeogeographic evolution of eastern Tethys. *Journal of Asian Earth Sciences, 66*, 1-33. doi:10.1016/j.jseaes.2012.12.020

Morlighem, M., Rignot, E., Binder, T., Blankenship, D., Drews, R., Eagles, G., Eisen, O., Ferraccioli, F., Forsberg, R., Fretwell, P., Goel, V., Greenbaum, J. S., Gudmundsson, H., Guo, J., Helm, V., Hofstede, C., Howat, I., Humbert, A., Jokat, W., Karlsson, N. B., Lee, W. S., Matsuoka, K., Millan, R., Mouginot, J., Paden, J., Pattyn, F., Roberts, J., Rosier, S., Ruppel, A., Seroussi, H., Smith, E. C., Steinhage, D., Sun, B., Broeke, M. R. v. d., Ommen, T. D. v., Wessem, M. v., & Young, D. A. (2020). Deep glacial troughs and stabilizing ridges unveiled beneath the margins of the Antarctic ice sheet. *Nature Geoscience*. doi:10.1038/s41561-019-0510-8

Morón, S., Cawood, P. A., Haines, P. W., Gallagher, S. J., Zahirovic, S., Lewis, C. J., & Moresi, L. (2019). Long-lived transcontinental sediment transport pathways of East Gondwana. *Geology, 47*(6), 513-516. doi:10.1130/g45915.1

Mulder, J. A., Halpin, J. A., Daczko, N. R., Orth, K., Meffre, S., Thompson, J. M., & Morrissey, L. J. (2019). A Multiproxy provenance approach to uncovering the assembly of East Gondwana in Antarctica. *Geology*. doi:10.1130/g45952.1

Norvick, M. (2004). Tectonic and stratigraphic history of the Perth Basin. *Geoscience Australia Record, 16*(2004), 30.

O'Donnell, J. P., & Nyblade, A. A. (2014). Antarctica's hypsometry and crustal thickness: Implications for the origin of anomalous topography in East Antarctica. *Earth and Planetary Science Letters, 388*, 143-155. doi:10.1016/j.epsl.2013.11.051

Pappa, F., Ebbing, J., Ferraccioli, F., & van der Wal, W. (2019). Modeling satellite gravity gradient data to derive density, temperature, and viscosity structure of the Antarctic lithosphere. *Journal of Geophysical Research: Solid Earth*.

Paxman, G. J. G., Jamieson, S. S. R., Ferraccioli, F., Bentley, M. J., Ross, N., Armadillo, E., Gasson, E. G. W., Leitchenkov, G., & DeConto, R. M. (2018). Bedrock Erosion Surfaces Record Former East Antarctic Ice Sheet Extent. *Geophysical Research Letters, 45*(9), 4114-4123. doi:10.1029/2018gl077268

Paxman, G. J. G., Jamieson, S. S. R., Ferraccioli, F., Bentley, M. J., Ross, N., Watts, A. B., Leitchenkov, G., Armadillo, E., & Young, D. A. (2019a). The Role of Lithospheric Flexure in the Landscape Evolution of the Wilkes Subglacial Basin and Transantarctic Mountains, East Antarctica. *Journal of Geophysical Research: Earth Surface, 124*(3), 812-829. doi:10.1029/2018jf004705

Paxman, G. J. G., Jamieson, S. S. R., Hochmuth, K., Gohl, K., Bentley, M. J., Leitchenkov, G., & Ferraccioli, F. (2019b). Reconstructions of Antarctic topography since the Eocene–Oligocene boundary. *Palaeogeography, Palaeoclimatology, Palaeoecology, 535*. doi:10.1016/j.palaeo.2019.109346

Paxman, G. J. G., Watts, A. B., Ferraccioli, F., Jordan, T. A., Bell, R. E., Jamieson, S. S. R., & Finn, C. A. (2016). Erosion-driven uplift in the Gamburtsev Subglacial Mountains of East Antarctica. *Earth and Planetary Science Letters, 452*, 1-14. doi:10.1016/j.epsl.2016.07.040

Pinet, N. (2016). Far-field effects of Appalachian orogenesis: A view from the craton. *Geology, 44*(2), 83-86. doi:10.1130/g37356.1

Reiners, P. W., Farley, K. A., & Hickes, H. J. (2002). He diffusion and (U–Th)/He thermochronometry of zircon: initial results from Fish Canyon Tuff and Gold Butte. *Tectonophysics, 349*(1-4), 297-308.

Reiners, P. W., Spell, T. L., Nicolescu, S., & Zanetti, K. A. (2004). Zircon (U-Th)/He thermochronometry: He diffusion and comparisons with 40Ar/39Ar dating. *Geochimica Et Cosmochimica Acta, 68*(8), 1857-1887.

Rolland, Y., Bernet, M., van der Beek, P., Gautheron, C., Duclaux, G., Bascou, J., Balvay, M., Héraudet, L., Sue, C., & Ménot, R.-P. (2019). Late Paleozoic Ice Age glaciers shaped East Antarctica landscape. *Earth and Planetary Science Letters, 506*, 123-133. doi:10.1016/j.epsl.2018.10.044

Sauermilch, I., Whittaker, J. M., Bijl, P. K., Totterdell, J. M., & Jokat, W. (2019). Tectonic, Oceanographic, and Climatic Controls on the Cretaceous-Cenozoic Sedimentary Record of the Australian-Antarctic Basin. *Journal of Geophysical Research: Solid Earth, 0*(0). doi:10.1029/2018JB016683

Thomson, S. N., Reiners, P. W., Hemming, S. R., & Gehrels, G. E. (2013). The contribution of glacial erosion to shaping the hidden landscape of East Antarctica. *Nature Geoscience, 6*(3), 203-207. doi:10.1038/ngeo1722

Tochilin, C. J., Reiners, P. W., Thomson, S. N., Gehrels, G. E., Hemming, S. R., & Pierce, E. L. (2012). Erosional history of the Prydz Bay sector of East Antarctica from detrital apatite and zircon geo- and thermochronology multidating. *Geochemistry, Geophysics, Geosystems, 13*(11), n/a-n/a. doi:10.1029/2012gc004364

Tucker, N. M., Hand, M., & Clark, C. (2020). The Bunger Hills: 60 years of geological and geophysical research. *Antarctic Science, 32*(2), 85-106.

Veevers, J. J. (2018). Gamburtsev Subglacial Mountains: Age and composition from morainal clasts and U–Pb and Hf-isotopic analysis of detrital zircons in the Lambert Rift, and potential provenance of East Gondwanaland sediments. *Earth-Science Reviews, 180*, 206-257. doi:10.1016/j.earscirev.2018.03.002

Veevers, J. J., & Powell, C. M. (1994). *Permian-Triassic Pangean basins and foldbelts along the Panthalassan margin of Gondwanaland* (Vol. 184): Geological Society of America.

Veevers, J. J., & Tewari, R. C. (1995). Gondwana master basin of Peninsular India between Tethys and the interior of the Gondwanaland Province of Pangea. In J. J. Veevers & R. C. Tewari (Eds.), (Vol. 187, pp. 0): Geological Society of America.

Wagner, G., Gleadow, A., & Fitzgerald, P. (1989). The significance of the partial annealing zone in apatite fission-track analysis: Projected track length measurements and uplift chronology of the Transantarctic Mountains. *Chemical Geology: Isotope Geoscience Section, 79*(4), 295-305.

Weber, U. D., Kohn, B. P., Gleadow, A. J. W., & Nelson, D. R. (2005). Low temperature Phanerozoic history of the Northern Yilgarn Craton, Western Australia. *Tectonophysics, 400*(1-4), 127-151. doi:10.1016/j.tecto.2005.03.008

Wildman, M., Brown, R., Beucher, R., Persano, C., Stuart, F., Gallagher, K., Schwanethal, J., & Carter, A. (2016). The chronology and tectonic style of landscape evolution along the elevated Atlantic continental margin of South Africa resolved by joint apatite fission track and (U-Th-Sm)/He thermochronology. *Tectonics, 35*(3), 511-545. doi:10.1002/2015tc004042

Wopfner, H. (1980). *Development of Permian intracratonic basins in Australia.* Paper presented at the Gondwana Five. Proceedings of the Fifth International Gondwana Symposium, Wellington, New Zealand.

Wopfner, H., & Jin, X. C. (2009). Pangea Megasequences of Tethyan Gondwana-margin reflect global changes of climate and tectonism in Late Palaeozoic and Early Triassic times—A review. *Palaeoworld, 18*(2-3), 169-192. doi:10.1016/j.palwor.2009.04.007

Young, D. A., Wright, A. P., Roberts, J. L., Warner, R. C., Young, N. W., Greenbaum, J. S., Schroeder, D. M., Holt, J. W., Sugden, D. E., Blankenship, D. D., van Ommen, T. D., & Siegert, M. J. (2011). A dynamic early East Antarctic Ice Sheet suggested by ice-covered fjord landscapes. *Nature, 474*(7349), 72-75.

Zalán, P. V., Wolff, S., Astolfi, M. A. M., Vieira, I. S., Concelcao, J. C. J., Appi, V. T., Neto, E. V., Cerqueira, J. R., & Marques, A. (1990). The Parana Basin, Brazil: Chapter 33: Part II. Selected Analog Interior Cratonic Basins: Analog Basins.

Chapter 4

Provenance of Late Jurassic–Early Cretaceous strata in the Mentelle Basin, southwestern Australia, reveals a trans-Gondwanan fluvial pathway

Alessandro Maritati[1], Jacqueline A. Halpin[1], Joanne M. Whittaker[1], Nathan R. Daczko[2], Carmine C. Wainman[3]

[1]*Institute for Marine and Antarctic Studies, University of Tasmania, Australia*

[2]*ARC Centre of Excellence for Core to Crust Fluid Systems and GEMOC, Department of Earth and Planetary Sciences, Macquarie University, Australia*

[3]*Australian School of Petroleum and Energy Resources, University of Adelaide, Australia*

Abstract

Australia, and East Gondwana more broadly, host extensive Paleozoic–Mesozoic sedimentary basins with thick siliciclastic sequences. These sediments were for the greater part transported by large-scale fluvial systems flowing from interior regions of East Gondwana. However sediment dispersal pathways remain poorly understood. We investigate the provenance of rift strata in the Mentelle Basin, Western Australia which was deposited during the Late Jurassic–Early Cretaceous breakup of India from Australia-Antarctica. Monazite U–Pb and zircon U–Pb–Hf isotopic signatures suggest that the Late Jurassic–Early Cretaceous syn-rift sediments were supplied predominately by a transcontinental river system draining sediment from interior regions of East Antarctica to the northern Gondwanan passive margin. This fluvial system was focused within the developing rift between India and Australia-Antarctica. Provenance of the transgressive marine post-breakup strata reflects a transition to a proximal sediment source and marks the end of the transcontinental fluvial system after the final breakup of India from Australia-Antarctica in the Valanginian (~136 Ma). Statistical comparison of detrital zircon spectra of Mentelle Basin syn-rift strata with other Australian and Antarctic Paleozoic–Mesozoic rift strata located along our proposed transport route suggests that the transcontinental fluvial pathway was active since the Late Paleozoic. We infer that this fluvial system was one of the principal modes of siliciclastic sediment delivery to rift and passive margin basins of East Gondwana.

1. Introduction

During the Paleozoic and Mesozoic, East Gondwana experienced a protracted extensional history which culminated in Late Mesozoic breakup (Matthews et al., 2016). Siliciclastic sequences deposited in both Paleozoic–Mesozoic rift and passive margin sedimentary basins across Australia, and East Gondwana more broadly, preserve a record of fluvial deposition and provide insights into the paleogeography during this changing continental configuration (e.g. Barham & Kirkland, 2019; Olierook et al., 2019). Most paleogeographic models propose sediment transport via transcontinental fluvial drainage systems radiating from high-standing regions of central East Antarctica (Kirkland et al., 2019; Morón et al., 2019; Veevers, 2018). However, the spatial and temporal patterns of transcontinental sediment dispersal systems are poorly documented in detail.

Rift successions along the west Australian margin represent some of the largest accumulation of siliciclastic deposits in East Gondwana (Crostella & Backhouse, 2000). These strata form part of a long-lived rift system at the heart of East Gondwana dominated by fluviatile sedimentary facies and can therefore provide a record of source regions and paleodrainage pathways. Existing provenance and paleocurrent data from onshore sedimentary rocks indicate that sedimentary sequences were derived by a predominately northward fluvial sediment transport that had its headwaters in East Antarctica (Cawood & Nemchin, 2000; Dillinger et al., 2018; Norvick, 2004). This northward fluvial transport continued until the Early Cretaceous, when continental rifting between Australia and Antarctica, and the Valanginian breakup of India from Australia-Antarctica led to a drastic reorganisation of paleodrainage patterns (Olierook et al., 2019). However, because of poor knowledge of sub-ice geology in East Antactica, the corresponding source-to-synk pathways of these deposits have remained largely uncharacterised.

Sandstones recovered at International Ocean Discovery Program (IODP) Site U1515 in the eastern Mentelle Basin, offshore southwestern Australia, provide the southernmost in-situ and only stratigraphic record across the regional Valanginian unconformity which marks the breakup of India from Australia-Antarctica. Here we present the first comprehensive provenance study of the Late Jurassic–Early Cretaceous stratigraphic interval in the Mentelle Basin. We combine monazite U–Pb and zircon U–Pb–Hf isotopic signatures to identify source regions and define the paleodrainage systems associated with these sedimentary strata. We compare the new data with the provenance

record of other Antarctic and Australian Paleozoic–Mesozoic strata to propose a sediment pathway connecting basement regions within the Kuunga Orogen in interior East Antarctica with the Tethyan Ocean via the west Australian rifting margin until the breakup of India from Australia-Antarctica.

2. Geological background

2.1 East Gondwana assembly

East Gondwana comprised the modern-day landmasses of India, Australia, East Antarctica, Madagascar, as well as several other microcontinental blocks. A coherent East Gondwana is believed to have formed by the amalgamation of the two continent-scale Precambrian domains of Indo-Antarctica and Australo-Antarctica along the 700–500 Ma Kuunga Orogen (e.g. Boger, 2011; Fitzsimons, 2000) (Fig. 1). This major Pan-African orogenic belt largely bypasses the Australian continent and is concealed under the ice in interior East Antarctica. The geometry of the Kuunga Orogen is interpreted to be defined by a combination of strike-slip and accretionary-collisional orogenic boundaries (Mulder et al., 2019). However, exposure of the Kunnga Orogen is limited largely to late- to post-orogenic Ediacaran–Early Cambrian magmatism/metamorphism represented in basement outcrops onshore East Antarctica (e.g. Mikhalsky et al., 2015; Sheraton et al., 1995), Shillong Plateau of northeast India (Chatterjee et al., 2011), southwestern Australia [i.e. Leeuwin Complex; Collins (2003); Naturaliste Plateau; Halpin et al. (2008)] and microcontinents in the Indian Ocean [i.e. Gulden Draak; Gardner et al. (2015); Batavia Knoll; Halpin et al. (2017)] which were located at the junction of the Indian, Australian and Antarctic plates in full-fit Gondwana reconstructions (Fig .1).

2.2 Rifting and breakup of East Gondwana

East Gondwana experienced two main extensional phases during the Paleozoic–Mesozoic which resulted in the formation of large sedimentary basins (Frizon de Lamotte et al., 2015) (Fig. 1). The first extensional phase in the Late Paleozoic–Triassic formed interior and passive margin sedimentary basins on the northern Gondwana margin (Maritati et al., 2020). These include an intra-Gondwanan rift system between Australia-Antarctica and India which formed one of the main extensional corridors within East Gondwana (Harrowfield et al., 2005). Renewed extension during Middle to Late Jurassic

rifting of India from Australia-Antarctica resulted in the development of a triple-arm rift system between Australia, East Antarctica and India. Rifting between India and Australia-Antarctica followed the trends of the older intra-Gondwanan rift system and culminated in the final separation of India from the rest of East Gondwana during the Valanginian (Gibbons et al., 2013). Extension commencing during the Late Jurassic between Australia and Antarctica eventually led to continental breakup in the Late Cretaceous (Williams et al., 2011).

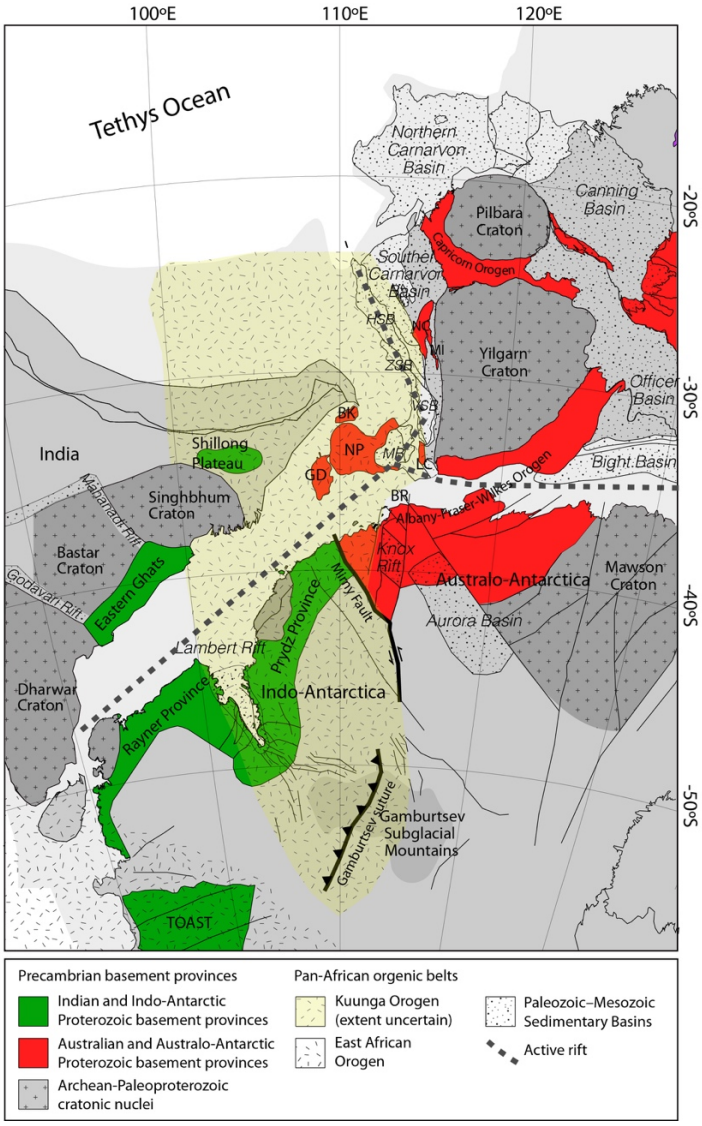

Figure 1. Paleogeographic reconstruction of East Gondwana during the Late Jurassic with Australia fixed in its present-day reference frame using GPlates and plate geometries and rotation poles of Matthews et al. (2016) showing the location of the main Precambrian–Early Cambrian basement provinces and Paleozoic–Mesozoic sedimentary basins. Outline of the Kuunga Orogen is adapted from Daczko et al. (2018); Geological provinces of Australia and India are modified from Raymond et al. (2018) and Ramakrishnan and Vaidyanadhan (2010) respectively. In Antarctica, structural lines and

basement provinces east of the Mirny Fault (Daczko et al., 2018) are from Aitken et al. (2014) and Maritati et al. (2016); Indo-Antarctic basement provinces west of the Mirny Fault are from Mulder et al. (2019); outline of the Tonian Oceanic Arc Super Terrane (TOAST) is from Ruppel et al. (2018); location of the Gamburtsev Suture is from Ferraccioli et al. (2011). Abbreviations are: BK – Batavia Knoll; BR – Bruce Rise; GD – Gulden Draak Knoll; HSB – Houtman sub-basin; MB – Mentelle Basin; MI – Mullingara Inlier; NC – Northampton Complex; NP – Naturaliste Plateau; VSB – Vlamingh sub-basin; ZSB – Zeewyck sub-basin.

2.3 Rift basins of the west Australian margin

On the southwestern part of the West Australian margin, the two main pulses of extension in the Late Paleozoic–Triassic and Mid to Late Jurassic through Early Cretaceous produced two major rift basins: the inboard Perth Basin (including the offshore Vlaming sub-basin), which extends northward beneath the coastal plain and continental shelf, and the outboard Mentelle Basin (Fig. 2a). IODP expedition 369 targeted the Mentelle Basin with 4 stratigraphic holes (Fig. 2a). The cored sequence at Site U1515 was located in the eastern Mentelle Basin beneath the continental slope in water depths of ~800 m (Huber, 2019) (Fig. 2b). Cored sandstones at Site U1515 comprise the upper part of a fluvio-lacustrine Late Jurassic–Early Cretaceous syn-rift sequence (analogous to the fluvial deposition of the Yarragadee Formation in the Perth Basin and other offshore depocentres) followed by Early Cretaceous marine transgression strata above the regional Valanginian breakup unconformity (Wainman et al., 2020).

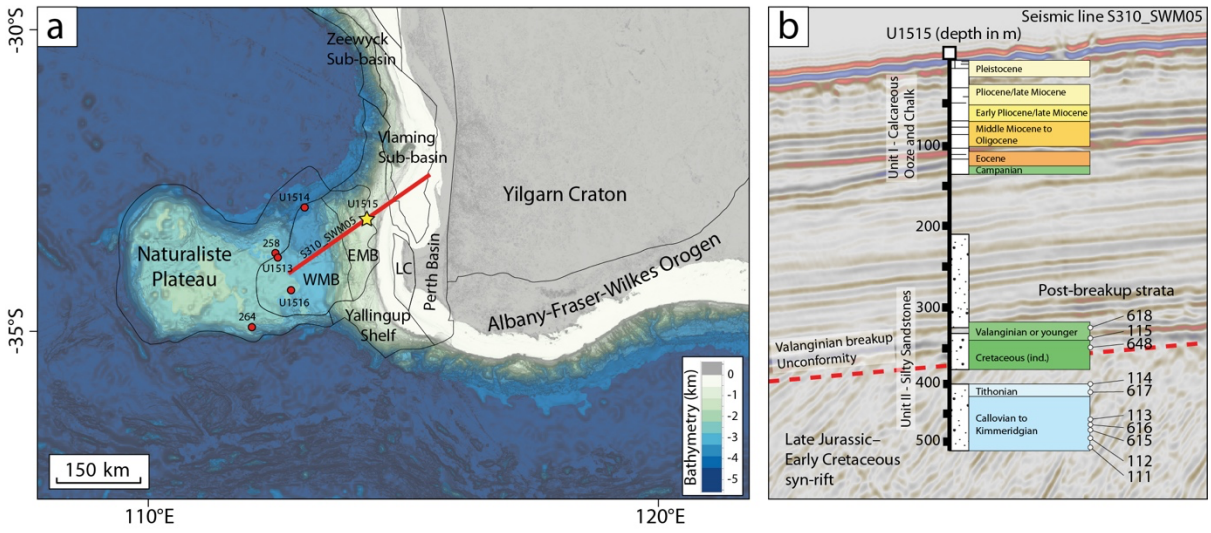

Figure 2. (**a**) Regional context of the Mentelle Basin, including the location of DSDP/IODP sites (red dots) and a major reflection seismic profile (red line) intersecting IODP Site U1515 (yellow star). EMB – eastern Mentelle Basin; LC – Leeuwin Complex; WMB – western Mentelle Basin. (**b**) Downhole

stratigraphy at Site U1515 overlaid on seismic line S310_SWM05. White dots indicate sampled intervals. Reflection seismic profile is from Huber (2019). Age constraints are from Huber (2019) and Wainman et al. (2020). Boxes use geological time scale colouring of Walker et al. (2018)

3. Sampling and analytical methods

3.1 Sampling and analytical strategy

Ten core intervals were sampled for isotopic analyses from the cored sedimentary sequence at Site U1515. Seven sandstone samples were selected from Late Jurassic–Early Cretaceous syn-rift strata; three sandstone samples were selected from core intervals from post-breakup Early Cretaceous strata (Fig. 1b). We investigate the provenance at these stratigraphic intervals using a combination detrital monazite U–Pb and zircon U–Pb–Hf isotopic analyses. Monazite is very reactive under various conditions (Varga et al., 2020 and references therein) and monazite ages can be used to fingerprint a range of source terranes based on the timing of monazite growth and/or regrowth during high-temperature metamorphic events (e.g. Halpin et al., 2008; Hietpas et al., 2010). Zircon U–Pb–Hf isotopes are widely used to discriminate between contemporary but potentially different source rocks based on their Hf isotopic composition. A summary of sampled core intervals and the analytical work performed on each of the selected samples is presented in Table 1.

Table 1. Sampled intervals, corresponding IODP core sections and isotopic analyses performed on each sample.

Sample number	IODP core section	Tectonic phase	Monazite U–Pb	Zircon U–Pb	Zircon Lu–Hf
618	U1515A-34R-2	Post-breakup	–	**X**	**X**
115	U1515A-35R-1	Post-breakup	**X**	**X**	–
648	U1515A-40R-2	Post-breakup	–	**X**	**X**
114	U1515A-45R-2	Syn-rift	**X**	**X**	**X**
617	U1515A-46R-1	Syn-rift	–	**X**	–
616	U1515A-48R-3	Syn-rift	–	**X**	**X**
113	U1515A-49R-2	Syn-rift	**X**	**X**	–
615	U1515A-50R-1	Syn-rift	–	**X**	–
112	U1515A-54R-1	Syn-rift	**X**	**X**	–
111	U1515A-55R-3	Syn-rift	**X**	**X**	**X**

3.2 Sample preparation

Samples were disaggregated using mortar and pestle, and then washed with water and placed in an ultrasonic bath to remove any supernatant dust. Detrital zircon and monazite grains were separated using a standard plastic pan and warm water and subsequent magnetic separation. Grains were transferred onto a sticky tape surface and mounted in 25mm diameter epoxy discs. Mounts were polished to half grain thickness to expose grain centres, cleaned, and then carbon-coated in preparation for imaging. Zircon and monazite grains suitable for U–Pb geochronology were identified using a FEI Quanta 600 Environmental Scanning Electron Microscope (ESEM) controlled by an automated mineral mapping software package (Mineral Liberation Analyser or MLA) at the Central Science Laboratory, University of Tasmania.

3.3 Monazite and zircon U–Pb geochronology

A total of ~ 250 representative monazite grains (> 10 μm) were selected on a subset of five samples (50 grains from each sample). U–Pb monazite analyses were performed on an Agilent 7900cs quadrupole inductively coupled plasma mass spectrometry (ICPMS) with a 193 nm Coherent Ar–F gas laser and a Resonetics S-155 ablation cell at the Discipline of Earth Sciences, University of Tasmania. Pre-ablation and ablation times follow the monazite methodology outlined in Halpin et al. (2014) with operating conditions of 5 Hz and ~2 J/cm^2 on a spot size of 13 μm. Isotopes measured include ^{27}Al, ^{31}P, ^{43}Ca, ^{140}Ce, ^{172}Yb, ^{202}Hg, ^{204}Pb, ^{206}Pb, ^{207}Pb, ^{208}Pb, ^{232}Th and ^{238}U. The international glass standard NIST610 was used as a primary standard for trace element quantification assuming stoichiometric Ce in monazite and as a primary standard for the ^{207}Pb/^{206}Pb ratio correction factor for monazite. The downhole fractionation, instrument drift and mass bias correction factors for Pb/U and Pb/Th ratios on monazite grains were calculated using two analyses on the primary standard (14971-Mon–in-house standard) and validated using one analysis on each of the secondary standard monazites RGL4b (Rubatto et al., 2001), Bananeira (Gonçalves et al., 2016) analysed at the beginning of the session and every 16–20 unknowns using the same spot size and conditions as used on the samples. Full tabulation of U–Pb isotopic data of monazite unknowns and standards are reported in Supplementary Table S1. Representative high-contrast backscatter electron (BSE) images of analysed monazite grains were taken on a Hitachi SU-70 Field Emission Scanning Electron Microscope (FE-SEM), at the Central Science Laboratory, University of Tasmania.

Zircon grains were imaged using a cathodoluminescence (CL) detector on the same ESEM previously used to identify mineral grains suitable for geochronology. U–Pb zircon ages were collected on the same LA-ICPMS system used to collect U–Pb detrital monazite ages as described above. Each analysis was pre-ablated with 5 laser pulses to remove any surface contamination then the blank gas was analysed for 30 s followed by 30 s of zircon ablation at 5 Hz and 2 J/cm^2 on a spot size of 29 μm. Elements measured include ^{49}Ti, ^{56}Fe, ^{90}Zr, ^{178}Hf, ^{202}Hg, ^{204}Pb, ^{206}Pb, ^{207}Pb, ^{208}Pb, ^{232}Th and ^{238}U with each element being measured sequentially every 0.16 s with longer counting time on the Pb isotopes compared to the other elements. The international glass standard NIST610 was ablated at the beginning and end of the analytical session to correct for mass bias on the ^{207}Pb /^{206}Pb ratio. Each run consisted of 30–50 analyses of our unknowns, bracketed by 4–6 analyses of the primary reference zircon standard 91500 (Wiedenbeck et al., 1995) used to correct for mass bias, machine drift and down-hole fractionation on the Pb/U and Pb/Th ratios, and 4 analyses (two each) of secondary standards TEMORA 1 (Black et al., 2003) and Plesovice (Sláma et al., 2008) to provide an independent control to assess accuracy and precision. Trace elements were quantified using ^{91}Zr as the internal standard, assuming stoichiometric proportions, and the NIST610 glass with GeoReM preferred values (Jochum et al., 2011). Full tabulation of U–Pb isotopic data of zircon unknowns and standards is reported in Supplementary Table S2.

Data reduction calculations and error propagations were done with Microsoft Excel® via macros designed at the University of Tasmania using the techniques outlined by Sack et al. (2011) and Halpin et al. (2014). All dates older than 1.5 Ga are presented as ^{207}Pb/^{206}Pb ages and dates younger than 1.5 Ga are presented as ^{206}Pb/^{238}U ages (Spencer et al., 2016). Kernel density estimate (KDE) and multi-dimensional scaling (MDS) plots were calculated with IsoplotR (Vermeesch, 2018) using the preferred ages and their 1σ uncertainties for data ≤±10% discordant [concordance = (^{206}Pb/^{238}U age)/(^{207}Pb/^{206}Pb age)].

3.4 In situ zircon Lu–Hf isotope analysis

Concordant (≤±10% discordant) U–Pb zircon analyses from 5 samples were complemented with in situ Lu–Hf isotopic analysis. In situ Lu–Hf isotopic analyses were performed on a subset of zircon grains already analysed for U–Pb using a Photon Machines Analyte G2 excimer (193 nm) laser ablation with HelEx II system, attached to a Nu Plasma

II multi-collector inductively coupled plasma mass spectrometer (LA-MC-ICPMS) at Macquarie GeoAnalytical (MQGA), Macquarie University. The detail of the methodology is described in Gain et al. (2019) with some modifications. Each measurement consists of 30 s of background followed by 60 s of ablation. The laser repetition and fluence were 5 Hz and 7–8 J J/cm^2, respectively. The beam diameter was between 40–50 μm depending on the size of the zircon grain. Helium was used as a carrier gas with a total flow rate of 0/8 L min^{-1} which was then mixed with Ar gas before introduction into to MC-ICP-MS. All Hf isotopes were measured, as well as ^{171}Yb, ^{172}Yb, ^{173}Yb, ^{175}Lu and ^{182}W to monitor and correct the isobaric interference on ^{176}Hf and ^{180}Hf. Isobaric interferences on ^{176}Hf were stripped using ^{176}Yb/^{173}Yb and ^{176}Lu/^{175}Lu. Instrumental mass bias was corrected by normalizing to ^{179}Hf/^{177}Hf=0.7325 using the law of exponential Patchett and Tatsumoto (1981). Zircons from the Mud Tank carbonatite locality were analysed together with the unknown in each session to monitor the accuracy of results. Temora-2 zircon was also run as an independent check to validate the Yb correction. The initial ^{176}Hf/^{177}Hf (Hf_i) value in zircon is calculated using the measured ^{176}Hf/^{177}Hf and ^{207}Pb corrected ^{238}U/^{206}Pb age. Calculation of Initial εHf ($εHf_i$) values employed the decay constant of Scherer et al. (2001) of 1.865×10^{-11}. Full tabulation of zircon Hf isotopic data of unknown and standards is presented in Supplementary Table S3. $εHf_i$ plots and two-dimensional kernel density estimate (2D KDE) sample contours and were constructed using the R packages 'detzrcr' (Kristoffersen et al., 2016).

4. Results

4.1 U–Pb monazite data

Monazite grains are sub-angular to sub-rounded with aspect ratios of 1:1–1:3 and do not preserve evidence of internal zoning (Fig. 3). A total of 151 near-concordant detrital monazite analyses were extracted from the 5 selected samples. Detrital monazite spectra yield a dominant 600–500 Ma age mode defined by a ~520 Ma age peak (Fig. 4a). Monazite within this age mode represent 70–90% of the total detrital signature in syn-rift strata and 65% in the Early Cretaceous post-breakup sample. Subordinate Archean–Late Mesoproterozoic peaks are present in each sample. The chemistry of analysed monazite grains across the five samples is broadly similar, with variable Th and Y (10^3–10^6 ppm) and U between 10^3 and 10^5 ppm (Supplementary Table S1). These characteristics are similar to

those of the analysed monazite standard RGL4b (Rubatto et al., 2001) and are consistent with a high-grade metamorphic origin.

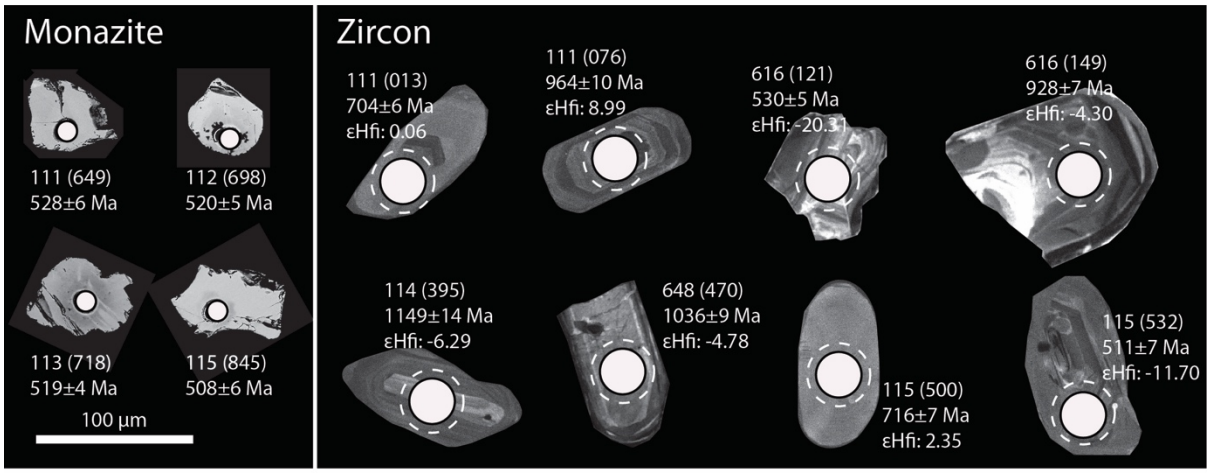

Figure 3. Representative high-contrast back-scatter electron images of monazite and cathodoluminescence (CL) images of zircon grains. U–Pb analysis locations are displayed as solid circles with corresponding spot number (in brackets), $^{238}U/^{206}Pb$ ages and respective uncertainties labelled at 1σ confidence. Location of Lu–Hf analyses (dashed circles) and corresponding initial epsilon Hf (εHfi) values are also shown for zircon grains.

4.2 U–Pb zircon data

Zircon grains in sampled stratigraphic intervals present a wide variety of morphologies and shapes, which indicate multiple source regions (Fig. 3). We randomly targeted ~100 grains in each sample and based provenance interpretations on comparison with isotopic signals of potential source regions. A total of 555 near-concordant detrital zircon analyses were extracted from 10 samples. In contrast to monazite, detrital zircon spectra across the sampled stratigraphic sequence preserve older Precambrian age components and yield variably dominant Mesoproterozoic–Cambrian (~1200–500 Ma) and subordinate Archean–Paleoproterozoic (~3000–1800 Ma) zircon age peaks (Fig. 4b). The Valanginian breakup unconformity marks a change in the relative distribution of these age peaks with a decrease of Archean–Mesoproterozoic age components in favour of Late Mesoproterozoic–Cambrian age components in the post-breakup strata. This relative change in provenance between syn-rift and post-breakup strata is evident from the statistical dissimilarity of zircon age spectra (Fig. 5).

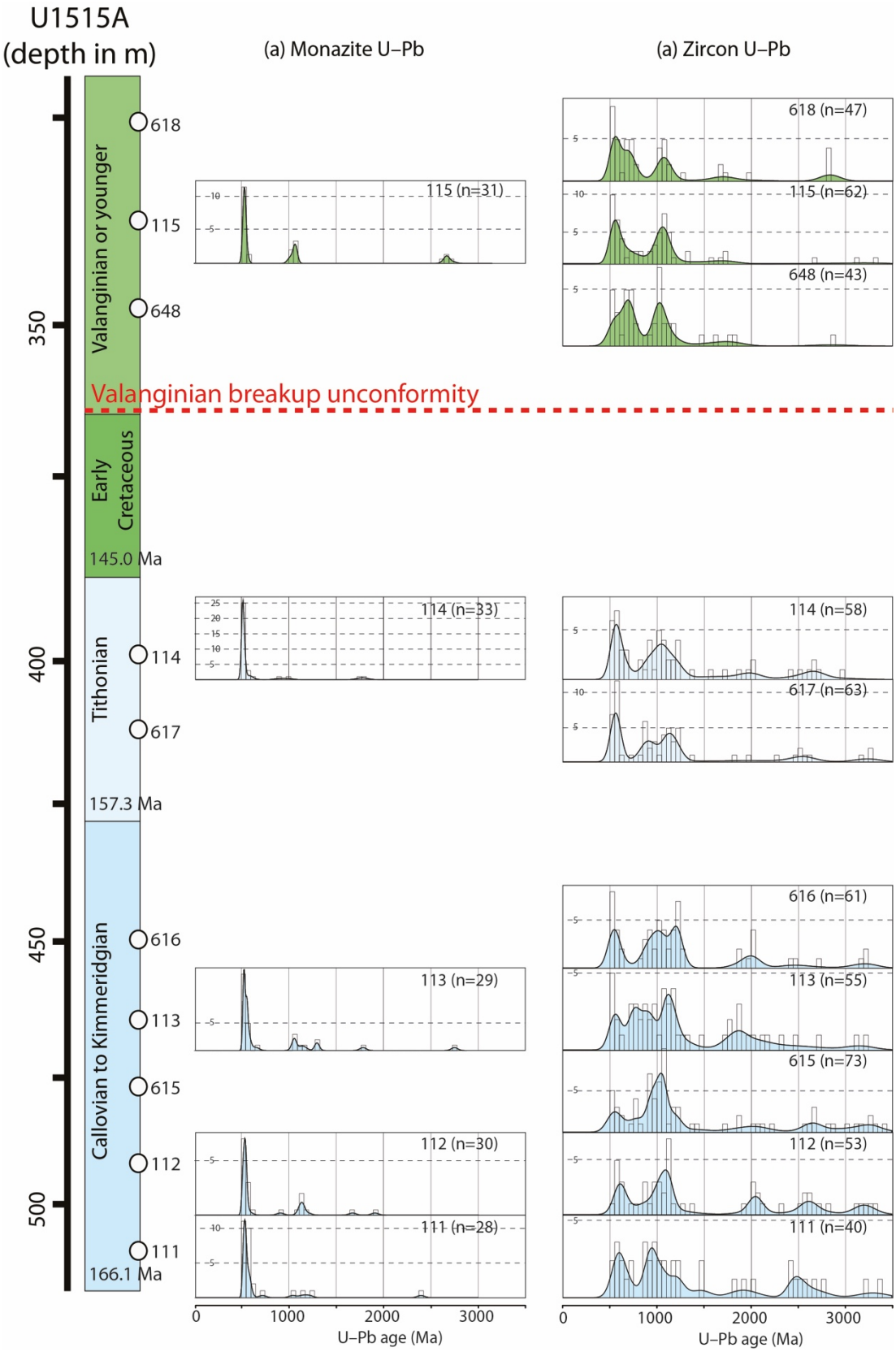

Figure 4. Kernel density estimate (KDE) plots of (**a**) detrital monazite and (**b**) detrital zircon age data of sampled stratigraphic intervals from the Late Jurassic–Early Cretaceous sedimentary sequence in the eastern Mentelle Basin. Histogram bin size in KDE plots is 50 Ma. Stratigraphic age constraints are from Wainman et al. (2020). Dashed red line indicates the location of the Valanginian breakup unconformity

in the stratigraphic sequence. All U–Pb age plots were calculated with IsoplotR (Vermeesch, 2018). Note: blue and green colours reflect geological timescale only and are not related to pre- or post-breakup status.

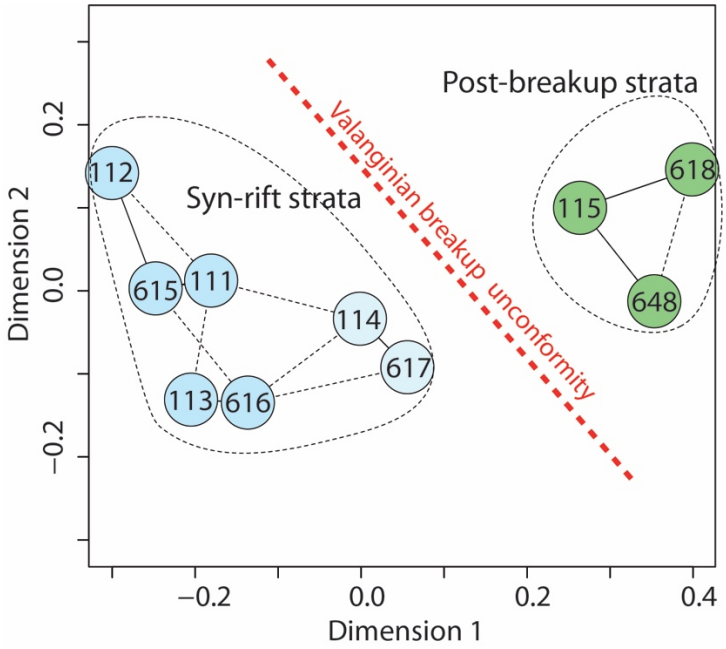

Figure 5. Nonmetric multidimensional scaling (MDS) plot for concordant U–Pb zircon data from the Mentelle Basin. Greater distances represent greater degrees of dissimilarity of detrital zircon age spectra. The dissimilarity between samples is given by the statistical distance between age distributions defined using the Kolmogorov-Smirnov (K-S) statistic. Solid lines and dashed lines indicate the closest and second closest neighbours, respectively. MDS plot was calculated with IsoplotR (Vermeesch, 2018).

4.3 Lu–Hf isotopic data

To further investigate changes in source regions for strata across the Valanginian unconformity, we combined the U–Pb–Hf zircon isotopic signature of 3 samples from syn-rift strata (n = 159) and 2 samples from post-breakup strata (n = 152) (Fig. 6). We employ 2D Kernel Density Estimation, which uses discrete bandwidths for both the x- and y-axes (25 Ma for U–Pb ages and 2.5 εHf_i values, respectively) to better visualize the zircon Hf data distribution and density against the U–Pb data. The contours in εHf_i vs apparent U–Pb age space for the syn-rift strata (blue; Fig. 6) show the presence of two main isotopic clusters. These comprise a 700–500 Ma age group with εHf_i values ranging between +8 and −30 and a 1200–850 Ma group with εHf_i values between + 10 and −20. Subordinate Archean and Paleoproterozoic isotopic clusters (εHf_i values ranging +5 and -20) are also present. The contours in εHf_i vs apparent U–Pb age space for the post-breakup strata (green; Fig. 6) show a more restricted distributive density primarily focused on three

predominant age modes of 550 Ma (εHf_i between +5 and –18), 700 Ma (εHf_i between +5 and –10) and 1060 Ma (εHf_i between 0 and –12).

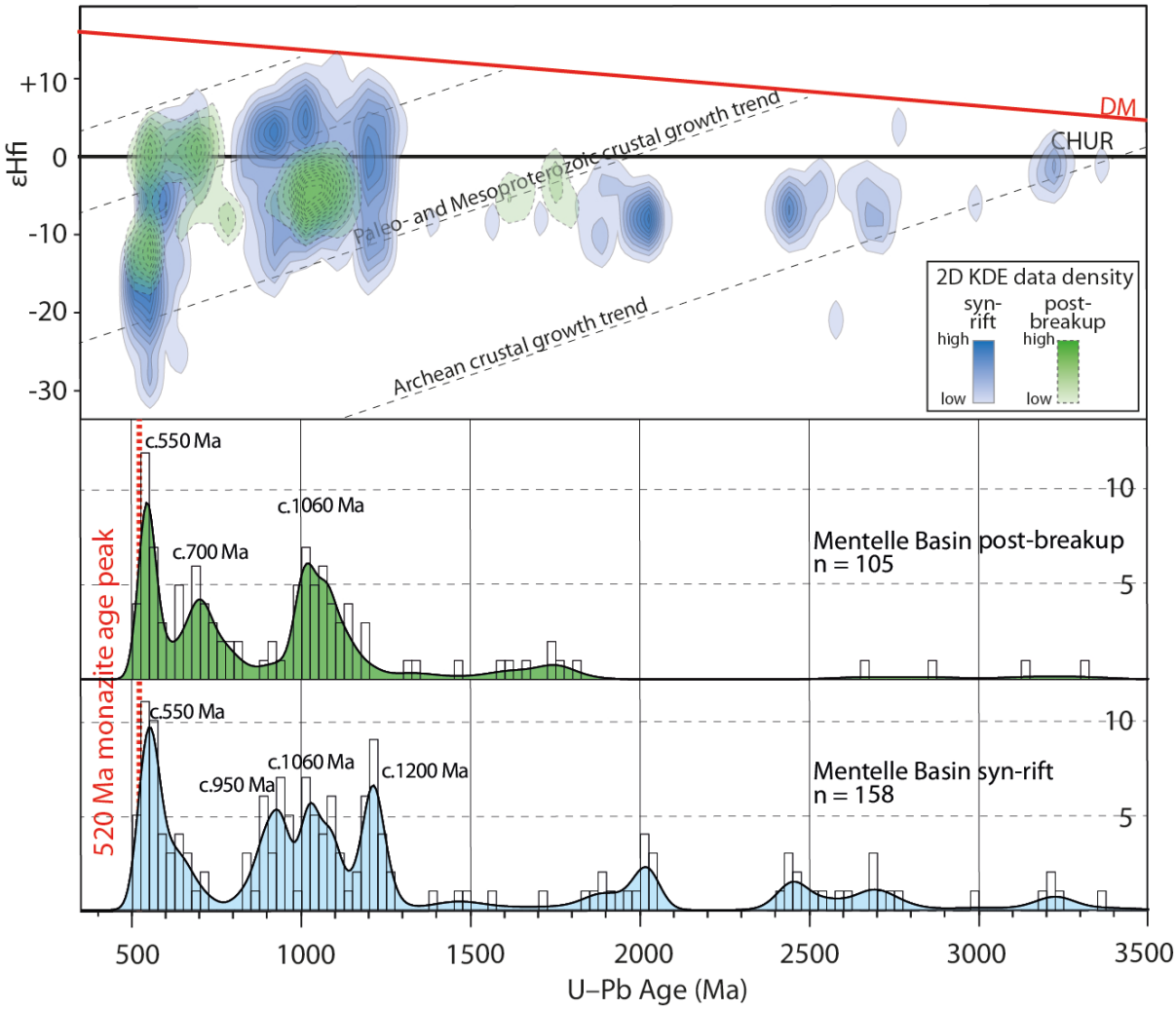

Figure 6. Composite kernel density estimate (KDE) for Late Jurassic–Early Cretaceous syn-rift (blue) and Early Cretaceous post-breakup strata (green) versus two-dimensional kernel density estimate (2D KDE) contours of their corresponding initial εHf (εHf_i) data. Histogram bin size in KDE plots is 25 Ma. εHfi sample contours were constructed using the R package 'detzrcr' (Kristoffersen et al., 2016) with an X and Y bandwidth of 25 and 2.5, respectively. Dashed red line indicates the dominant 520 Ma detrital monazite age peak across the stratigraphic sequence. CHUR – chondritic uniform reservoir; DM – depleted mantle. Archean and Paleo- and Mesoproterozoic crustal growth trends using a bulk crust value of $^{176}Lu/^{177}Hf = 0.01563$ are also shown.

5. Discussion

5.1 Provenance of Late Jurassic–Early Cretaceous sedimentary strata in the Mentelle Basin

5.1.1 Provenance of Late Jurassic–Early Cretaceous syn-rift strata

Detrital monazite grains in syn-rift samples show a consistent unimodal age distribution dominated by a ~520 Ma age mode (Fig. 4a). This Early Cambrian age peak corresponds to the timing of magmatism and high temperature metamorphism attributed to the latest stages of the Ediacaran–Cambrian Kuunga Orogeny (e.g. Boger, 2011; Daczko et al., 2018 and references therein) and therefore constrains the provenance of syn-rift strata predominantly to basement regions that experienced monazite growth and/or recrystallisation during the assembly of Gondwana. Subordinate Archean–Mesoproterozoic age peaks suggest minor input from basement terranes that did not experience pervasive high temperature conditions during the Kuunga Orogeny and may therefore characterise source regions in the Australo-Antarctic basement east of the Mentelle Basin (e.g. Albany-Fraser-Wilkes Province and Yilgarn Craton).

Figure 7 (next page). 2D KDE contours of Mentelle Basin syn-rift strata overlain by U–Pb–Hf zircon analyses from most likely provenance sources (left) and their location on the Late Jurassic (~150 Ma) plate reconstruction of East Gondwana shown in Figure 1 (right). (**a**) Australo-Antarctic basement sources: Batavia Knoll (Halpin et al., 2017), Bruce Rise (Halpin et al., 2020), offhore Albany-Fraser-Wilkes Orogen [i.e. Gulden Draak (Gardner et al., 2015) and Naturaliste Plateau (Halpin et al., 2020)] and representative rocks for the onshore Albany-Fraser-Wilkes Orogen [i.e. Bunger Hills (Tucker et al., 2017). (**b**) Indo-Antarctic basement sources: Rayner Province ≤ 1100 Ma (Halpin et al., 2005; Liu et al., 2017); Shillong Plateau (Majumdar & Dutta, 2016); Tonian Oceanic Arc Super Terrane (Elburg et al., 2015). (**c**) 700–500 Ma zircon from Paleozoic–Mesozoic sedimentary sequences of the Northern Carnarvon, Canning and Officer basins (Morón et al., 2019 and references therein) and Permian–Triassic Amery Group in the Lambert Rift of East Antarctica (Veevers & Saeed, 2008) representing sediment proxies for the convergent section of the Kuunga Orogen (inferred provenance indicated on the plate reconstruction panel with blue arrows). Coloured bars in the U–Pb–Hf diagrams indicate the main age ranges for Australo-Antarctic and Indo-Antarctic basement, and Kuunga Orogen (Daczko et al., 2018). Abbreviations on maps are: BH – Bunger Hills; BK – Batavia Knoll; BR – Bruce Rise; CB – Canning Basin; GD – Gulden Draak Knoll; GSM – Gamburtsev Subglacial Mountains; MB – Mentelle Basin; NCB – Northern Carnarvon Basin; NP – Naturaliste Plateau; OB – Officer Basin; TOAST – Tonian Oceanic Arc Super Terrane; SP – Shillong Plateau.

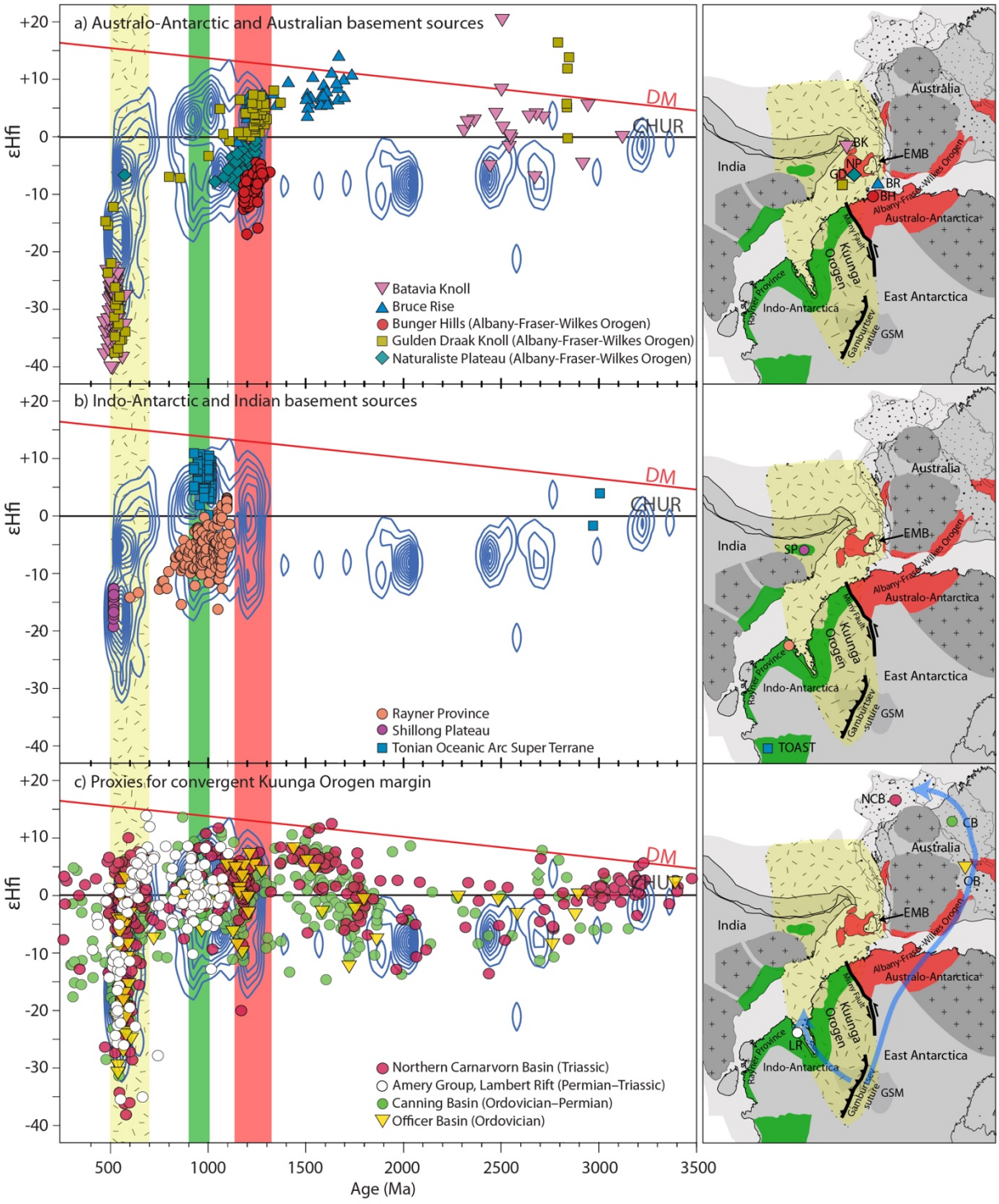

The syn-rift detrital zircon U–Pb spectra (Fig. 4b) together with the U–Pb–Hf signatures (Fig. 6) allows to further discriminate the provenance of sediments within the Kuunga Orogen. 700–500 Ma zircon form a continuous array of detrital ages and exhibit a positively skewed unimodal distibution with mode centred at ~550 Ma. The corresponding εHf_i isotopic pattern comprise an older radiogenic component (700–600 Ma zircon) and

younger evolved crustal reservoir signature (600–500 Ma zircon) (Fig. 6). While Ediacaran–Cambrian (580–510 Ma) granitoids from the Gulden Draak and Batavia knolls (Gardner et al., 2015; Halpin et al., 2017) (Fig. 7a) and Shillong Plateau (Majumdar & Dutta, 2016) (Fig. 7b) may explain part of the evolved εHf_i component (εHf_i values between 0 and –30) of 550–500 Ma zircon, a source for the older (~700–600 Ma) and more radiogenic age components is lacking in the region. Conversely, continuous arrays of detrital zircon ages matching the full spectrum of Hf isotopic compositions of 700–500 Ma grains in the Mentelle Basin syn-rift strata are widespread in Paleozoic–Mesozoic sedimentary sequences of central and northern Australia (Haines et al., 2013; Morón et al., 2019; Veevers, 2018), and East Antarctica (Veevers & Saeed, 2008) as well as in modern-day sands of southwestern Australia (Kirkland et al., 2019; Sircombe & Freeman, 1999) (Fig. 7c). Provenance studies have interpreted the distinctive εHf_i isotopic trend of 700–500 Ma zircon in these sedimentary rocks to fingerprint a geodynamic evolution of subduction and collision (Daczko et al., 2015; Halpin et al., 2018; Kirkland et al., 2019; Veevers, 2018). We suggest that statististical distribution of 700–500 Ma zircon from the Mentelle Basin syn-rift strata and their corresponding Hf signature indicates that a significant portion of this age population was derived from convergent-margin rocks (Gamburtsev suture) within the Kuunga Orogen (Mulder et al., 2019) in interior East Antarctica (Fig. 8a).

1200–850 Ma zircon age components overlap with basement ages associated with Grenvillian-aged orogenic provinces in both Australo-Antarctica and Indo-Antarctica (Fitzsimons, 2003). The ~1200 Ma age population with εHf_i values between +10 and −18 overlap with the isotopic composition of nearby basement rocks in the Albany-Fraser-Wilkes Orogen of Australo-Antarctica, including both onshore basement rocks [i.e. Bunger Hills (Tucker et al., 2017)], and now dispersed submarine continental fragments [i.e. Gulden Draak (Gardner et al., 2015) and Naturaliste Plateau (Halpin et al., 2020)] (Fig. 7a). The ~1060 Ma detrital population may reflect derivation from basement rocks of the 1090–1060 Ma Pinjarra Orogen, which include the basement to the nearby south Perth Basin (Bodorkos et al., 2016) and Mesoproterozoic protoliths in the Leeuwin Complex (Collins, 2003). Overall, we suggest that the 1200–1040 Ma age components reflect detrital contribution from relatively proximal Australo-Antarctic basement sources.

1000–850 Ma zircon ages defined by a ~950 Ma age mode and a broadly negative εHf_i character are consistent with protolith ages and isotopic signature of Rayner Province

of Indo-Antarctica (Daczko et al., 2018; Halpin et al., 2005; Liu et al., 2017; Mulder et al., 2019). Approximately 15 zircons from the 1000–850 Ma age group have a distinctively more radiogenic εHf_i signature that does not match that of zircon from the Rayner Province. We suggest that this population could be instead derived from the ~1000–900 Ma Tonian Oceanic Arc Super Terrane (TOAST) in Dronning Maud Land of East Antarctica which represents one of the rare occurrences of Early Neoproterozoic juvenile arc terranes in Gondwana (Elburg et al., 2015; Jacobs et al., 2015) (Fig. 7b).

Archean-Paleoproterozoic (3400–1800 Ma) zircon age components comprise 35–20% of the total detrital signature of the syn-rift samples and could indicate derivation from distal cratonic nuclei of East Antarctica and India or reflect minor proximal input from the Yilgarn Craton and reworked Paleoproterozoic terranes at its southern margin (e.g. Bunger Hills; Tucker et al., 2017).

5.1.2 Provenance of Early Cretaceous post-rift strata

Detrital monazite grains in the post-rift sample are dominated by a ~520 Ma age mode, suggesting provenance from basement regions that experienced high-temperature conditions during the assembly of Gondwana. However, compared to the syn-rift strata, U–Pb–Hf contours of detrital zircon in post-breakup strata (green; Fig. 6) show a more restricted distributive density primarily focused on the 550 Ma, 700 Ma and 1060 Ma age modes (Fig. 6). Unlike syn-rift strata, the 550 Ma and 700 Ma age modes form two distinct detrital peaks, suggesting a change in source regions for these zircon. These two detrital peaks overlap in age with the 540 Ma and 750 Ma intrusive complexes in the Leeuwin Complex (Collins, 2003), which forms the eastern shoulder of the Mentelle Basin. The ~1060 Ma detrital population may also reflect derivation from Mesoproterozoic protoliths of the Pinjarra Orogen exposed in the Leeuwin Complex (Collins, 2003). While Hf isotopic data is not currently available, whole-rock Sm–Nd model ages of basement samples from the Leeuwin Complex (T_{DM} = 1083–1160 Ma) and Pinjarra Orogen (T_{DM} = 2200–2100 Ma) (Fletcher & Libby, 1993) suggest relatively more juvenile isotopic characteristics for the Neoproterozoic Leeuwin Complex rocks compared to the more evolved Mesoproterozoic Pinjarra Orogen rocks. Our U–Pb–Hf detrital zircon dataset is consistent with this pattern (Fig. 6) and we therefore suggest that the combination of the 550 Ma, 700 Ma and 1060 Ma zircon age components in post-breakup strata fingerprints an overall local provenance of

sediments from the eastern shoulder of the Mentelle Basin (i.e. Leeuwin Complex). Furthermore, the lack of detrital zircon U–Pb–Hf signatures characteristic of the syn-rift strata indicates predominantly first-cycle provenance of sediments in Early Cretaceous post-breakup strata in the Mentelle Basin.

5.2 Source-to-sink system of Late Jurassic–Early Cretaceous sedimentary strata in the Mentelle Basin

Source region associations provide the opportunity to define the source-to-sink system of Late Jurassic–Early Cretaceous syn-rift strata in the Mentelle Basin. The youngest detrital zircon population of 700–500 Ma grains is consistent with derivation from rocks within the inferred convergent section of the Kuunga Orogen (Gamburtsev Suture) (Mulder et al., 2019) in interior East Antarctica (Fig. 8a). This region corresponds to the Gamburtsev Subglacial Mountains (GSM) which, together with the Dronning Maud Land Mountains, represent the most prominent topographic feature of the broader East Antarctic Plateau (O'Donnell & Nyblade, 2014) (Fig. 8a). Thermochronology data indicates that significant uplift of the plateau (including the GSM) took place during the Paleozoic–Mesozoic and that these regions have been at high elevation since that time (e.g. Cox et al., 2010). Furthermore, the GSM preserve a dendritic fluvial landscape which dates back to at least Triassic times (Paxman et al., 2016) and laid at the centre of several fluvial systems that dispersed a large volume of East Antarctic sediments across East Gondwana (Veevers, 2018). We therefore interpret the bulk of the 700–500 Ma detrital component to be derived from the physiographic region of the GSM (Fig. 8a). 1000–900 Ma age components derived from the TOAST in eastern Dronning Maud Land could also indicate subsidiary headwaters in regions of the East Antarctic Plateau west of the GSM.

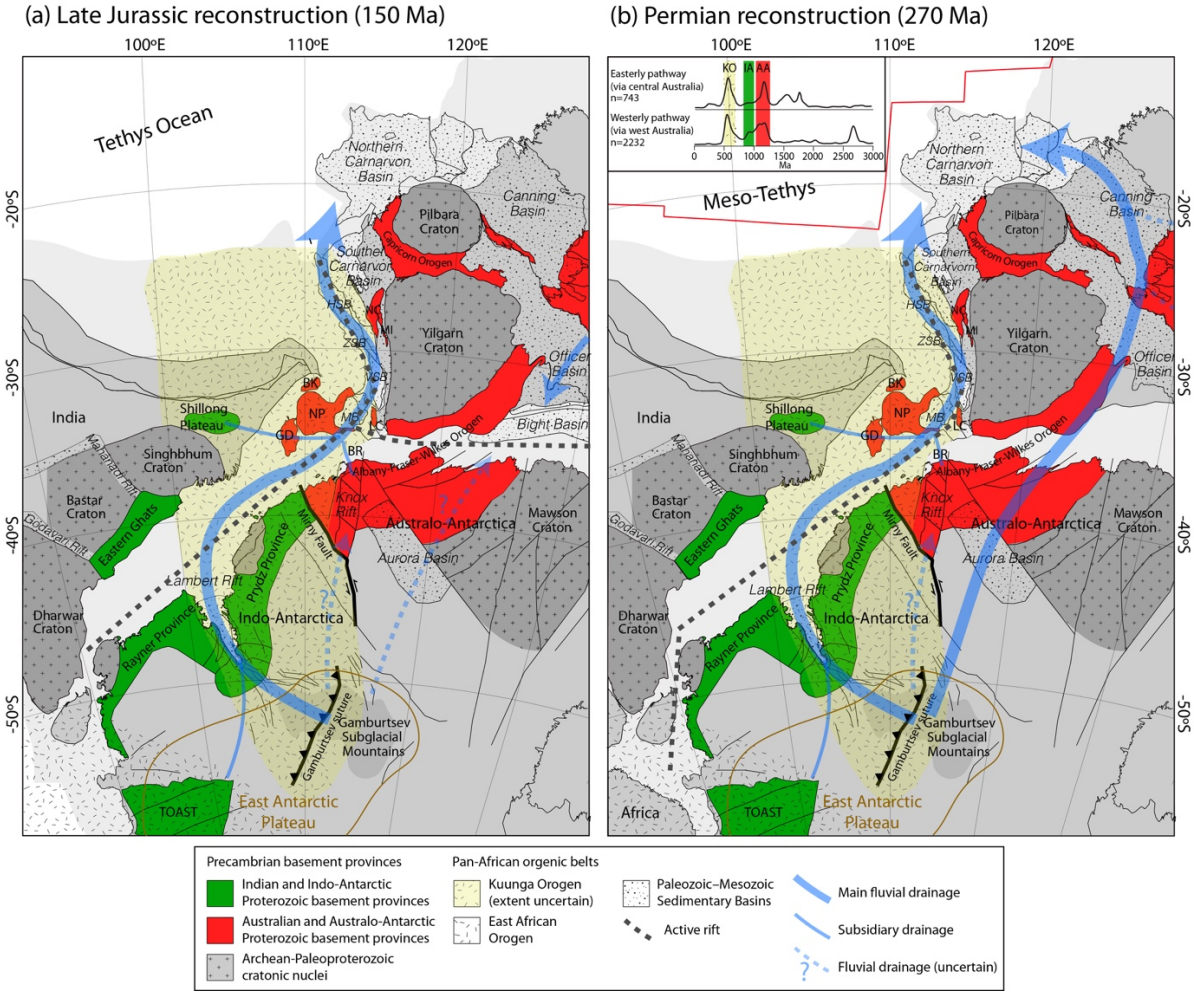

Figure 8. Paleogeographic reconstruction of East Gondwana during the (**a**) Late Jurassic and (**b**) Early Permian showing the fluvial pathways active at each time slice. In both reconstructions, Australia is fixed in its present-day frame of reference. Inset in panel b shows KDE plots of a compilation of detrital zircon ages of sediments along each fluvial pathway. Geological provinces, structural lines and abbreviations are the same as Figure 1. Approximate outline of the East Antarctic Plateau (brown) is based on O'Donnell and Nyblade (2014). Abbreviations in Panel b inset are: KO – Kuunga Orogen; IA – Indo-Antarctic basement; AA – Australo-Antarctic basement.

The mixing of detritus from the East Antarctic Plateau with zircon ages characteristic of Indo-Antarctic (1000–850 Ma age components with negative εHf_i value) and Australo-Antarctic (1200–1040 Ma age components with both positive and negative εHf_i values) basement domains indicates that the fluvial system progressively incorporated axially-derived detritus from these regions. We suggest that a pathway for the Late Jurassic–Early Cretaceous fluviatile system that satisfies such provenance follows the Late Paleozoic Lambert Rift, which preserves evidence for both GSM- and TOAST-derived

detritus in Permian-Triassic outcrops of the Amery Group (Veevers & Saeed, 2008), and feeds into the Late Jurassic–Early Cretaceous continental rift between India and Australia-Antarctica (Fig. 8a). The proposed transport route moves from the high-standing East Antarctic Plateau to the low-lying Mentelle Basin, progressively sourcing Indo-Antarctic basement rocks (i.e. Rayner Province exposed on the flanks of the Lambert Rift) and both radiogenic (Gulden Draak) and evolved (Naturaliste Plateau) offshore basement regions of the Albany-Fraser-Wilkes Orogen. This transport pathway might have also been fed by subsidiary systems originating from India and onshore regions of the Albany-Fraser-Wilkes Orogen of Australo-Antarctica to the south and east of the Mentelle Basin. An alternative and more direct route from the GSM to the Mentelle Basin may follow the Knox Rift of Australo-Antarctica, which plate reconstructions place along strike the Mentelle Basin during the Late Jurassic–Early Cretaceous (Maritati et al., 2016) (Fig. 8a). We do not discard the presence of a paleodrainage system from the GSM to the Knox Rift as proposed by Veevers (2018) (dashed blue arrow in Fig. 7), but point to the absence of radiogenic 1800–1300 Ma detrital components in the Mentelle Basin syn-rift strata, which are instead a key feature of basement north of the rift [i.e. Bruce Rise; Halpin et al. (2020)] (Fig. 7a), which limits the significance of this paleodrainage system to the Mentelle Basin and west Australian margin at least in the Late Jurassic–Early Cretaceous.

Located at the nexus of the Australian, Antarctic and Indian plates during Late Jurassic–Early Cretaceous rifting of East Gondwana, the Mentelle Basin represented a major depocenter for our proposed paleo-fluvial drainage model. The fluvial system likely continued northward following the trend of the developing rift between Australia and India, supplying sediments to other Late Jurassic–Early Cretaceous depocenters of the Perth Basin on the west Australian rifting margin (i.e. from south to north, Vlaming, Zeewyck and Houtman sub-basins). We suggest that the Late Jurassic–Early Cretaceous transcontinental fluvial system eventually ended in the Tethys Ocean marking the deposition of the Latest Tithonian–Berrasian fluvial-deltaic Barrow Group in the Northern Carnarvon Basin during the final phase of rifting in the Northern Carnarvon Basin. Here, provenance data from the lower Barrow group identifies a significant 700–500 Ma zircon age population that is consistent with the delta being fed by a predominantly south-north transportation system along the west Australian margin with minor input from Archean terranes in north-eastern Australia (i.e. Pilbara Craton) (Lewis & Sircombe, 2013). The

Barrow Delta may have therefore been the final point of the Late Jurassic–Early Cretaceous transcontinental fluvial system connecting East Antarctica to the Tethyan Ocean. Above the Valanginian unconformity, sediment provenance becomes restricted to basement rocks of the proximal Leeuwin Complex which flanks the Mentelle Basin to the east. This change in provenance corresponds with the transition from fluviatile to shallow marine transgressive depositional facies observed in strata across the Valanginian unconformity (Wainman et al., 2020) and support the shift in paleodrainage pattern during continental breakup from a predominantly fluviatile transcontinental axial transport system during mechanical extension to a much more restricted local provenance during the post-breakup phase (Olierook et al., 2019).

5.3 A long-lived fluvial transport pathway at the heart of East Gondwana

When visualised in the Euclidean space using non-metric MDS, the detrital zircon signature of Late Jurassic–Early Cretaceous syn-rift strata in the Mentelle Basin shows similarities in age spectra with older Permian–Early Jurassic sedimentary strata in the onshore Perth Basin as well as those of the Permian-Triassic Amery Group in Lambert Rift (Fig. 9). All these sedimentary sequences are located along our proposed transport route. Synthetic age spectra representative of Australo-Antarctic and Indo-Antarctic basement, and the convergent section of the Kuunga Orogen, cluster around Paleozoic–Mesozoic sedimentary strata on the MDS map which indicates an overall contribution of these basement sources across Paleozoic–Mesozoic rift strata, albeit in differing proportions (Fig. 9). This pattern suggests that the Late Jurassic–Early Cretaceous source-to-sink system may be shared by the majority of Paleozoic–Mesozoic rift strata and argues for a long-lived sediment dispersal pathway from the East Antarctic Plateau to the Tethyan margin of East Gondwana. Intra-basinal recycling could also produce similar detrital signatures across sedimentary strata. However, sediment recycling should have diluted distal detrital components favouring proximal Australo-Antarctic components. Instead, we argue that the relative abundance of 700–500 Ma and 1000–850 Ma age components reflecting distal Antarctic detrital inputs compared to proximal 1200–1040 Ma age components is indicative of a predominantly first-cycle provenance. Sediment provenance may be controlled by tectonic phases of extension as previously noted by Olierook et al. (2019), where mechanical extension phases incorporate higher proportions of distal axially-derived

detritus from distal sources while proximal detrital components become instead more prominent during thermal subsidence phases and brief marine incursions.

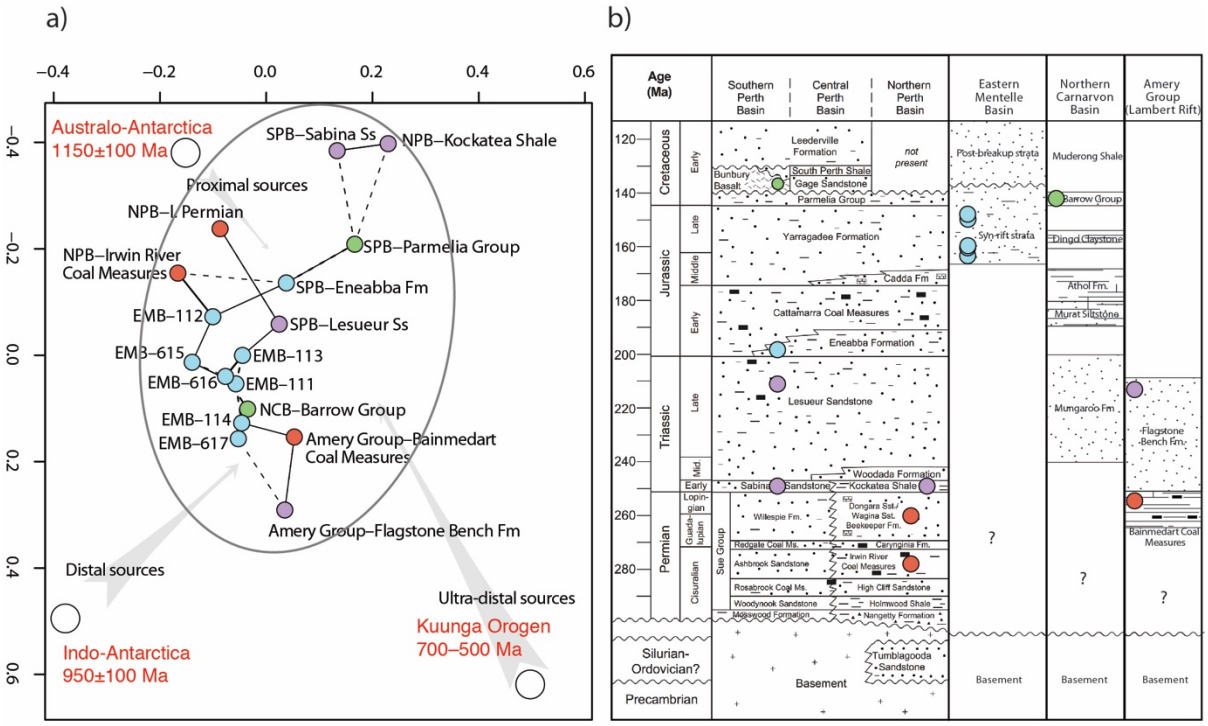

Figure 9. (**a**) Nonmetric multidimensional scaling (MDS) plot of the detrital zircon age spectra of Permian–Cretaceous sedimentary strata deposited along the proposed Late Jurassic–Early Cretaceous fluvial pathway. Detrital zircon populations are colour-coded by stratigraphic age (red – Permian; purple – Triassic; light blue – Jurassic; green – Cretaceous). Sources for U–Pb detrital zircon data are: Amery Group (Veevers & Saeed, 2008); north and south Perth Basin (Olierook et al., 2019 and references therein) ; Barrow Group (Lewis & Sircombe, 2013) and Mentelle basin (this study). Plotted are also synthetic age spectra designed to represent potential detrital zircon source regions of the Australo-Antarctic and Indo-Antarctic basement, and the convergent section of the Kuunga Orogen (Gamburtsev Subglacial Mountains) following the approach of Spencer & Kirkland (2016). Australo-Antarctic and Indo-Antarctic basement synthetic age spectra are created as normally-distributed sets of 100 random synthetic data points with mean of 1150 and 950, respectively and standard deviation of 100; Kuunga Orogen synthetic age spectrum is created as positively skewed set of 100 random data points ranging 700–500 with mode of 550 and skewness factor of 0.5. (**b**) Location of samples within the stratigraphy of the Perth Basin (Olierook et al., 2019), Eastern Mentelle Basin (Wainman et al., 2020), Northern Carnarvon Basin (Lewis & Sircombe, 2013) and Amery Group (Veevers & Saeed, 2008). Abbreviations are: LR – Lambert Rift; EMB – eastern Mentelle Basin; NCB – Northern Carnarvon Basin; NPB – northern Perth Basin; SPB – southern Perth Basin.

We infer that the transcontinental fluvial pathway linking East Antarctica to the northern Gondwana margin via the rifting west Australian margin started in the Late Carboniferous–Permian with the onset of major uplift on the East Antarctic Plateau triggered by widespread intracontinental extension across East Gondwana (Maritati et al., 2020) Tectonic uplift and rifting allowed for the establishment of a sediment source in interior East Antarctica and the formation of a long-lived fluvial sediment pathway in the main extensional corridors of this intra-Gondwanan rift system. Continental breakup and fast subsidence along the entire rifted margin resulted in the dramatic severance of the transcontinental fluvial connection between East Antarctica and the Tethyan Ocean and a large-scale reorganisation of drainage patterns to a localised transport that persists to the present day.

5.4 Transcontinental fluvial pathways of East Gondwana

Paleogeographic reconstructions advocate for similar ultra-distal transport pathways of East Antarctic detrital material to the northern Gondwana margin via Late Paleozoic–Triassic sedimentary and passive margin basins of central and northwestern Australia (Morón et al., 2019) (Fig. 8b). The presence of 700–500 Ma zircons in Late Paleozoic–Triassic sedimentary sequences in the Officer, Canning, Northern Carnarvon basins have also been suggested to fingerprint a source for this fluvial system in the GSM (Veevers, 2018). However, sedimentary sequences in these basins incorporate a significant radiogenic 1800–1300 Ma detrital component which reflects sourcing from Nuna–Rodina accretionary elements typical of Australo-Antarctica and southern Australia east of the Albany-Fraser-Wilkes Orogen (Fig. 7c) (Halpin et al., 2020; Kirkland et al., 2017; Maritati et al., 2019) and is largely absent in the detrital cargo of sedimentary rocks along our proposed route (Fig. 8b inset).

We suggest that during the Late Paleozoic–Triassic, two transcontinental fluvial systems concurrently transported detritus from the Kuunga Orogen to the forming Tethyan margin along two distinct pathways. The westerly pathway routed sediments via the Lambert Rift and rift basins of the intra-Gondwana rift system while the easterly pathway routed sediments through Wilkes Land and central Australia feeding Late Paleozoic–Triassic sag basins in the interior of East Antarctica (i.e. Aurora Basin) and Australia (i.e. Officer and Canning basins), and passive margin deltaic sequences of the

Northern Carnarvon Basin (i.e. Mungaroo Formation) (Fig. 8b). A modern-day analogue for the physiography of such transcontinental sediment routing regimes may be provided by the Yangtze and Yellow river systems of mainland China. Both river systems originate from the Tibetan plateau and debouch into the East China Sea; however, the respective detrital zircon cargo of fluvial sediments in their lower reaches reflects the different fluvial pathways draining the distinct tectonic elements of northern and southern China (Zheng et al., 2013).

Early rifting between Australia and Antarctica in the Late Jurassic and uplift of the Australia-Antarctic rift shoulder (Harrington et al., 2019) likely caused the severance of the easterly transcontinental fluvial system and the reorganisation of sediment pathways to a predominantly NE–SW paleodrainage from Eastern Australia to the forming Bight Basin (Barham et al., 2018; Lloyd et al., 2016) (Fig. 8a). By contrast, the westerly branch continued supplying sediments to Late Jurassic–Early Cretaceous siliciclastic and fluvio-deltaic sequences until the Early Cretaceous continental breakup of India from Australia-Antarctica.

6. Summary

We provide the first in-situ provenance study for the Mentelle Basin of southwestern Australia across the Late Jurassic–Early Cretaceous sedimentary sequence which marks the syn-rift to post-rift transition of the basin during the breakup of India from Australia-Antarctica. Combined detrital monazite U–Pb and zircon U–Pb–Hf isotopic data reveal that Late Jurassic–Early Cretaceous syn-rift sediments in the Mentelle Basin were supplied by a transcontinental fluvial system with headwaters in the East Antarctic Plateau (i.e. Gamburtsev Subglacial Mountains and eastern Dronning Maud Land) flowing northward to the Tethys Ocean following the trends of the Lambert Rift and the Jurassic rift between India and Australia-Antarctica. Provenance of the transgressive marine post-breakup sedimentary strata in the Mentelle Basin reflects transition to a proximal sediment source and marks the end of the transcontinental fluvial system during the final breakup of India from Australia-Antarctica in the Valanginian (~136 Ma). Using statistical comparison of detrital zircon spectra of Mentelle Basin syn-rift strata and other Australian and Antarctic Paleozoic–Mesozoic rift strata, we show that the transcontinental fluvial pathway routing sediments from East Antarctica to Tethyan Ocean via the west

Australian margin existed from the Late Paleozoic until continental breakup of India from Australia-Antarctica and constituted one of the main sediment fluvial pathways of East Gondwana.

Acknowledgements

This research used samples provided by the International Ocean Discovery Program (IODP). We thank IODP and the Australia-New Zealand IODP Consortium (ANZIC), which enabled Alessandro Maritati and Carmine Wainman to participate in IODP Expedition 369 and awarded post-expedition funding to Alessandro Maritati for this study. ANZIC is supported by the Australian Government through the Australian Research Council's LIEF funding scheme LE160100067 and the Australian and New Zealand consortium of universities and government agencies. We thank the IODP Expedition 369 participants for their assistance during the drilling of Site U1515 and the analysis of data on the JOIDES Resolution. J. Thompson and J. Tolley (ARC Centre of Excellence in Ore Deposit, CODES, University of Tasmania), K. Goemann and S. Feig (Central Science Laboratory, University of Tasmania) and Y. Lai (ARC Centre of Excellence for Core to Crust Fluid Systems, CCFS, Macquarie University, Australia) are thanked for analytical assistance. Alessandro Maritati is supported by an Australian Government Research Training Program (RTP) Scholarship and the Australian Research Council's Special Research Initiative for Antarctic Gateway Partnership (Project ID SR140300001).

References

Aitken, A. R. A., Young, D. A., Ferraccioli, F., Betts, P. G., Greenbaum, J. S., Richter, T. G., Roberts, J. L., Blankenship, D. D., & Siegert, M. J. (2014). The subglacial geology of Wilkes Land, East Antarctica. *Geophysical Research Letters, 41*(7), 2014GL059405. doi:10.1002/2014gl059405

Barham, M., & Kirkland, C. L. (2019). Changing of the guards: Detrital zircon provenance tracking sedimentological reorganization of a post-Gondwanan rift margin. *Basin Research*. doi:10.1111/bre.12403

Barham, M., Reynolds, S., Kirkland, C. L., O'Leary, M. J., Evans, N. J., Allen, H. J., Haines, P. W., Hocking, R. M., & McDonald, B. J. (2018). Sediment routing and basin evolution

in Proterozoic to Mesozoic east Gondwana: A case study from southern Australia. *Gondwana Research, 58*, 122-140. doi:10.1016/j.gr.2018.03.006

Black, L. P., Kamo, S. L., Allen, C. M., Aleinikoff, J. N., Davis, D. W., Korsch, R. J., & Foudoulis, C. (2003). TEMORA 1: a new zircon standard for Phanerozoic U–Pb geochronology. *Chemical Geology, 200*(1), 155-170.

Bodorkos, S., Fitzsimons, I. C. W., Hall, L. S., Sircombe, K. N., & Lewis, C. J. (2016). Beneath the Perth Basin: New U–Pb SHRIMP zircon ages from the Pinjarra Orogen, Western Australia. *Record 2016/31. Geoscience Australia, Canberra.* doi:http://dx.doi.org/10.11636/Record.2016.031

Boger, S. D. (2011). Antarctica - Before and after Gondwana. *Gondwana Research, 19*(2), 335-371.

Cawood, P. A., & Nemchin, A. A. (2000). Provenance record of a rift basin: U/Pb ages of detrital zircons from the Perth Basin, Western Australia. *Sedimentary Geology, 134*(3), 209-234. doi:https://doi.org/10.1016/S0037-0738(00)00044-0

Chatterjee, N., Bhattacharya, A., Duarah, B. P., & Mazumdar, A. C. (2011). Late Cambrian Reworking of Paleo-Mesoproterozoic Granulites in Shillong-Meghalaya Gneissic Complex (Northeast India): Evidence from PT Pseudosection Analysis and Monazite Chronology and Implications for East Gondwana Assembly. *The Journal of Geology, 119*(3), 311-330. doi:10.1086/659259

Collins, A. S. (2003). Structure and age of the northern Leeuwin Complex, Western Australia: constraints from field mapping and U-Pb isotopic analysis. *Australian Journal of Earth Sciences, 50*(4), 585-599. doi:doi:10.1046/j.1440-0952.2003.01014.x

Cox, S. E., Thomson, S. N., Reiners, P. W., Hemming, S. R., & van de Flierdt, T. (2010). Extremely low long-term erosion rates around the Gamburtsev Mountains in interior East Antarctica. *Geophysical Research Letters, 37*(22), n/a-n/a. doi:10.1029/2010gl045106

Crostella, A., & Backhouse, J. (2000). *Geology and petroleum exploration of the central and southern Perth Basin, Western Australia*: Geological Survey of Western Australia Perth, WA.

Daczko, N., Halpin, J., Whittaker, J., & Fitzsimons, I. (2015). *The Neoproterozoic East Gondwana suture: reconciling geological and geophysical evidence.* Paper presented at

the Riding the Wave: GSA Specialist Group in Tectonics and Structural Geology Conference.

Daczko, N. R., Halpin, J. A., Fitzsimons, I. C. W., & Whittaker, J. M. (2018). A cryptic Gondwana-forming orogen located in Antarctica. *Scientific Reports, 8*(1), 8371. doi:10.1038/s41598-018-26530-1

Dillinger, A., George, A. D., & Parra-Avila, L. A. (2018). Early Permian sediment provenance and paleogeographic reconstructions in southeastern Gondwana using detrital zircon geochronology (Northern Perth Basin, Western Australia). *Gondwana Research, 59*, 57-75. doi:10.1016/j.gr.2018.02.020

Elburg, M., Jacobs, J., Andersen, T., Clark, C., Läufer, A., Ruppel, A., Krohne, N., & Damaske, D. (2015). Early Neoproterozoic metagabbro-tonalite-trondhjemite of Sør Rondane (East Antarctica): Implications for supercontinent assembly. *Precambrian Research, 259*(0), 189-206. doi:http://dx.doi.org/10.1016/j.precamres.2014.10.014

Ferraccioli, F., Finn, C. A., Jordan, T. A., Bell, R. E., Anderson, L. M., & Damaske, D. (2011). East Antarctic rifting triggers uplift of the Gamburtsev Mountains. *Nature, 479*(7373), 388-392. doi:10.1038/nature10566

Fitzsimons, I. C. W. (2000). Grenville-age basement provinces in East Antarctica: Evidence for three separate collisional orogens. *Geology, 28*(10), 879-882. doi:10.1130/0091-7613(2000)28<879:gbpiea>2.0.co;2

Fitzsimons, I. C. W. (2003). Proterozoic basement provinces of southern and southwestern Australia, and their correlation with Antarctica. *Geological Society, London, Special Publications, 206*(1), 93-130. doi:10.1144/gsl.sp.2003.206.01.07

Fletcher, I., & Libby, W. (1993). Further isotopic evidence for the existence of two distinct terranes in the southern Pinjarra Orogen, Western Australia. *Geological Survey of Western Australia Report, 37*, 81-83.

Frizon de Lamotte, D., Fourdan, B., Leleu, S., Leparmentier, F., & de Clarens, P. (2015). Style of rifting and the stages of Pangea breakup. *Tectonics, 34*(5), 1009-1029. doi:10.1002/2014tc003760

Gain, S. E., Gréau, Y., Henry, H., Belousova, E., Dainis, I., Griffin, W. L., & O'reilly, S. Y. (2019). Mud Tank Zircon: Long-term evaluation of a reference material for U-Pb dating, Hf-isotope analysis and trace element analysis. *Geostandards and Geoanalytical Research, 43*(3), 339-354.

Gardner, R. L., Daczko, N. R., Halpin, J. A., & Whittaker, J. M. (2015). Discovery of a microcontinent (Gulden Draak Knoll) offshore Western Australia: Implications for East Gondwana reconstructions. *Gondwana Research, 28*(3), 1019-1031. doi:10.1016/j.gr.2014.08.013

Gibbons, A. D., Whittaker, J. M., & Muller, R. D. (2013). The breakup of East Gondwana: Assimilating constraints from Cretaceous ocean basins around India into a best-fit tectonic model. *Journal of Geophysical Research-Solid Earth, 118*(3), 808-822. doi:10.1002/jgrb.50079

Gonçalves, G. O., Lana, C., Scholz, R., Buick, I. S., Gerdes, A., Kamo, S. L., Corfu, F., Marinho, M. M., Chaves, A. O., Valeriano, C., & Nalini, H. A. (2016). An assessment of monazite from the Itambé pegmatite district for use as U–Pb isotope reference material for microanalysis and implications for the origin of the "Moacyr" monazite. *Chemical Geology, 424*, 30-50. doi:10.1016/j.chemgeo.2015.12.019

Haines, P. W., Wingate, M. T. D., & Kirkland, C. L. (2013). Detrital Zircon U–Pb Ages from the Paleozoic of the Canning and Officer Basins, Western Australia: Implications for Provenance and Interbasin connections. *In Keep, M., and Moss, SJ, The Sedimentary Basins of Western Australia IV: Proceedings of the Petroleum Exploration Society of Australia Symposium, Perth, Western Australia: Perth, Petroleum Exploration Society of Australia.*

Halpin, J., Daczko, N., Fitzsimons, I., Whittaker, J., & Mulder, J. (2018). *Anatomy of the Kuunga Orogen in East Antarctica.* Paper presented at the Australian Geoscience Council Convention.

Halpin, J. A., Daczko, N. R., Direen, N. G., Mulder, J. A., Murphy, R. C., & Ishihara, T. (2020). Provenance of rifted continental crust at the nexus of East Gondwana breakup. *Lithos, 354-355*. doi:10.1016/j.lithos.2019.105363

Halpin, J. A., Daczko, N. R., Kobler, M. E., & Whittaker, J. M. (2017). Strike-slip tectonics during the Neoproterozoic–Cambrian assembly of East Gondwana: Evidence from a newly discovered microcontinent in the Indian Ocean (Batavia Knoll). *Gondwana Research*.

Halpin, J. A., Gerakiteys, C., Clarke, G. L., Belousova, E. A., & Griffin, W. L. (2005). In-situ U-Pb geochronology and Hf isotope analyses of the Rayner Complex, east Antarctica. *Contributions to Mineralogy and Petrology, 148*, 689-706.

Halpin, J. A., Jensen, T., McGoldrick, P., Meffre, S., Berry, R. F., Everard, J. L., Calver, C. R., Thompson, J., Goemann, K., & Whittaker, J. M. (2014). Authigenic monazite and detrital zircon dating from the Proterozoic Rocky Cape Group, Tasmania: Links to the Belt-Purcell Supergroup, North America. *Precambrian Research, 250*(0), 50-67. doi:http://dx.doi.org/10.1016/j.precamres.2014.05.025

Harrington, L., Zahirovic, S., Salles, T., Braz, C., & Müller, R. D. (2019). Tectonic, geodynamic and surface process driving forces of Australia's paleogeography since the Jurassic. *in KEEP, M. & MOSS, S.J. (Eds), The Sedimentary Basins of Western Australia V: Proceedings of the Petroleum Exploration Society of Australia Symposium, Perth, WA, 2019, 29 pp.*

Harrowfield, M., Holdgate, G. R., Wilson, C. J. L., & McLoughlin, S. (2005). Tectonic significance of the Lambert graben, East Antarctica: Reconstructing the Gondwanan rift. *Geology, 33*(3), 197. doi:10.1130/g21081.1

Hietpas, J., Samson, S., Moecher, D., & Schmitt, A. K. (2010). Recovering tectonic events from the sedimentary record: Detrital monazite plays in high fidelity. *Geology, 38*(2), 167-170. doi:10.1130/g30265.1

Huber, B. T., Hobbs, R.W., Bogus, K.A., Batenburg, S.J., Brumsack, H.-J., do Monte Guerra, R., Edgar, K.M., Edvardsen, T., Garcia Tejada, M.L., Harry, D.L., Hasegawa, T., Haynes, S.J., Jiang, T., Jones, M.M., Kuroda, J., Lee, E.Y., Li, Y.-X., MacLeod, K.G., Maritati, A., Martinez, M., O'Connor, L.K., Petrizzo, M.R., Quan, T.M., Richter, C., Riquier, L., Tagliaro, G.T., Wainman, C.C., Watkins, D.K., White, L.T., Wolfgring, E., Xu, Z. (2019). Site U1515. *In Hobbs, R.W., Huber, B.T., Bogus, K.A., and the Expedition 369 Scientists, Australia Cretaceous Climate and Tectonics. Proceedings of the International Ocean Discovery Program, 369: College Station, TX (International Ocean Discovery Program). https://doi.org/10.14379/iodp.proc.369.106.2019*.

Jacobs, J., Elburg, M., Läufer, A., Kleinhanns, I. C., Henjes-Kunst, F., Estrada, S., Ruppel, A. S., Damaske, D., Montero, P., & Bea, F. (2015). Two distinct Late Mesoproterozoic/Early Neoproterozoic basement provinces in central/eastern Dronning Maud Land, East Antarctica: The missing link, 15–21°E. *Precambrian Research, 265*(0), 249-272. doi:http://dx.doi.org/10.1016/j.precamres.2015.05.003

Jochum, K. P., Weis, U., Stoll, B., Kuzmin, D., Yang, Q., Raczek, I., Jacob, D. E., Stracke, A., Birbaum, K., Frick, D. A., Günther, D., & Enzweiler, J. (2011). Determination of

Reference Values for NIST SRM 610-617 Glasses Following ISO Guidelines. *Geostandards and Geoanalytical Research, 35*(4), 397-429. doi:10.1111/j.1751-908X.2011.00120.x

Kirkland, C. L., Barham, M., & Danišík, M. (2019). Find a match with triple-dating: Antarctic sub-ice zircon detritus on the modern shore of Western Australia. *Earth and Planetary Science Letters*. doi:10.1016/j.epsl.2019.115953

Kirkland, C. L., Smithies, R. H., Spaggiari, C. V., Wingate, M. T. D., Quentin de Gromard, R., Clark, C., Gardiner, N. J., & Belousova, E. A. (2017). Proterozoic crustal evolution of the Eucla basement, Australia: Implications for destruction of oceanic crust during emergence of Nuna. *Lithos, 278-281*, 427-444. doi:10.1016/j.lithos.2017.01.029

Kristoffersen, M., Andersen, T., Elburg, M. A., & Watkeys, M. K. (2016). Detrital zircon in a supercontinental setting: locally derived and far-transported components in the Ordovician Natal Group, South Africa. *Journal of the Geological Society, 173*(1), 203-215.

Lewis, C. J., & Sircombe, K. N. (2013). Use of U-Pb geochronology to delineate provenance of North West Shelf sediments, Australia. *In The Sedimentary Basins of Western Australia IV: Proceedings of the Petroleum Exploration Society of Australia Symposium (pp. 1-27).*

Liu, X., Zhao, Y., Chen, H., & Song, B. (2017). New zircon U–Pb and Hf–Nd isotopic constraints on the timing of magmatism, sedimentation and metamorphism in the northern Prince Charles Mountains, East Antarctica. *Precambrian Research, 299*, 15-33. doi:10.1016/j.precamres.2017.07.012

Lloyd, J., Collins, A. S., Payne, J. L., Glorie, S., Holford, S., & Reid, A. J. (2016). Tracking the Cretaceous transcontinental Ceduna River through Australia: The hafnium isotope record of detrital zircons from offshore southern Australia. *Geoscience Frontiers, 7*(2), 237-244. doi:10.1016/j.gsf.2015.06.001

Majumdar, D., & Dutta, P. (2016). Geodynamic evolution of a Pan-African granitoid of extended Dizo Valley in Karbi Hills, NE India: Evidence from Geochemistry and Isotope Geology. *Journal of Asian Earth Sciences, 117*, 256-268. doi:10.1016/j.jseaes.2015.12.015

Maritati, A., Aitken, A. R. A., Young, D. A., Roberts, J. L., Blankenship, D. D., & Siegert, M. J. (2016). The tectonic development and erosion of the Knox Subglacial Sedimentary

Basin, East Antarctica. *Geophysical Research Letters, 43*(20), 10728-10737. doi:10.1002/2016gl071063

Maritati, A., Danišík, M., Halpin, J. A., Whittaker, J. M., & Aitken, A. R. A. (2020). Pangea rifting shaped the East Antarctic landscape. *Tectonics*.

Maritati, A., Halpin, J. A., Whittaker, J. M., & Daczko, N. R. (2019). Fingerprinting Proterozoic Bedrock in Interior Wilkes Land, East Antarctica. *Scientific Reports, 9*(1). doi:10.1038/s41598-019-46612-y

Matthews, K. J., Maloney, K. T., Zahirovic, S., Williams, S. E., Seton, M., & Müller, R. D. (2016). Global plate boundary evolution and kinematics since the late Paleozoic. *Global and Planetary Change, 146*, 226-250. doi:10.1016/j.gloplacha.2016.10.002

Mikhalsky, E. V., Belyatsky, B. V., Presnyakov, S. L., Skublov, S. G., Kovach, V. P., Rodionov, N. V., Antonov, A. V., Saltykova, A. K., & Sergeev, S. A. (2015). The geological composition of the hidden Wilhelm II Land in East Antarctica: SHRIMP zircon, Nd isotopic and geochemical studies with implications for Proterozoic supercontinent reconstructions. *Precambrian Research, 258*, 171-185. doi:10.1016/j.precamres.2014.12.011

Morón, S., Cawood, P. A., Haines, P. W., Gallagher, S. J., Zahirovic, S., Lewis, C. J., & Moresi, L. (2019). Long-lived transcontinental sediment transport pathways of East Gondwana. *Geology, 47*(6), 513-516. doi:10.1130/g45915.1

Mulder, J. A., Halpin, J. A., Daczko, N. R., Orth, K., Meffre, S., Thompson, J. M., & Morrissey, L. J. (2019). A Multiproxy provenance approach to uncovering the assembly of East Gondwana in Antarctica. *Geology*. doi:10.1130/g45952.1

Norvick, M. (2004). Tectonic and stratigraphic history of the Perth Basin. *Geoscience Australia Record, 16*(2004), 30.

Olierook, H. K. H., Barham, M., Fitzsimons, I. C. W., Timms, N. E., Jiang, Q., Evans, N. J., & McDonald, B. J. (2019). Tectonic controls on sediment provenance evolution in rift basins: Detrital zircon U–Pb and Hf isotope analysis from the Perth Basin, Western Australia. *Gondwana Research, 66*, 126-142. doi:10.1016/j.gr.2018.11.002

O'Donnell, J. P., & Nyblade, A. A. (2014). Antarctica's hypsometry and crustal thickness: Implications for the origin of anomalous topography in East Antarctica. *Earth and Planetary Science Letters, 388*, 143-155. doi:10.1016/j.epsl.2013.11.051

Patchett, P., & Tatsumoto, M. (1981). A routine high-precision method for Lu-Hf isotope geochemistry and chronology. *Contributions to Mineralogy and Petrology, 75*(3), 263-267.

Paxman, G. J. G., Watts, A. B., Ferraccioli, F., Jordan, T. A., Bell, R. E., Jamieson, S. S. R., & Finn, C. A. (2016). Erosion-driven uplift in the Gamburtsev Subglacial Mountains of East Antarctica. *Earth and Planetary Science Letters, 452*, 1-14. doi:10.1016/j.epsl.2016.07.040

Ramakrishnan, M., & Vaidyanadhan, R. (2010). Geology of India (Vol. 1 & 2). *GSI Publications, 2*(1).

Raymond, O. L., Totterdell, J. M., Stewart, A. J., & Woods, M. A. (2018). Australian Geological Provinces, 2018.01 edition [Digital Dataset]. Geoscience Australia, Commonwealth of Australia, Canberra. http://www.ga.gov.au.

Rubatto, D., Williams, I. S., & Buick, I. S. (2001). Zircon and monazite response to prograde metamorphism in the Reynolds Range, central Australia. *Contributions to Mineralogy and Petrology, 140*(4), 458-468.

Ruppel, A., Jacobs, J., Eagles, G., Läufer, A., & Jokat, W. (2018). New geophysical data from a key region in East Antarctica: Estimates for the spatial extent of the Tonian Oceanic Arc Super Terrane (TOAST). *Gondwana Research, 59*, 97-107. doi:10.1016/j.gr.2018.02.019

Sack, P. J., Berry, R. F., Meffre, S., Falloon, T. J., Gemmell, J. B., & Friedman, R. M. (2011). In situ location and U-Pb dating of small zircon grains in igneous rocks using laser ablation–inductively coupled plasma–quadrupole mass spectrometry. *Geochemistry, Geophysics, Geosystems, 12*(5).

Scherer, E., Münker, C., & Mezger, K. (2001). Calibration of the Lutetium-Hafnium Clock. *Science, 293*(5530), 683.

Sheraton, J. W., Tingey, R. J., Oliver, R. L., & Black, L. P. (1995). *Geology of the Bunger Hills-Denman Glacier region, East Antarctica* (Vol. 244): Australian Geological Survey Organisation Bulletin.

Sircombe, K. N., & Freeman, M. J. (1999). Provenance of detrital zircons on the Western Australia coastline - implications for the geologic history of the Perth basin and denudation of the Yilgarn craton.(Statistical Data Included). *Geology, 27*(10), 879. doi:10.1130/0091-7613(1999)027<0879:PODZOT>2.3.CO;2

Sláma, J., Košler, J., Condon, D. J., Crowley, J. L., Gerdes, A., Hanchar, J. M., Horstwood, M. S. A., Morris, G. A., Nasdala, L., Norberg, N., Schaltegger, U., Schoene, B., Tubrett, M. N., & Whitehouse, M. J. (2008). Plešovice zircon - A new natural reference material for U-Pb and Hf isotopic microanalysis. *Chemical Geology, 249*(1-2), 1-35. doi:http://dx.doi.org/10.1016/j.chemgeo.2007.11.005

Spencer, C. J., & Kirkland, C. L. (2016). Visualizing the sedimentary response through the orogenic cycle: A multidimensional scaling approach. *Lithosphere, 8*(1), 29-37. doi:10.1130/l479.1

Spencer, C. J., Kirkland, C. L., & Taylor, R. J. M. (2016). Strategies towards statistically robust interpretations of in situ U–Pb zircon geochronology. *Geoscience Frontiers, 7*(4), 581-589. doi:10.1016/j.gsf.2015.11.006

Tucker, N. M., Payne, J. L., Clark, C., Hand, M., Taylor, R. J. M., Kylander-Clark, A. R. C., & Martin, L. (2017). Proterozoic reworking of Archean (Yilgarn) basement in the Bunger Hills, East Antarctica. *Precambrian Research, 298*, 16-38. doi:http://dx.doi.org/10.1016/j.precamres.2017.05.013

Varga, J., Raimondo, T., Daczko, N. R., Adam, J. (2020). Experimental alteration of monazite in granitic melt: Variable U–Th–Pb and REE mobility during melt-mediated coupled dissolution-precipitation. *Chemical Geology, 544*, 119602. doi:http://dx.doi.org/10.1016/j.chemgeo.2020.119602

Veevers, J. J. (2018). Gamburtsev Subglacial Mountains: Age and composition from morainal clasts and U–Pb and Hf-isotopic analysis of detrital zircons in the Lambert Rift, and potential provenance of East Gondwanaland sediments. *Earth-Science Reviews, 180*, 206-257. doi:10.1016/j.earscirev.2018.03.002

Veevers, J. J., & Saeed, A. (2008). Gamburtsev Subglacial Mountains provenance of Permian-Triassic sandstones in the Prince Charles Mountains and offshore Prydz Bay: Integrated U-Pb and TDM ages and host-rock affinity from detrital zircons. *Gondwana Research, 14*(3), 316-342.

Vermeesch, P. (2018). IsoplotR: A free and open toolbox for geochronology. *Geoscience Frontiers, 9*(5), 1479-1493. doi:10.1016/j.gsf.2018.04.001

Wainman, C. C., Borissova, I., Harry, D. L., Hobbs, R. W., Mantle, D. J., Maritati, A., Lee, E. Y., & Scientists, t. E. (2020). Evidence for non-marine Jurassic to earliest Cretaceous sediments in the pre-breakup section of the Mentelle Basin, southwestern Australia.

Australian Journal of Earth Sciences, 67(1), 89-105. doi:10.1080/08120099.2019.1627581

Walker, J., Geissman, J., & Bowring, S. (2018). Geologic Time Scale v. 5.0 (LE Babcock, Compilers). *Geological Society of America*.

Wiedenbeck, M., Alle, P., Corfu, F., Griffin, W., Meier, M., Oberli, F. v., Quadt, A. v., Roddick, J., & Spiegel, W. (1995). Three natural zircon standards for U-Th-Pb, Lu-Hf, trace element and REE analyses. *Geostandards and Geoanalytical Research, 19*(1), 1-23.

Williams, S. E., Whittaker, J. M., & Müller, R. D. (2011). Full-fit, palinspastic reconstruction of the conjugate Australian-Antarctic margins. *Tectonics, 30*(6), TC6012. doi:10.1029/2011tc002912

Zheng, H., Clift, P. D., Wang, P., Tada, R., Jia, J., He, M., & Jourdan, F. (2013). Pre-Miocene birth of the Yangtze River. *Proceedings of the National Academy of Sciences, 110*(19), 7556-7561. doi:10.1073/pnas.1216241110

Chapter 5

Discussion

5.1 Summary and significance of findings

The three chapters presented in this thesis improve the knowledge of the geological record and tectonic history of underexplored regions of Australo-Antarctica and southern Australia. This final chapter discusses the significance of the findings of each chapter in relation to the specific objectives of the thesis outlined in **Chapter 1** to better elucidate the evolution of Australo-Antarctica. Prospective avenues for future research are also outlined to address key, unanswered questions that have arisen from the findings of this thesis.

(1) Test and refine the relationship between the Precambrian basement provinces of Australo-Antarctica and southern Australia

The vast, largely unknown tract of Precambrian basement between the Windmill Islands and Terre Adélie in interior Wilkes Land has long hampered our understanding of the Mesoproterozoic evolution of Australo-Antarctica. The newly identified c. 1475–1389 Ma Nuyina and c. 1610–1490 Ma Banzare provinces in Wilkes Land (**Chapter 2**) resolve a geometric framework for Precambrian Australia-Antarctic correlations and in doing so reveal new insight into crustal accretion during Nuna-to-Rodinia plate reorganisations. At a broad level, this new basement characterisation provides support to models advocating subduction-driven convergence between the Mawson Craton and the West Australian Craton through a series of westward-migrating extensional-accretionary events between c. 1600–1300 Ma (e.g. Aitken et al., 2016a; Smits et al., 2014; Spaggiari et al., 2018; Wise et al., 2018). The termination of these events in the west occurred with the accretion of arc terranes and obduction of ophiolite slivers in the Madura Province and its Antarctic extension (i.e. Nuyina Province) onto the West Australian Craton along the Albany-Fraser-Wilkes Province between 1389 and 1330 Ma (Spaggiari et al., 2018). Subsequent intraplate magmatism between 1192 Ma and 1125 Ma led to cratonisation of Proterozoic oceanic crust and halted the closure between the Mawson Craton and the West Australian Craton (Kirkland et al., 2017).

By comparison, the architecture of magmatic arc systems between the Mawson Craton and Banzare Province remains poorly defined. In Australia, the western margin of the Gawler Craton preserves evidence of reworking by the c. 1633–1608 Ma St Peter Suite (Reid et al., 2019) which is coeval with the Toolgana Supersuite of the Coompana Province and marks the easternmost expression of c. 1600 Ma arc magmatism (Dutch et al., 2018; Spaggiari et al., 2020). Arc rocks of this age are as yet unknown in the western sector of the Mawson Craton, where instead only the c. 1765–1690 Ma metasedimentary rocks in the Cape Hunter and Dumont D'Urville basins (Oliver & Fanning, 1997; Peucat et al., 1999) are exposed. However, evidence for c. 1600 Ma tectono-thermal activity in the region is supported by $^{40}Ar/^{39}Ar$ ages of exposed crustal rocks (Naumenko-Dèzes et al., 2020) and the presence of c. 1600 Ma felsic volcanic material in glacial moraines previously linked to the Gawler Range Volcanics (Peucat et al., 2002). In addition, the detrital zircon record of offshore sediments near the Mawson Craton-Banzare Province boundary preserves a significant c. 1560 Ma detrital population which is not reflected in the onshore geology (Pierce et al., 2014). Further analysis of glacial clasts and nunataks west of Dumont D'Urville station (i.e. Rocher X, Rocher Janet) may inform on the earliest evidence of arc magmatism in the western Mawson Craton and refine the poorly defined transition from the reworked cratonic margin to the oceanic Banzare Province in Antarctica.

Mesoproterozoic accretionary events similar to those preserved in the Madura/Nuyina and Coompana/Banzare basement are recognised in the pre-Grenville basement of Laurentia (Whitmeyer & Karlstrom, 2007) and may help inform broader Nuna-to-Rodinia plate configurations. In particular, the 1490–1370 Ma trans-Laurentian igneous suite presents similar ages and isotopic characteristics to the Madura/Nuyina province; its continuation into Australo-Antarctica has been established based on the correlation between c. 1450 Ma A-type granites in Laurentia and glacial clasts in the Transantarctic Mountains (TAM) (Goodge et al., 2017) in the Rodinia SWEAT (southwestern United States-East Antarctica) configuration (Goodge et al., 2008). Such a connection is interpreted to support a link between Mesoproterozoic accretionary events of Australia and Laurentia along the southern and western edge of the Mawson Craton; it would also imply an extension of the Grenville Orogen of Laurentia into interior East Antarctica possibly sampled by c. 1200–1100 Ma glacial igneous clasts in the TAM (Goodge et al., 2017). The geometrical

framework presented in **Chapter 2** suggests a termination of the Nuyina province in Wilkes Land and would not support direct linkages with accretionary events in Laurentia. Instead, the termination of Late Mesoproterozoic accretionary-collisional events at the Nuyina and Wilkes provinces would be compatible with models invoking continuity of the Grenville, Musgrave and Albany-Fraser-Wilkes orogens in the AUSMEX (Australia-Mexico) Rodinia configuration, followed by transition into a SWEAT configuration via dextral displacement during the final stages of Rodinia assembly (c. 1000–900 Ma) (Mulder et al., 2018). The low resolution or complete absence of aerogeophysical data in the East Antarctic interior limits a more thorough assessment of the continuation of Proterozoic basement provinces into Australo-Antarctica. Further geometrical constraints informing the correlation of 1600–1300 Ma accretionary events within the broader framework of the Nuna-to-Rodinia cycle may instead be revealed via integration of satellite gravity data (Ebbing et al., 2018) or probabilistic approaches (Stål et al., 2019).

(2) Constrain the age and tectonic origin of Australo-Antarctic sedimentary basins

Subglacial sedimentary basins in interior Australo-Antarctica represent some of the most enigmatic tectonic features of East Antarctica. The new insights on the age and tectonic origin of Australo-Antarctic sedimentary basins presented in **Chapters 2 and 3** constrain basin formation during two phases of extensional tectonism associated with the breakup of Rodinia in the Neoproterozoic and the early stages of Gondwana–Pangea rifting in the Paleozoic–Mesozoic.

Depositional age and detrital zircon correlations between newly dated Sabrina Basin Neoproterozoic (c. 1038–633 Ma) erratic samples and Neoproterozoic strata deposited elsewhere in Australo-Antarctica (Goodge et al., 2004) and southern Australia (Fraser & Neumann, 2016) suggest the presence of a much larger Neoproterozoic sedimentary basin extending from the interior to the proto-Pacific rifting margin (**Chapter 2**). The Beardmore Group (TAM) is interpreted to be a craton-margin succession of thickness comparable to the Sabrina Basin (1–2 km-thick) (Goodge et al., 2002), with a sedimentary source in the Mesoproterozoic basement provinces in the Australo-Antarctic interior (Goodge et al., 2004). If both of these sequences represent remnants of a larger Neoproterozoic basin as

proposed in **Chapter 2**, their geometry and provenance would be consistent with deposition within an extensive epicontinental, but relatively thin, passive-margin basin similar in scale to the Centralian Superbasin of Australia. This implies that, similar to central and southern Australia, interior Australo-Antarctica may have experienced widespread subsidence during Rodinia breakup.

Due to the limited geological samples available, the extent and spatial distribution of Neoproterozoic sedimentary sequences across Australo-Antarctica remains largely unconstrained. The lack of significant Archean–Paleoproterozoic age signatures characteristic of the Mawson Craton in detrital spectra of the Neoproterozoic Sabrina Basin and Beardmore Group may, however, suggest that the Mawson Craton was covered with sediments and thus support the hypothesis of a larger Late Neoproterozoic sedimentary basin extending between the Sabrina Basin and the TAM. Further analysis of rare sedimentary erratics occurring along the Wilkes Land coast may help define spatial and tectonic links between the Neoproterozoic Sabrina Basin and other Antarctic and Australian Neoproterozoic strata.

The low-temperature thermochronology record of exposed basement rock across East Antarctica presented in **Chapter 3** provides evidence for widespread cooling and exhumation of Precambrian basement during Late Paleozoic–Triassic. The discussion of **Chapter 3** proposes that basement exhumation across East Antarctica is related to a single denudational event driven by intraplate extension and basin formation during the earliest stages of Pangea/Gondwana rifting. Extensional deformation triggered the exhumation of large sections of Precambrian basement in the continental interior of East Antarctica and formation of large sedimentary basins across East Antarctica and Gondwana. These include the Knox, Aurora, Vincennes and Wilkes basins of Australo-Antarctica, all of which are shown to be consistent with the broader geodynamic framework of Late Paleozoic–Triassic intraplate tectonics. This event may have also disrupted the once contiguous Australo-Antarctic Late Neoproterozoic basin similarly to how intraplate uplift during the Neoproterozoic Petermann and Palaeozoic Alice Springs orogenies segmented the Australian Centralian Superbasin into the smaller Amadeus, Georgina, Ngalia, and Officer basins (Lindsay & Leven, 1996). In the Knox Basin however, the record of Late Paleozoic–

Triassic extension and basin formation contrasts with recent studies advocating an older Precambrian sedimentary fill based on isotopic data from glacial moraines (Kolesik, 2016) and *in situ* sedimentary rocks exposed within the basin (Mikhalsky et al., 2020). Additional work in the region will be necessary to reconcile the record of Phanerozoic tectonism interpreted from low-temperature thermochronology data with evidence for older Precambrian sedimentary rocks within the basin.

The impact of Gondwana-breakup tectonism across Australo-Antarctica remains unconstrained. While basement in other sectors of East Antarctica (e.g. Indo-Antarctica), preserve evidence for thermal events related to the breakup of India from East Gondwana, the low-temperature thermochronology record of Australo-Antarctica west of the Bunger Hills region does not reflect any major onshore tectonic activity after the Late Paleozoic–Triassic extensional event. This is in stark contrast with geophysical studies suggesting substantial Cretaceous–Cenozoic extensional activity onshore Australo-Antarctica (Aitken et al., 2014; Cianfarra & Maggi, 2017; Eagles, 2019; Maritati et al., 2016). A possible explanation for this dichotomy provided in **Chapter 3** is that post-Triassic events may not be detectable by low-temperature thermochronology methods, which require either cooling from a sufficiently high thermal anomaly (c. 100°C) or removal of least 2–3 km of overburden in order to induce resetting of the AHe and AFT systems. Therefore, any Cretaceous or younger thermal event between the Bunger Hills region and the TAM may be limited in terms of cooling and denudation and not recorded by currently available AHe and AFT data at the coast. Alternatively, it is also possible that the imprint of younger tectonism may only be preserved in regions away from the coast; recent reconnaissance low-temperature thermochronology of detrital grains sourced from eroded bedrock inland from the TAM appear to support this hypothesis (Goodge & Fitzgerald, 2019) and may help constrain the magnitude and timing of Cretaceous-Cenozoic tectonic events in the interior of Australo-Antarctica.

(3) *Examine the offshore sedimentary record to characterise source-to-sink pathways during East Gondwana rifting*

Phanerozoic sedimentary rocks in Australo-Antarctica are completely obscured by ice; however, the relatively more accessible sedimentary record of rift sequences in Australian Paleozoic–Mesozoic basins provides insights into the provenance of their Antarctic counterparts and help refine source-to-sink pathways during East Gondwana rifting. One such basin is the offshore Late Jurassic–Early Cretaceous Mentelle Basin, which has been reconstructed along strike of the Knox Rift (Maritati et al., 2016). **In Chapter 4**, source region interpretations based on detrital zircon and monazite isotopic data suggest that the Mentelle Basin was part of a transcontinental fluvial pathway traversing East Gondwana and connecting the Gamburtsev Subglacial Mountains with the Tethyan margin until the breakup of India in the Early Cretaceous. This fluvial pathway does not directly connect the Knox Rift with the Mentelle Basin; instead, sediments were transported along the long-lived Early Permian–Early Cretaceous intra-Gondwanan rift between Antarctica, Australia and India as evidenced by the similar sediment provenance shared by Late Jurassic strata in the Mentelle Basin with other Early Permian–Late Jurassic strata along the proposed pathway in Antarctica (Amery Group), western Australia (Perth Basin) and Exmouth Plateau (Barrow Group). This provenance interpretation does not support a direct and continuous link between the Knox and Mentelle basin and the two basins may consequently not be tectonically related. The provenance of Phanerozoic sedimentary sequences in the Knox Rift remains therefore unconstrained. The ~2-4 km basement exhumation on the western rift flank during the Late Paleozoic–Triassic (**Chapter 3**) may have provided a sufficient source for the ~7 km of sediments in the Knox Basin. However, it is also possible that some sediments were derived from the topographically upstream GSM, as proposed by Veevers (2018).

The findings of **Chapter 4** reinforce the growing body of literature supporting transport of clastic material to Paleozoic–Mesozoic sedimentary basins via transcontinental fluvial drainage systems radiating from high-standing regions of central East Antarctica (e.g. Lewis & Sircombe, 2013; Morón et al., 2019; Veevers, 2018; Veevers et al., 2006). These drainage systems could have also supplied clastic material to the Aurora, Vincennes and Wilkes basins en route to Australia. The establishment of these large-scale sediment dispersal pathways during Palaeozoic–Mesozoic are consistent with the findings of **Chapter 3;** continent-scale exhumation and erosion of East Antarctic basement during

intracontinental extension likely generated a significant volume of clastic material that was accommodated within the vast network of Paleozoic–Mesozoic sedimentary basins across East Gondwana. The Gondwana–Pangea supercontinent configuration sustained the dispersal of sediments via large-scale fluvial pathways until the Jurassic–Cretaceous separation of India and Australia from East Antarctica.

(4) Explore the impact of onshore extension on the topographic evolution of Australo-Antarctica

Onshore sedimentary basins of Australo-Antarctica exert a primary control on the amplitude of topographic relief and influence the selective nature of fluvial and glacial erosion patterns on the continent. The new work presented in this thesis provides a broader understanding of the tectonic controls on the topographic framework of Australo-Antarctica and its long-term landscape evolution. **Chapter 3** overall supports the template-forming role of Paleozoic–Triassic tectonics on the long-term topographic evolution of Australo-Antarctica, suggesting that the different morphologies inherited from Late Paleozoic–Triassic extension had a profound influence on the style of erosion. The Knox Rift focused fluvial and glacial erosion, which caused amplification of topographic relief through selective erosion and associated flexural responses. This erosional regime led to the formation of a deep subglacial depression within the rift, which includes a canyon beneath the Denman ice stream that reaches the deepest continental point on Earth (Morlighem et al., 2020). By contrast, the broad and low-elevation morphology of basins in the central Australo-Antarctic domain allowed for the development of larger fluvial braided systems and river deltas (Paxman et al., 2019; Sauermilch et al., 2019) followed by dynamic erosion from a marine-based ice sheet (Aitken et al., 2016b; Paxman et al., 2018; Young et al., 2011).

However, vast uncertainties remain regarding the rates and style of landscape evolution of Australo-Antarctica during the Mesozoic–Cenozoic. Previous discussions in this chapter highlighted the number of studies supporting onshore extension during Gondwana breakup and/or Cenozoic intraplate tectonism in interior Australo-Antarctica. However, except for minor Jurassic–Cretaceous reactivation of the Knox Rift in the Bunger Hills

region, these events are undetectable by available low-temperature thermochronology data at the coast and did not lead to a complete reformation of the topographic template. In particular, extension leading up to continental breakup between Australia and Antarctica led to the formation of a generally low-standing passive margin and did not cause significant uplift of magnitude similar to that of the high-standing breakup margin of Indo-Antarctica (e.g. Sirevaag et al., 2018). It is however possible that any post-Triassic tectonism in the interior of Australo-Antarctica may have influenced the landscape evolution at a local scale. Another particularly unconstrained aspect of the landscape evolution of Australo-Antarctica is the magnitude and timing of erosion of onshore sedimentary basins and the sediment transfer to the offshore passive margins after the breakup of Australia and Antarctica. Future studies aimed at reconstructing linkages between onshore erosion with offshore seismic data and marine sediment cores may help to provide a time-integrated estimate of sediment delivery to the continental shelf. In addition, low-temperature thermochronology dating of detrital grains in glacio-marine sediments offshore glacial outlets such as the Denman, Totten and Mertz glaciers may also help resolve the erosional history of their corresponding large catchment areas in interior Australo-Antarctica.

5.2 References

Aitken, A. R. A., Betts, P. G., Young, D. A., Blankenship, D. D., Roberts, J. L., & Siegert, M. J. (2016a). The Australo-Antarctic Columbia to Gondwana transition. *Gondwana Research, 29*(1), 136-152. doi:10.1016/j.gr.2014.10.019

Aitken, A. R. A., Roberts, J. L., van Ommen, T. D., Young, D. A., Golledge, N. R., Greenbaum, J. S., Blankenship, D. D., & Siegert, M. J. (2016b). Repeated large-scale retreat and advance of Totten Glacier indicated by inland bed erosion. *Nature, 533*(7603), 385-389. doi:10.1038/nature17447

Aitken, A. R. A., Young, D. A., Ferraccioli, F., Betts, P. G., Greenbaum, J. S., Richter, T. G., Roberts, J. L., Blankenship, D. D., & Siegert, M. J. (2014). The subglacial geology of Wilkes Land, East Antarctica. *Geophysical Research Letters, 41*(7), 2014GL059405. doi:10.1002/2014gl059405

Cianfarra, P., & Maggi, M. (2017). Cenozoic extension along the reactivated Aurora Fault System in the East Antarctic Craton. *Tectonophysics, 703-704*, 135-143. doi:https://doi.org/10.1016/j.tecto.2017.02.019

Dutch, R., Wise, T., Pawley, M., & Petts, A. (2018). Coompana Drilling and Geochemistry Workshop 2018 extended abstracts. *Department for Energy and Mining, Adelaide, South Australia, Report Book 2018/00019*.

Eagles, G. (2019). A little spin in the Indian Ocean plate circuit. *Tectonophysics, 754*, 80-100.

Ebbing, J., Haas, P., Ferraccioli, F., Pappa, F., Szwillus, W., & Bouman, J. (2018). Earth tectonics as seen by GOCE-Enhanced satellite gravity gradient imaging. *Scientific Reports, 8*(1), 1-9.

Fraser, G. L., & Neumann, N. L. (2016). Under the Nullarbor: New SHRIMP UPb zircon ages from the Coompana, Madura and Albany-Fraser Provinces, and Officer Basin, western South Australia and eastern Western Australia: July 2014–June 2015. Record 2016/16. Geoscience Australia, Canberra.

Goodge, J. W., Fanning, C. M., Fisher, C. M., & Vervoort, J. D. (2017). Proterozoic crustal evolution of central East Antarctica: Age and isotopic evidence from glacial igneous clasts, and links with Australia and Laurentia. *Precambrian Research, 299*, 151-176. doi:10.1016/j.precamres.2017.07.026

Goodge, J. W., & Fitzgerald, P. G. (2019). *Origin and exhumation history of central East Antarctic igneous crust obtained from glacial erratics and by subglacial access drilling.* Paper presented at the XII International Symposium on Antarctic Earth Science (ISAES 2015), Incheon, Korea.

Goodge, J. W., Myrow, P., Phillips, D., Fanning, C. M., & Williams, I. S. (2004) Siliciclastic record of rapid denudation in response to convergent-margin orogenesis, Ross Orogen, Antarctica. In*: Vol. 378* (pp. 105-126).

Goodge, J. W., Myrow, P., Williams, I. S., & Bowring, S. A. (2002). Age and provenance of the Beardmore Group, Antarctica: Constraints on Rodinia supercontinent breakup. *Journal of Geology, 110*(4), 393-406.

Goodge, J. W., Vervoort, J. D., Fanning, C. M., Brecke, D. M., Farmer, G. L., Williams, I. S., Myrow, P. M., & DePaolo, D. J. (2008). A positive test of East Antarctica-Laurentia juxtaposition within the Rodinia supercontinent. *Science, 321*(5886), 235-240.

Kirkland, C. L., Smithies, R. H., Spaggiari, C. V., Wingate, M. T. D., Quentin de Gromard, R., Clark, C., Gardiner, N. J., & Belousova, E. A. (2017). Proterozoic crustal evolution of the Eucla basement, Australia: Implications for destruction of oceanic crust during emergence of Nuna. *Lithos, 278-281*, 427-444. doi:10.1016/j.lithos.2017.01.029

Kolesik, P. (2016). U–Pb geochronology of volcano–sedimentary moraine sediments of the Bunger Hills: Implications for Mesoproterozoic evolution of East Antarctica. *University of Adelaide - Honours Degree in Geology - Thesis*.

Lewis, C. J., & Sircombe, K. N. (2013). Use of U-Pb geochronology to delineate provenance of North West Shelf sediments, Australia. *In The Sedimentary Basins of Western Australia IV: Proceedings of the Petroleum Exploration Society of Australia Symposium (pp. 1-27).*

Lindsay, J. F., & Leven, J. H. (1996). Evolution of a Neoproterozoic to Palaeozoic intracratonic setting, Officer Basin, South Australia. *Basin Research, 8*(4), 403-424. doi:doi:10.1046/j.1365-2117.1996.00223.x

Maritati, A., Aitken, A. R. A., Young, D. A., Roberts, J. L., Blankenship, D. D., & Siegert, M. J. (2016). The tectonic development and erosion of the Knox Subglacial Sedimentary Basin, East Antarctica. *Geophysical Research Letters, 43*(20), 10728-10737. doi:10.1002/2016gl071063

Mikhalsky, E. V., Tkacheva, D. A., Skublov, S. G., Leitchenkov, G. L., Rodionov, N. V., Kapitonov, I. N., & Kunakkuzin, E. L. (2020). Low-grade Sandow Group metasediments of the Denman Glacier area (East Antarctica): Chemical composition, age and provenance from U–Pb detrital zircon data, with some palaeotectonic implications. *Polar Science*, 100587. doi:https://doi.org/10.1016/j.polar.2020.100587

Morlighem, M., Rignot, E., Binder, T., Blankenship, D., Drews, R., Eagles, G., Eisen, O., Ferraccioli, F., Forsberg, R., Fretwell, P., Goel, V., Greenbaum, J. S., Gudmundsson, H., Guo, J., Helm, V., Hofstede, C., Howat, I., Humbert, A., Jokat, W., Karlsson, N. B., Lee, W. S., Matsuoka, K., Millan, R., Mouginot, J., Paden, J., Pattyn, F., Roberts, J., Rosier, S., Ruppel, A., Seroussi, H., Smith, E. C., Steinhage, D., Sun, B., Broeke, M. R. v. d., Ommen, T. D. v., Wessem, M. v., & Young, D. A. (2020). Deep glacial troughs and stabilizing ridges unveiled beneath the margins of the Antarctic ice sheet. *Nature Geoscience*. doi:10.1038/s41561-019-0510-8

Morón, S., Cawood, P. A., Haines, P. W., Gallagher, S. J., Zahirovic, S., Lewis, C. J., & Moresi, L. (2019). Long-lived transcontinental sediment transport pathways of East Gondwana. *Geology, 47*(6), 513-516. doi:10.1130/g45915.1

Mulder, J. A., Karlstrom, K. E., Halpin, J. A., Merdith, A. S., Spencer, C. J., Berry, R. F., & McDonald, B. (2018). Rodinian devil in disguise: Correlation of 1.25–1.10 Ga strata between Tasmania and Grand Canyon. *Geology, 46*(11), 991-994.

Naumenko-Dèzes, M. O., Rolland, Y., Lamarque, G., Duclaux, G., Gallet, S., Bascou, J., & Ménot, R. P. (2020). Petrochronology of the Terre Adélie Craton (East Antarctica) evidences a long-lasting Proterozoic (1.7–1.5 Ga) tectono-metamorphic evolution — Insights for the connections with the Gawler Craton and Laurentia. *Gondwana Research, 81*, 21-57. doi:10.1016/j.gr.2019.11.010

Oliver, R. L., & Fanning, C. M. (1997). Australia and Antarctica; precise correlation of Palaeoproterozoic terrains. In A. Ricci Carlo (Ed.), *The Antarctic region; geological evolution and processes; proceedings of the VII international symposium on Antarctic earth sciences.* (Vol. 7, pp. 163-172). Siena, Italy: Terra Antarctica Publication.

Paxman, G. J. G., Jamieson, S. S. R., Ferraccioli, F., Bentley, M. J., Ross, N., Armadillo, E., Gasson, E. G. W., Leitchenkov, G., & DeConto, R. M. (2018). Bedrock Erosion Surfaces Record Former East Antarctic Ice Sheet Extent. *Geophysical Research Letters, 45*(9), 4114-4123. doi:10.1029/2018gl077268

Paxman, G. J. G., Jamieson, S. S. R., Ferraccioli, F., Bentley, M. J., Ross, N., Watts, A. B., Leitchenkov, G., Armadillo, E., & Young, D. A. (2019). The Role of Lithospheric Flexure in the Landscape Evolution of the Wilkes Subglacial Basin and Transantarctic Mountains, East Antarctica. *Journal of Geophysical Research: Earth Surface, 124*(3), 812-829. doi:10.1029/2018jf004705

Peucat, J. J., Capdevila, R., Fanning, C. M., Ménot, R. P., Pécora, L., & Testut, L. (2002). 1.60 Ga felsic volcanic blocks in the moraines of the Terre Adélie Craton, Antarctica: Comparisons with the Gawler Range Volcanics, South Australia. *Australian Journal of Earth Sciences, 49*(5), 831-845. doi:10.1046/j.1440-0952.2002.00956.x

Peucat, J. J., Menot, R. P., Monnier, O., & Fanning, C. M. (1999). The Terre Adelie basement in the East-Antarctica Shield: Geological and isotopic evidence for a major 1.7 Ga thermal event; comparison with the Gawler Craton in South Australia. *Precambrian Research, 94*(3-4), 205-224.

Pierce, E. L., Hemming, S. R., Williams, T., van de Flierdt, T., Thomson, S. N., Reiners, P. W., Gehrels, G. E., Brachfeld, S. A., & Goldstein, S. L. (2014). A comparison of detrital U–Pb zircon, 40Ar/39Ar hornblende, 40Ar/39Ar biotite ages in marine sediments off East Antarctica: Implications for the geology of subglacial terrains and provenance studies. *Earth-Science Reviews, 138*, 156-178. doi:http://dx.doi.org/10.1016/j.earscirev.2014.08.010

Reid, A. J., Pawley, M. J., Wade, C., Jagodzinski, E. A., Dutch, R. A., & Armstrong, R. (2019). Resolving tectonic settings of ancient magmatic suites using structural, geochemical and isotopic constraints: the example of the St Peter Suite, southern Australia. *Australian Journal of Earth Sciences, 67*(1), 31-58. doi:10.1080/08120099.2019.1632224

Sauermilch, I., Whittaker, J. M., Bijl, P. K., Totterdell, J. M., & Jokat, W. (2019). Tectonic, Oceanographic, and Climatic Controls on the Cretaceous-Cenozoic Sedimentary Record of the Australian-Antarctic Basin. *Journal of Geophysical Research: Solid Earth, 0*(0). doi:10.1029/2018JB016683

Sirevaag, H., Ksienzyk, A., Jacobs, J., Dunkl, I., & Läufer, A. (2018). Tectono-Thermal Evolution and Morphodynamics of the Central Dronning Maud Land Mountains, East Antarctica, Based on New Thermochronological Data. *Geosciences, 8*(11). doi:10.3390/geosciences8110390

Smits, R. G., Collins, W. J., Hand, M., Dutch, R., & Payne, J. (2014). A Proterozoic Wilson cycle identified by Hf isotopes in central Australia: Implications for the assembly of Proterozoic Australia and Rodinia. *Geology, 42*(3), 231-234. doi:10.1130/G35112.1

Spaggiari, C., Smithies, R., Kirkland, C., Wingate, M., England, R., & Lu, Y. (2020). Stratigraphic and co-funded drilling of the Eucla basement — the Proterozoic geology beneath the Nullarbor Plain. *Geological Survey of Western Australia, Report 204, 147 p*.

Spaggiari, C. V., Smithies, R. H., Kirkland, C. L., Wingate, M. T. D., England, R. N., & Lu, Y.-J. (2018). Buried but preserved: The Proterozoic Arubiddy Ophiolite, Madura Province, Western Australia. *Precambrian Research, 317*, 137-158. doi:10.1016/j.precamres.2018.08.025

Stål, T., Reading, A. M., Halpin, J. A., & Whittaker, J. M. (2019). A multivariate approach for mapping lithospheric domain boundaries in East Antarctica. *Geophysical Research Letters, 46*(17-18), 10404-10416.

Veevers, J. J. (2018). Gamburtsev Subglacial Mountains: Age and composition from morainal clasts and U–Pb and Hf-isotopic analysis of detrital zircons in the Lambert Rift, and potential provenance of East Gondwanaland sediments. *Earth-Science Reviews, 180*, 206-257. doi:10.1016/j.earscirev.2018.03.002

Veevers, J. J., Belousova, E. A., Saeed, A., Sircombe, K., Cooper, A. F., & Read, S. E. (2006). Pan-Gondwanaland detrital zircons from Australia analysed for Hf-isotopes and trace elements reflect an ice-covered Antarctic provenance of 700–500 Ma age, TDM of 2.0–1.0 Ga, and alkaline affinity. *Earth-Science Reviews, 76*(3-4), 135-174. doi:10.1016/j.earscirev.2005.11.001

Whitmeyer, S. J., & Karlstrom, K. E. (2007). Tectonic model for the Proterozoic growth of North America. *Geosphere, 3*(4), 220-259.

Wise, T., Dutch, R., Pawley, M., Foss, C., & Thiel, S. (2018). Building the Coompana Province. *MESA Journal, 88*, 25-37.

Young, D. A., Wright, A. P., Roberts, J. L., Warner, R. C., Young, N. W., Greenbaum, J. S., Schroeder, D. M., Holt, J. W., Sugden, D. E., Blankenship, D. D., van Ommen, T. D., & Siegert, M. J. (2011). A dynamic early East Antarctic Ice Sheet suggested by ice-covered fjord landscapes. *Nature, 474*(7349), 72-75.

Conclusion

Australo-Antarctica is one of the few continental regions on Earth involved in all known supercontinent configurations. Its subglacial bedrock should therefore preserve an abundant record of plate tectonic processes related to supercontinent assembly and breakup; however, a clear understanding of the continental evolution of Australo-Antarctica throughout supercontinent cycles has been largely missing due to its poorly characterised subglacial geology and tectonic architecture. The work conducted as part of this thesis investigated notable gaps in the geological knowledge of Australo-Antarctica and helps constrain its continental evolution within the most recent models of supercontinent assembly and breakup.

The formation of a coherent Australo-Antarctica is regarded to have occurred in the Mesoproterozoic during plate-scale reorganisations spanning the breakup of Nuna and assembly of Rodina. Paleogeographic models suggest that the assembly of Australo-Antarctica and conjoined parts of southern Australian occurred via westward motion of the Mawson Craton relative to West and North Australian cratons, possibly triggered by rifting between the Mawson Craton and Laurentia during Nuna breakup. The revised basement architecture of interior Wilkes Land supports recent consensus models invoking convergence between the continental blocks via the accretion of a series westerly younging sequence of c. 1600–1300 Ma arc-related magmatic supersuites now preserved in the Madura and Coompana provinces of southern Australia and interpreted Antarctic counterparts (i.e. Nuyina and Banzare provinces).

The tectonic evolution of Australo-Antarctica from Rodinia to Gondwana is largely unrepresented in the exposed geological record. The breakup of Rodinia during the Neoproterozoic resulted in the formation of a rifted margin between Australo-Antarctica and Laurentia. Rifting along the eastern sector of Australo-Antarctica led to passive-margin extension and sedimentation of the siliciclastic Beardmore Group in Late Neoproterozoic (c. 670–580 Ma). The age and provenance of Neoproterozoic glacial sedimentary erratics from the Sabrina Basin of interior Australo-Antarctica support stratigraphic and tectonic links of this basin with Late Neoproterozoic siliciclastic units in the Beardmore Group. Sedimentary rocks of the Sabrina Basin and Beardmore Group may represent the remnants

of a larger Late Neoproterozoic platform basin extending from the interior to the proto-pacific passive margin of Rodinia similar in scale to the large intraplate systems of central Australia.

The incorporation of Australo-Antarctica into Gondwana via Ediacaran–Early Cambrian orogenic systems was followed by significant intraplate extension during the Late Paleozoic–Triassic triggered by intensified geodynamic activity at the periphery of Gondwana. These events caused the exhumation of large sections of Precambrian basement and the formation of sedimentary basins across the hinterland of East Antarctica and Gondwana more broadly. In Australo-Antarctica, these include the Knox Rift in the Bunger Hills region, the Aurora and Vincennes basins in interior Wilkes Land and the Wilkes Basin in George V Land. Kilometre scale basement exhumation and erosion across the East Antarctic interior generated a large volume of sediments that were dispersed to a large network of Antarctic and Australian sedimentary basins via transcontinental fluvial systems.

Late Paleozoic–Triassic intraplate extension was the last widespread tectonic event to have a significant impact on the continental evolution of Australo-Antarctica. Unlike other sectors of East Antarctica, Mesozoic–Cenozoic extensional tectonism related to the breakup of Gondwana did not lead to significant uplift and erosion along the rifting margin of Australo-Antarctica. The breakup of Gondwana also marked the end of trans-Gondwanan fluvial systems and the accumulation of thick Late Cretaceous–Cenozoic passive margin deposits offshore Australo-Antarctica. The topographic template established during Late Paleozoic–Triassic extension had a key role in influencing the landscape evolution of Australo-Antarctica after the Mesozoic breakup and the transfer of sediments from onshore region to the passive margin basins, largely through the selective preservation of highlands, and focusing of enhanced fluvial and glacial erosion in low-lying areas.

Appendix

This appendix contains supplementary information for the three research chapters. Large data tables are available for download at https://cloudstor.aarnet.edu.au/plus/s/pXw3oX71ioRBpix. Supplementary material for Chapters 2 and 3 is also available for download with the online version of the respective publications. The online version of Chapter 2 and 3 is also included at the end of this appendix.

Supplementary material for Chapter 2 – Fingerprinting Proterozoic Bedrock in Interior Wilkes Land, East Antarctica

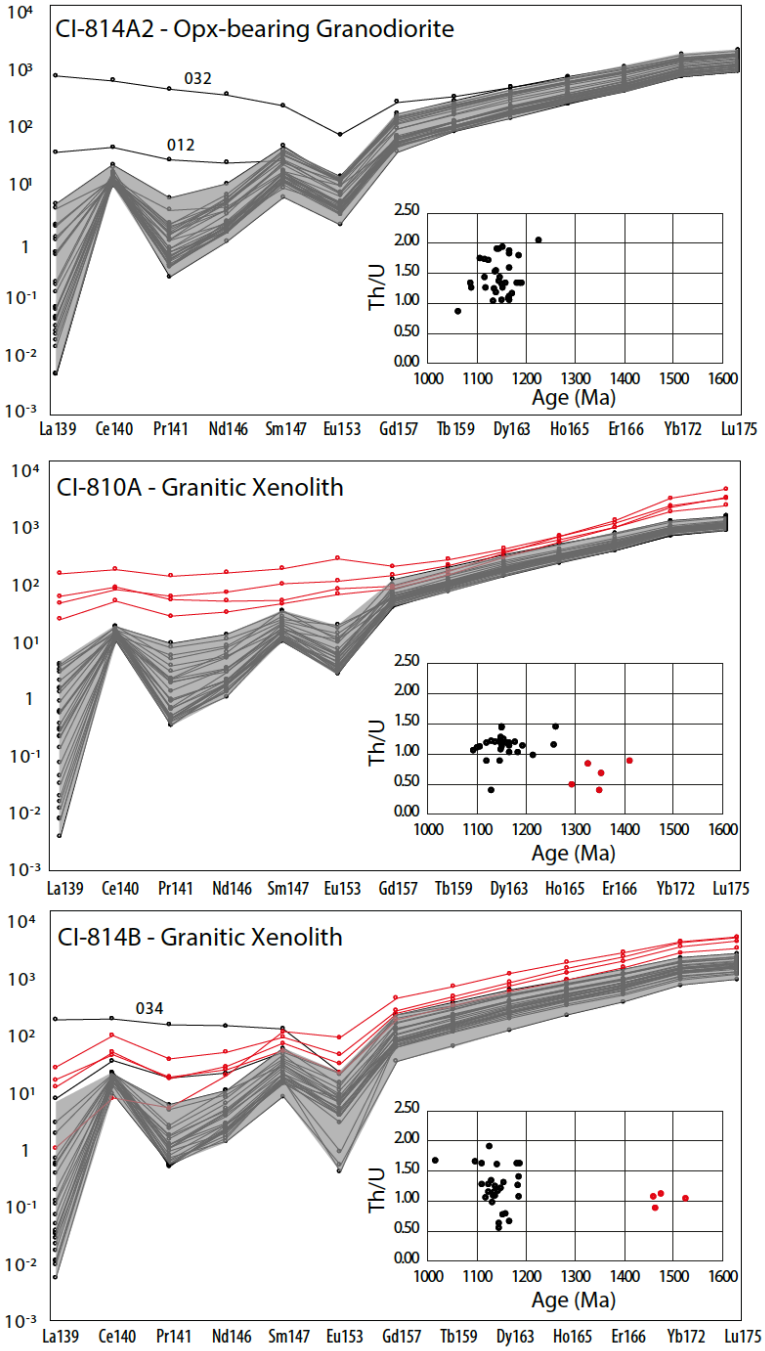

Supplementary Figure S1. Chondrite-normalized rare earth element (REE) spider diagrams of zircon from Chick Island samples. In each sample, grey field denotes the overall variation in the primary c.1150 Ma zircon population. REE pattern of inherited zircon is shown in red. Analysis spots 012 and 032 (sample CI-814A2) and 034 (sample CI-814B) exhibit a slight enrichment in LREE, due to ablation of an apatite inclusion during analysis. Normalizing values are from Sun and McDonough (1989). Inset in each diagram shows Th/U ratio of primary (black dots) and inherited (red dots) zircon.

Sun, S. S., McDonough, W. F, 1989. Chemical and isotopic systematics of oceanic basalts: implications for mantle compositions and processes: In: Saunders, A. D., Norry, M. J. (Eds), Magmatism in the Ocean Basins. *Geological Society, London, Special Publication* **42**, pp. 313-345.

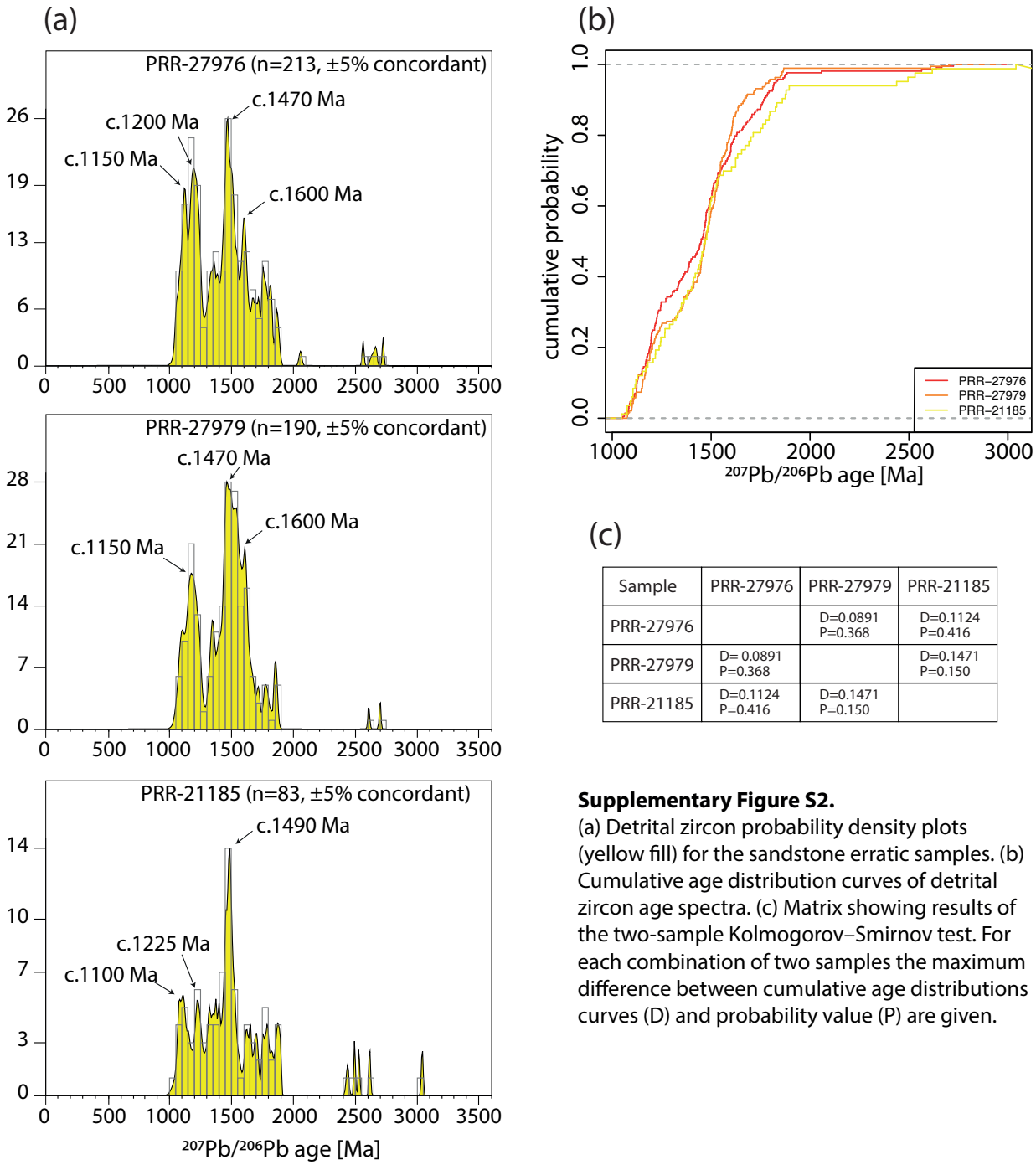

(c)

Sample	PRR-27976	PRR-27979	PRR-21185
PRR-27976		D=0.0891 P=0.368	D=0.1124 P=0.416
PRR-27979	D= 0.0891 P=0.368		D=0.1471 P=0.150
PRR-21185	D=0.1124 P=0.416	D=0.1471 P=0.150	

Supplementary Figure S2.
(a) Detrital zircon probability density plots (yellow fill) for the sandstone erratic samples. (b) Cumulative age distribution curves of detrital zircon age spectra. (c) Matrix showing results of the two-sample Kolmogorov–Smirnov test. For each combination of two samples the maximum difference between cumulative age distributions curves (D) and probability value (P) are given.

The following supplementary material is available for download at

https://cloudstor.aarnet.edu.au/plus/s/44MCQZ3itGIcEbX

Supplementary Table S1 – Summary of samples location in separate Excel (.xlsx) file.

Supplementary Table S2 – U–Pb zircon geochronology

Supplementary Table S3 – Zircon Hf isotopic data

Supplementary Table S4 – Compilation of zircon U–Pb–Hf isotopic data

Supplementary Table S5 – *In situ* U-Pb monazite geochronology

Sample code	Location	Rock type	Lat	Long	Elevation (m)	Elevation source	U-Pb zircon age	Reference
86285815	Booth Peninsula	Quartz monzonite	-66.11	101.19	75.0	Sheraton et al. (1995)	1150 Ma crystallization	Sheraton et al. (1995)
86286231	Grace Rocks	Quartz monzonite	-66.42	100.55	126.0	Sheraton et al. (1995)	1170 Ma crystallization	Sheraton et al. (1995)
86285807	Obruchev Hills	Tonalitic gneiss	-66.55	99.96	229.0	Sheraton et al. (1995)	2690 Ma emplacement; 1140 Ma metamorphism	Daczko et al. (2018); Sheraton et al. (1995)
86285801	Obruchev Hills	Felsic orthogneiss	-66.54	99.87	229.0	Sheraton et al. (1995)	1900 Ma emplacement; 1180 Ma metamorphism	Sheraton et al. (1995)
86286119	Chugunov Island	Granite	-65.92	99.50	45.0	SCAR Gazetteer	*515 Ma crystallization*	*Halpin et al, unpub.*
86286118	Chugunov Island	Granodiorite	-65.92	99.50	45.0	SCAR Gazetteer	*2900 Ma crystallization; 550 Ma metamorphism*	*Halpin et al, unpub.*
DE-566 BR	Cape Jones	Felsic orthogneiss	-66.66	99.39	56.5	GPS	*n.d.*	*n.d.*
86286001	Mount Strathcona	Felsic gneiss	-67.42	99.19	1380.0	Sheraton et al. (1995)	1800 Ma crystallization; 1160 Ma metamorphism	Daczko et al. (2018); Sheraton et al. (1995)
SC-581D BR	Mount Strathcona	Gabbro	-67.42	99.16	1205.8	GPS	*1190 Ma crystallization*	*Halpin et al, unpub.*
86286006	Cape Harrison	Granitic gneiss	-66.70	99.09	118.0	Sheraton et al. (1995)	1190 Ma crystallization; 530 Ma metamorphism	Daczko et al. (2018); Sheraton et al. (1995)
86286024	Watson Bluff	Syenite	-66.42	98.95	227.0	Sheraton et al. (1995)	515 Ma crystallization	Sheraton et al. (1995)
86286100	Possession Rocks	Granitic gneiss	-66.74	98.92	118.0	Sheraton et al. (1995)	*1170 Ma crystallization; 530 Ma metamorphism*	*Halpin et al, unpub.*
H277278	Hippo Rocks	Diorite	-66.42	98.18	9.1	GPS	*530 Ma crystallization*	*Halpin et al, unpub.*
G151152	Gillies Island	Microgabbro	-66.52	96.36	82.6	GPS	*530 Ma crystallization*	*Halpin et al, unpub.*

Table S1. Summary of sample codes, locations, lithology, and U–Pb crystallization/metamorphic age

		ZHe			*AHe*			*Thermal paths*	
Sample	**Locality**	**Model**	**Measured**	**GOF**	**Model**	**Measured**	**GOF**	**Good**	**Acceptable**
Model 1 – Late Paleozoic–Triassic extension									
DE-566 BR	Cape Jones	457.7	*458.0 ± 24.8*	0.99	177.5	*175.7 ± 20.2*	0.97	709	2121
86286119	Chugunov Island	340.6	*334.1 ± 17.6*	0.71	262.0	*261.9 ± 20.0*	1.00	41	274
G151152	Gillies Island	477.0	*475.9 ± 25.3*	0.97	300.2	*301.0 ± 47.6*	0.99	254	719
86286231	Grace Rocks	536.7	*544.4 ± 29.6*	0.80	192.2	*193.7 ± 21.0*	0.97	208	920
SC-581D BR	Mount Strathcona	534.6	*541.5 ± 29.1*	0.81	282.6	*282.5 ± 17.4*	1.00	74	349
86286006	Cape Harrison	429.3	*429.1 ± 23.9*	0.99	223.9	*224.2 ± 15.4*	0.98	366	1265
86286100	Possession Rocks	454.5	*456.2 ± 24.7*	0.95	167.9	*167.4 ± 11.5*	1.00	609	1772
Model 2 – Late Jurassic–Cretaceous extension									
DE-566 BR	Cape Jones	458.3	*458.0 ± 24.8*	0.99	176.5	*175.7 ± 20.2*	0.97	222	1416
86286119	Chugunov Island	332.8	*334.1 ± 17.6*	0.97	262.5	*261.9 ± 20.0*	0.97	21	76
G151152	Gillies Island	478.1	*475.9 ± 25.3*	0.93	297.7	*301.0 ± 47.6*	0.95	158	333
86286231	Grace Rocks	539.0	*544.4 ± 29.6*	0.85	192.0	*193.7 ± 21.0*	0.94	36	363
SC-581D BR	Mount Strathcona	538.3	*541.5 ± 29.1*	0.92	282.6	*282.5 ± 17.4*	0.99	41	237
86286006	Cape Harrison	426.4	*429.1 ± 23.9*	0.98	223.9	*224.2 ± 15.4*	0.91	94	374
86286100	Possession Rocks	457.9	*456.2 ± 24.7*	0.94	168.0	*167.4 ± 11.5*	0.99	170	1023
Model 3 – Two-stage extension									
DE-566 BR	Cape Jones	459.8	*458.0 ± 24.8*	0.94	176.4	*175.7 ± 20.2*	0.97	283	1156
86286119	Chugunov Island	332.8	*334.1 ± 17.6*	0.94	274.3	*261.9 ± 20.0*	0.54	1	32
G151152	Gillies Island	477.7	*475.9 ± 25.3*	0.94	316.7	*301.0 ± 47.6*	0.74	2	31
86286231	Grace Rocks	537.1	*544.4 ± 29.6*	0.8	199.4	*193.7 ± 21.0*	0.79	52	328
SC-581D BR	Mount Strathcona	517.3	*541.5 ± 29.1*	0.41	284.1	*282.5 ± 17.4*	0.93	7	41
86286006	Cape Harrison	423.9	*429.1 ± 23.9*	0.83	224.0	*224.2 ± 15.4*	0.99	64	406
86286100	Possession Rocks	458.4	*456.2 ± 24.7*	0.93	167.8	*167.4 ± 11.5*	0.99	285	1032

Table S3. Summary of time-temperature simulation results for the three modelling scenarios. GOF; goodness-of-fit value.

The following supplementary material is available for download at https://cloudstor.aarnet.edu.au/plus/s/zUrMbXkOkbDjbxS

Supplementary Table S2 – Zircon and apatite (U–Th)/He data

Supplementary material for Chapter 4 – Provenance of Late Jurassic–Early Cretaceous strata in the Mentelle Basin, southwestern Australia, reveals a trans-Gondwanan fluvial pathway

The following supplementary material is available for download at

https://cloudstor.aarnet.edu.au/plus/s/elkKjxETDonKfNq

Supplementary Table S1 – U–Pb monazite geochronology of Site U1515 samples.

Supplementary Table S2 – U–Pb zircon geochronology of Site U1515 samples.

Supplementary Table S3 – Zircon Hf isotopic data of Site U1515 samples.

SCIENTIFIC REPORTS

OPEN

Fingerprinting Proterozoic Bedrock in Interior Wilkes Land, East Antarctica

Received: 5 March 2019
Accepted: 2 July 2019
Published online: 15 July 2019

Alessandro Maritati[1], Jacqueline A. Halpin[1], Joanne M. Whittaker[1] & Nathan R. Daczko[2]

Wilkes Land in East Antarctica remains one of the last geological exploration frontiers on Earth. Hidden beneath kilometres of ice, its bedrock preserves a poorly-understood tectonic history that mirrors that of southern Australia and holds critical insights into past supercontinent cycles. Here, we use new and recently published Australian and Antarctic geological and geophysical data to present a novel interpretation of the age and character of crystalline basement and sedimentary cover of interior Wilkes Land. We combine new zircon U–Pb and Hf isotopic data from remote Antarctic outcrops with aeromagnetic data observations from the conjugate Australian-Antarctic margins to identify two new Antarctic Mesoproterozoic basement provinces corresponding to the continuation of the Coompana and Madura provinces of southern Australia into Wilkes Land. Using both detrital zircon U–Pb–Hf and authigenic monazite U–Th–Pb isotopic data from glacial erratic sandstone samples, we identify the presence of Neoproterozoic sedimentary rocks covering Mesoproterozoic basement. Together, these new geological insights into the ice-covered bedrock of Wilkes Land substantially improve correlations of Antarctic and Australian geological elements and provide key constraints on the tectonic architecture of this sector of the East Antarctic Shield and its role in supercontinent reconstructions.

Exploring Subglacial Geology in Interior Wilkes Land

The interior of Wilkes Land remains one of the most remote and unexplored sectors of the Precambrian East Antarctic Shield. Revealing ice-covered geology in this region is critical to understanding the assembly and breakup of the Nuna/Columbia, Rodinia and Gondwana supercontinents of which Wilkes Land was a centrepiece[1,2]. The bedrock also exerts important controls on the evolution of the Antarctic ice sheet[3], underlying some of East Antarctica's largest and most vulnerable glacial drainage basins (i.e. Vanderford, Totten, Moscow University Ice Shelf–MUIS) which together have the potential to contribute up to 3 m of global sea level rise in a warming climate[4]. However, due to thick ice cover and very limited rock exposure/sampling, our understanding of the age and composition of the Wilkes Land interior is inferred from the largely unconstrained projection of Australian geological counterparts into Antarctica[1] and ages of detrital grains from glacio-marine sediments offshore of East Antarctica[5,6].

Recent tectonic reconstructions of Gondwana that reconcile geological and geophysical signatures from the conjugate Australian and Antarctic plates revealed the presence of three large-scale Proterozoic basement provinces in Wilkes Land that accreted during supercontinent assembly[7]. The Wilkes province (Fig. 1a) occupies the region west of the Totten Glacier, including the well-studied outcrops of the Windmill Islands to the west of Law Dome[8,9]. This province has relatively robust links with two main peaks of magmatism and metamorphism (c. 1330–1260 Ma and c. 1220–1140 Ma) also documented in the Nornalup Zone of the Albany Fraser Orogen of southwestern Australia[10]. The Mawson Craton (East Mawson Craton of Aitken *et al.*[11]) comprises the Archean to Paleoproterozoic rocks in Terre Adélie and George V Lands and has geological affinities with the Gawler Craton of South Australia[2] (Fig. 1a).

The intervening region (West Mawson Craton of Aitken *et al.*[11]), underlying most of the combined Vanderford-Totten-MUIS continental ice sheet, is only characterised by sparse legacy geological data[12,13] and remains vastly underexplored. This region is interpreted to be the Antarctic extension of the unexposed

[1]Institute for Marine and Antarctic Studies, University of Tasmania, Private Bag 129, Hobart, TAS, 7001, Australia. [2]ARC Centre of Excellence for Core to Crust Fluid Systems and GEMOC, Department of Earth and Planetary Sciences, Macquarie University, Sydney, NSW, 2109, Australia. Correspondence and requests for materials should be addressed to A.M. (email: alessandro.maritati@utas.edu.au)

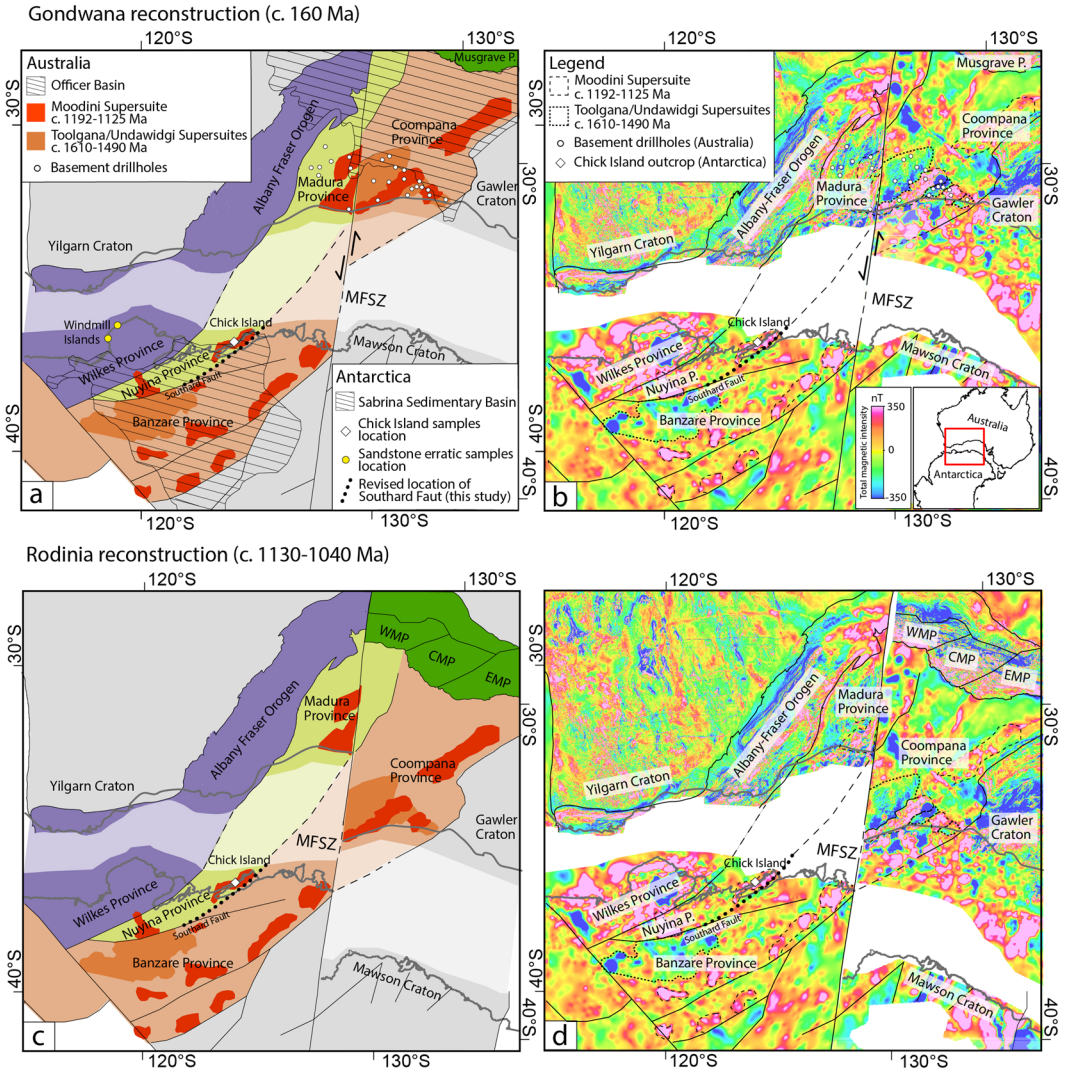

Figure 1. (Top) Reconstruction of (**a**) conjugate Proterozoic tectonic provinces and (**b**) total magnetic intensity (TMI) anomaly data of southwestern Australia and Wilkes Land in the Gondwana full-fit model of Aitken *et al.*[11] with Australia fixed in its present-day reference frame. (Bottom) Reconstruction of (**c**) conjugate Proterozoic tectonic provinces and (**d**) total magnetic intensity (TMI) anomaly data of southwestern Australia and Wilkes Land in the late Mesoproterozoic reconstruction of the Rodinia configuration (c. 1130–1040 Ma) of Aitken *et al.*[7] following retro-deformation of approximately 330 km of sinistral offset on the Mundrabilla-Frost Shear Zone. Australian tectonic elements are simplified from Raymond *et al.*[61]; interpretation of tectonic elements, geophysical lineaments and intrusive suites in Wilkes Land is from Aitken *et al.*[11]; simplified outline of the Sabrina Sedimentary Basin is adapted from Aitken *et al.*[3]; half arrows next to the Mundrabilla-Frost Shear Zone indicate sinistral displacement. Abbreviations are: CMP–central Musgrave Province; EMP–eastern Musgrave Province; MFSZ–Mundrabilla-Frost Shear Zone; WMP–West Musgrave Province.

Coompana and/or Madura provinces of southern Australia[7] (Fig. 1a). Recent isotopic and geochemical data from drillhole samples in these Australian provinces fingerprint a distinctively juvenile isotopic character, similar to the central Australian Musgrave Province, that has been interpreted to represent c. 1950 Ma oceanic crust reworked by a series of accretionary tectonic events throughout the Mesoproterozoic, involving significant mantle input[14–16]. The Coompana Province is characterised by two dominant magmatic supersuites – the c. 1610 Ma Toolgana Supersuite with chemical and isotopic characteristics of primitive arc, and the rift-related c. 1490 Ma Undawidgi Supersuite[14,17,18], while the Madura Province comprises a series of oceanic crustal assemblages that define oceanic subduction-related events between 1475 and 1389 Ma[19,20]. Both the Coompana and Madura provinces are extensively intruded by granitic rocks of the c. 1192–1125 Ma Moodini Supersuite[17–19]. The Coompana and Madura provinces are separated by the transcontinental Mundrabilla-Frost Shear Zone which experienced approximately 330 km sinistral offset during the last phases of Rodinia assembly (1130–1040 Ma)[7,20] and extends into East Antarctica (Fig. 1a,c). While strike-slip movement resulted in the truncation of structural trends and the displacement of the original boundary between the two provinces in Australia, this shear zone cuts east of the conjugate crust of East Antarctica into the Mawson Craton (Fig. 1).

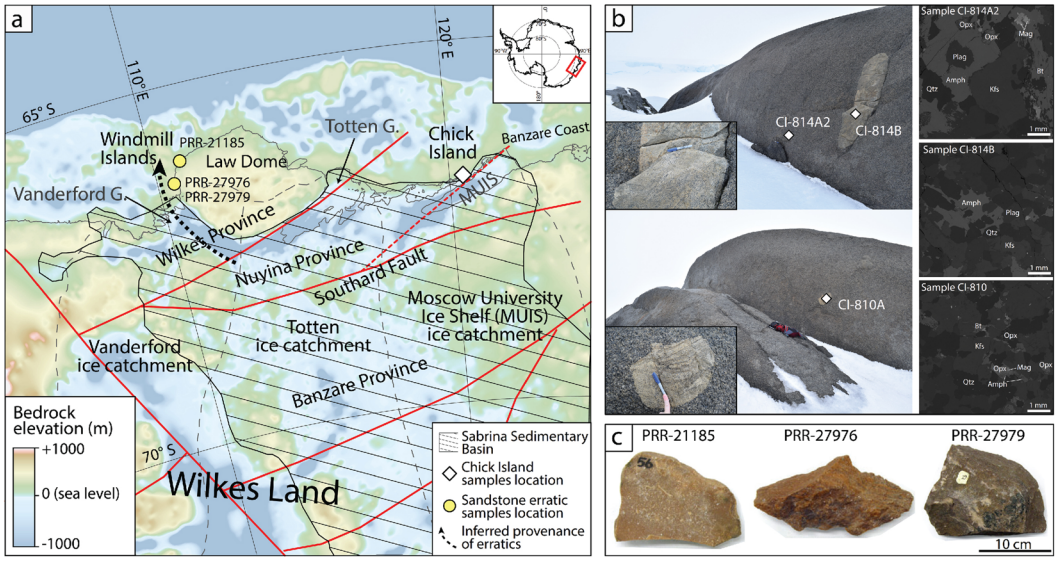

Figure 2. (**a**) Subglacial bedrock elevation map showing location of samples of this study, ice catchment basins[31] (dashed black lines) and major structural lines[7] (solid red lines); revised path of the Southard Fault is also shown as dotted red segment; (**b**) (left) Location of sampling sites at Chick Island and (right) annotated detail of backscatter electron (BSE) image of each sample; (**c**) glacial sandstone erratic samples used in this study. Abbreviations are: Amph–Amphibole; Bt–Biotite; Kfs–K-feldspar; Mag–Magnetite; Opx–Orthopyroxene; Plag–Plagioclase; Qtz–Quartz.

2D gravity modelling and depth to magnetic basement estimates also reveal that large areas of the interior Wilkes Land are blanketed by the ≥1 km-thick Sabrina Sedimentary Basin, covering an area of approximately 500,000 km^2[,3] (Fig. 1a). In Australia, parts of the Coompana and Madura provinces are covered by extensive sedimentary basins, including the Neoproterozoic to Devonian Officer Basin (part of Centralian Superbasin)[21] and the Mesozoic Bight and Cenozoic Eucla basins[22,23]. Aitken *et al.*[11] correlated the Sabrina Sedimentary Basin and the Bight/Eucla basins based on the pre-Gondwanan breakup proximity. The Sabrina Sedimentary Basin is not exposed, although, the presence of rare glaciogenic sedimentary material along the Wilkes Land coast[24–26] provides a unique opportunity to study this basin.

In this paper, we analyse geological samples from crystalline basement and sedimentary cover in order to characterise part of the subglacial bedrock of interior Wilkes Land between the Wilkes Province and Mawson Craton. We combine new U–Pb–Hf isotopic data of coastal basement outcrops in Antarctica with the aeromagnetic signature of conjugate Australian-Antarctic basement domains to identify two new Mesoproterozoic basement provinces of Coompana and Madura affinity in Wilkes Land and resolve their geometry in their Rodinian and Gondwanan configurations. We then use detrital zircon U–Pb–Hf and authigenic monazite U–Th–Pb isotopic data from rare sandstone erratic samples to suggest the presence of Neoproterozoic sedimentary rocks in the Sabrina Sedimentary Basin and correlate this basin with the eastern Neoproterozoic Officer Basin. Our new interpretations of subglacial bedrock strengthen correlations between Antarctic and Australian geological counterparts and provide key constraints for global supercontinent reconstructions.

U–Pb–Hf Geochronology of Chick Island

We analysed zircon from three igneous bedrock samples from the remote Chick Island outcrop east of the Totten Glacier and along the Banzare Coast (Fig. 2a), including one sample of the main pluton and two petrologically-similar xenolith samples (Fig. 2b), to provide constraints on the age and composition of Precambrian basement in this poorly exposed region.

Sample CI-814A2, the main rock type exposed at Chick Island, is a coarse-grained orthopyroxene-bearing granodiorite (based on Quartz-Alkali Feldspar-Plagioclase (QAP) modal classification of Streckeisen[27]) and contains quartz (~33%), K-feldspar (~19%), plagioclase (~43%) as well as biotite, orthopyroxene, amphibole, ilmenite and magnetite (~5%), with accessory apatite and zircon (Fig. 2b). Zircon grains extracted from this sample are 100–250 μm long and equant to elongate, with aspect ratios from 1:1–4:1 (Fig. 3a). Under cathodoluminescence (CL), zircon grains are medium to brightly luminescent, commonly displaying oscillatory (e.g. spot 008, 017) and/or sector (e.g. spot 021) zoning (Fig. 3a). Thirty-six U–Pb analyses were collected from 31 grains across the spectrum of internal domains observed under CL. However, regardless of zonation, concordant analyses yield a $^{207}Pb/^{206}Pb$ weighted average age of 1148 ± 11 Ma (n = 34, mean square of weighted deviates [MSWD] = 1.34), interpreted to represent the crystallisation age of this sample (Fig. 3a). These zircon grains possess a steep HREE pattern, positive Ce and negative Eu anomalies and a Th/U ratio (0.86–2.03) consistent with magmatic zircon (see Supplementary Fig. S1). Twenty-four Hf isotope analyses of concordant primary igneous zircon grains yield initial $^{176}Hf/^{177}Hf$ (Hf_i) ratios in the range 0.28206–0.28216 (Fig. 4) and initial epsilon Hf (εHf_i) values between −0.53 and +4.87. A single outlier (spot 019) yielding Hf_i ratio of 0.28101 and εHf_i of −36.74 was excluded from the interpretation.

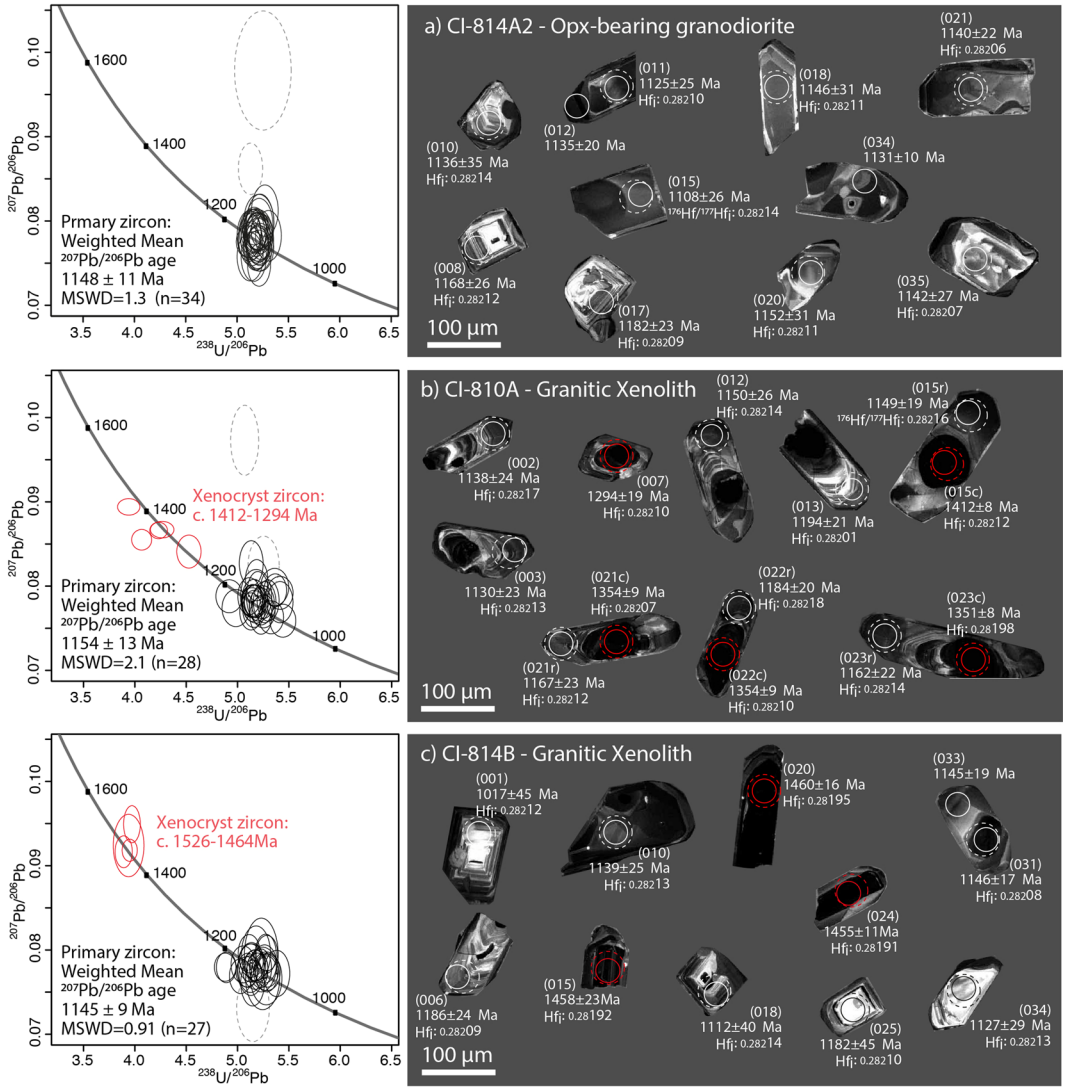

Figure 3. (left) U–Pb Tera-Wasserburg plots and (right) representative zircon CL images from each Chick Island sample. On Tera–Wasserburg plots, dashed grey ellipses denote analyses that have been excluded from age calculations on the basis of discordance (>10%). On CL images, U–Pb and Lu–Hf analysis locations are displayed as solid and dashed circles, respectively. Corresponding spot number (in brackets), apparent $^{207}Pb/^{206}Pb$ ages and initial $^{177}Hf/^{176}Hf$ ratio (Hf_i) and are also given for each analysis. Solid red ellipses on Tera–Wasserburg plots and red circles on CL images correspond to xenocryst zircon analyses.

Two xenoliths hosted in the granodiorite bedrock (samples CI-810A and CI-814B) have a granitic composition and contain igneous microstructures characterised by a lack of recrystallisation and the presence of interstitial igneous green amphibole. Samples contain quartz (~38%), K-feldspar (~24%), plagioclase (~33%) as well as amphibole and orthopyroxene (~5%) and accessory apatite and zircon (Fig. 2b). The apparent foliation observed at the outcrop scale is due to magmatic compositional banding into K-feldspar-rich versus plagioclase-rich domains that may reflect accumulation or magmatic flow processes.

Zircon grains in sample CI-810A are 100–200 µm long and have aspect ratios that vary from 1:2–1:4. Under CL (Fig. 3b), the majority of zircon grains contain dark resorbed cores with low-CL response (e.g. spots 023c, 021c) that are overgrown by moderate CL oscillatory zoned rims (e.g. spots 002, 021r) or more diffusely zoned rims (e.g. 015r). Thirty-five U–Pb analyses were collected from twenty-one zircon grains, including seven grains where both cores and rims were analysed. Rim domains represent the main concordant zircon population, which yields a $^{207}Pb/^{206}Pb$ weighted average age of 1154 ± 13 Ma (n = 28, MSWD = 2.1; Fig. 3b), within error of the interpreted age of crystallisation of the host granodiorite (sample CI-814A2). This c. 1154 Ma population possesses high (0.38–1.45) Th/U ratios, steep HREE patterns, positive Ce and negative Eu anomalies (Supplementary Fig. S1), consistent with those of primary igneous zircon in sample CI-814A2. Accordingly, we interpret this c. 1154 Ma population in the xenoliths to date cognate inclusions. Hf isotopic analyses of eighteen concordant zircon grains from the c. 1154 Ma zircon population yield Hf_i ratios in the range 0.28200–0.28222 (Fig. 4) and εHf_i values from −1.47 to +5.45. Five older analyses corresponding to dark CL cores reveal high concentrations of

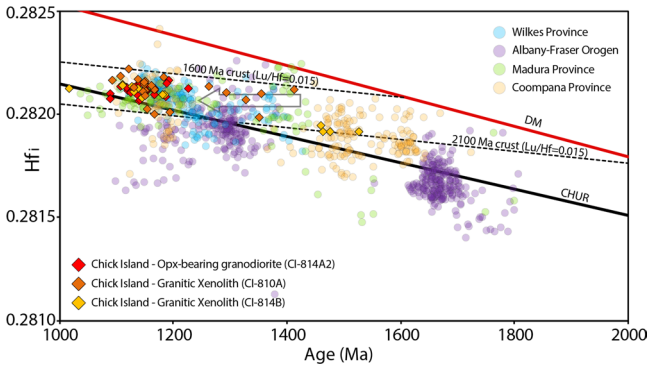

Figure 4. Initial $^{177}Hf/^{176}Hf$ ratios (Hf_i) for concordant zircon from Chick Island samples. The ratios are plotted against the apparent $^{207}Pb/^{206}Pb$ age for each analysis. Hf_i of Chick Island zircon is compared to U–Pb–Hf data of igneous zircon from: Albany-Fraser Orogen (GSWA as compiled by Smits *et al.*[62]), Windmill Islands[8,9], Coompana and Madura provinces[14]. Grey arrow indicates possible Pb-loss trajectory in xenocryst zircon from sample CI-814A. Zircons plotting below the CHUR (chondritic uniform reservoir) reference line reflect an increasingly crustal melt source, whereas those plotting at progressively more positive Hf_i values above CHUR reflect an increasing contribution from the depleted mantle (DM) to magmas from which the zircon formed. Crustal growth curves using a bulk crust value of $^{176}Lu/^{177}Hf = 0.015$[63] are drawn through the most evolved (c. 2100 Ma) and least evolved (c. 1600 Ma) Chick Island zircon.

U (419–3565 ppm) with individual apparent $^{207}Pb/^{206}Pb$ ages spread along Concordia bet]ween c. 1412 Ma to c. 1294 Ma (Fig. 3b). Trace element ratios (Th/U) and REE patterns for these zircon cores are distinct from the primary igneous zircon population (Supplementary Fig. S1). Five core domains yield Hf_i ratios in the range 0.28198–0.28212 (Fig. 4) and εHf_i values from +2.05 to +8.30. We interpret this population to represent xenocrystic components, and the spread in apparent ages as the result of variable resetting of metamict zircon (alpha dose >8 $\alpha/mg \times 10^{15}$) during post-crystallisation modification (Supplementary Table S2).

Zircon grains in sample CI-814B are 70–200 μm long and have aspect ratios that vary from 1:1–1:4. Many of the larger zircon grains show medium to high CL response (Fig. 3c) with oscillatory (e.g. spots 001, 006) or diffuse banded (e.g. spot 33) zoning. A subset of the grains contain low-CL domains that are typically unzoned (e.g. spot 020). Thirty-two analyses were collected from thirty-one grains representing the range of observed morphologies and zonation. The main concordant zircon population yields a $^{207}Pb/^{206}Pb$ weighted average age of 1145 ± 9 Ma (n = 27, MSWD = 0.91; Fig. 3c), with the majority of these grains exhibiting high (0.54–1.90) Th/U ratios and REE trace element signatures typical of igneous zircon (Supplementary Fig. S1). Hf isotopic analyses from the c. 1145 Ma zircon population yield Hf_i ratios in the range 0.28208–0.28214 (Fig. 4) and εHf_i values between −0.47 to +2.37. As for sample CI-814B, we interpret this population as indicating a cognate inclusion relationship for both xenoliths. Four older analyses on homogenous dark zircon domains yield apparent $^{207}Pb/^{206}Pb$ ages ranging from c. 1526 Ma to c. 1464 Ma, have slightly more REE-enriched compositions compared to the main population (Fig. 3c) and yield Hf_i ratios in the range 0.28191–0.28195 (Fig. 4) and εHf_i values between +2.17 to +3.64. We interpret this population to represent xenocrysts and suggest their clustered U–Pb–Hf signature fingerprints the character of early Mesoproterozoic (c. 1500 Ma) basement at depth.

Basement Correlations Between Wilkes Land and Australia

Aeromagnetic signatures from the conjugate Australian-Antarctic margins suggest the presence of similar basement domains in the Coompana/Madura Provinces and Wilkes Land. In southern Australia, the Coompana Province has variable magnetic intensity[28] and is characterised by large areas of low to moderate magnetic intensity (<−300 nT) associated with the c. 1610–1490 Ma plutons of the Toolgana and Undawidgi Supersuites (Fig. 1b). In contrast, the Madura Province exhibits overall higher-frequency anomalies with moderate to strong magnetic intensity (0–100 nT). The c. 1192–1125 Ma Moodini Supersuite in both the Coompana and Madura provinces exhibits a distinct NE directional trend and is the source of the highest magnetic intensities (up to 400 nT) in both provinces (Fig. 1b).

In Antarctica, we suggest that two large and magnetically distinct intrusive suites identified by Aitken *et al.*[11] match, in type and character, the magnetic anomalies associated with the Undawidgi–Toolgana and Moodini supersuites (Fig. 1b). The older suite is characterised by strong relative magnetic lows, providing a good match with magnetic anomalies corresponding to the Toolgana and Undawidgi supersuites. The younger suite, is interpreted to occur throughout the entire region based on identical high magnetic character and north-easterly directional trend as c. 1150 Ma granitoids across southwestern Australia[11] which crosscut the major regional structural grain. We suggest this suite is likely equivalent to the Moodini Supersuite granites.

The spatial distribution of these suites in Wilkes Land defines two distinct geophysical domains with different magnetic character: these are separated by a previously un-named ENE-WSW geophysical lineament[11] that marks a sharp change in overall intensity and frequency of magnetic anomalies (Fig. 1b). We suggest that the presence of high-amplitude magnetic anomalies associated with Undawidgi–Toolgana and Moodini supersuites exclusively south of this lineament fingerprints a Coompana-type basement complex. In contrast, the overall

relatively higher magnetic intensity and frequency of magnetic anomalies combined with the absence of a geophysical signal like that of the Undawidgi–Toolgana plutons indicates the presence of a Madura-type basement complex in the portion of Wilkes Land wedged between the ENE-WSW lineament and the Wilkes Province (Fig. 1b). We identify this ENE-WSW lineament as the boundary between Coompana- and Madura-type crust in Antarctica and name the Antarctic conjugates of the Coompana and Madura provinces the Banzare Province and Nuyina Province, respectively.

The Chick Island outcrop corresponds with an interpreted Moodini Supersuite pluton located approximately 100 km north of the inferred boundary between the Banzare and Nuyina provinces (Fig. 1a,b); our new U–Pb–Hf zircon data provide insight into its crustal affinity and a test of the tectonic correlation based on aeromagnetic data. The Chick Island granodiorite pluton (sample CI-814A2) has a crystallisation age of c. 1148 Ma and Hf_i isotopic values consistent with the emplacement age and Hf signature of the Moodini Supersuite in the Coompana and Madura provinces[14], as well as isotopically-similar igneous rocks found in the Wilkes Province (e.g. Ardery Charnockite in the Windmill Islands[8]) (Fig. 4). Two cognate inclusions yield c. 1150 Ma primary zircon populations and xenocrystic zircon grains that fingerprint crustal contamination. The distinct Hf_i isotopic character of xenocrystic zircon suggests at least two isotopically different components in the source: the less radiogenic xenocrysts (c. 1526–1464 Ma; sample CI-814B) overlap in age and Hf signature with zircon from the Coompana Province, and the more radiogenic xenocryst group (c. 1412–1294 Ma; sample CI-810A), though displaying variable Pb loss possibly from c. 1420 Ma, overlap the isotopic signature of the more juvenile Madura Province (Fig. 4). We suggest that these U–Pb–Hf patterns are indicative of crustal contamination from both Coompana- (c. 1610–1490 Ma) and Madura-type (c. 1475–1389 Ma) crust at depth, and thus fingerprint the presence of a tectonic boundary between the Banzare and Nuyina provinces in Antarctica, with Chick Island being the most likely coastal location of this boundary.

Based on our new geological data, we revise the path of the tectonic boundary between the Banzare and Nuyina provinces identified in aeromagnetic data (ENE-WSW lineament of Aitken *et al.*[11]) to intersect the coast in the proximity of the Chick Island outcrop (dotted segment in Figs 1 and 2). We name this composite tectonic boundary the Southard Fault (after Cape Southard).

Correlations of the Coompana/Madura and Banzare/Nuyina provinces across Australia-Antarctica are offset by approximately 330 km sinistral strike-slip motion along the Mundrabilla-Frost Shear Zone (Fig. 1). To reconstruct the configuration of these provinces prior to this motion, we link the Southard Fault with a major NE-trending structure identified in aeromagnetic data by Aitken *et al.*[11], which we suggest may represent the conjugate boundary between the Coompana and Madura provinces in Australia (Fig. 1c,d). Despite the lack of geological data from this region, this structure appears to represent the southerly expression of the boundary between the West Musgrave and central Musgrave provinces which preserve evidence of tectono-magmatic affinity with the Madura and Coompana provinces, respectively[7,29] (Fig. 1c,d). This connection allows the Madura Province to continue across the Mundrabilla-Frost Shear Zone in Australia and resolves the geometry of Coompana and Madura provinces and the conjugate Banzare and Nuyina provinces before and after strike-slip motion in their Rodinia (c. 1130–1040 Ma) and Gondwana (c. 160 Ma) configurations.

Provenance and Age of Sandstone Erratics

To probe the provenance and age of sedimentary rocks overlying crystalline basement in interior Wilkes Land, we analysed three glacially-transported sedimentary samples (Fig. 2c) collected at two localities in the Windmill Islands[26] (Fig. 2a) by combining detrital zircon and authigenic monazite dating. The glacial erratics are faceted and angular, suggesting these samples were derived from a proximal sedimentary source (Fig. 2a). Samples are well sorted quartz-arenites (Fig. 5) dominated by monocrystalline quartz (>95%, derived from point counting) and small proportions of K-feldspar (up to 3%). This composition suggests a dominantly granitic sediment source and a "craton interior" tectonic provenance for the three samples. The presence of fine-grained (~10 μm) interstitial muscovite and sericitised feldspar grains (Fig. 5) indicates post-depositional interaction with hydrothermal fluids.

Heavy liquid separation of 100 g of crushed material from each of the three samples provided a total of ~1000 zircon grains in the size range of 20–140 μm. The size fraction of the analysed zircons ranges from ~40–120 μm. Zircons are sub-rounded to sub-euhedral, with the majority of grains (~80%) having aspect ratios from 1:2–1:3 and indicating an overall local sourcing of sediments. U–Pb zircon ages from the three samples reveal similar age peaks and have a statistically similar detrital distribution according to the performed Kolmogorov–Smirnov (K-S) test (maximum difference between age distribution curves [D] = 0.0891–0.1471 and p-values > 0.05) (see Supplementary Fig. S2). The composite detrital zircon age spectrum, derived from a total of 468 concordant (<± 5% discordant) U–Pb zircon analyses from the three samples, indicates sedimentary source regions dominated by c. 1600–1470 Ma (48% of total) and c. 1180 Ma zircons (34%), with a lower proportion of zircons in the age range from c. 2400 Ma to 1700 Ma (18%) (Fig. 6). Most zircon grains in the two main groups display oscillatory zoning (Fig. 5) and average Th/U of ~0.64, typical of igneous zircon. An estimate of the maximum deposition age for the sandstones is 1091 ± 7 Ma (n = 40, MSWD = 1.4), based on the youngest detrital zircon population. The zircon εHf_i data from the sandstone erratic samples are dominated by positive values in each of the main detrital populations reflecting a significant mantle contribution in the source magmas. The c. 1600–1470 Ma zircons have overall positive εHf_i values between +11.52 and −1.08, while the c. 1180 zircons have a range of εHf_i values between +9.34 to −2.67 (Fig. 6).

Rare monazite typically occurs as irregular grains (~15–50 μm) amongst the fine-grained interstitial muscovite (Fig. 7 inset). This texture, together with the relatively high Th (mostly ~10,000 ppm) and low U (mostly <100 ppm), suggests the analysed monazite grains are authigenic and likely formed due to an interaction with hydrothermal fluids during or after deposition[30]. A total of 32 grains were analysed from the three sandstone erratic samples. Seven analysis were discarded due to low analytical signal intensity for the U, Th and Pb isotopes.

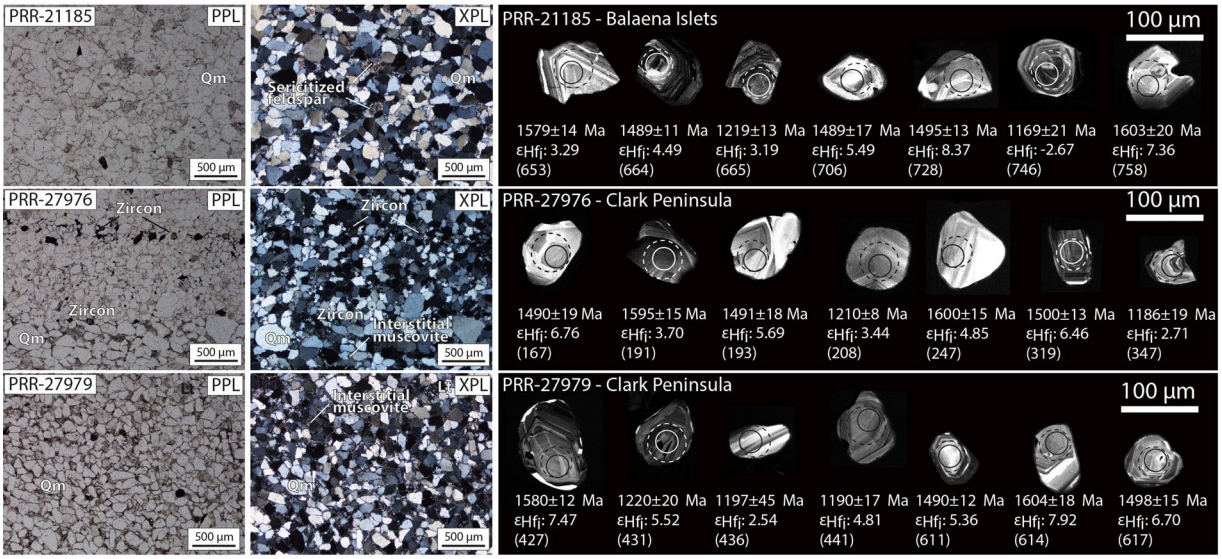

Figure 5. (left to right) Plane-polarised (PPL) and cross-polarised (XPL) microphotographs with descriptive labels, and CL images of representative detrital zircons used for U–Pb–Hf dating from each sandstone erratic sample. On CL images, U–Pb and Lu–Hf analysis locations are displayed as solid and dashed circles, respectively. Corresponding apparent $^{207}Pb/^{206}Pb$ ages (Ma), initial epsilon Hf (εHf_i) and spot number (in brackets) are also shown for each analysis. Abbreviations are: Lt–Lithic fragment; Qm–Quartz monocrystalline.

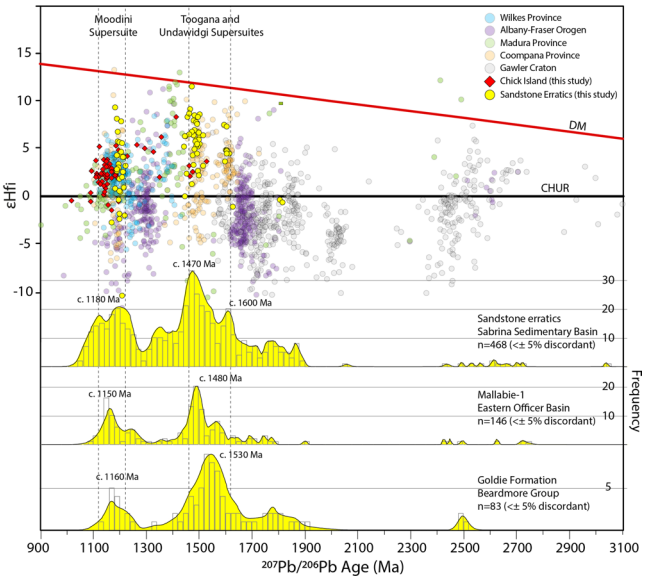

Figure 6. Initial epsilon Hf (εHf_i) values (yellow dots) versus probability density plot (yellow fill) and histograms for detrital zircon from the sandstone erratic samples. εHf_i ratio is compared to the same U–Pb–Hf data compilation used in Fig. 3 with the addition of >1500 Ma zircon from Gawler Craton[37]. Composite probability density plots and histograms for the Mallabie-1 sedimentary samples (Officer Basin)[38] and the Goldie Formation (Beardmore Group)[36] are also shown for comparison.

U/Pb systems in analysed monazite grains are overall disturbed due to common Pb contamination and depletion of U relative to Th, resulting in overestimated $^{206}Pb/^{238}U$ ages and large analytical uncertainties (Fig. 7). The well-resolved $^{208}Pb/^{232}Th$ ages obtained confirm instead minor disturbance of the Pb/Th systems and provide more reasonable age estimates.

Fifteen authigenic monazite grains analysed in sample PRR-21185 yield apparent $^{232}Th/^{208}Pb$ ages ranging between c. 639–490 Ma (Fig. 7). Eight authigenic monazite analyses from sample PRR-27976 yield ages ranging between c. 627–449 Ma (Fig. 7). A $^{232}Th/^{208}Pb$ apparent age of c. 1038 Ma obtained for one older monazite grain core exhibiting relatively lower Th (4282 ppm) and higher U (1664 ppm) is interpreted as a detrital relict. A single analysis obtained from sample PRR-27979 yielded an apparent $^{232}Th/^{208}Pb$ age of 577 ± 17 Ma (Fig. 7).

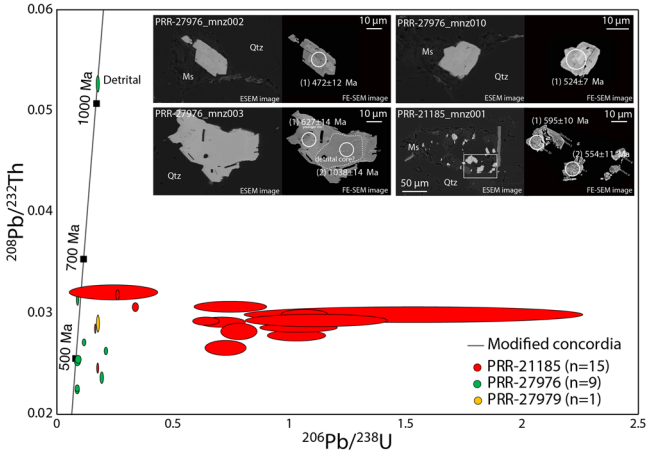

Figure 7. $^{206}Pb/^{238}U$ vs $^{208}Pb/^{232}Th$ modified concordia diagram with twenty-five analyses obtained by *in situ* U–Th–Pb dating for twenty-one monazite grains. Data-point error ellipses are 1σ; (inset) annotated ESEM image (left) and FE-SEM image (right) of four representative monazite grains used for *in situ* U–Th–Pb dating. Sample and grain number are indicated for each image. U–Th–Pb spots are 9 μm; spot numbers are shown in brackets; apparent ages are reported as $^{208}Pb/^{232}Th$ ages; Abbreviations are: Ms–Muscovite; Qtz–Quartz.

The observed spread in $^{232}Th/^{208}Pb$ ages could indicate different stages of authigenic monazite formation during the Late Neoproterozoic-Cambrian; we suggest that the oldest analyses in samples PRR-21185 and PRR-27976 may be closer to the depositional age of the sandstone while the apparently younger analyses record subsequent generation(s) of post-depositional authigenic monazite formation/hydrothermal alteration. An age of c. 633 Ma (average of two oldest $^{232}Th/^{208}Pb$ ages in samples PRR-21185 and PRR-27976) is therefore considered a minimum deposition age for the sandstone samples. The age of the single detrital monazite core also further constrains the maximum deposition age of the sandstones to 1038 ± 16 Ma.

A neoproterozoic Sedimentary Basin in Interior Wilkes Land

New zircon U–Pb–Hf isotopic data from sandstone erratic samples allowed us to investigate, for the first time, the age and provenance of the enigmatic Sabrina Sedimentary Basin, interpreted to cover vast tracts of interior Wilkes Land (Figs 1a and 2a). Present-day ice divides and ice-flow directions[31,32] indicate that the sandstone erratics were likely eroded from inland areas of the Vanderford ice catchment and transported to their present locations during a former expansion of the Vanderford Glacier[24,25] (Fig. 2a). To our knowledge, these sandstone erratics represent the first samples of the Sabrina Sedimentary Basin ever to be examined in detail.

The Sabrina Sedimentary Basin has been interpreted as the Antarctic equivalent of Australian Mesozoic-Cenozoic break-up sedimentary basins[11]. However, U–Pb dating of detrital zircon and *in-situ* authigenic monazite constrain a much older Neoproterozoic (c. 1038–633 Ma) depositional age range for at least part of the basin. This is further supported by the lack of Pan-African aged (c. 600–500 Ma) detrital zircon which instead are consistently present in younger Australian Palaeozoic to Cenozoic sedimentary deposits[33,34]. This age range broadly corresponds to the deposition of the Neoproterozoic sedimentary sequences in the eastern Officer Basin[35] of southern Australia (Fig. 1a), as well as Neoproterozoic sedimentary rocks of the Beardmore Group in the Transantarctic Mountains[36]. We therefore suggest that sedimentary cover similar in age and composition to the Neoproterozoic eastern Officer Basin and Beardmore Group occupies an area of approximately 100,000 km^2 in the Vanderford ice catchment, and could extend over large parts of the Sabrina Sedimentary Basin further east.

The detrital signature of the sandstone erratics is defined by a broadly bimodal distribution: (1) the c. 1600–1470 Ma detrital zircon age and εHf_i signatures match the character of igneous zircons from the Toolgana and Undawidgi supersuites in the Coompana Province (Fig. 6), and (2) the c. 1180 Ma detrital zircon population is broadly similar in age and εHf_i to igneous zircons of the Moodini Supersuite of the Coompana and Madura provinces[14], and Chick Island (this study), as well as isotopically-similar granitic rocks found in the Wilkes Province (e.g. Ardery Charnockite[8]; Fig. 6). We suggest granitic source rocks of these ages and isotopic compositions contribute to the main detrital zircon signature in Neoproterozoic sedimentary rocks in the Sabrina Sedimentary Basin and indicate a predominantly local derivation of sediments from the Banzare and Nuyina provinces and/or Australian equivalent basement provinces. Older age components between c. 1700 Ma and 2400 Ma, correlate with the age of known magmatic events in the Gawler/Mawson cratons[37] (Fig. 6) and could be interpreted to indicate minor sedimentary input from the east.

In Australia, the southerly extension of the eastern Officer Basin in the Coompana and Madura provinces is poorly known and concealed by the Mesozoic and Cenozoic cover of the Bight and Eucla basins. Two sandstone samples from the Mallabie-1 drill hole in the Coompana Province are tentatively linked to the eastern Officer Basin and yield similar age spectra to our sandstone erratic samples[38] (Fig. 6). While we note some differences in the dominant peak ages in the zircon age spectra between these Officer Basin sedimentary rocks and our samples, the overall detrital zircon age spectra signatures in the former also suggests a strong influence of proximal sediment contributions (i.e. Coompana Province and Musgrave Province)[39]. A similar provenance is also shared by parts of the Neoproterozoic Beardmore Group (i.e. Goldie Formation) which is also interpreted to reflect a dominantly Mesoproterozoic sediment source form interior Wilkes Land[36].

Implications of Subglacial Geology

Our new zircon U–Pb–Hf and monazite U–Th–Pb geochronology, combined with regional age data and aero-geophysical observations have allowed us to interpret the age and composition of bedrock in interior Wilkes Land and test tectonic models.

We provide the first geological evidence for the Antarctic counterparts of the Mesoproterozoic Coompana and Madura provinces, previously only documented in southern Australia and resolve the geometry of these conjugate Mesoproterozoic basement provinces in both a Rodinia and Gondwana configuration. The addition of these two new Antarctic provinces confirm the presence of a progressively westerly-younging sequence of juvenile magmatic arc-related rocks retreating away from the Mawson Craton and provides additional evidence for a subduction-driven Mesoproterozoic evolution of Australo-Antarctica as supported by recent tectonic models[7]. The improved geometrical correlation between basement provinces of Wilkes Land and southern Australia will be fundamental in further understanding the Mesoproterozoic evolution of Australo-Antarctica and as such, inform plate tectonic models for the amalgamation of Nuna and Rodinia and the configuration of Gondwana.

New zircon and monazite data from sandstone erratics demonstrate the presence of Neoproterozoic sedimentary rocks in the Sabrina Sedimentary Basin that are equivalent in age and provenance to the eastern Officer Basin of Australia and Beardmore Group in the Transantarctic Mountains. The occurrence of sedimentary rocks of this age was previously unknown for this sector of East Antarctica and has broader implications for understanding the Rodinia-to-Gondwana transition during the Neoproterozoic. Similarities in age and provenance between our sandstone erratics and the Beardmore Group in the Transantarctic Mountains suggest that Neoproterozoic sedimentary rocks may have once covered a large sector of East Antarctica, forming an extensive platform basin on the proto-pacific rifting Rodina margin[36]. However, due to the limited geological samples available, we are unable to define the extent of the newly identified Neoproterozoic Sabrina Basin outside the confines of the Vanderford ice catchment region. It therefore remains unclear whether the Neoproterozoic Sabina Basin formed an Antarctic extension of the larger Centralian Superbasin or constitutes a different Neoproterozoic Antarctic basin sharing provenance similarities with the Officer Basin. Furthermore, we do not exclude the presence of a younger Mesozoic or Cenozoic basin phase in the Sabrina Sedimentary Basin as previously hypothesised by Aitken *et al.*[11], which could overlie older sedimentary sequences as seen in southern Australia with the overlap of the Bight and Eucla basins over the Officer Basin.

Our improved geological correlation between southern Australia and Wilkes Land, and interpretation of age and composition of subglacial bedrock, can also help inform estimations of the spatial distribution of crustal radiogenic heat production[40] and geothermal heat flow[41] across the Australian-Antarctic margin, with potential implications for ice sheet models that simulate past and future Antarctic ice sheet behaviour.

Methods

Zircon sample preparation and U–Pb–Hf analyses. Location of samples used in this study is given in Supplementary Table S1. Igneous zircon grains were separated from crushed rocks using a standard plastic pan and warm water and subsequent magnetic separation. Detrital zircon were separated from crushed rocks using heavy liquid separation. Grains were mounted in 25-mm diameter epoxy discs. Mounts were polished to half grain thickness to expose grain centres, carbon coated and imaged using a cathodoluminescence (CL) detector on a FEI Quanta 600 Environmental Scanning Electron Microscope (ESEM) at Central Science Laboratory, University of Tasmania, to identify compositional domains for analysis.

U–Pb zircon ages were collected at the University of Tasmania, Australia using laser ablation-inductively coupled plasma-mass spectrometry (LA-ICP-MS). U–Pb zircon analyses were performed in two different sessions on an Agilent 7900cs quadrupole ICPMS with a 193 nm Coherent Ar–F gas laser and a Resonetics S-155 ablation cell at the School of Earth Sciences, University of Tasmania. Each analysis was pre-ablated with 5 laser pulses to remove any surface contamination then the blank gas was analysed for 30 s followed by 30 s of zircon ablation at 5 Hz and 2 J/cm^2 on a spot size of 29 μm. Elements measured include ^{49}Ti, ^{56}Fe, ^{90}Zr, ^{178}Hf, ^{202}Hg, ^{204}Pb, ^{206}Pb, ^{207}Pb, ^{208}Pb, ^{232}Th and ^{238}U with each element being measured sequentially every 0.16 s with longer counting time on the Pb isotopes compared to the other elements. The international glass standard NIST610 was ablated at the beginning and end of the analytical session to correct for mass bias on the ^{207}Pb/^{206}Pb ratio. Each run consisted of 30–50 analyses of our unknowns, bracketed by 4–6 analyses of the primary reference zircon standard 91500[42] used to correct for mass bias, machine drift and down-hole fractionation on the Pb/U and Pb/Th ratios, and 4 analyses (two each) of secondary standards TEMORA 1[43] and GJ-1[44]/Plesovice[45] to provide an independent control to assess accuracy and precision. Full tabulation of U–Pb isotopic data of unknowns and standards is reported in Supplementary Table S2. Data reduction calculations and error propagations were done with Microsoft Excel® via macros designed at the University of Tasmania using the techniques outlined by Sack *et al.*[46]. The degree of metamictisation was also determined in igneous zircon by using U and Th concentrations and ^{207}Pb/^{206}Pb ages to calculate the dose of α-events for each zircon grain. Zircon grains were classified as 'highly crystalline' when alpha dose was <3 α/mg $\times 10^{15}$, 'moderately damaged' when >3 and <8 α/mg $\times 10^{15}$ and 'highly metamict' when >8 α/mg $\times 10^{15}$[47]. U–Pb Tera-Wasserburg plots of igneous zircons were constructed using isoplotR[48]. Error ellipses on Tera-Wasserburg plots are calculated at the two-sigma level. ^{207}Pb/^{206}Pb data are used for all age determinations. The quoted analytical uncertainties on individual analyses are given at the 2r level. Weighted mean ages are calculated to their 95% confidence level using analyses that are $\leq \pm 10\%$ discordant (within 2r uncertainty of concordia). Probability density plots (PDP) of detrital zircon were calculated with DensityPlotter[49] using ^{207}Pb/^{206}Pb ages and their 1σ uncertainties for data $\leq \pm 5\%$ discordant. Histogram bin size in all PDPs is 20 Myr. Two-sample Kolmogorov–Smirnov (K-S) tests were performed on the detrital zircon age data using the online statistics calculator of Kirkman[50] to determine if the samples were derived from different sources by comparing the distance between the cumulative age distribution curves.

Lu–Hf isotope analyses were performed on a subset of zircon grains already analysed for U–Pb using a New Wave/Merchantek LUV213 laser-ablation microprobe, attached to a Nu Plasma multi-collector inductively coupled plasma mass spectrometer (LA-MC-ICPMS) at GEMOC, Macquarie University (Sydney, Australia). Griffin *et al.*[51] describe the methodology in detail. A blank gas was analysed for 60 s followed by 120 s of ablation at 5 Hz and 2 J/cm^2 and a beam diameter of 40–50 µm (depending on the size of the zircon grain). Zircon CL images were used to ensure that Hf isotope analyses were contained within the same domain analysed for U–Pb. Our samples were measured in two analytical sessions. Zircons from the Mud Tank carbonatite locality were analysed together with the samples in each session to monitor accuracy of the results. Most data and the mean $^{176}Hf/^{177}Hf$ value are within 2 standard deviations (SD) of the recommended value [0.282522 ± 42 (2σ)][52]. Temora zircon was also run as an independent check on the accuracy of the Yb correction. Temora zircon has an average $^{176}Yb/^{177}Hf$ ratio of 0.04, which is similar to the mean $^{176}Yb/^{177}Hf$ ratio of zircon in this study. The average $^{176}Hf/^{177}Hf$ ratio for Temora is consistent with the published value for the Temora standard [0.282687 ± 24 (2σ)[53]]. The initial $^{176}Hf/^{177}Hf$ (Hf_i) value in zircon is calculated using the measured $^{176}Hf/^{177}Hf$ and apparent $^{207}Pb/^{206}Pb$ age. Calculation of εHf_i values employed the decay constant of Scherer *et al.*[54] of 1.865×10^{-11}. Full tabulation of zircon Hf isotopic data of unknown and standards is presented in Supplementary Table S3. Initial $^{176}Hf/^{177}Hf$ and εHf_i plots were constructed in Microsoft Excel®; zircon U–Pb and Hf isotopes from our samples are compared to a compilation of Australian and Antarctic isotopic data (provided in Supplementary Table S4).

Monazite sample preparation and *in situ* U–Th–Pb analyses. Rock chips for *in situ* U–Th–Pb monazite dating were mounted with epoxy resin in ~12 mm thick x 25 mm diameter steel cylinder and polished using a 0.25 µm diamond polishing lap. Monazite grains were identified in rock chip laser mounts using Sparse Phase Liberation-Lite analysis (SPL-LT). Representative images of monazite grains selected for geochronology were taken using a FEI Quanta 600 SEM. Grains were also imaged using high contrast BSE imaging to detect zoning within the grains on a Hitachi SU-70 Field Emission Scanning Electron Microscope (FE-SEM).

Monazite grains from each of the three sandstone erratic samples were investigated for *in situ* U–Th–Pb analyses following the analytical procedures reported in Halpin *et al.*[55] on the same LA-ICP-MS system used to collect U–Pb detrital zircon ages. Pre-ablation and ablation times follow the monazite methodology highlighted in Halpin *et al.*[55] with operating conditions of 5 Hz and ~2 J/cm^2 on a spot size of 9 µm. Elements measured include ^{27}Al, ^{31}P, ^{43}Ca, ^{140}Ce, ^{172}Yb, ^{202}Hg, ^{204}Pb, ^{206}Pb, ^{207}Pb, ^{208}Pb, ^{232}Th and ^{238}U. The international glass standard NIST610 was used as a primary standard for trace element quantification assuming stoichiometric Ce in monazite and as a primary standard for the $^{207}Pb/^{206}Pb$ ratio correction factor for monazite. The down hole fractionation, instrument drift and mass bias correction factors for Pb/U and Pb/Th ratios on monazite grains were calculated using two analyses on the primary standard (14971-Mon–in-house standard) and one analysis on each of the secondary standard monazites RGL4B[56], Bananeira[57], and 94–222[58] analysed at the beginning of the session and every 16–20 unknowns using the same spot size and conditions as used on the samples. Following the recommendations of Seydoux-Guillaume *et al.*[30], Grand'Homme *et al.*[59], $^{208}Pb/^{232}Th$ ages are preferred to the $^{206}Pb/^{238}U$ ages in all age determinations due to common Pb contamination and the relatively high Th/U ratio of monazite. Results are presented graphically in a $^{206}Pb/^{238}U$ vs $^{208}Pb/^{232}Th$ modified concordia plot. Uncertainties on individual spot ages are 1σ. Full tabulation of U–Th–Pb isotopic data of monazite unknowns and standards and modified concordia plot are reported in Supplementary Table S5. Data reduction calculations and error propagations were done with Microsoft Excel® via macros designed at the University of Tasmania using the techniques outlined by Sack *et al.*[46] and Halpin *et al.*[55]. Age calculations. $^{206}Pb/^{238}U$ vs $^{208}Pb/^{232}Th$ modified Concordia diagrams were made in Microsoft Excel®.

Aeromagnetic data interpretation and tectonic reconstructions. We use the most recent magnetic anomaly map of the Antarctic (ADMAP-2)[60] and the comparable Australian dataset available from Geoscience Australia in conjunction with geological data to match the aeromagnetic signature of the Coompana/Madura provinces and interior Wilkes Land in the Gondwana full-fit (c. 160 Ma) plate reconstruction framework of Aitken *et al.*[7] and identify broad basement domains and lineaments. Our interpretation of Antarctic aeromagnetic data builds on the most recent tectonic model of Wilkes Land of Aitken *et al.*[11] and preliminary interpretation of the 2015 Coompana aeromagnetic survey[28] based on the most recent drillhole data available from the Coompana Province. We reproduce the Late Mesoproterozoic reconstruction of the Rodinia configuration (c. 1130–1040 Ma) of Aitken *et al.*[7] with reversal of approximately 330 km of sinistral offset on the Mundrabilla-Frost Shear Zone to reconstruct the geometry of the Madura/Coompana and Antarctic conjugate provinces across Australia-Antarctica.

References

1. Boger, S. D. Antarctica - Before and after Gondwana. *Gondwana Research* **19**, 335–371 (2011).
2. Fitzsimons, I. C. W. Proterozoic basement provinces of southern and southwestern Australia, and their correlation with Antarctica. *Geological Society, London, Special Publications* **206**, 93–130, https://doi.org/10.1144/gsl.sp.2003.206.01.07 (2003).
3. Aitken, A. R. A. *et al.* Repeated large-scale retreat and advance of Totten Glacier indicated by inland bed erosion. *Nature* **533**, 385–389, https://doi.org/10.1038/nature17447 (2016).
4. Gulick, S. P. S. *et al.* Initiation and long-term instability of the East Antarctic Ice Sheet. *Nature* **552**, 225–229, https://doi.org/10.1038/nature25026 (2017).
5. Pierce, E. L. *et al.* A comparison of detrital U–Pb zircon, 40Ar/39Ar hornblende, 40Ar/39Ar biotite ages in marine sediments off East Antarctica: Implications for the geology of subglacial terrains and provenance studies. *Earth-Science Reviews* **138**, 156–178, https://doi.org/10.1016/j.earscirev.2014.08.010 (2014).
6. Roy, M., van de Flierdt, T., Hemming, S. R. & Goldstein, S. L. 40Ar/39Ar ages of hornblende grains and bulk Sm/Nd isotopes of circum-Antarctic glacio-marine sediments: Implications for sediment provenance in the southern ocean. *Chemical Geology* **244**, 507–519, https://doi.org/10.1016/j.chemgeo.2007.07.017 (2007).
7. Aitken, A. R. A. *et al.* The Australo-Antarctic Columbia to Gondwana transition. *Gondwana Research* **29**, 136–152, https://doi.org/10.1016/j.gr.2014.10.019 (2016).

8. Morrissey, L. J. *et al*. Linking the Windmill Islands, east Antarctica and the Albany–Fraser Orogen: Insights from U–Pb zircon geochronology and Hf isotopes. *Precambrian Research* **293**, 131–149, https://doi.org/10.1016/j.precamres.2017.03.005 (2017).
9. Zhang, S. H. *et al*. U-Pb geochronology and geochemistry of the bedrocks and moraine sediments from the Windmill Islands: Implications for Proterozoic evolution of East Antarctica. *Precambrian Research* **206–207**, 52–71 (2012).
10. Spaggiari, C. V. *et al*. *The Geology of the East Albany-Fraser Orogen: A Field Guide*. (Geological Survey of Western Australia, 2011).
11. Aitken, A. R. A. *et al*. The subglacial geology of Wilkes Land, East Antarctica. *Geophysical Research Letters* **41**, 2014GL059405, https://doi.org/10.1002/2014gl059405 (2014).
12. McLeod, I. R. & Gregory, C. M. *Geological investigations along the Antarctic coast between longitudes 108°E and 166°E*. (Bureau of Mineral Resources, Geology and Geophysics, 1967).
13. Ravich, M. G., Solov′ev, D. S. & Klimov, L. V. *The Pre-Cambrian of East Antarctica. 344–353* (Israel Program for Scientific Translations [available from the U.S. Dept. of Commerce, Clearinghouse for Federal Scientific and Technical Information, Springfield, Va.], 1968).
14. Kirkland, C. L. *et al*. Proterozoic crustal evolution of the Eucla basement, Australia: Implications for destruction of oceanic crust during emergence of Nuna. *LITHOS* **278–281**, 427–444, https://doi.org/10.1016/j.lithos.2017.01.029 (2017).
15. Spaggiari, C. V. & Smithies, R. H. Eucla basement stratigraphic drilling results release workshop extended abstracts *Geological Survey of Western Australia*, *Record 2015/10*, 70p (2015).
16. Hartnady, M. I. H., Kirkland, C. L., Dutch, R. I., Bodorkos, S. & Jagodzinski, E. A. Zircon Hf isotopic signatures of the Coompana Province in South Australia. *In R Dutch*, *T Wise*, *M Pawley and A Petts eds*, *Coompana Drilling and Geochemistry Workshop 2018 extended abstracts*, *Report Book 2018/00019*. *Department for Energy and Mining*, *South Australia*, *Adelaide* (2018).
17. Wingate, M. T. D., Kirkland, C. L., Spaggiari, C. V. & Smithies, R. H. U–Pb geochronology of the Forrest Zone of the Coompana Province. *Eucla basement stratigraphic drilling results release workshop: extended abstracts compiled by CV Spaggiari and RH Smithies: Geological Survey of Western Australia*, *Record* 2015/10, p. 37–40 (2015).
18. Jagodzinski, E. A. & Bodorkos, S. U-Pb geochronology of the eastern Coompana Province, South Australia. *In R Dutch*, *T Wise*, *M Pawley and A Petts eds*, *Coompana Drilling and Geochemistry Workshop 2018 extended abstracts*, *Report Book 2018/00019*. *Department for Energy and Mining*, *South Australia*, *Adelaide* (2018).
19. Wingate, M. T. D., Kirkland, C. L., Spaggiari, C. V. & Smithies, R. H. *U–Pb geochronology of the Madura Province*. *Eucla basement stratigraphic drilling results release workshop: extended abstracts compiled by CV Spaggiari and RH Smithies: Geological Survey of Western Australia*, *Record 2015/10*, p. 14–16 (2015).
20. Spaggiari, C. V. *et al*. Buried but preserved: The Proterozoic Arubiddy Ophiolite, Madura Province, Western Australia. *Precambrian Research* **317**, 137–158, https://doi.org/10.1016/j.precamres.2018.08.025 (2018).
21. Lindsay, J. F. & Leven, J. H. Evolution of a Neoproterozoic to Palaeozoic intracratonic setting, Officer Basin, South Australia. *Basin Research* **8**, 403–424, https://doi.org/10.1046/j.1365-2117.1996.00223.x (1996).
22. Lowry, D. C. *Geology of the Western Australian part of the Eucla Basin*. (Geological Survey of Western Australia, 1970).
23. Espurt, N. *et al*. Transition from symmetry to asymmetry during continental rifting: an example from the Bight Basin–Terre Adélie (Australian and Antarctic conjugate margins). *Terra Nova* **24**, 167–180 (2012).
24. Mackintosh, A. N. *et al*. Retreat history of the East Antarctic Ice Sheet since the Last Glacial Maximum. *Quaternary Science Reviews* **100**, 10–30, https://doi.org/10.1016/j.quascirev.2013.07.024 (2014).
25. Goodwin, I. D. On the Antarctic contribution to Holocene sea-level [Doctoral dissertation]: University of Tasmania, 111 p (1995).
26. Goldthwait, R. P. USNC-IGY Antarctic glaciological data field work 1957 and 1958. *The Ohio State University Research Foundation* Report. 825-2-Part VI, 17–18 (1959).
27. Streckeisen, A. To each plutonic rock its proper name. *Earth-Science Reviews* **12**, 1–33, https://doi.org/10.1016/0012-8252(76)90052-0 (1976).
28. Wise, T. W., Pawley, M. J. & Dutch, R. A. Preliminary interpretations from the 2015 Coompana aeromagnetic survey. *MESA Journal* **79**, 22–30 (2015).
29. Howard, H. M. *et al*. The burning heart — The Proterozoic geology and geological evolution of the west Musgrave Region, central Australia. *Gondwana Research* **27**, 64–94, https://doi.org/10.1016/j.gr.2014.09.001 (2015).
30. Seydoux-Guillaume, A. M. *et al*. Low-temperature alteration of monazite: Fluid mediated coupled dissolution-precipitation, irradiation damage, and disturbance of the U-Pb and Th-Pb chronometers. *Chemical Geology* **330**, 140–158 (2012).
31. Mouginot, J., Scheuchl, B. & Rignot, E. MEaSUREs Antarctic Boundaries for IPY 2007–2009 from Satellite Radar, Version 2. [Indicate subset used]. Boulder, Colorado USA. NASA National Snow and Ice Data Center Distributed Active Archive Center, https://doi.org/10.5067/AXE4121732AD. [24-04-2018] (2017).
32. Rignot, E., Mouginot, J. & Scheuchl, B. Ice flow of the antarctic ice sheet. *Science* **333**, 1427–1430, https://doi.org/10.1126/science.1208336 (2011).
33. Yao, W., Li, Z.-X., Spencer, C. J. & Martin, E. L. Indian-derived sediments deposited in Australia during Gondwana assembly. *Precambrian Research* **312**, 23–37, https://doi.org/10.1016/j.precamres.2018.05.006 (2018).
34. Reid, A., Keeling, J., Boyd, D., Belousova, E. & Hou, B. Source of zircon in world-class heavy mineral placer deposits of the Cenozoic Eucla Basin, southern Australia from LA-ICPMS U–Pb geochronology. *Sedimentary Geology* **286–287**, 1–19, https://doi.org/10.1016/j.sedgeo.2012.10.008 (2013).
35. Wade, B. P., Hand, M. & Barovich, K. M. Nd isotopic and geochemical constraints on provenance of sedimentary rocks in the eastern Officer Basin, Australia; implications for the duration of the intracratonic Petermann Orogeny. *Journal of the Geological Society of London* **162, Part 3**, 513–530, https://doi.org/10.1144/0016-764904-001 (2005).
36. Goodge, J. W., Williams, I. S. & Myrow, P. Provenance of Neoproterozoic and lower Paleozoic siliciclastic rocks of the central Ross orogen, Antarctica: Detrital record of rift-, passive-, and active-margin sedimentation. *Bulletin of the Geological Society of America* **116**, 1253–1279 (2004).
37. Belousova, E. A., Reid, A. J., Griffin, W. L. & O'Reilly, S. Y. Rejuvenation vs. recycling of Archean crust in the Gawler Craton, South Australia: Evidence from U–Pb and Hf isotopes in detrital zircon. *Lithos* **113**, 570–582, https://doi.org/10.1016/j.lithos.2009.06.028 (2009).
38. Fraser, G. L. & Neumann, N. L. Under the Nullarbor: New SHRIMP UPb zircon ages from the Coompana, Madura and Albany-Fraser Provinces, and Officer Basin, western South Australia and eastern Western Australia: July 2014–June 2015. Record 2016/16. Geoscience Australia, Canberra (2016).
39. Barham, M. *et al*. Sediment routing and basin evolution in Proterozoic to Mesozoic east Gondwana: A case study from southern Australia. *Gondwana Research* **58**, 122–140, https://doi.org/10.1016/j.gr.2018.03.006 (2018).
40. Carson, C. J., McLaren, S., Roberts, J. L., Boger, S. D. & Blankenship, D. D. Hot rocks in a cold place: high sub-glacial heat flow in East Antarctica. *Journal of the Geological Society* **171**, 9–12, https://doi.org/10.1144/jgs2013-030 (2014).
41. Pollett, A. *et al*. Constraining basal heat flux in eastern Antarctica using new heat flow data from formerly contiguous geological terranes of southern Australia. *Geophysical Research Abstracts* Vol. 20, EGU2018-5774, 2018. EGU General Assembly 2018 (2018).
42. Wiedenbeck, M. *et al*. Three natural zircon standards for U-Th-Pb, Lu-Hf, trace element and REE analyses. *Geostandards and Geoanalytical Research* **19**, 1–23 (1995).
43. Black, L. P. *et al*. TEMORA 1: a new zircon standard for Phanerozoic U–Pb geochronology. *Chemical Geology* **200**, 155–170 (2003).
44. Jackson, S. E., Pearson, N. J., Griffin, W. L. & Belousova, E. A. The application of laser ablation-inductively coupled plasma-mass spectrometry to *in situ* U–Pb zircon geochronology. *chemical Geology* **211**, 47–69 (2004).

45. Sláma, J. *et al*. Plešovice zircon - A new natural reference material for U-Pb and Hf isotopic microanalysis. *Chemical Geology* **249**, 1–35, https://doi.org/10.1016/j.chemgeo.2007.11.005 (2008).
46. Sack, P. J. *et al*. *In situ* location and U-Pb dating of small zircon grains in igneous rocks using laser ablation–inductively coupled plasma–quadrupole mass spectrometry. *Geochemistry*, *Geophysics*, *Geosystems* **12** (2011).
47. Markwitz, V. & Kirkland, C. L. Source to sink zircon grain shape: Constraints on selective preservation and significance for Western Australian Proterozoic basin provenance. *Geoscience Frontiers* **9**, 415–430, https://doi.org/10.1016/j.gsf.2017.04.004 (2018).
48. Vermeesch, P. IsoplotR: A free and open toolbox for geochronology. *Geoscience Frontiers* **9**, 1479–1493, https://doi.org/10.1016/j.gsf.2018.04.001 (2018).
49. Vermeesch, P. On the visualisation of detrital age distributions. *Chemical Geology* **312–313**, 190–194, https://doi.org/10.1016/j.chemgeo.2012.04.021 (2012).
50. Kirkman, T. W. Statistics to use, http://www.physics.csbsju.edu/stats/ (3 Mar 2019) (1996).
51. Griffin, W. L., Belousova, E. A., Shee, S. R., Pearson, N. J. & O'Reilly, S. Y. Archean crustal evolution in the northern Yilgarn Craton: U–Pb and Hf-isotope evidence from detrital zircons. *Precambrian Research* **131**, 231–282, https://doi.org/10.1016/j.precamres.2003.12.011 (2004).
52. Griffin, W. L., Pearson, N. J., Belousova, E. A. & Saeed, A. Comment: Hf-isotope heterogeneity in zircon 91500. *Chemical Geology* **233**, 358–363, https://doi.org/10.1016/j.chemgeo.2006.03.007 (2006).
53. Hawkesworth, C. J. & Kemp, A. I. Evolution of the continental crust. *Nature* **443**, 811–817, https://doi.org/10.1038/nature05191 (2006).
54. Scherer, E., Münker, C. & Mezger, K. Calibration of the Lutetium-Hafnium Clock. *Science* **293**, 683 (2001).
55. Halpin, J. A. *et al*. Authigenic monazite and detrital zircon dating from the Proterozoic Rocky Cape Group, Tasmania: Links to the Belt-Purcell Supergroup, North America. *Precambrian Research* **250**, 50–67, https://doi.org/10.1016/j.precamres.2014.05.025 (2014).
56. Rubatto, D., Williams, I. S. & Buick, I. S. Zircon and monazite response to prograde metamorphism in the Reynolds Range, central Australia. *Contributions to Mineralogy and Petrology* **140**, 458–468 (2001).
57. Gonçalves, G. O. *et al*. An assessment of monazite from the Itambé pegmatite district for use as U–Pb isotope reference material for microanalysis and implications for the origin of the "Moacyr" monazite. *Chemical Geology* **424**, 30–50, https://doi.org/10.1016/j.chemgeo.2015.12.019 (2016).
58. Maidment, D. W. Palaeozoic high-grade metamorphism within the Centralian Superbasin, Harts Range region, central Australia (2005).
59. Grand'Homme, A., Janots, E., Bosse, V., Seydoux-Guillaume, A. M. & De Ascenção Guedes, R. Interpretation of U-Th-Pb *in-situ* ages of hydrothermal monazite-(Ce) and xenotime-(Y): evidence from a large-scale regional study in clefts from the western alps. *Mineralogy and Petrology* **110**, 787–807, https://doi.org/10.1007/s00710-016-0451-5 (2016).
60. Golynsky, A. V. *et al*. New Magnetic Anomaly Map of the Antarctic. *Geophysical Research Letters* **45**, 6437–6449, https://doi.org/10.1029/2018GL078153 (2018).
61. Raymond, O. L., Totterdell, J. M., Stewart, A. J. & Woods, M. A. Australian Geological Provinces, 2018.01 edition [Digital Dataset]. Geoscience Australia, Commonwealth of Australia, Canberra, http://www.ga.gov.au (2018).
62. Smits, R. G., Collins, W. J., Hand, M., Dutch, R. & Payne, J. A Proterozoic Wilson cycle identified by Hf isotopes in central Australia: Implications for the assembly of Proterozoic Australia and Rodinia. *Geology* **42**, 231–234, https://doi.org/10.1130/G35112.1 (2014).
63. Griffin, W. L. *et al*. Zircon chemistry and magma mixing, SE China: *In-situ* analysis of Hf isotopes, Tonglu and Pingtan igneous complexes. *Lithos* **61**, 237–269, https://doi.org/10.1016/S0024-4937(02)00082-8 (2002).

Acknowledgements

We thank S. Phipps and T. Staal for fieldwork at Chick Island. S. Meffre, J. Mulder, A. Stepanov and J. Thompson (ARC [Australian Research Council] Centre of Excellence in Ore Deposit, CODES, University of Tasmania), K. Goemann and S. Feig (Central Science Laboratory, University of Tasmania) and Y. Greau (ARC Centre of Excellence for Core to Crust Fluid Systems, CCFS, Macquarie University, Australia) are thanked for analytical assistance. This research used samples provided by the Polar Rock Repository (PRR). The PRR is sponsored by the National Science Foundation Office of Polar Programs. A.M. is supported by an Australian Government Research Training Program (RTP) Scholarship. This research is supported by the Australian Research Council's Special Research Initiative for Antarctic Gateway Partnership (Project ID SR140300001). We thank two anonymous reviewers for their constructive reviews on the manuscript.

Author Contributions

A.M. is responsible for U–Pb zircon and monazite geochronology of sandstone erratic samples, Hf analyses and aeromagnetic data interpretation; U–Pb geochronology of Chick Island samples was conducted by J.H., J.H., J.W. and N.D. provided funding and contributed to data interpretation. All authors contributed to writing and revision of the paper and approve its publication.

Additional Information

Supplementary information accompanies this paper at https://doi.org/10.1038/s41598-019-46612-y.

Competing Interests: The authors declare no competing interests.

Publisher's note: Springer Nature remains neutral with regard to jurisdictional claims in published maps and institutional affiliations.

Tectonics

RESEARCH ARTICLE
10.1029/2020TC006180

Key Points:
- First low-temperature thermochronology (LTT) study of the Bunger Hills basement in East Antarctica
- LTT data record widespread cooling and exhumation of East Antarctic basement associated with Pangea-wide extension
- Large-scale topographic framework established during intracontinental extension has influenced long-term landscape evolution of East Antarctica

Supporting Information:
- Supporting Information S1
- Table S1

Correspondence to:
A. Maritati,
alessandro.maritati@utas.edu.au

Citation:
Maritati, A., Danišík, M., Halpin, J. A., Whittaker, J. M., & Aitken, A. R. A. (2020). Pangea rifting shaped the East Antarctic landscape. *Tectonics*, *39*, e2020TC006180. https://doi.org/10.1029/2020TC006180

Received 4 MAR 2020
Accepted 4 AUG 2020
Accepted article online 7 AUG 2020

Pangea Rifting Shaped the East Antarctic Landscape

Alessandro Maritati[1], Martin Danišík[2], Jacqueline A. Halpin[1], Joanne M. Whittaker[1], and Alan R. A. Aitken[3]

[1]Institute for Marine and Antarctic Studies, University of Tasmania, Hobart, Tasmania, Australia, [2]John de Laeter Centre/The Institute for Geoscience Research, Curtin University, Perth, Western Australia, Australia, [3]School of Earth Sciences, University of Western Australia, Perth, Western Australia, Australia

Abstract East Antarctica remains one of the few continental regions on Earth where an understanding of the origin and causal processes responsible for topographic relief is largely missing. Low-temperature thermochronology studies of exposed Precambrian basement revealed discrete episodes of cooling and denudation during the Paleozoic–Mesozoic; however, the significance of these thermal events and their relationship to topography across the continental interior remains unclear. Here we use zircon and apatite (U-Th)/He thermochronology to resolve the low-temperature thermal evolution of a poorly exposed section of East Antarctic basement in the Bunger Hills region and gain insights into the chronology and style of landscape evolution across East Antarctica. Thermal history modeling results indicate that Precambrian basement in the Bunger Hills region experienced a distinct cooling episode during the Late Paleozoic–Triassic, which we relate to ~2–4 km of regional exhumation associated with intracontinental rifting, followed by a second episode of localized cooling and ≤1 km exhumation during the Late Jurassic–Cretaceous separation of India from East Gondwana. These findings, combined with existing thermochronological and tectonic evidence, support a continent-scale denudation event associated with uplift and exhumation of large sections of Precambrian basement during Late Paleozoic–Triassic Pangea-wide intracontinental extension. By contrast, continental extension associated with the Jurassic–Cretaceous breakup of East Gondwana resulted in significant denudation only locally in regions west of the Bunger Hills. We propose that the combined effects of these Paleozoic–Mesozoic tectonic events had a profound impact on the topography across the East Antarctic interior and influenced the long-term landscape evolution of East Antarctica.

1. Introduction

The origin of topographic relief in old and tectonically stable continental interiors is a long-standing problem in continental dynamics (e.g., Ferraccioli et al., 2011; Hu et al., 2018). East Antarctica comprises one of the largest composite Precambrian shields on Earth and is a chief example of a vast continental region with topographic variability akin to tectonically active regions (Creyts et al., 2014). The most significant morphological variations across East Antarctica broadly correlate with the Precambrian domains of Australo-Antarctica and Indo-Antarctica, which amalgamated during the ~600–550 Ma assembly of Gondwana (e.g., Mulder et al., 2019). Despite preserving Precambrian crust with broadly similar thicknesses (Pappa et al., 2019), these two domains exhibit remarkably distinct hypsometry (O'Donnell & Nyblade, 2014; Figure 1a). Indo-Antarctica possesses elevated, high-relief topography above the global average with narrow and deep rift basins (Ferraccioli et al., 2011). By contrast, the Australo-Antarctic domain comprises smoother topography at longer wavelengths and features large subglacial sedimentary basins where the vast majority of topography is below sea level (Aitken et al., 2014; Frederick et al., 2016; Maritati et al., 2016). Proposed models for the origin and long-term evolution of topography of ancient cratonic regions include high-standing passive margin formation during continental breakup (e.g., southern Africa; Wildman et al., 2016), large-scale denudation of Phanerozoic cover (e.g., Yilgarn Craton; Weber et al., 2005), and far-field deformation transmitted from collisional plate interactions (e.g., Canadian Shield; Pinet, 2016). However, an understanding of the causal processes responsible for the large-scale hypsometric variability across East Antarctica remains largely missing due to its poorly understood Phanerozoic landscape evolution.

Low-temperature (<300°C) thermochronology (LTT) has been widely used to quantify spatial and temporal patterns of cooling in continental settings, which in turn can provide constraints on the rates and

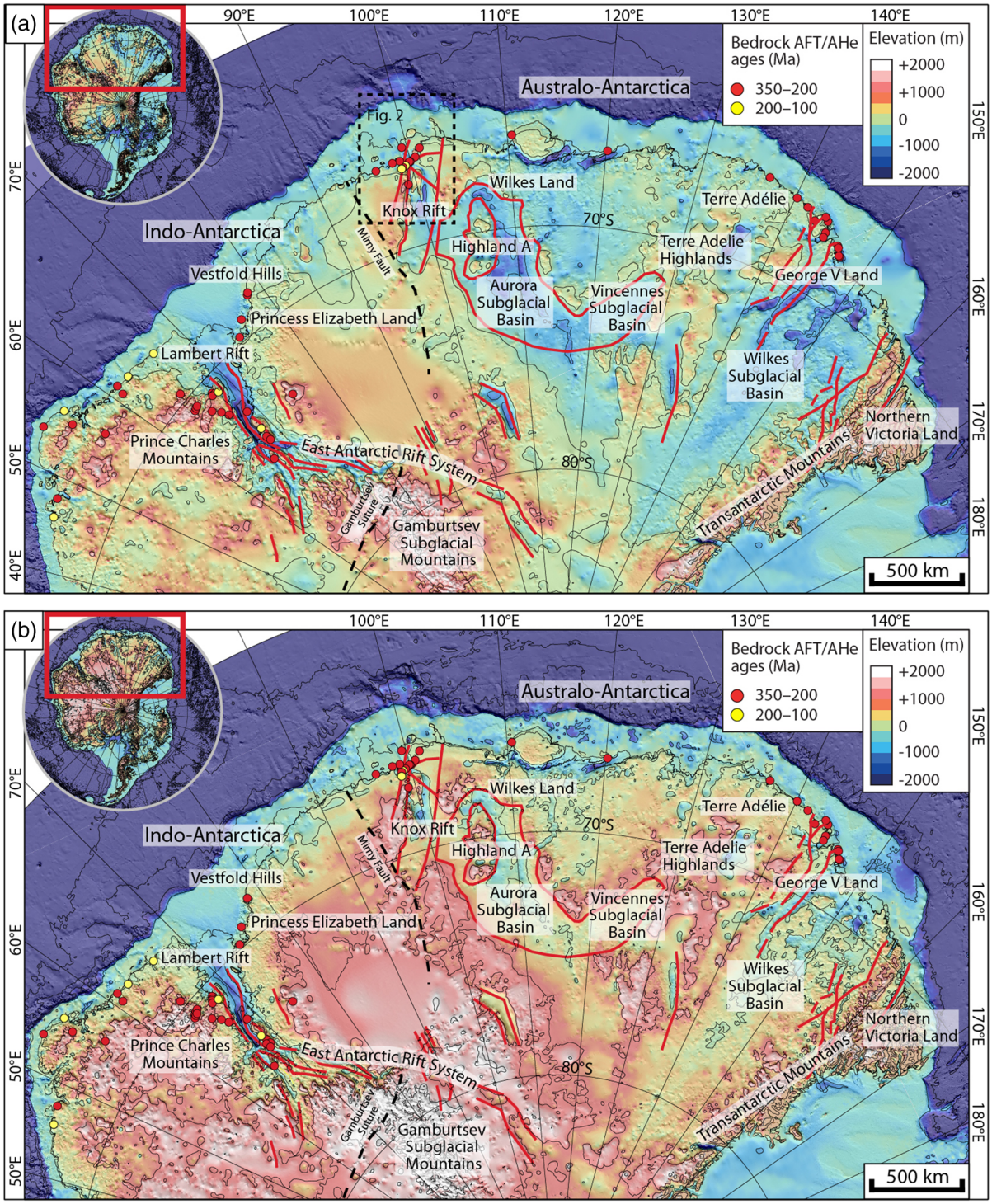

Figure 1. (a) Present-day bedrock topography of the Indo-Antarctic and Australo-Antarctic sectors of East Antarctica from BedMachine (Morlighem et al., 2020); (b) bedrock topography after isostatic rebound due to the removal of the present-day ice load (Paxman, Jamieson, Hochmuth, et al., 2019). Bedrock elevations on both grids are contoured at 1 km intervals. Colored circles show published bedrock AFT and AHe data from the Lambert Rift area (Arne, 1994; Lisker et al., 2003; Lisker, Gibson, et al., 2007), Vestfold Hills (Lisker, Wilson, & Gibson, 2007), and Terre Adélie/George V Land (Lisker & Olesch, 2003; Rolland et al., 2019) as well as reconnaissance AFT data of Arne et al. (1993). Sedimentary basin-bounding faults in the EARS (Ferraccioli et al., 2011), Knox Rift (Maritati et al., 2016), Aurora and Vincennes Subglacial Basins, (Aitken, Roberts, et al., 2016), Wilkes Subglacial Basin (Paxman, Jamieson, Ferraccioli, et al., 2019, and references therein) are highlighted in red; dashed black lines correspond to the inferred path the Mirny Fault (Daczko et al., 2018) and Gamburtsev Suture (Ferraccioli et al., 2011), which together represent the paleoplate boundary between Indo-Antarctica and Australo-Antarctica (Mulder et al., 2019); dashed box in panel (a) indicates a detail of the Bunger Hills region shown in Figure 2.

mechanisms of landscape evolution (Kohn & Gleadow, 2019). Existing LTT data from Precambrian basement outcrops in the Indo-Antarctic and Australo-Antarctic domains suggest major cooling of East Antarctic basement during the Paleozoic–Mesozoic (Figure 1); however, the significance of these observed Paleozoic–Mesozoic tectonothermal events across interior East Antarctica, and any link in establishing the different topographic response of each domain, remains elusive. In the Indo-Antarctic domain, apatite fission track (AFT) data from basement rocks in the northern Prince Charles Mountains (PCM) and Vestfold Hills record cooling associated with up to 5 km of basement exhumation during two discrete phases of continental rifting in the Lambert Rift (Arne, 1994; Lisker et al., 2003; Lisker, Gibson, et al., 2007; Lisker, Wilson, & Gibson, 2007) and broader East Antarctic Rift System (EARS; Ferraccioli et al., 2011) in the Late Paleozoic–Triassic (~310–200 Ma) and Cretaceous (~120–100 Ma). In the Australo-Antarctic domain west of the Transantarctic Mountains (TAM), AFT and apatite (U-Th)/He (AHe) data record a single Late Paleozoic–Triassic cooling event between ~350 and 200 Ma. This cooling has been interpreted to result from 3–4 km denudation triggered by either tectonic uplift synchronous with extension in the Wilkes Subglacial Basin (Lisker & Olesch, 2003), or denudation during large-scale glacial erosion of the Late Paleozoic Ice Age (Rolland et al., 2019). Investigations based on geophysical data and plate reconstructions have also suggested significant Cretaceous–Cenozoic onshore extensional tectonic activity in the interior of the Australo-Antarctic domain associated with plate divergence during the breakup of East Gondwana (Aitken et al., 2014; Eagles, 2019; Maritati et al., 2016) or intraplate strike-slip tectonics (e.g., Cianfarra & Maggi, 2017).

In this paper, we seek to establish a link between LTT data and Phanerozoic continent-scale geodynamic processes and the generation of variable hypsometry across East Antarctica. We use new (U-Th)/He data on zircon and apatite to reconstruct the low-temperature thermal evolution of Precambrian basement in the Bunger Hills region, located near the transition between high-relief regions of Indo-Antarctica and the low-lying subglacial basins of Australo-Antarctica. Our new results, combined with existing thermochronological, stratigraphic, and tectonic constraints, provide evidence for a major denudational event across the East Antarctic interior associated with Late Paleozoic–Triassic intracontinental extension. We interpret these new results in the context of their Pangea-wide tectonic setting and discuss the influence of topographic development at this stage on the landscape evolution of East Antarctica.

2. The Bunger Hills Region

Located in the western Wilkes Land sector of East Antarctica, the Bunger Hills region features a series of Precambrian–Early Cambrian coastal basement outcrops and remote inland nunataks, which together comprise the largest ice-free oasis in the western Australo-Antarctic domain (Tucker et al., 2020; Figure 2). These outcrops lie east of the inferred crustal boundary between Indo-Antarctica and Australo-Antarctica and record a complex tectonic history that culminated in the suturing of Australo-Antarctica and Indo-Antarctica along the Ediacaran–Cambrian Kuunga Orogen (Mulder et al., 2019). Exposed basement in the region forms the western flank of the Knox Rift, a Phanerozoic rift basin that is characterized solely from geophysical data (Maritati et al., 2016; Figure 2). The Knox Rift overprints basement and exerts a key influence on the regional topographic relief: While its flanks exhibit elevated (~1,200 m) and rugged topography, its central depression has focused erosion from the Denman and Scott Glaciers, two of the largest ice streams in the region, and hosts the deepest continental trench on Earth (Morlighem et al., 2020). The timing of extension in the Knox Rift, as well as the age of the sedimentary infill, is poorly known; plate reconstructions overall support a tectonic correlation with the Paleozoic–Mesozoic Perth Basin of western Australia within Gondwana. However, different phases of extension have been proposed in the Late Paleozoic–Triassic coeval with the Lambert Rift and EARS (Veevers, 2018) and during the Late Jurassic–Cretaceous separation of India from East Gondwana (Maritati et al., 2016).

3. Methods

3.1. (U-Th)/He Analysis

(U-Th)/He analysis was performed at the John de Laeter Centre (Curtin University, Perth). A summary of the samples used is given in the supporting information (Table S1). Apatite and zircon crystals of suitable size, shape, and quality were handpicked from mineral concentrates or plucked from epoxy mounts,

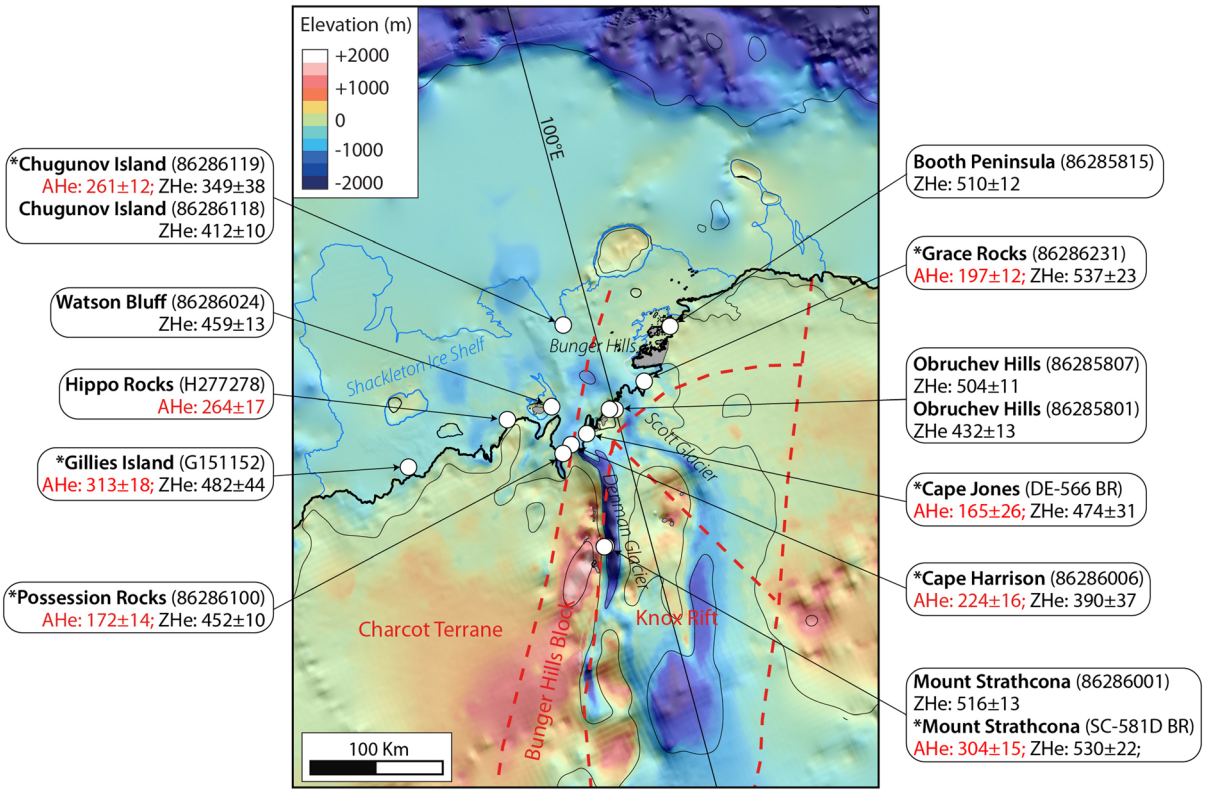

Figure 2. Bedrock topography map of Bunger Hills region showing exposed bedrock (gray areas), coastline (solid black line), and topographic contours at 1 km intervals (thin black lines). Simplified regional tectonic lineaments from Maritati et al. (2016) are shown as dashed red lines. The basement domains of the Bunger Hills Block and Charcot Terrane form the western flank of the Knox Rift. White circles represent location of Precambrian basement samples. For each sample, the weighted mean AHe (red) and ZHe ages (black) and respective 1σ uncertainties in Ma are indicated. Asterisks indicate samples for which modeled time-temperature (*t-T*) diagrams are presented in Figure 3.

previously used for U-Pb geochronology. Selected grains were then photographed and measured for dimensions to calculate alpha ejection correction factor and individually loaded in Pt (apatite) and Nb microtubes (zircon). Radiogenic ^{4}He was extracted at ~1250°C (zircon) or ~960°C (apatite) under ultrahigh vacuum using a diode laser, and its amount was determined by isotope dilution using ^{3}He spike on a Pfeiffer Prisma QMS 200 mass spectrometer. Following the ^{4}He measurements, microtubes containing the crystals were retrieved from the laser cell, spiked with ^{235}U and ^{230}Th, and dissolved in acids following the procedure of Evans et al. (2005), and the solutions were analyzed by isotope dilution for U and Th and by external calibration for Sm on an Agilent 7500 ICP-MS. Total analytical uncertainty of uncorrected (U-Th)/He ages was calculated by propagating uncertainties of U, Th, Sm, and He measurements. The uncorrected zircon (U-Th)/He (ZHe) and AHe ages were corrected for α-ejection (Ft correction) after Farley et al. (1996), whereby a homogenous distribution of U, Th, and Sm was assumed for the crystals. The accuracy of (U-Th)/He dating procedure was monitored by replicate analyses of Fish Canyon Tuff zircon (n = 11) and Durango apatite (n = 12) measured over the period of this study as internal standards, yielding mean (U-Th)/He ages of 29.2 ± 1.0 and 31.8 ± 1.1 Ma, respectively. These ages are in good agreement with the reference ages of 28.3 ± 1.3 Ma (Fish Canyon Tuff; Reiners et al., 2002) and 31.13 ± 1.01 Ma (Durango; McDowell et al., 2005). (U-Th)/He analytical results are presented in Table S2.

3.2. Time-Temperature Modeling of LTT Data

Inverse thermal history modeling was carried out using HeFTy v1.9 software (Ketcham, 2005) to find time-temperature (*t-T*) paths that that can reproduce measured thermochronological data and test plausible geological evolution scenarios. Only samples for which both zircon and apatite (U-Th)/He data are available were modeled. The models were parameterized as follows: Diffusion kinetic parameters for zircon and

apatite (U-Th)/He systems were adopted from Reiners et al. (2004) and Farley (2000), respectively; radii of the spherical diffusion domains were based on the measured size of the analyzed crystals and calculated equivalent sphere size; measured single-grain ages that were closest to the population mean age were modeled as representative for the samples. A Monte Carlo search method with 10,000 search tries was applied to find thermal trajectories that could reconcile the predefined parameters and constraints. "Acceptable" and "good" thermal paths were defined as having a goodness of fit (GOF) of >0.05 and >0.5, respectively.

4. Results and Interpretation

4.1. Zircon and Apatite (U-Th)/He Thermochronology Results

We report 72 zircon and 57 apatite single-grain (U-Th)/He ages from 14 basement outcrop samples from the western flank of the Knox Rift (Figure 2 and Table S2). Reproducibility of replicates within samples is good with the majority of single-grain ages overlapping within uncertainty. Our analysis shows that ZHe ages are in the range of ~537–365 Ma. In contrast, AHe ages are systematically younger than ZHe ages in each sample and range between ~313 and 165 Ma. AHe ages are consistent with an AFT age of 243 ± 13 Ma previously reported for a single sample from the Bunger Hills (Arne et al., 1993) and overall confirm the Late Paleozoic–Mesozoic age trend of AHe and AFT basement ages in the Indo-Antarctic and Australo-Antarctic domains. Sampling resolution is limited to mainly coastal and low-elevation basement outcrops hindering identification of spatial age trends across the Bunger Hills region. However, we note that AHe ages around the Denman and Scott glaciers (i.e., Possession Rocks, Cape Harrison, Cape Jones, and Grace Rocks) appear to form a cluster of relatively younger Triassic–Jurassic (224–165 Ma) ages while progressively older Late Carboniferous–Permian AHe ages occur to the west (Gillies Island and Hippo Rocks), south (Mount Strathcona), and north (Chugunov Island).

4.2. Phanerozoic Thermal History of the Bunger Hills Region

We explore the implications of the (U-Th)/He data for the Phanerozoic thermal history of Precambrian basement in the Bunger Hills region using *t-T* modeling of seven samples for which we have both ZHe and AHe data. To extract realistic thermal histories, we have incorporated in our models a framework of *t-T* constraints based on available geological constraints: In all model runs, the end of the *t-T* path was set to −10°C according to the present-day annual mean surface temperature recorded at the Antarctic station of Casey; the starting point was set to a temperature of 500°C at 550 Ma reflecting minimum peak temperatures during the Kuunga orogenic event. Although not exposed in outcrop, we presume that the contact between Precambrian basement and sedimentary rocks at the base of the Knox Rift likely forms an erosional unconformity. A similar erosional surface separating Precambrian basement rocks from the overlying glaciogenic Latest Carboniferous–Permian sedimentary sequences exists in the conjugate south Perth Basin in Australia (Norvick, 2004). We therefore incorporate this constraint in our models and force a cooling to near-surface temperatures ($T = -10$–20°C) between 350 and 300 Ma. Using these three fixed constraints, we model three different scenarios to test presence and magnitude of reheating during proposed extensional phases of the Knox Rift in the Late Paleozoic–Triassic (Veevers, 2018), Late Jurassic–Cretaceous (Maritati et al., 2016), and in both of these periods. Accordingly, for these periods we introduce additional constraints permitting temperatures of 30–220°C reflecting near-surface temperature conditions and maximum temperature limit of He retention in zircon, respectively. More specifically, the Late Paleozoic–Triassic extension was implemented by forcing reheating to temperatures between 30°C and 220°C during the Late Paleozoic–Triassic (300–200 Ma) from Carboniferous near-surface temperatures. Late Jurassic–Cretaceous extension was implemented by forcing the samples to a surface temperature of ~20°C in the Early Jurassic (200–160 Ma) from Carboniferous near-surface temperatures, followed by reheating between 30°C and 220°C in the Late Jurassic–Cretaceous (160–120 Ma). Finally, a two-stage extension scenario where Late Paleozoic–Triassic extension is followed by rapid cooling in the Late Triassic–Early Jurassic and renewed reheating in the Late Jurassic–Cretaceous was also implemented by combining the constraints of the two previous scenarios. In all models, timing of extension is calibrated to the conjugate Perth Basin which possesses well-documented stratigraphic and kinematic evidences for both a Late Paleozoic–Triassic and a Late Jurassic–Cretaceous extensional phase (Norvick, 2004). A summary of *t-T* modeling results is given in Figure 3 and in the supporting information (Table S3).

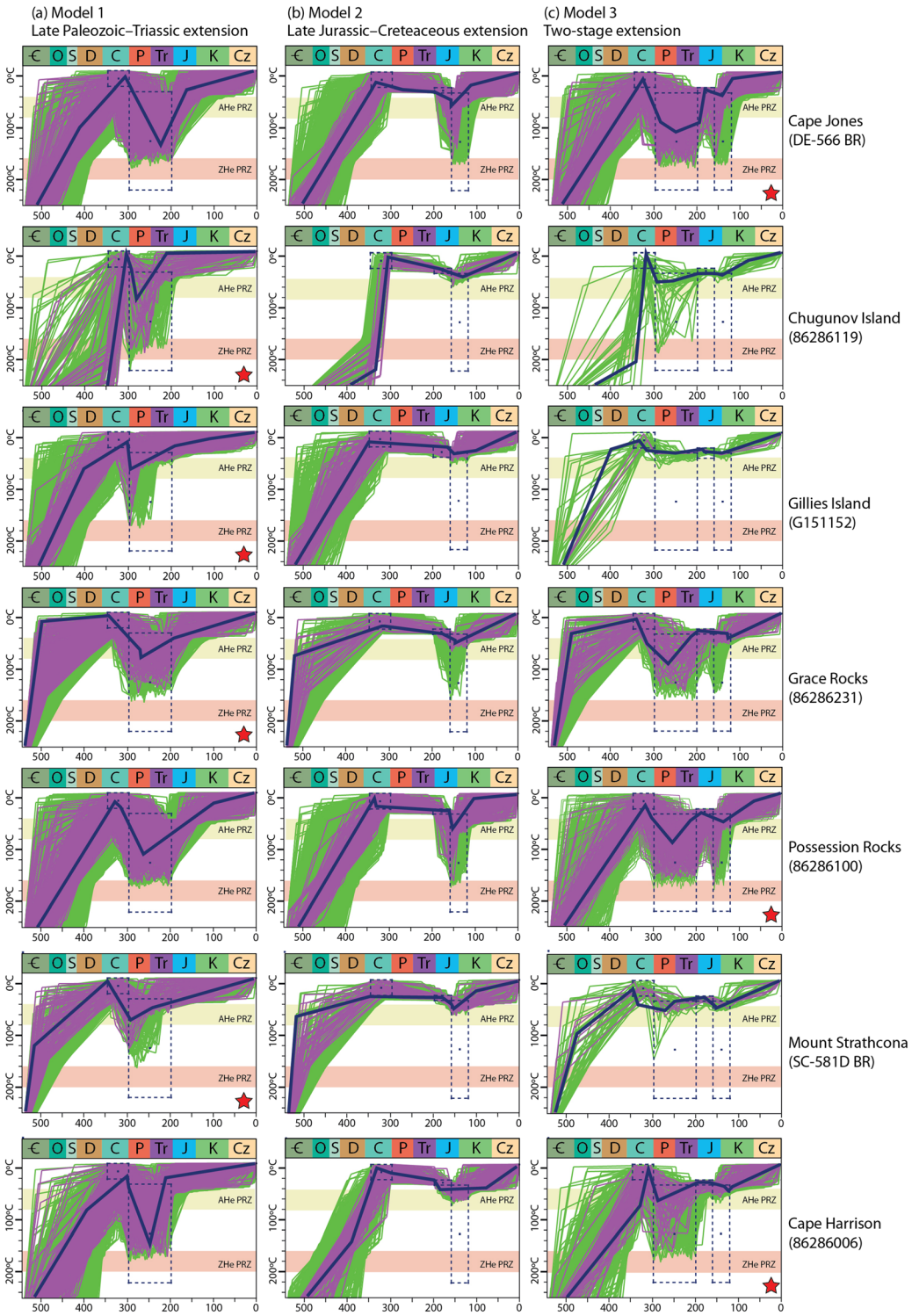

Figure 3. Modeled thermal histories of seven basement samples from the Bunger Hills region displayed as time-temperature (*t-T*) diagrams. *t-T* diagrams are shown for each of the three model scenarios (a–c). In each *t-T* diagram, green and pink lines indicate "acceptable" (GOF > 0.05) and "good" (GOF > 0.5) thermal trajectories, respectively; thick blue lines represent the best fit trajectories; dashed boxes represent predefined *t-T* constraints; red star indicates the preferred model scenario for each sample. Approximate temperature ranges of AHe partial retention zone (AHe PRZ, 40–80°C; Farley, 2000) and ZHe partial retention zone (ZHe PRZ, 160–200°C; Reiners et al., 2004) are also shown. Measured and modeled ZHe and AHe ages with their respective GOF values for each set of models are indicated in Table S3 in the supporting information.

Thermal history models reveal that cooling of Precambrian basement in the Bunger Hills region to near-surface temperatures (~30°C) after the Kuunga Orogeny 350–300 Ma must have been followed by at least one reheating-cooling episode between the Late Paleozoic and/or Cretaceous. Given that all our samples are located on the western rift flank in regions that are free of sedimentary cover and likely did not experience substantial (km-scale) burial of sedimentary rocks (Maritati et al., 2016), we infer the reheating-cooling episodes were achieved by an increase in the regional geothermal gradient due to rift-related processes.

Thermochronology data for Gillies Island, Mount Strathcona, Grace Rocks, and Chugunov Island are best reproduced with a single reheating-cooling episode in the Late Paleozoic–Triassic reaching peak temperatures of ~90–60°C (Figure 3a). Paleogeothermal gradient estimates during extension in the Lambert Rift suggest an increase to ~30°C km^{-1} in the vicinity of the rift from a stable geothermal gradient of 19–20°C km^{-1} (Lisker et al., 2003). Similar estimates may be also reasonable during extension in the Knox Rift, where a geothermal gradient increase of similar magnitude (~10°C km^{-1}) would explain the resetting of AHe systems from near-surface temperatures in basement samples on the western rift flank (Figure 4a). Cooling of basement samples at Gillies Island, Mount Strathcona, Grace Rocks, and Chugunov Island was most likely produced by thermal relaxation of the rift-related anomaly; for any assumed geothermal gradient estimates between 20°C km^{-1} and 30°C km^{-1}, cooling must have been associated with a maximum exhumation and erosion of ~ 2–4 km of basement overburden at these localities (Figure 4a). Thermal models for these samples also indicate that a phase of reheating between ~160 and 120 Ma is unlikely as samples could not exceed temperatures of 40°C in both the Late Jurassic–Cretaceous extension and two-stage extension scenarios (Figures 3b and 3c).

Thermal histories for Cape Jones, Cape Harrison, and Possession Rocks permit reheating to temperatures greater than 40°C in the Late Paleozoic–Triassic, Late Jurassic–Cretaceous, or in both these intervals (Figures 3a–3c). Maximum paleotemperatures in models simulating a single reheating phase in the Late Paleozoic–Triassic range between 160°C and 120°C and require the development of a substantially elevated paleogeothermal gradient in excess of 60°C km^{-1} (Figure 3a). The two-stage extension scenario, in contrast, suggests lower Late Paleozoic–Triassic maximum paleotemperatures of ~90–60°C, which are consistent with those extracted from the Gillies Island, Mount Strathcona, Grace Rocks, and Chugunov Island samples and indicate ~2 km of post-Permian basement exhumation (Figures 3c and 4b). Furthermore, it allows for a second phase of modest rift-related reheating of basement to temperatures of ~40–50°C from Late Jurassic surface temperatures of 20°C in the Late Jurassic–Cretaceous, which indicates ≤1 km of post-Cretaceous basement exhumation (assuming a paleogeothermal gradient of ~20–30°C km^{-1}) in addition to ~2 km of Permian–Jurassic basement exhumation (Figure 4b).

In summary, thermal history models support regional cooling to Late Paleozoic near-surface temperatures after the Kuunga tectonothermal event, followed by reheating and cooling through ~90–60°C during Late Paleozoic–Triassic triggered by the rift-related thermal anomaly and exhumation of Precambrian basement on the western rift flank. The magnitude of cooling suggests ~2–4 km exhumation for reasonable amounts of assumed paleogeothermal gradients. A second thermal event in the Late Jurassic–Cretaceous and minor exhumation of ≤1 km is identified locally in three samples near the coast and may be associated with localized reactivation of rift structures during the onset of early rifting between Antarctica, Australia, and India. These results are consistent with the establishment of topographic relief during continental extension and associated rift flank basement uplift predominantly in the Late Paleozoic–Triassic, with additional localized uplift during the Late Jurassic–Cretaceous in the Denman Glacier area.

5. Discussion

5.1. Phanerozoic Thermal History of the Indo-Antarctic and Australo-Antarctic Basement

Inversion of thermochronological data allowed to interrogate the low-temperature thermal history of Precambrian basement in the Bunger Hills region, providing key constraints to understand the pattern and magnitude of cooling, and to reconstruct the morphotectonic evolution of this sector of East Antarctica during the Phanerozoic. Circa 313–200 Ma AHe ages from the Bunger Hills region are consistent with the predominantly Late Paleozoic–Triassic age trend recorded by previously published AFT and AHe thermochronometers in the Indo-Antarctic and Australo-Antarctic domains, supporting a single

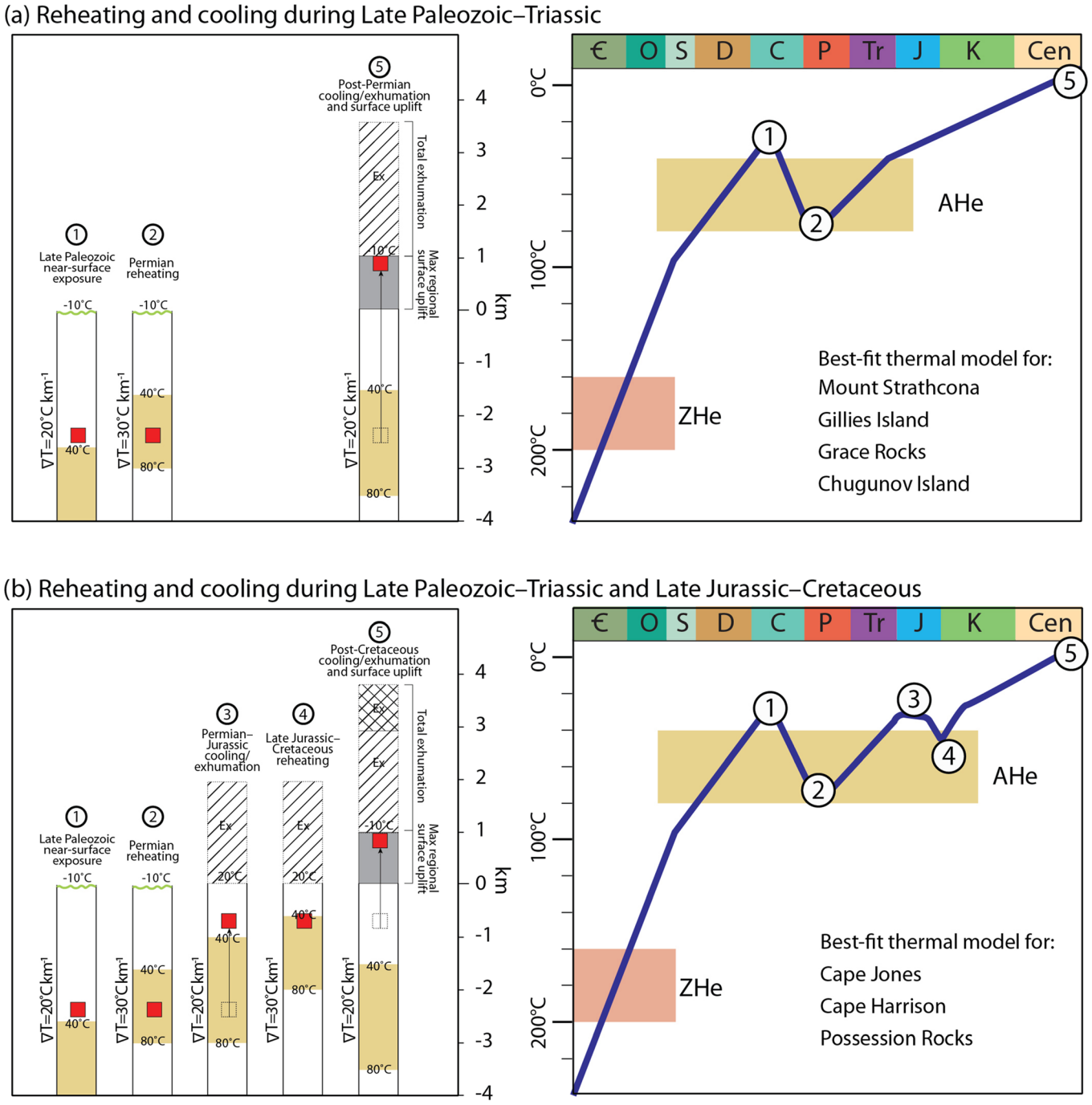

Figure 4. Schematic representation of the relationship between reheating-cooling episodes of basement samples (red squares) and rock uplift with respect to best fit time-temperature (*t-T*) trajectories modeled for the (a) Late Paleozoic–Triassic extension scenario and (b) two-stage extension scenario. Rock uplift equals to the amount of exhumation (Ex) plus the amount of surface uplift (gray shading) with respect to a reference surface (England & Molnar, 1990). Surface temperature used in *t-T* models and approximate temperature ranges of AHe partial retention zone (AHe PRZ, 40–80°C, brown fill; Farley, 2000) and ZHe partial retention zone (ZHe PRZ, 160–200°C, red fill; Reiners et al., 2004) are also shown.

large-scale cooling event of East Antarctic basement from temperatures of at least 120°C (upper limit of AFT partial annealing zone [PAZ]; Wagner et al., 1989). Our thermal models suggest that the cooling pattern of Precambrian basement in the Bunger Hills region requires ~2–4 km exhumation during Late Paleozoic–Triassic (~300–200 Ma) intracontinental extension in the Knox Rift. This interpretation is consistent with

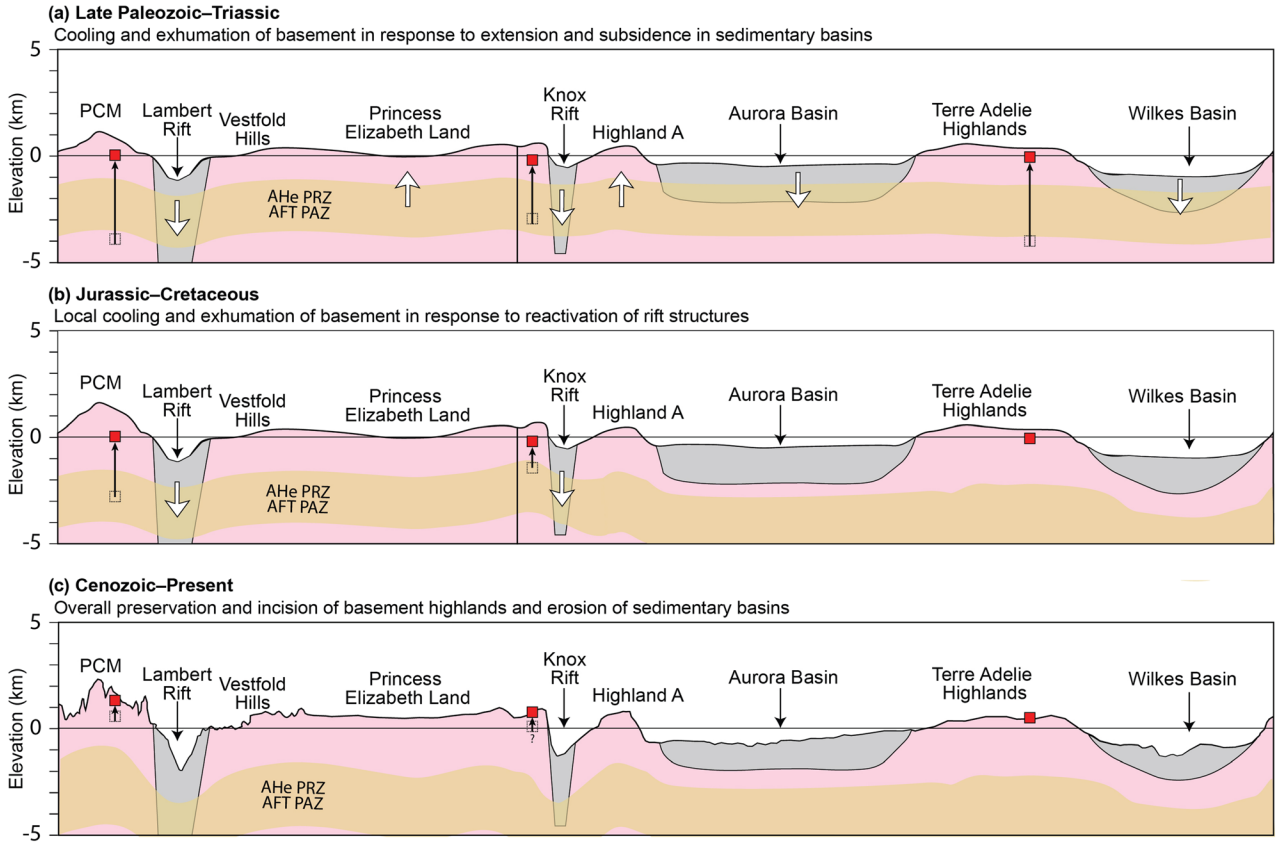

Figure 5. Conceptual cartoon illustrating the interpreted morphotectonic evolution of the Indo-Antarctic and Australo-Antarctic domains. (a) Exhumation of Precambrian basement in response to widespread extension and subsidence in sedimentary basins during Pangea-wide rifting. (b) Exhumation of Precambrian basement in response to reactivation of structures during the Jurassic–Cretaceous breakup of East Gondwana (i.e., Lambert and Knox Rifts). (c) Slow cooling of uplifted basement to present-day surface temperatures and overall preservation of high-standing topographic features throughout the Cenozoic. In each panel, red squares represent the position of representative samples as inferred from LTT data. Approximate temperature ranges of the combined AHe PRZ and AFT PAZ (40–120°C) are shown in each panel. For accuracy, we show the possible effects of increased geothermal gradient during rifting phases and the influence of finite-amplitude topography on the morphology of the combined AHe PRZ and AFT PAZ in each schematic profile. Elevations in the Late Paleozoic–Triassic and Jurassic–Cretaceous panels are approximate.

the timing and style of Late Paleozoic–Triassic cooling and exhumation associated with extension in the Lambert Rift (Lisker et al., 2003), and the Wilkes Subglacial Basin (Lisker & Olesch, 2003), and indicates that the East Antarctic basement between the Lambert Rift and George V Land may have been part of a single denudational system. We therefore suggest that the uplift and erosion of large sections of Precambrian basement during Late Paleozoic–Triassic intracontinental extension provide an explanation for the cooling pattern of AFT and AHe systems in Precambrian basement rocks across both Indo-Antarctica and Australo-Antarctica which can be reconciled with the tectonic and topographic response of extension in the Lambert Rift–EARS, Knox Rift, and Wilkes Subglacial Basin (Figure 5a). Furthermore, the formation of high-relief topography in the vicinity of these tectonic structures requires coeval basement exhumation and subsidence in the basins and is incompatible with the concept of large-scale homogenous denudation of East Antarctic basement during the Late Paleozoic Ice Age (~340–300 Ma) proposed by Rolland et al. (2019).

Our thermal modeling results allow modest localized Late Jurassic–Cretaceous cooling of basement in the Bunger Hills region during East Gondwana breakup from palaeotemperatures of ~40°C, which refers to an additional ≤1 km of exhumation in the Denman Glacier area. These estimates do not support significant regional exhumation of a magnitude comparable to the ~4 km Cretaceous exhumation across the Lambert Rift (Arne, 1994; Lisker et al., 2003) and are instead overall consistent with the slow and meager denudation of the low-standing margin segments of the Australo-Antarctic domain as suggested by AFT results reported

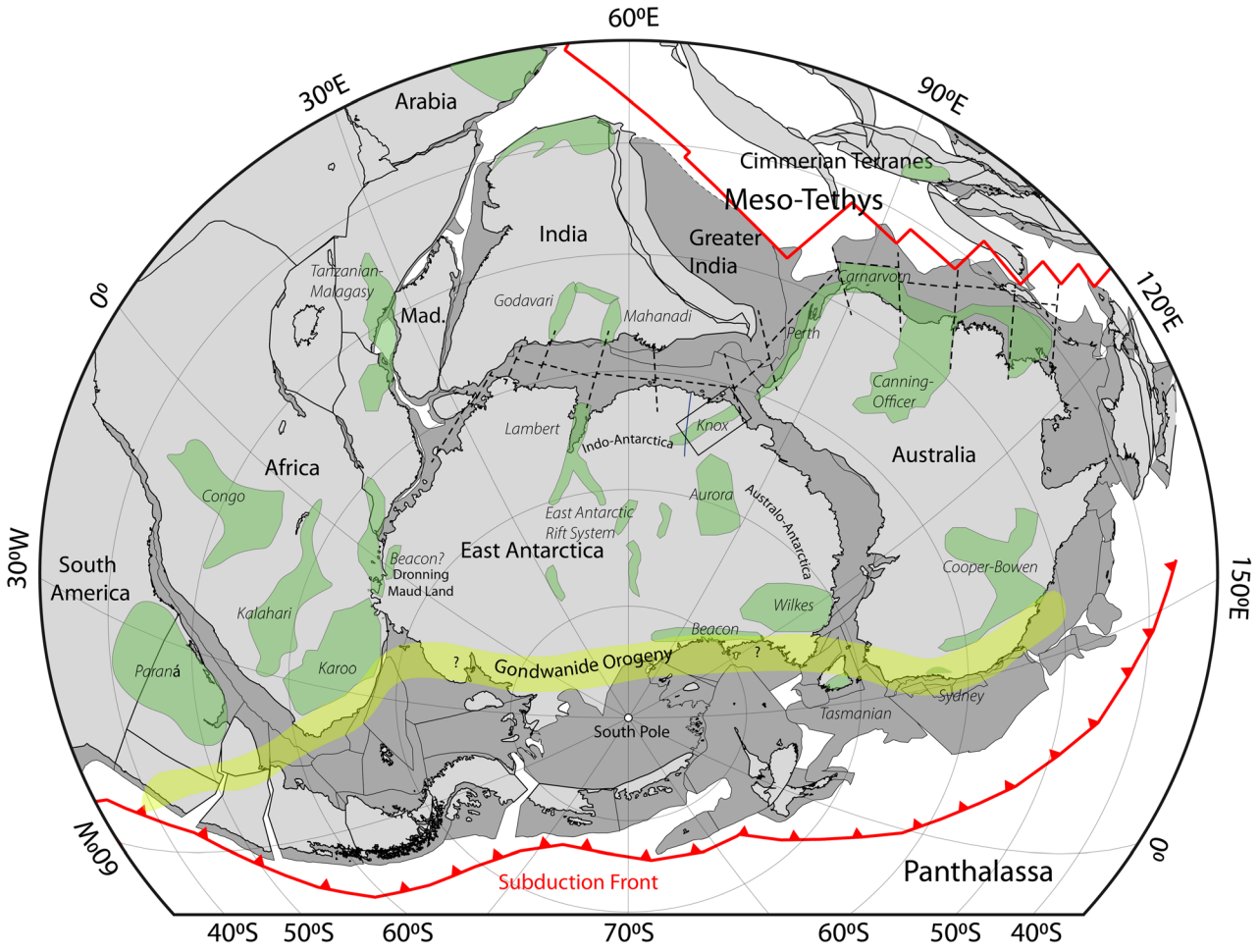

Figure 6. Permian Gondwana tectonic reconstruction (~270 Ma) using GPlates and plate geometries and rotation poles of Matthews et al. (2016). Widespread extensional deformation across the supercontinent was driven by plate convergence along the Panthalassan margin and rifting on the northern margin of Gondwana which resulted in the separation of the Cimmerian Continent and opening of the Meso-Tethys behind it (Metcalfe, 2013). The intracontinental East Gondwanan Late Carboniferous–Triassic rift system (dashed black line; modified from Harrowfield et al., 2005), the distribution of sedimentary basins containing the Pangea Megasequence (green polygons; after Wopfner & Jin, 2009), and the approximate location of the Gondwanide orogenic front (yellow shading) are also shown. The location of the Bunger Hills region and Knox Rift is indicated by the black box.

by Arne et al. (1993) and Lisker and Olesch (2003) (Figure 5b). We therefore suggest that if any significant Cretaceous or younger thermal events between the Bunger Hills region and the TAM occurred, these must be limited in terms of cooling and denudation and therefore not recorded by currently available LTT at the coast.

5.2. Linking Late Paleozoic–Triassic Cooling to Geodynamic Processes and Topographic Relief

The widespread Late Paleozoic–Triassic heating-cooling pattern of East Antarctic basement overlaps with a major phase of thermal instability throughout Pangea marked by geodynamic activity at the periphery of the supercontinent (Frizon de Lamotte et al., 2015). During this time, the propagation of far-field stresses from active plate boundaries resulted in large-scale intracontinental extension and the deposition of ~300–200 Ma Pangea Megasequences in sedimentary basins across all former Gondwana continents (Wopfner & Jin, 2009; Figure 6). We suggest that this phase of extensive intracontinental extension across the hinterland of Gondwana triggered the exhumation of large sections of Precambrian basement in the continental interior of East Antarctica (Figure 5a). Plate convergence along the Panthalassan convergent margin (Veevers & Powell, 1994) led to the deposition of the foreland and back-arc deposits of the Beacon Supergroup in the Wilkes Subglacial Basin (Ferraccioli et al., 2009) and TAM (Elliot, 2013) in Antarctica and the Cooper-Bowen, Sydney (Korsch et al., 2009), and Tasmanian (Fielding et al., 2010) basins of eastern Australia.

Divergence on the northern Gondwana margin resulted in the opening of the Paleo-Tethys Ocean and in the development of a complex Late Carboniferous–Triassic intra-Gondwana rift system (Harrowfield et al., 2005) which includes the Lambert Rift–EARS and Knox Rift together with their Indian (i.e., Mahanadi Basin; Veevers & Tewari, 1995) and Australian (i.e., Perth Basin; Norvick, 2004) conjugate basins. Finally, thermal sag and transtension controlled large Permian–Triassic interior basins like those of central Australia (e.g., Canning and Cooper basins; Wopfner, 1980), subequatorial western Africa (e.g., Congo and Karoo basins; Catuneanu et al., 2005) and South America (e.g., Parana Basin; Zalán et al., 1990). A similar geodynamic origin may be plausible for the broad Aurora Subglacial Basin in the interior of the Australo-Antarctic domain where Late Paleozoic–Mesozoic intracontinental transtension along large-scale faults has been proposed (Aitken, Betts, et al., 2016). Together, these geodynamic processes provide a driver for extensional tectonic activity onshore East Antarctica, which can be reconciled with thermochronological, structural, and stratigraphic evidence supporting widespread Late Paleozoic–Triassic extension. Furthermore, the pattern of ~350–200 Ma AFT and AHe cooling ages on basement highs near Late Paleozoic–Triassic depocenters supports the formation of topographic relief predominantly via differential basement uplift during Late Paleozoic–Triassic intracontinental extension. Low-magnitude denudation of sections of uplifted basement may have also provided sediment sources for intracontinental basins in East Antarctica and on adjacent continents (e.g., Australia; Morón et al., 2019).

While the imprint of Late Paleozoic–Triassic Pangea-wide tectonics is widespread in both the Indo-Antarctic and Australo-Antarctic domains, significant Jurassic–Cretaceous thermal events associated with the breakup of East Gondwana are not equally observed across the two domains (Figure 5b). In the Indo-Antarctic domain, Cretaceous cooling and exhumation of Precambrian basement occurs locally in the Lambert Rift and may be coincident with reactivation of older Late Paleozoic–Triassic structures during large igneous province activity and/or continental rifting between East Antarctica and India (Lisker et al., 2003; Lisker, Gibson, et al., 2007). Geophysical models also predict significant Cretaceous uplift in the interior of the Indo-Antarctic domain along the EARS (Ferraccioli et al., 2011); however, Cretaceous cooling ages are not documented in the offshore detrital LTT record of Prydz Bay (Tochilin et al., 2012), and any significant Cretaceous extensional tectonism in the interior remains therefore poorly constrained. In the Australo-Antarctic domain, onshore Cretaceous–Cenozoic tectonic activity had been suggested on the basis of geophysical data and plate reconstructions (Aitken et al., 2014; Cianfarra & Maggi, 2017; Eagles, 2019; Maritati et al., 2016). However, limited post-Triassic cooling reported across the Australo-Antarctic domain indicates that rifting between Australia and Antarctica did not significantly impact the long-term landscape evolution of the domain and may have only produced local and relatively minor denudational responses (cf. Bunger Hills region).

The record of large-scale topographic evolution driven by Paleozoic–Mesozoic extensional events helps to fill a critical gap in our understanding of the mechanisms responsible for relief variability in the East Antarctic interior. We propose that large-scale variations in amplitude and wavelength of topographic relief across Indo-Antarctica and Australo-Antarctica can largely be accounted for by the effects of intracontinental rifting of Precambrian crust during the Late Paleozoic–Triassic and the subsequent local reactivation of rift structures during Jurassic–Cretaceous breakup of East Gondwana. Phases of continental extension in the Lambert Rift, EARS, and Knox Rift produced narrow rift zones which are responsible for the majority of the high-relief topography that is characteristic of Indo-Antarctic domain and the Bunger Hills region across the transition with the Australo-Antarctic domain. The extensional regime marked by Late Paleozoic–Triassic thermal sag and back-arc extension in most of the Australo-Antarctic domain may instead have led to a more diffuse deformation and the overall low-amplitude long-wavelength topography that characterizes the Australo-Antarctic domain.

5.3. Influence of Tectonic Relief on the Long-Term Landscape Evolution of East Antarctica

The interpreted morphotectonic evolution of the Indo-Antarctic and Australo-Antarctic domains highlights the key role of Paleozoic–Mesozoic tectonic relief in influencing the long-term landscape evolution of East Antarctica. Paleozoic–Mesozoic LTT bedrock ages indicate low long-term erosion rates (10–20 m Ma^{-1}) for uplifted basement highs and suggest the overall preservation of high-standing topographic features at broad wavelengths throughout the Cenozoic (Figure 5c). Subglacial basement highs in the continental interior may also represent tectonically uplifted basement and be characterized by similarly low erosion rates as

suggested by detrital LTT studies (e.g., Cox et al., 2010). Examples of such regions are Highland A in the Aurora Subglacial Basin and Terre Adélie Highlands in Australo-Antarctica, as well as plateau regions such as Princess Elizabeth Land in Indo-Antarctica, all of which can be seen at isostatically rebounded elevations of 1,500–2,000 m (Figure 1b). Flexural models for high-standing bedrock in the Gamburtsev Subglacial Mountains demonstrate that fluvial incision and alpine-style glacial erosion may have also contributed to the long-term landscape evolution of basement highs and be responsible for ~500–700 m of flexural uplift in response to unloading (Paxman et al., 2016). However, the magnitude of cooling and denudation associated with these events is below the detection limit of the AHe and AFT methods, which requires at least 2–3 km of denudation.

Long-term erosion was instead preferentially steered within sedimentary basins, reflecting the strong contrast in erodibility potential between cover sediments and crystalline rocks. However, we suggest that the different morphologies inherited from Late Paleozoic–Triassic extension had a profound influence on the style of erosion. Narrow rifts such as the Lambert and Knox Rifts focused on fluvial and glacial erosion, which caused amplification of topographic relief through selective erosion (Jamieson et al., 2005; Maritati et al., 2016; Thomson et al., 2013) and associated flexural uplift of these structures (Paxman et al., 2016). In contrast, the broad and low-elevation morphology of basins in the central Australo-Antarctic domain allowed for the development of larger fluvial braided systems and river deltas (Paxman, Jamieson, Ferraccioli, et al., 2019; Sauermilch et al., 2019), which provided a substantial amount of detrital material to the Gondwana breakup passive margin basins (Sauermilch et al., 2019). The expansion of the East Antarctic Ice Sheet since the Eocene exacerbated these conditions with high erosion rates (~100 m Ma^{-1}) in the Lambert Rift (Thomson et al., 2013) and dynamic erosion from a marine-based ice sheet in the Aurora (Young et al., 2011) and Wilkes Subglacial Basin (Paxman et al., 2018; Paxman, Jamieson, Ferraccioli, et al., 2019). Together, these observations suggest that tectonic-controlled relief has exerted a key influence on long-term denudation rates and the evolution of the subglacial landscape of East Antarctica, providing a unique example of a continental interior where long-term erosion and associated dynamic responses (i.e., flexure) over millions of years acted to reinforce preexisting topographic relief.

6. Conclusions

We present a model for the origin of topography in the sector of interior East Antarctica between the Lambert Rift and George V Land which establishes a link between Paleozoic–Mesozoic AFT and AHe cooling ages and continent-scale geodynamic processes. We used new ZHe and AHe data from Precambrian basement outcrops to determine the timing, magnitude, and style of Phanerozoic cooling of the Bunger Hills region, a poorly exposed section of East Antarctic basement near the boundary between the two large-scale basement domains of Indo-Antarctica and Australo-Antarctica. Our results indicate that Precambrian basement experienced cooling and ~2–4 km regional exhumation during the Late Paleozoic–Triassic associated with the formation of the Knox Rift, followed by a second episode of localized cooling and $\leq$1 km exhumation associated with the reactivation of rift structures during the Late Jurassic–Cretaceous separation of India from East Gondwana. Late Paleozoic–Triassic cooling and exhumation in the Bunger Hills region is consistent with the timing and magnitude of rift-related cooling and exhumation reported in the Lambert Rift and George V Land, suggesting a single denudational system driven by Pangea-wide extension. We propose that this event had a profound impact on the formation of topographic relief of East Antarctica via the exhumation of large sections of basement and the formation of vast intracontinental sedimentary deposits across the East Antarctic interior. By contrast, extension associated with the Jurassic–Cretaceous breakup of East Gondwana did not provide an equally widespread denudational response across the East Antarctic interior. The topographic framework formed during the Paleozoic–Mesozoic had a significant impact on the long-term landscape evolution of East Antarctica and provided a template for Cenozoic erosion on the continent.

Data Availability Statement

New zircon and apatite (U-Th)/He data are made available in the supporting information (Table S2) and can also be downloaded from the Australian Antarctic Data Centre (following the link https://data.aad.gov.au/metadata/records/AAS_4460_Thermochronology).

Acknowledgments

This research is supported through funding from the Australian Government's Australian Antarctic Program (Project ID 4460) and the Australian Research Council's Special Research Initiative for Antarctic Gateway Partnership (Project ID SR140300001). A. M. is supported by an Australian Government Research Training Program (RTP) Scholarship. M. D. was supported by ARC Discovery funding scheme (DP160102427), the AuScope NCRIS2 program and Curtin Research Fellowship. M. D. acknowledges the help of C. May, C. Scadding, and A. Frew with solution ICP-MS analyses, and I. Dunkl for sharing PepiFLEX software for ICP-MS data reduction. We thank Fausto Ferraccioli and an anonymous reviewer for their constructive criticism and helpful comments which greatly helped improve the manuscript.

References

Aitken, A. R. A., Betts, P. G., Young, D. A., Blankenship, D. D., Roberts, J. L., & Siegert, M. J. (2016). The Australo-Antarctic Columbia to Gondwana transition. *Gondwana Research*, *29*(1), 136–152. https://doi.org/10.1016/j.gr.2014.10.019

Aitken, A. R. A., Roberts, J. L., van Ommen, T. D., Young, D. A., Golledge, N. R., Greenbaum, J. S., et al. (2016). Repeated large-scale retreat and advance of Totten Glacier indicated by inland bed erosion. *Nature*, *533*(7603), 385–389. https://doi.org/10.1038/nature17447

Aitken, A. R. A., Young, D. A., Ferraccioli, F., Betts, P. G., Greenbaum, J. S., Richter, T. G., et al. (2014). The subglacial geology of Wilkes Land, East Antarctica. *Geophysical Research Letters*, *41*, 2390–2400. https://doi.org/10.1002/2014gl059405

Arne, D. C., Kelly, P. R., Brown, R. W., & Gleadow, A. (1993). Reconnaissance apatite fission-track data from the East Antarctic Shield. In *Gondwana symposium* (pp. 605–611).

Arne, D. C. (1994). Phanerozoic exhumation history of northern Prince Charles Mountains (East Antarctica). *Antarctic Science*, *6*(1), 69–84. https://doi.org/10.1017/S0954102094000106

Catuneanu, O., Wopfner, H., Eriksson, P., Cairncross, B., Rubidge, B., Smith, R., & Hancox, P. (2005). The Karoo basins of south-central Africa. *Journal of African Earth Sciences*, *43*(1–3), 211–253. https://doi.org/10.1016/j.jafrearsci.2005.07.007

Cianfarra, P., & Maggi, M. (2017). Cenozoic extension along the reactivated Aurora fault system in the East Antarctic Craton. *Tectonophysics*, *703-704*, 135–143. https://doi.org/10.1016/j.tecto.2017.02.019

Cox, S. E., Thomson, S. N., Reiners, P. W., Hemming, S. R., & van de Flierdt, T. (2010). Extremely low long-term erosion rates around the Gamburtsev Mountains in interior East Antarctica. *Geophysical Research Letters*, *37*, L22307. https://doi.org/10.1029/2010gl045106

Creyts, T. T., Ferraccioli, F., Bell, R. E., Wolovick, M., Corr, H., Rose, K. C., et al. (2014). Freezing of ridges and water networks preserves the Gamburtsev Subglacial Mountains for millions of years. *Geophysical Research Letters*, *41*, 8114–8122. https://doi.org/10.1002/2014GL061491

Daczko, N. R., Halpin, J. A., Fitzsimons, I. C. W., & Whittaker, J. M. (2018). A cryptic Gondwana-forming orogen located in Antarctica. *Scientific Reports*, *8*(1), 8371. https://doi.org/10.1038/s41598-018-26530-1

Eagles, G. (2019). A little spin in the Indian Ocean plate circuit. *Tectonophysics*, *754*, 80–100. https://doi.org/10.1016/j.tecto.2019.01.015

Elliot, D. H. (2013). The geological and tectonic evolution of the Transantarctic Mountains: A review. *Geological Society, London, Special Publications*, *381*(1), 7–35. https://doi.org/10.1144/sp381.14

England, P., & Molnar, P. (1990). Surface uplift, uplift of rocks, and exhumation of rocks. *Geology*, *18*(12), 1173–1177. https://doi.org/10.1130/0091-7613(1990)018<1173:Suuora>2.3.Co;2

Evans, N., Wilson, N., Cline, J., McInnes, B., & Byrne, J. (2005). Fluorite (U–Th)/He thermochronology: Constraints on the low temperature history of Yucca Mountain, Nevada. *Applied Geochemistry*, *20*(6), 1099–1105. https://doi.org/10.1016/j.apgeochem.2005.02.008

Farley, K. (2000). Helium diffusion from apatite: General behavior as illustrated by Durango fluorapatite. *Journal of Geophysical Research*, *105*(B2), 2903–2914. https://doi.org/10.1029/1999JB900348

Farley, K., Wolf, R., & Silver, L. (1996). The effects of long alpha-stopping distances on (U–Th)/He ages. *Geochimica et Cosmochimica Acta*, *60*(21), 4223–4229. https://doi.org/10.1016/S0016-7037(96)00193-7

Ferraccioli, F., Armadillo, E., Jordan, T., Bozzo, E., & Corr, H. (2009). Aeromagnetic exploration over the East Antarctic Ice Sheet: A new view of the Wilkes Subglacial Basin. *Tectonophysics*, *478*(1–2), 62–77. https://doi.org/10.1016/j.tecto.2009.03.013

Ferraccioli, F., Finn, C. A., Jordan, T. A., Bell, R. E., Anderson, L. M., & Damaske, D. (2011). East Antarctic rifting triggers uplift of the Gamburtsev Mountains. *Nature*, *479*(7373), 388–392. https://doi.org/10.1038/nature10566

Fielding, C. R., Frank, T. D., Isbell, J. L., Henry, L. C., & Domack, E. W. (2010). Stratigraphic signature of the late Palaeozoic Ice Age in the Parmeener Supergroup of Tasmania, SE Australia, and inter-regional comparisons. *Palaeogeography, Palaeoclimatology, Palaeoecology*, *298*(1–2), 70–90. https://doi.org/10.1016/j.palaeo.2010.05.023

Frederick, B. C., Young, D. A., Blankenship, D. D., Richter, T. G., Kempf, S. D., Ferraccioli, F., & Siegert, M. J. (2016). Distribution of subglacial sediments across the Wilkes Subglacial Basin, East Antarctica. *Journal of Geophysical Research: Earth Surface*, *121*, 790–813. https://doi.org/10.1002/2015jf003760

Frizon de Lamotte, D., Fourdan, B., Leleu, S., Leparmentier, F., & de Clarens, P. (2015). Style of rifting and the stages of Pangea breakup. *Tectonics*, *34*, 1009–1029. https://doi.org/10.1002/2014tc003760

Harrowfield, M., Holdgate, G. R., Wilson, C. J. L., & McLoughlin, S. (2005). Tectonic significance of the Lambert graben, East Antarctica: Reconstructing the Gondwanan rift. *Geology*, *33*(3), 197. https://doi.org/10.1130/g21081.1

Hu, J., Liu, L., Faccenda, M., Zhou, Q., Fischer, K. M., Marshak, S., & Lundstrom, C. (2018). Modification of the western Gondwana craton by plume–lithosphere interaction. *Nature Geoscience*, *11*(3), 203–210. https://doi.org/10.1038/s41561-018-0064-1

Jamieson, S. S. R., Hulton, N. R. J., Sugden, D. E., Payne, A. J., & Taylor, J. (2005). Cenozoic landscape evolution of the Lambert basin, East Antarctica: The relative role of rivers and ice sheets. *Global and Planetary Change*, *45*(1–3), 35–49. https://doi.org/10.1016/j.gloplacha.2004.09.015

Ketcham, R. A. (2005). Forward and inverse modeling of low-temperature thermochronometry data. *Reviews in Mineralogy and Geochemistry*, *58*(1), 275–314. https://doi.org/10.2138/rmg.2005.58.11

Kohn, B., & Gleadow, A. (2019). Application of low-temperature thermochronology to craton evolution. In M. G. Malusà, & P. G. Fitzgerald (Eds.), *Fission-track thermochronology and its application to geology* (pp. 373–393). Cham: Springer International Publishing. https://doi.org/10.1007/978-3-319-89421-8_21

Korsch, R. J., Totterdell, J. M., Cathro, D. L., & Nicoll, M. G. (2009). Early Permian east Australian rift system. *Australian Journal of Earth Sciences*, *56*(3), 381–400. https://doi.org/10.1080/08120090802698703

Lisker, F., Brown, R., & Fabel, D. (2003). Denudational and thermal history along a transect across the Lambert Graben, northern Prince Charles Mountains, Antarctica, derived from apatite fission track thermochronology. *Tectonics*, *22*(5), 1055. https://doi.org/10.1029/2002TC001477

Lisker, F., Gibson, H., Wilson, C., & Läufer, A. (2007). Denudation and uplift of the Mawson Escarpment (eastern Lambert Graben, Antarctica) as indicated by apatite fission track data and geomorphological observation. *Antarctica. In: Cooper, AK & Raymond, CR (eds) A Keystone in a Changing World–Online Proceedings of the 10th ISAES. USGS Open-File Report, 6*.

Lisker, F., & Olesch, M. (2003). Long-term landscape evolution of George V Land as indicated by fission track data. *Terra Antartica*, *10*(3), 249–256. Retrieved from. https://eurekamag.com/research/019/337/019337137.php

Lisker, F., Wilson, C. J. L., & Gibson, H. J. (2007). Thermal history of the Vestfold Hills (East Antarctica) between Lambert rifting and Gondwana break-up, evidence from apatite fission track data. *Antarctic Science*, *19*(1), 97–106. https://doi.org/10.1017/s0954102007000144

Maritati, A., Aitken, A. R. A., Young, D. A., Roberts, J. L., Blankenship, D. D., & Siegert, M. J. (2016). The tectonic development and erosion of the Knox Subglacial Sedimentary Basin, East Antarctica. *Geophysical Research Letters*, *43*, 10,728–10,737. https://doi.org/10.1002/2016gl071063

Matthews, K. J., Maloney, K. T., Zahirovic, S., Williams, S. E., Seton, M., & Müller, R. D. (2016). Global plate boundary evolution and kinematics since the late Paleozoic. *Global and Planetary Change*, *146*, 226–250. https://doi.org/10.1016/j.gloplacha.2016.10.002

McDowell, F. W., McIntosh, W. C., & Farley, K. A. (2005). A precise ^{40}Ar–^{39}Ar reference age for the Durango apatite (U–Th)/He and fission-track dating standard. *Chemical Geology*, *214*(3–4), 249–263. https://doi.org/10.1016/j.chemgeo.2004.10.002

Metcalfe, I. (2013). Gondwana dispersion and Asian accretion: Tectonic and palaeogeographic evolution of eastern Tethys. *Journal of Asian Earth Sciences*, *66*, 1–33. https://doi.org/10.1016/j.jseaes.2012.12.020

Morlighem, M., Rignot, E., Binder, T., Blankenship, D., Drews, R., Eagles, G., et al. (2020). Deep glacial troughs and stabilizing ridges unveiled beneath the margins of the Antarctic ice sheet. *Nature Geoscience*, *13*(2), 132–137. https://doi.org/10.1038/s41561-019-0510-8

Morón, S., Cawood, P. A., Haines, P. W., Gallagher, S. J., Zahirovic, S., Lewis, C. J., & Moresi, L. (2019). Long-lived transcontinental sediment transport pathways of East Gondwana. *Geology*, *47*(6), 513–516. https://doi.org/10.1130/g45915.1

Mulder, J. A., Halpin, J. A., Daczko, N. R., Orth, K., Meffre, S., Thompson, J. M., & Morrissey, L. J. (2019). A multiproxy provenance approach to uncovering the assembly of East Gondwana in Antarctica. *Geology*, *47*(7), 645–649. https://doi.org/10.1130/g45952.1

Norvick, M. (2004). Tectonic and stratigraphic history of the Perth Basin. *Geoscience Australia Record*, *16*(2004), 30.

O'Donnell, J. P., & Nyblade, A. A. (2014). Antarctica's hypsometry and crustal thickness: Implications for the origin of anomalous topography in East Antarctica. *Earth and Planetary Science Letters*, *388*, 143–155. https://doi.org/10.1016/j.epsl.2013.11.051

Pappa, F., Ebbing, J., Ferraccioli, F., & van der Wal, W. (2019). Modeling satellite gravity gradient data to derive density, temperature, and viscosity structure of the Antarctic lithosphere. *Journal of Geophysical Research: Solid Earth*, *124*, 12,053–12,076. https://doi.org/10.1029/2019JB017997

Paxman, G. J. G., Jamieson, S. S. R., Ferraccioli, F., Bentley, M. J., Ross, N., Armadillo, E., et al. (2018). Bedrock Erosion surfaces record former East Antarctic Ice Sheet extent. *Geophysical Research Letters*, *45*, 4114–4123. https://doi.org/10.1029/2018gl077268

Paxman, G. J. G., Jamieson, S. S. R., Ferraccioli, F., Bentley, M. J., Ross, N., Watts, A. B., et al. (2019). The role of lithospheric flexure in the landscape evolution of the Wilkes Subglacial Basin and Transantarctic Mountains, East Antarctica. *Journal of Geophysical Research: Earth Surface*, *124*, 812–829. https://doi.org/10.1029/2018jf004705

Paxman, G. J. G., Jamieson, S. S. R., Hochmuth, K., Gohl, K., Bentley, M. J., Leitchenkov, G., & Ferraccioli, F. (2019). Reconstructions of Antarctic topography since the Eocene–Oligocene boundary. *Palaeogeography, Palaeoclimatology, Palaeoecology*, *535*, 109346. https://doi.org/10.1016/j.palaeo.2019.109346

Paxman, G. J. G., Watts, A. B., Ferraccioli, F., Jordan, T. A., Bell, R. E., Jamieson, S. S. R., & Finn, C. A. (2016). Erosion-driven uplift in the Gamburtsev Subglacial Mountains of East Antarctica. *Earth and Planetary Science Letters*, *452*, 1–14. https://doi.org/10.1016/j.epsl.2016.07.040

Pinet, N. (2016). Far-field effects of Appalachian orogenesis: A view from the craton. *Geology*, *44*(2), 83–86. https://doi.org/10.1130/g37356.1

Reiners, P. W., Farley, K. A., & Hickes, H. J. (2002). He diffusion and (U–Th)/He thermochronometry of zircon: Initial results from Fish Canyon Tuff and Gold Butte. *Tectonophysics*, *349*(1–4), 297–308. https://doi.org/10.1016/S0040-1951(02)00058-6

Reiners, P. W., Spell, T. L., Nicolescu, S., & Zanetti, K. A. (2004). Zircon (U-Th)/He thermochronometry: He diffusion and comparisons with $^{40}Ar/^{39}Ar$ dating. *Geochimica et Cosmochimica Acta*, *68*(8), 1857–1887. https://doi.org/10.1016/j.gca.2003.10.021

Rolland, Y., Bernet, M., van der Beek, P., Gautheron, C., Duclaux, G., Bascou, J., et al. (2019). Late Paleozoic ice age glaciers shaped East Antarctica landscape. *Earth and Planetary Science Letters*, *506*, 123–133. https://doi.org/10.1016/j.epsl.2018.10.044

Sauermilch, I., Whittaker, J. M., Bijl, P. K., Totterdell, J. M., & Jokat, W. (2019). Tectonic, oceanographic, and climatic controls on the cretaceous-Cenozoic sedimentary record of the Australian-Antarctic Basin. *Journal of Geophysical Research: Solid Earth*, *124*, 7699–7724. https://doi.org/10.1029/2018JB016683

Thomson, S. N., Reiners, P. W., Hemming, S. R., & Gehrels, G. E. (2013). The contribution of glacial erosion to shaping the hidden landscape of East Antarctica. *Nature Geoscience*, *6*(3), 203–207. https://doi.org/10.1038/ngeo1722

Tochilin, C. J., Reiners, P. W., Thomson, S. N., Gehrels, G. E., Hemming, S. R., & Pierce, E. L. (2012). Erosional history of the Prydz Bay sector of East Antarctica from detrital apatite and zircon geo- and thermochronology multidating. *Geochemistry, Geophysics, Geosystems*, *13*, Q11015. https://doi.org/10.1029/2012gc004364

Tucker, N. M., Hand, M., & Clark, C. (2020). The Bunger Hills: 60 years of geological and geophysical research. *Antarctic Science*, *32*(2), 85–106. https://doi.org/10.1017/s0954102019000403

Veevers, J. J. (2018). Gamburtsev Subglacial Mountains: Age and composition from morainal clasts and U–Pb and Hf-isotopic analysis of detrital zircons in the Lambert Rift, and potential provenance of east Gondwanaland sediments. *Earth-Science Reviews*, *180*, 206–257. https://doi.org/10.1016/j.earscirev.2018.03.002

Veevers, J. J., & Powell, C. M. (1994). Permian-Triassic Pangean basins and foldbelts along the Panthalassan margin of Gondwanaland (Vol. 184): Geological Society of America.

Veevers, J. J., & Tewari, R. C. (1995). Gondwana master basin of Peninsular India between Tethys and the interior of the Gondwanaland Province of Pangea. In J. J. Veevers & R. C. Tewari (Eds.), (Vol. 187, pp. 0): Geological Society of America.

Wagner, G., Gleadow, A., & Fitzgerald, P. (1989). The significance of the annealing zone in apatite fission-track analysis: Projected track length measurements and uplift chronology of the Transantarctic Mountains. *Chemical Geology: Isotope Geoscience Section*, *79*(4), 295–305.

Weber, U. D., Kohn, B. P., Gleadow, A. J. W., & Nelson, D. R. (2005). Low temperature Phanerozoic history of the northern Yilgarn Craton, Western Australia. *Tectonophysics*, *400*(1–4), 127–151. https://doi.org/10.1016/j.tecto.2005.03.008

Wildman, M., Brown, R., Beucher, R., Persano, C., Stuart, F., Gallagher, K., et al. (2016). The chronology and tectonic style of landscape evolution along the elevated Atlantic continental margin of South Africa resolved by joint apatite fission track and (U-Th-Sm)/He thermochronology. *Tectonics*, *35*, 511–545. https://doi.org/10.1002/2015tc004042

Wopfner, H. (1980). Development of Permian intracratonic basins in Australia. Paper Presented at the Gondwana Five. Proceedings of the Fifth International Gondwana Symposium, Wellington, New Zealand.

Wopfner, H., & Jin, X. C. (2009). Pangea Megasequences of Tethyan Gondwana-margin reflect global changes of climate and tectonism in Late Palaeozoic and Early Triassic times—A review. *Palaeoworld*, *18*(2–3), 169–192. https://doi.org/10.1016/j.palwor.2009.04.007

Young, D. A., Wright, A. P., Roberts, J. L., Warner, R. C., Young, N. W., Greenbaum, J. S., et al. (2011). A dynamic early East Antarctic Ice Sheet suggested by ice-covered fjord landscapes. *Nature*, *474*(7349), 72–75. Retrieved from. https://doi.org/10.1038/nature10114

Zalán, P. V., Wolff, S., Astolfi, M. A. M., Vieira, I. S., Concelcao, J. C. J., Appi, V. T., et al. (1990). The Parana Basin, Brazil: Chapter 33: Part II. Selected Analog Interior Cratonic Basins: Analog Basins.